Voltage Properties of Optically Injected Long Wavelength VCSELs: Theory and Experiment

AIDAN DALY

NATIONAL UNIVERSITY OF IRELAND, CORK

A thesis presented for the degree of

DOCTOR OF PHILOSOPHY

DEPARTMENT OF PHYSICS

UNIVERSITY COLLEGE CORK

TYNDALL NATIONAL INSTITUTE

Supervisor: Mr. Brian Corbett

Co-Supervisor: Dr. Frank Peters

Head of Department: Prof. John McInerney

JANUARY 2014

By its nature, every endeavour employing the scientific method requires a significant amount of effort. This thesis is no different but having the privilege of contributing to the body of human knowledge easily justifies the toil involved.

I certify that this thesis is my own work and that I have not obtained a degree from University College Cork or from any other university on the basis of the work submitted in this thesis.

Aidan Daly

Acknowledgements

I've always had an interest in light and lasers so during the third year of my undergraduate degree I asked my optics and electromagnetism lecturer, Dr. Frank Peters, did he know anyone in the Tyndall National Institute who would take me on as a summer intern. Frank recommended I contact the head of the III-V Materials and Devices group, Brian Corbett. If I had known how much work would arise from such an innocent request I'm not sure I'd have asked! Brian graciously took me on and over the summer I learned the basics of semiconductor lasers and optical experiments. I thoroughly enjoyed my internship and was eager to continue with more serious research so I expressed my interest in starting a PhD. Luckily, Brian was involved with an EU FP7 project on tuneable long wavelength VCSELs called Subtune which was starting at good time for me. So, in September 2008, I proudly became a Doctoral Candidate with Brian as my supervisor and Frank as my co-supervisor. Having started confidently, over the next six months I began to realise just how out of my depth I was and how good everyone else around me seemed to be! The next four and a half years were a rollercoaster ride of hard work, countless mistakes/learning opportunities and blind alleys characterised by months of theoretical and laboratory efforts dotted with occasional successes in a desperate struggle to keep my head above water....all standard PhD. stuff.

Over the course of my PhD. I got to know a staggering number of people so it will be impossible to mention everyone but I am thankful to every person for making my time in Tyndall so memorable.

I am sincerely grateful to Brian Corbett for being a fantastic supervisor. Despite being very busy, he was always available. Our meetings were always

conducted at a level just above my own which meant I was constantly learning and being challenged but his advice was always encouraging and constructive. I appreciate that Brian was rapid in reviewing any writing or results I had sent to him and also for ensuring I was always supported financially. By example, he set high standards and taught me how to question, test, analyse and interpret the world around me in a scientific way. Brian's appearances in the lab usually meant my experiments would inevitably fail. As time went by his 'visitor effect' radius thankfully got smaller. I'm also grateful for the chance he gave me to be exposed to all aspects of the semiconductor industry before leaving Tyndall.

My co-supervisor Frank Peters always had constructive advice and direction whenever we discussed my work and continually made his lab facilities available to me. Frank's ever positive disposition makes approaching him to take advantage of his vast technical knowledge all the easier.

Thank you to my Viva Voce examiners, Prof. Krassimir Panajotov and Prof. John McInerney, for taking the time to read my thesis in detail and put me through my paces. Your questions were considered and thought provoking.

I would like to express my deep gratitude to two senior researchers in the III-V group, John Justice and Dr. Brendan Roycroft. John, who has an uncanny ability to jump rapidly from theory to the clean room to the test lab and back again seemingly without breaking stride, was responsible for re-explaining a lot of the fundamentals of VCSELs to me if I was struggling. He became both my mentor and general go-to guy for nearly everything and I thank him for being both a good colleague and friend. Brendan and I shared an interest in optical injection and worked closely in the lab and on theory as we bounced ideas off each other. I regularly had invaluable discussions with Brendan as we tried to develop our understanding of the relationship between the descriptive mathematics and the device physics. Their guidance in the test lab on performing comprehensive optical measurements was invaluable.

Thanks also to the rest of the III-V gang too for being easy to get on with and making life enjoyable: Donagh, Farzan, Pleun, Mahbub, Ian, James, Carmel, Roger, Carmel, Bill, Michael, Pawel, Alin, Usman, Omar, Ragh,

Roberto, Liam, Peter, Nan and Nazmul. I'd also like to thank my friends from Prof. Paul Townsend's Photonics Systems Group: Alan, Stefano, Aisling, Cleitus and Daniel with whom I did the transmissions experiments and to Eddie, Chris and Padraic from Frank's Integrated Photonics Group for being my next lab door neighbours. Also thanks to Dr. Simon Osborne and Eoin Clerkin for always being good for a chat about bifurcations and for their vital help with the tricky piece of software that is AUTO. Our interns Federica, Sandra and Andreas were great at keeping me on my toes and keeping things lively in the lab.

My thanks goes to Prof. Peter Meißner for his excellent co-ordination of Subtune. Thanks to my colleagues and friends who I met through Subtune, especially Benjamin, Tobias, Christian and Karolina, some of whom I went on to work with professionally at Vertilas. Between them they make the best long wavelength MEMS-VCSELs in the world! I would like to acknowledge the non-student partners in the project particularly Prof. Markus-Christian Amann and Dr. Markus Ortsiefer without whom long wavelength VCSEL technology would not be where it is today.

It's not where you are but who you're with that counts and I was surrounded by great people who were wading their own path through the non-Newtonian fluid that is a PhD. In particular, I have to thank the core of the Block A tea group, my very good friends Brian, Rose, Mark, Conor, Cormac and Donal as sometimes the only thing that can keep you sane is a tea break with a rant and some puns! Given the amount of tea we drank, our sanity was clearly an issue! Without you my PhD. time would have been duller - I might have been finished sooner though! I'd like to especially thank all round nice guy Brian McCarthy for being a genuine friend and decent flat mate.

Fortunately, I made so many friends that it's impractical to name you all so I'll have to summarise: The fantastic Tyndall tag rugby team, the ever changing 3.2.52 crowd, UCC Karate and everyone from Block A & Block B! The original Tyndall bunch: Colm, Claire, Rathnait, Padraig, Ronan, Santosh, Nick, Pierre, Courtney, Dorota, Nicolas, Finbarr and Jeff. The wise cracking funniest circle of friends I've ever had. My UCC friends: Gráinne,

Tara, Eoin, Brian Mc, Gearóid, Diarmuid, Brendan, Eddie, Colm, Brian, Laura, Mary and the others. You're all really cool and fun people. My friends from school: Conrad, Rory, Brian, Danny, Mike, John, Dan, Seamus, Micheál, JP and Chris. We're scattered across the globe at the moment but you're the people I'd be hanging out with if I could. The South Coast Divers motley crew for being a breath of compressed air compared to academia. A Sunday spent diving on the Old Head with you guys really helps off-gas the stress of the rest of the week. To Jane and her family for being more welcoming and kind than I could ever have wished for. Everyone who keeps Tyndall ticking along smoothly - Facilities, CFF, IT (especially Don and Alan), Finance, HR, the security staff, ISS, Donal and Dermot in the workshops and anyone else I forgot: thank you all very much.

A special heartfelt mention goes to my girlfriend, Monika Żygowska, who bore the brunt of my crankiness over the last few years. You have been my constant companion and even with your own PhD. and life woes you have always been able to make me smile. Your boundless energy, cheekiness and love has enriched my life. Dziękuje bardzo also to Marta, Iwona and Helenka for all their best wishes from Polska.

My deepest thanks however must go to my parents, Mary and Neil, for the ceaseless support and love they have shown me my whole life. I will be forever appreciative of all of the opportunities they have given me. Thanks to the rest of my family Conor, Grace and Breda for the interest, support and understanding you have always shown me. I'm lucky to have you all.

To my parents

Abstract

Future high speed communications networks will transmit data predominantly over optical fibres. As consumer and enterprise computing will remain the domain of electronics, the electro-optical conversion will get pushed further downstream towards the end user. Consequently, efficient tools are needed for this conversion and due to many potential advantages, including low cost and high output powers, long wavelength Vertical Cavity Surface Emitting Lasers (VCSELs) are a viable option. Drawbacks, such as broader linewidths than competing options, can be mitigated through the use of additional techniques such as Optical Injection Locking (OIL) which can require significant expertise and expensive equipment. This thesis addresses these issues by removing some of the experimental barriers to achieving performance increases via remote OIL.

Firstly, numerical simulations of the phase and the photon and carrier numbers of an OIL semiconductor laser allowed the classification of the stable locking phase limits into three distinct groups. The frequency detuning of constant phase values (ϕ) was considered, in particular $\phi = 0$ where the modulation response parameters were shown to be independent of the linewidth enhancement factor, α. A new method to estimate α and the coupling rate in a single experiment was formulated.

Secondly, a novel technique to remotely determine the locked state of a VCSEL based on voltage variations of $2\,\mathrm{mV} - 30\,\mathrm{mV}$ during detuned injection has been developed which can identify oscillatory and locked states. 2D & 3D maps of voltage, optical and electrical spectra illustrate corresponding behaviours.

Finally, the use of directly modulated VCSELs as light sources for passive optical networks was investigated by successful transmission of data at 10 Gbit/s over 40 km of single mode fibre (SMF) using cost effective electronic dispersion compensation to mitigate errors due to wavelength chirp. A widely tuneable MEMS-VCSEL was established as a good candidate for an externally modulated colourless source after a record error free transmission at 10 Gbit/s over 50 km of SMF across a 30 nm single mode tuning range. The ability to remotely set the emission wavelength using the novel methods developed in this thesis was demonstrated.

Publication List

Journal Articles

- Daly, A., Gierl, C., Gründl, T., Grasse, C., Zogal, K., Carey, D., Townsend, P., Amann, M.-C., Meissner, P. and Corbett, B. *10 Gbit/s transmission over 50 km of SMF using MEMS tunable VCSEL*, Electronics Letters, vol. 48, no. 7, pp. 394–396, (2012)

- Daly, A., Gründl, T., Hüber, S., Müller, M., Roycroft, B., Amann, M.-C., and Corbett, B. *Voltage Spectroscopy and the Operating State of an Optically Injected Long Wavelength VCSEL*, Photonics Technology Letters, IEEE, vol. 24, no. 14, pp. 1245–1247 (2012)

- Aidan Daly, Brendan Roycroft and Brian Corbett. *Stable locking phase limits of optically injected semiconductor lasers*, Optics Express, vol. 21, no. 25, pp. 30126-30139 (2013)

- F. Gity, A. Daly, B. Snyder, F. Peters, J. Hayes, C. Colinge, A. Morrison and B. Corbett. *Ge/Si heterojunction photodiodes fabricated by low temperature wafer bonding*, Optics Express vol. 21, no 14, pp. 17309-17314 (2013)

Conference Talks

- Daly, Aidan, Brendan Roycroft, Frank H. Peters, Markus Ortsiefer and Brian Corbett. *Dynamics of 1.55 μm Buried Tunnel Junction VCSELs under optical injection around threshold*, Proc. SPIE 7615, Vertical-Cavity Surface-Emitting Lasers XIV, 76150Q (2010)

- C. Gierl, K. Zogal, S. Jatta, H. A. Davani, F. Küppers, P. Meissner, T. Gründl, C. Grasse, M.-C. Amann, A. Daly, B. Corbett, B. Kögel, A. Haglund, J. Gustavsson, P. Westbergh, A. Larsson, P. Debernardi and M. Ortsiefer. *Tuneable VCSEL aiming for the application in interconnects and short haul systems.* Proc. SPIE 7959, Optical Metro Networks and Short-Haul Systems III, 795908 (2011)

Conference Posters

- A. Daly, B. Roycroft, J. Justice, F. H. Peters and B. Corbett. *Dynamics of optically injected 1.55 μm VCSELs*, Photonics Ireland (2009)

- A. Daly, T. Gründl, A. M. Clarke, C. Grasse, M. Müller, M.-C. Amann, B. Corbett and P. D. Towsend. 10 Gbit/s *Direct Modulated Long-Wavelength VCSELs for Upstream Hybrid TDMA/WDM PON*, Photonics Ireland (2011)

Contents

List of Figures

List of Tables

Chapter 1

Introduction

When the first lasers were developed in the early 1960s, contemporary critics described them as "a solution looking for a problem". Indeed, the 'problem' was quickly found and today lasers are ubiquitous, playing crucial roles in the modern developed world.

Laser mice come with every new desktop computer while bar code scanners help with the identification and management of items from supermarket shelves to operating theatres. Optical storage media still plays a large role despite the increasing growth in solid state memory devices. Red and green laser pointers are found in many businesses and universities while also being used for entertainment purposes supporting concerts and nightclub events. Lasers have been employed in a number of military applications including high power weapon systems, targeting and ranging.

In addition, they are regularly used for scientific purposes including the areas of spectroscopy, laser cooling and optical tweezers. The list of applications continuously grows and covers gas detection, atmospheric sensing and structural integrity monitoring. Industries dependent on laser light in some way currently employ millions of people worldwide. Despite the many successful uses which have already been found, new application fields are constantly explored. For instance, energy generation through controlled nuclear fusion initiated by a constellation of high energy laser beams is currently an exciting and important active research topic.

One major application area was omitted from the above list as it deserves special mention with regards to this thesis: the field of optical communications. Following the introduction of the Internet in the mid-1990s there has been a ceaseless increase in the demand for faster, international digital links with the current driving factor being the desire to stream large amounts of information in the form of high definition video content. As the economies of developing nations grow stronger and technology begins to permeate and diffuse into the daily lives of their citizens, it is anticipated this interest will only increase further.

In order to try to satisfy this demand, both national governments and private enterprise have invested large sums of money to develop and adapt ideas in advanced research laboratories and integrate them into the worldwide communications networks. Scientists and engineers continually find new ways to increase bandwidths and to reduce the energy consumption of existing components while inventing new technologies to replace those elements of the system which can no longer cope with the volume of data traffic. Lasers play a fundamental role in this process as they are used to transmit vast quantities of information in the form of pulses of differing intensity and phase over optical fibres at speeds and distances which far surpass traditional copper wire systems.

Despite the huge amount of R&D work already done on the various aspects of these networks, there are always more avenues worth investigating. In this thesis, the physics of an optically injected laser are theoretically and experimentally examined from a new perspective. The goal of this work is to generate a new method to determine the locked state of an optically injected long wavelength Vertical Cavity Surface Emitting Laser through a study of the voltage change and demonstrate its usefulness in relation to state of the art optical communications.

1.1 Light Amplification through the Stimulated Emission of Radiation

Compared to other light sources, laser light is highly monochromatic with the components sharing a common propagation direction, polarisation and phase. Light with these properties is described as being coherent and can be focused, collimated and create interference fringes better than non-coherent light.

Fundamentally, all lasers have a similar structure based around a resonant cavity defined by two mirrors with reflectivities R_1 and R_2 separated by a distance L as shown in fig. 1.1 (a). These cavities are mostly passive, with a loss of α per unit length, but will contain an externally excited active region capable of providing optical gain through the interaction of light already in the cavity with the electronic structure of the active region material. The power in the oscillating light will have decreased during a single round trip of the cavity due to leakage at both mirrors and due to scattering and absorption in the cavity. The round trip optical path length will be $2nL$ where n is the average refractive index of the cavity but, for VCSELs, the length of the active region, l, will be significantly less than L. If enough gain is available to compensate for the round trip losses, the laser is said to be above threshold and the intensity of the light oscillation in the cavity can begin to build up. The condition for threshold gain, g_{th}, can be stated as:

$$g_{th} = \frac{1}{2l}(2\alpha L - \ln R_1 R_2).$$

In real terms, once this condition is satisfied, further external excitation results in increasing the intensity of the light in the cavity and hence the output power of the laser.

The mechanism for the optical gain/light amplification by stimulated emission can be explained by considering an electronic transition between two energy levels E_1 and E_2. Under normal conditions, an electron will exist in the lowest possible energy state, E_1. If through some excitation mecha-

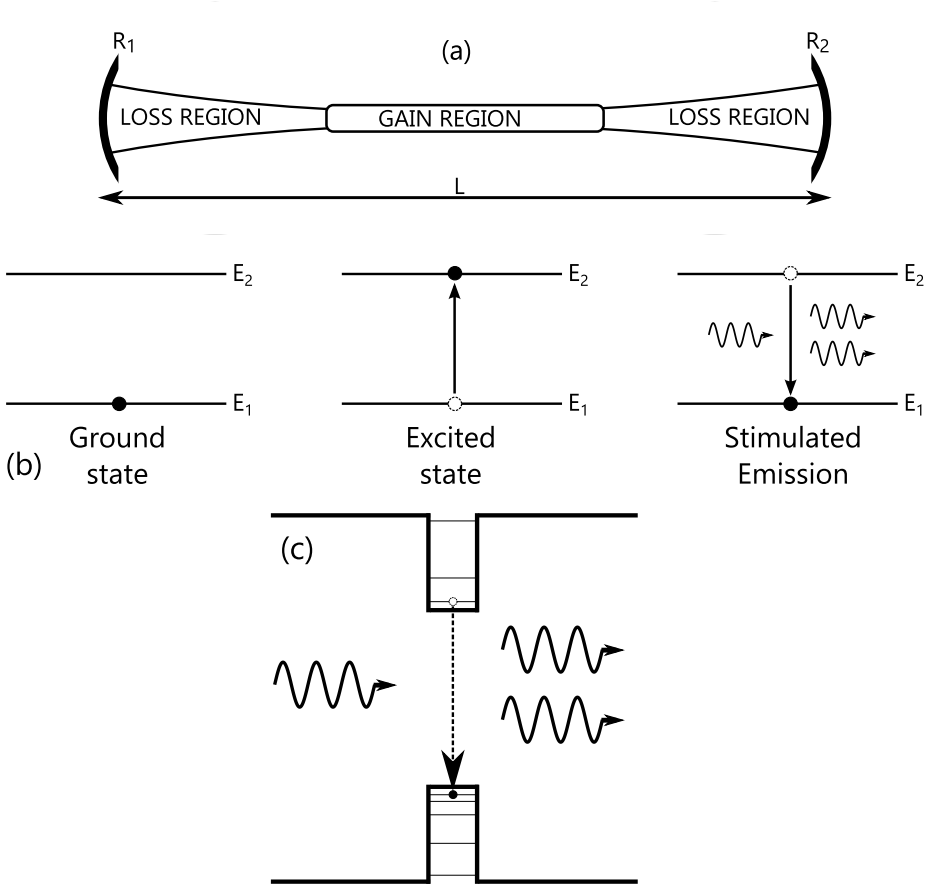

Figure 1.1: (a) Basic cavity structure of a laser which is composed of a stable resonator with a region that provides optical gain, (b) Overview of the mechanism of stimulated emission. An electron gets excited from its ground state to an unstable higher energy state. Radiation or a photon with the same energy as the difference between the two states stimulates the electronic transition resulting in the emission of an identical photon. (c) An overview of a semiconductor quantum well showing quantized energy levels and a transition across the semiconductor bandgap.

nism energy is imparted to the electron, it can transition to the higher level E_2. Since the electron is unstable while occupying this higher energy level, it will eventually drop back to E_1. During this transition, a photon of light with an energy equal to the difference between E_2 and E_1 will be emitted. The frequency of this photon, ν, is given by:

$$\nu = \frac{E_2 - E_1}{h}$$

where h is Planck's Constant. This process is referred to as spontaneous emission and the direction and polarisation of this photon are random. However, if while the electron was in its excited, unstable state (E_2) another photon with frequency ν was to pass through the same part of the active material, the excited electron could be stimulated into its transition at that instant. A photon emitted through a stimulated emission process has the same frequency, polarisation, phase and propagation direction as the photon which initiated the stimulated transition, fig. 1.1 (b). While a single photon may have entered the active region, two identical photons exited, illustrating the basic mechanism for the amplification of light. Various materials can be used to provide the optical gain including gas (HeNe, CO_2), solid-state rare Earth elements (Nd:YAG, Ti:Al_2O_3) or semiconductors (AlGaAs, InGaAsP).

Modern semiconductor lasers use quantum wells to define the energy levels involved in the electronics transitions required for lasing. When a very thin ($< 30\,\text{nm}$) layer of a semiconductor material is grown between two thicker layers, the effects of quantum confinement cause a set of discrete energy levels to replace the pseudo-continuum of energy states which exist in a bulk material. Electrons can be excited or 'pumped' into the higher energy level either electrically or optically using light of a higher frequency than the desired laser transition. The exact energy difference between the two levels involved in the transition depends on the thickness and composition of the quantum well layers, the pumping conditions and some intrinsic properties of the materials. A general schematic of a quantum well is given in fig. 1.1 (c). In real devices, multiple quantum wells are often stacked on top of each other to increase the amount of available optical gain. A more formal discussion on

the physics of semiconductor lasers such as quantum well energy band structures, the population inversion condition for net optical gain, the dependence on charge carrier concentrations and spontaneous versus stimulated emission can be found in [10].

1.2 VCSELs

Vertical Cavity Surface Emitting Lasers or VCSELs are a type of semiconductor laser which use quantum wells to provide optical gain. As the name suggests, the direction of the light emission is vertical, rather that parallel to the substrate which is the case for many other semiconductor lasers generically referred to here as edge emitting lasers. Schematic structures for an edge emitter and a short wavelength VCSEL are shown in fig. 1.2 to illustrate the differences between the two designs. The VCSEL configuration introduces a number of attractive features at both production and application level.

During the fabrication stage each device can be tested on-wafer prior to being diced into individual units. This parallel processing approach offers a significant cost reduction over the case where the optical cavity isn't necessarily defined until each laser has been individually cleaved from the wafer and manually tested to determine its properties.

Once manufactured, VCSELs have low operational power requirements and can lase with very low threshold currents ($\ll 1\,\mathrm{mA}$) due to their small active volumes although this does place other restrictions on the quality of the optical cavity. In the case where strict wavelength control is not required, VCSELs can generally operate without any form of cooling system and can be designed to have optimal output powers across a range of temperatures. High coupling efficiencies (up to 50%) to standard single mode fibres are found due to a circular emission profile from the the fundamental Laguerre-Gaussian mode, see fig. 1.3 where the fundamental mode, L_{00}, and some less desirable but still possible higher order modes are shown. Ignoring potential polarisation switching, VCSELs will not hop between longitudinal modes with increased bias current as it is the cavity geometry rather than the peak

of the optical gain determines which mode will lase. A side benefit of this is that, while the output power rises as the gain peak and cavity mode come into optimal alignment with increasing current, it also decreases at higher currents beyond this point. This does limit the maximum output power but eliminates the possibility of catastrophic optical damage to the mirrors due to high power densities, aiding device reliability and extending operating lifetimes.

Even though long wavelength (1550 nm) VCSELs are steadily approaching the 10 mW output power level while operating in a single fundamental mode [9], higher powers may be required. Their planar form naturally lends itself to two dimensional arrays of various shapes and sizes. Each VCSEL may be addressed individually, as in multi-channel geometries, or else a group of lasers can be biased in parallel for high power applications.

A simple edge emitting design will use the cleaved ends of the semiconductor bars as the mirrors to establish the resonator cavity. This single semiconductor air interface only reflects about 30% of the incident light. These large losses are compensated for by active regions spanning the entire length of the cavity which provide ample optical gain. VCSELs, on the other hand, have very short active regions: an intrinsic restriction imposed by their geometry. These quantum well layers are typically approx. 10 nm thick but multiple quantum wells are usually grown in close proximity and located near an anti-node of the electric field to increase their effect. Some designs have placed individual quantum wells at separate anti-nodes to maximize the gain [11]. Due to the limited amount of optical gain which can be provided, resonator losses must be minimized. Mirrors consisting of alternating layers of quarter wavelength thick semiconductor materials with different refractive indices, known as Distributed Bragg Reflectors (DBRs), are used to define the optical cavity. These mirrors must typically provide reflectivities above 99.9% in order to satisfy the necessary conditions for lasing. In the case of a DBR made out of semiconductors with a refractive index difference of 0.02, 40 mirror pairs will be required to achieve a reflectivity above 99%. A dielectric DBR can have a much higher index contrast of around 2.4 meaning that only 3 mirror pairs are necessary to achieve a reflectivity over 99.8%.

Relative to edge emitters, a VCSEL cavity is very short, generally on the order of 5 optical wavelengths. A large free spectral range is an intrinsic property of a short cavity so that VCSELs typically operate in only a single longitudinal mode. The transverse optical mode properties are dictated by an aperture which serves to confine the current to attain the high current density needed to achieve population inversion and lasing. For small enough diameters, no high order transverse modes will be sustained but the maximum output power will also be limited due to effects such as spatial hole burning. This aperture is usually formed in a steam chamber by oxidising a high Aluminium content layer from the outside of the mesa in towards the middle. While technically easy to implement, attaining a high level of repeatability is difficult. Alternatively, proton implantation can be used to destroy the crystal lattice everywhere except for the area through which the current must pass. The simplest current paths are shown in fig. 1.2 (b) where the electrical contacts are deposited on the top DBR and onto the underside of the (thinned) substrate.

1.2.1 Long wavelength VCSELs

A schematic of a long wavelength VCSEL is shown in fig. 1.4. In order for the VCSEL to emit around 1550 nm, an AlInGaAs active region is grown via Molecular Beam Epitaxy onto lattice matched InP. Different strain gradients in the active region are used depending on whether the VCSEL will be used for a high speed or a high power application.

Due to high series resistance caused by low hole mobility, there is a heat generation issue when using p-InP on the p side of the InGaAlAs active region. These drawbacks are negated by implementing a Buried Tunnel Junction (BTJ) consisting of a p^{++}-AlInGaAs and an n^{++}-InGaAs layer which only allows current conduction through a photolithographically structured aperture. The BTJ utilizes quantum tunnelling to allow electrons cross the material band gap without a radiative emission allowing the use of high mobility n-type on the p-side of the active region [12].

The BTJ naturally provides current confinement for control over the op-

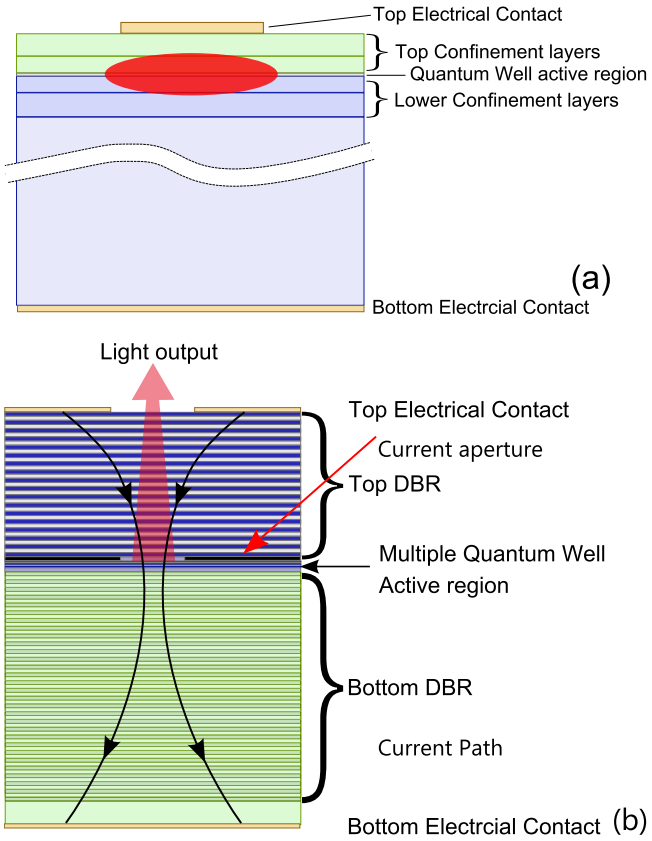

Figure 1.2: (a) Schematic of an edge emitter which has a horizontal cavity and emits with an elliptically beam out of the page (b) Schematic of a short wavelength VCSEL which has a vertical cavity and emits with a circular output beam. The original versions of these images were sourced from wikipedia.org. and are used under the Creative Commons Attribution-ShareAlike license system.

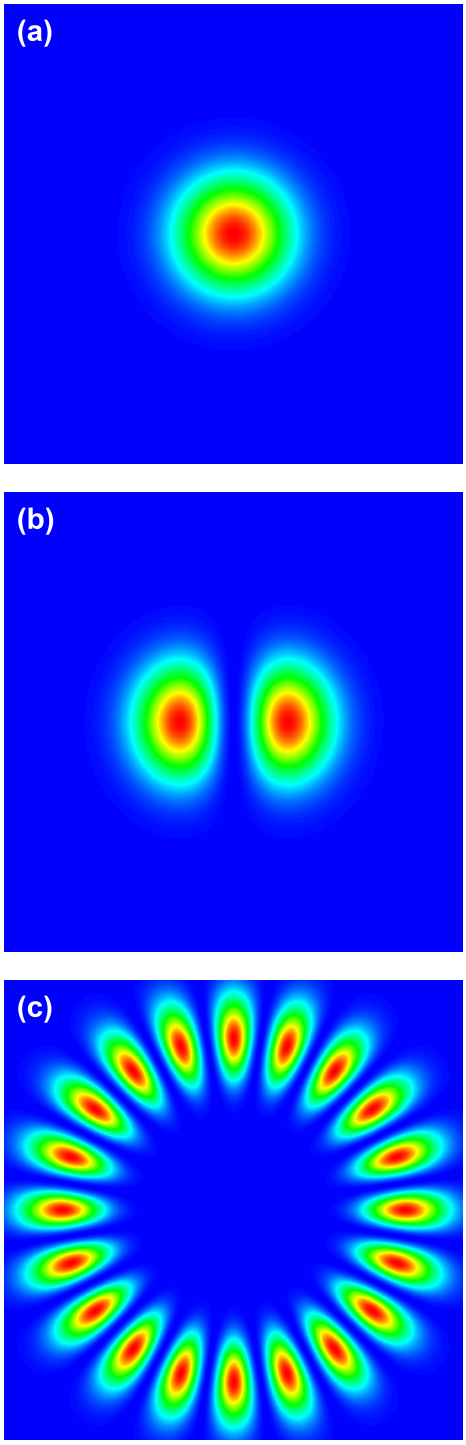

Figure 1.3: Potential emission profiles of VCSELs. Emission in (a) the fundamental Gaussian mode TEM_{00}, (b) a low order transverse mode TEM_{01} and (c) a high order transverse mode TEM_{010} [1]. These Laguerre-Gaussian mode were calculated using the solutions to the cylindrically symmetric paraxial wave equation [2].

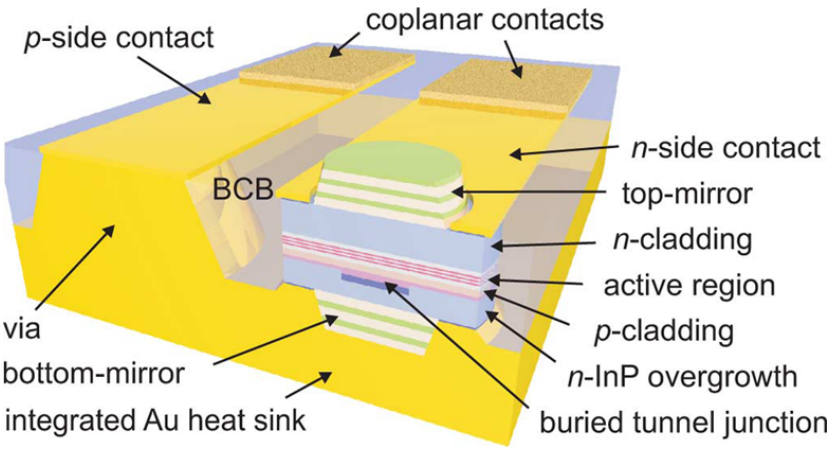

Figure 1.4: Pictorial representation of the short cavity Vertical Cavity Surface Emitting Laser used in this thesis [3]. The device is composed of an AlInGaAs active region, a Buried Tunnel Junction and two dielectric DBR mirrors. High speed, co-planar contacts and BCB encapsulation aid direct modulation at over 15 GHz.

tical modes in the cavity. The n^+ side of the BTJ is later overgrown with a n^+-InP current spreading layer before three and half pairs of CaF_2/α-Si are deposited to serve as the bottom DBR. A 60 µm gold layer is electrodeposited over the mirror to aid mechanical stability, heat dissipation and mirror functionality. The entire InP substrate is removed with further etching, defining a mesa around each BTJ. Back filling with a plastic called benzocyclobutene (BCB) helps to reduce parasitic effects during high speed operation. Finally, both contacts are deposited on the top of the device, with a via-hole through the BCB completing the circuit to the *p*-side of the active region, along with the top dielectric mirror (CaF_2/ZnS). Sample power-voltage-current curves and optical spectra for these devices are given in section 4.1. Record output powers of 8 mW [9] and record resonance responses of 17 GHz frequencies [13] have been achieved with similar designs.

The VCSELs used in this thesis were developed and produced by researchers in the group of Prof. Dr. Markus-Christian Amann at the Walter Schottky Institute of the Technische Universität München (TUM) [13]. Related devices which have an epitaxial semiconductor top DBR are also used in section 4.2. These devices were kindly provided by Vertilas GmbH under

the European Union funded project Subtune. Vertilas was founded by TUM researchers to commercialize the long wavelength VCSEL technology developed under Prof. Amann [14]. Tuneable long wavelength VCSELs have also been developed in a long term partnership between TUM and the Technical University of Darmstadt. In those devices, the top mirror is placed onto a membrane, varying the cavity length in response to the heating effect of an electric current [15], [16]. Further details of these VCSELs are given in chapter 2 and section 5.2.1.

1.3 Introduction to locked systems

At a general level, the concept of injection locking can be considered as the coupling of two otherwise independent oscillators. While the usual example for the earliest study in the field is that of Christiaan Huygens observing the synchronization of pendulum clocks through micro-vibrations while hanging from a common beam in the 1600s, unbeknownst to themselves some of the earliest natural philosophers were struggling with a related problem as they tried to understand the motion of the moon around the earth. For Huygen's the oscillations were the motion of the pendula, for the celestrial bodies the oscillations are the orbital rotations.

In a phenomenon called tidal locking, the same gravitational forces which cause our oceans on Earth to move in response to the moon's orbit induce tidal forces in the lunar mass. This pulling effect is small but over time this mutual interaction will cause the rotational periods of both bodies to synchronise with each other. The effect on the moon is much greater due to the size difference between the two bodies.

Several billion years ago, the moon and earth had completely different rotational properties. Currently a full lunar rotation nearly matches the time needed for a full orbit around the Earth (28 days) and results in only 70% of the moon's surface being visible from Earth. Eventually the rotational rates of both bodies will slow and fully synchronize so that the same 50% of the moon will constantly face the Earth. Other factors, such as the effect of the Sun; the reduction in the strength of tidal pulling due to decreased

rotational rates and changes in the Earth-Moon distance due to angular momentum conservation reasons, will influence the final steady state.

1.3.1 Optically injected lasers

An analogous system for lasers occurs when light from one laser is incident into the optical cavity of another. The simplest case does not include bi-directional coupling [17], which is unavoidable in the case of tidal locking. Whereas in the gravitational case the various parameters are fixed naturally through the size of the bodies and the laws of Newtonian gravity, for an optically injected laser there are many adjustable parameters through which the system can be investigated.

Under free running conditions the injected laser, referred to here as the VCSEL, will emit at a certain frequency and output power, both of which are dependent on gain, bias and optical cavity considerations. The injected light is fully independent and will usually have a much narrower linewidth. Once the injected light is coupled into the VCSEL cavity an interaction between the cavity light and the injected light occurs. Assuming matched polarisations of the injected light and the VCSEL output, three metrics are normally used to describe the injected light:

Frequency Detuning: The difference in frequency between the injected light and cavity light. The cavity frequency will change due to the injection but the detuning is always quantified relative to the free running value. The induced dynamics will be dependent on detuning which can be easily changed by using a tuneable laser as the source of the injected light.

Injection Strength: The amount of light injected into the VCSEL cavity is also important and greatly effects the dynamics. It can be experimentally given in terms of the estimated power incident into the VCSEL cavity, usually quantified relative to the original free running VCSEL output power. Issues such as optical mode mismatches or reflections from the top mirror influence the accuracy of these estimates. The

theoretical work as part of this thesis considers the number of photons entering the VCSEL cavity.

Coupling Rate: The extent to which the injected and VCSEL field interact with each other is also influential. For instance, if there is zero coupling between the fields it will make no difference what the frequency detuning or injection strength is and the VCSEL will act as if free running. A high coupling rate means that even extremely weak injection will have a sizable effect. The actual coupling rate is fixed for a given laser but varies from device to device.

1.3.2 Injection locked rate equations

A mathematical model of such an injected system was developed from work on optical feedback by Lang and Kobayashi [18]. This model, referred to as the single mode optical injection locking rate equations, is a set of three coupled ordinary differential equations for the photon number, S, carrier number, N, and locked phase, ϕ. These rate equations have been widely investigated over the last several decades [19], [7], [20], [6]:

$$\frac{dS}{dt} = [G_0(N - N_{tr}) - \gamma_p]S + 2k\sqrt{S_{inj}S}\cos(\phi) \tag{1.1}$$

$$\frac{d\phi}{dt} = \frac{\alpha}{2}(G_0(N - N_{tr}) - \gamma_p) - 2\pi\Delta\nu - k\sqrt{\frac{S_{inj}}{S}}\sin(\phi) \tag{1.2}$$

$$\frac{dN}{dt} = \frac{I}{q} - \gamma_n N - G_0(N - N_{th})S \tag{1.3}$$

This system can be derived through phenomenological arguments as in appendix A. A list of the meanings of the parameters used and their values is given in table 1.1. Unless otherwise stated, these values are used throughout this thesis.

Most of these parameters have fixed values but the number of injected photons, S_{inj}, and the linear frequency detuning, $\Delta\nu$ are considered as free parameters which will be varied both theoretically and experimentally. It is

convenient to use the injection ratio defined in deciBel relative to the free running photon number as $R = 10\log_{10}(S_{inj}/S_{fr})$ for discussion even though it doesn't appear directly in the equations.

In addition, the extent to which injected photons influence the cavity dynamics must be considered. The coupling rate, k, is that measure of the strength of this interaction. Schunk [21] and Chrostowski [22] have derived expressions for k based on the mirror reflectivity but noted that these expression do not match to experimental results for high-Q cavities. Often this parameter is used for fitting theoretical work to experimental results [23]. A new experimental method to determine k is proposed in chapter 3. The terms in eqs. (1.1) to (1.3) relating to the injection always contain the combination $k\sqrt{S_{inj}}$ and not either individual quantity in isolation.

In principle, the DBR mirror through which the injected light passes has a reflectivity which is a function of frequency so that even for a constant injection power the amount which gets to the active region is not necessarily constant. This could be taken into account with a coupling rate which is also a function of detuning but is not addressed here.

The transparency carrier number, $N_{tr} = 3.16673 \times 10^6$, is the minimum carrier number required for optical gain. A lower carrier number than this means the quantum well is an absorbing rather than transparent element of the cavity. The value chosen here equates to a carrier density of $1.5 \times 10^{18}\,\mathrm{cm}^{-3}$ based on a circular active region of diameter 8 µm, corresponding to a 5.5 µm BTJ diameter, and depth 42 nm as these values are appropriate for the long wavelength VCSELs [8] used for experimental studies in chapter 4.

When the VCSEL is biased at $I = 0.8\,\mathrm{mA}$, or approximately 2.1 times the calculated threshold current of 0.38 mA, the free-running photon, S_{fr}, and carrier, N_{fr} numbers can be approximated from the rate equations in the absence of optical injection (S_{inj} or $k = 0$) as:

$$N_{fr} = N_{tr} + \gamma_p/G_0 \tag{1.4}$$
$$= 4.67465 \times 10^6 \tag{1.5}$$
$$S_{fr} = I/\gamma_p q - \gamma_n N_{tr}/\gamma_p - \gamma_n/G_0 \tag{1.6}$$
$$= 14378 \tag{1.7}$$

The linewidth enhancement factor, α, which is a unique feature of semiconductor lasers, quantifies the change in refractive index to the change in gain [19] and is chosen to have a value of 2. This value is chosen as, while values up to 5 are reported for long wavelength VCSELs [24], $\alpha = 2$ keeps the physics discussed in this thesis clear without a loss of detail. The effects of gain saturation due to high photon numbers are not taken into account in this model. Similarly, Langevin noise terms which could be added to each rate equation are also omitted [25].

The modal gain co-efficient G_0 decomposes as $G_0 = \Gamma v_g g/V$ where Γ is the longitudinal confinement factor, v_g is the group velocity, g is the differential gain and V is the active region volume and accounts for the incomplete spatial overlap between the optical mode and region of the laser with optical gain.

The lasers have a low photon lifetime value as the two dielectric DBRs create a shorter effective cavity relative to one defined by semiconductor mirrors. This is because of the low penetration depths into the mirrors due to the refractive index contrast for the dielectric mirror ($\Delta n \simeq 2.4$) being higher than for the semiconductor ($\Delta n \simeq 0.02$).

1.3.3 Possible dynamical trajectories

This system is capable of highly non-linear dynamics and the rate equations can be numerically integrated to determine the variation of S, N and ϕ with time for a given detuning and injection ratio. In this work, the integration was performed using the in-built solvers in the commercial computational software Wolfram *Mathematica* [26] and the code used is included in appendix B. Unstable states include oscillations with a single, two or many

Table 1.1: The symbols used in the investigation of the optical injection equations and the values used in the case of physical constants. The values used were influenced by [4], [5], [6], [7] and private correspondence with the author of [8] and [9].

Parameter	Symbol	Value	Unit
Photon No.	S		
Phase	ϕ		rad
Carrier No.	N		
Injection Ratio	R		
Injected Photon No.	$S_{inj} = 10^{\frac{R}{10}} S_{fr}$		
Linear Frequency Detuning	$\Delta\nu$		
Coupling Rate	k	400×10^9	s^{-1}
Free Running Carrier No.	N_{fr}	$4.674\,69 \times 10^6$	
Free Running Photon No.	S_{fr}	14 379	
Speed of Light	c	3×10^8	$\mathrm{m\,s}^{-1}$
Group Refractive Index	n_g	3.73	
Group Velocity	$v_g = {}^{c}/_{n_g}$	8.102×10^7	$\mathrm{m\,s}^{-1}$
Confinement Factor	Γ	0.04	
Differential Gain	g	8×10^{-20}	m^2
Volume of the Active Region	V	2.111×10^{-18}	m^3
Gain Coefficient	$G_0 = \Gamma \frac{v_g g}{V}$	122 800	s^{-1}
Carrier Lifetime	τ_n	2	ns
Photon Lifetime	τ_p	5.4	ps
Carrier Recombination Rate	$\gamma_n = {}^{1}/_{\tau_n}$	0.5	GHz
Photon Recombination Rate	$\gamma_p = {}^{1}/_{\tau_p}$	185.185	GHz
Transparency Carrier No.	N_{tr}	$3.166\,73 \times 10^6$	
Linewidth Enhancement Factor	α	2	
Threshold Current	I_{th}	0.375	mA
Bias Current	I	0.8	mA
Electron Charge	q	1.6×10^{-19}	C

frequency components and complex chaotic oscillations. The frequencies of the oscillations are functions of the parameters used in the equations and the system can change its behaviour at bifurcation points, see appendix C.

A combination of the experimental evidence and theoretical knowledge of the dynamics which could result in such observations facilitates the determination of the operating state of the VCSEL. The types of dynamics most relevant to this work are:

Stable Locking: The injected laser emits continuously at the injected frequency rather than the frequency of the cavity mode. Internal changes in the injected laser's carrier density are required.

Period 1 Dynamics: The output from the injected laser varies sinusoidally with an amplitude and frequency related to the injection parameters. This is also known as a limit cycle.

Period 2/Period Doubled Dynamics: A second frequency component at half the Period 1 frequency can appear in the oscillating output of the injected laser at a period doubling bifurcation. Successive period doubling bifurcations introduce more frequency components.

Chaos: Chaotic behaviour means that complex deterministic oscillations occur in the laser but with an extreme sensitivity to its initial or noise conditions. The set of discrete frequency components is replaced with a continuous frequency spread.

The most well known method through which chaotic behaviour develops is called the period doubling route to chaos. Here, successive period doubling bifurcations introduce new components so that the output contains a pseudo-continuous range of frequencies. These period doubling bifurcations are nested within each other and obey the Feigenbaum scaling rule so that they occur closer and closer to each other on variation of an injection parameter such as the frequency detuning [27]. Two dimensional systems cannot display chaos and it was thought that optical injection was needed to introduce the third dimension (ϕ) needed. However, recent work on free running

quantum dot VCSELs has shown the existence of chaos due to the non-linear coupling between the two polarisation modes [28].

A relatively complicated example is used to illustrate the interactions of the photon number, phase and carrier number as a function of time and various injection configurations in fig. 1.5.

Injection into a free running VCSEL at a frequency detuning of $\Delta\nu = -1\,\text{GHz}$ is initiated at $t = 1\,\text{ns}$. Some transient relaxation oscillations occur as the laser tends towards a locked state (SIL). The detuning is changed to $\Delta\nu = 1\,\text{GHz}$ and an oscillation with a single frequency is excited (P1). With $\Delta\nu = -3.5\,\text{GHz}$, the VCSEL locks again and with $\Delta\nu = 4.1\,\text{GHz}$ an oscillation with two frequency components is induced (P2). For each different detuning the average photon and carrier numbers are different. When the VCSEL is locked the phase remains constant but during unstable dynamics (P1, P2) it changes non-linearly with time. The injection ratio is $R = -25\,\text{dB}$.

1.3.4 Optical communications

Optical communication networks exist on several scales. There are long haul fibres such as those across the North Atlantic and Pacific oceans, as shown in fig. 1.6 (a), which form the backbone of the Internet. Smaller Metropolitan Area Networks (MANs) deliver data to customers on a city or provincial scale through Internet Service Providers (ISPs) using Access Networks and Local Area Networks which can operate in the 100s to 10s of meters. Many countries around the world are investing in their communication networks, upgrading connections based on copper wire and bringing high speed optical fibre lines closer to the end user who benefits from an increased bandwidth. This, of course, is no trivial problem and myriad technical obstacles, along with sourcing adequate investment, have to be overcome.

Passive Optical Networks (PONs) are of particular interest to this work. PONs operate on the 50 km scale and their individual constituent components should, in principle, require no external power (no amplifiers, no thermoelectric coolers etc.) with exceptions such as the transmitter and receiver

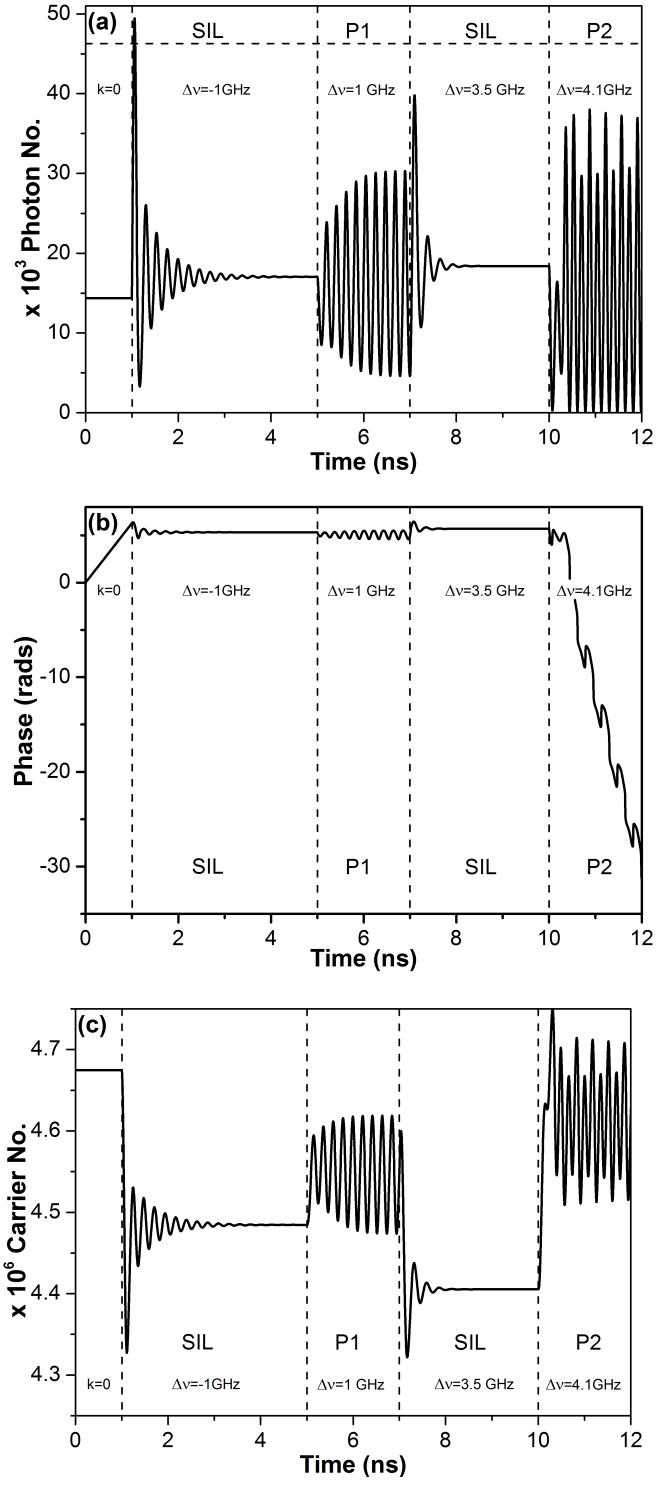

Figure 1.5: Simulated traces for the (a) photon number S (b) locked phase ϕ and (c) carrier number N of an optically injected VCSEL for an injection ratio of $R = -25\,\mathrm{dB}$. At different times, the injected frequency is changed resulting in dynamics which include Stable Injection Locking (SIL), Period 1 dynamics (P1) and Period 2 dynamics (P2).

elements [29]. Minimizing the number of components aids such a power efficient goal which is why directly modulated VCSELs are an attractive light source. Implementations of various architectures such as Dense Wavelength Division Multiplexing (DWDM) [30] and modulation schemes such as polarisation-switched and polarisation-multiplexed quadrature phase-shift keying (PS-QPSK and PM-QPSK) are used to maximise the data rates [31]. A schematic outline of a PON in which the fixed wavelength VCSEL could be used is shown in fig. 1.6 (b).

Dispersion is the phenomenon that the different frequency components of an optical pulse travel with different propagation speeds in an optical fibre. The origin of this is related to the resonant absorption of the optical field by the fibre material whereby the complex electric susceptibility will change depending on the difference between the frequency passing through the fibre and the resonant absorption frequency. Due to the Kramers-Kronig relations and the definitions of the electric permittivity, it follows that a frequency dependent change in refractive index will also occur changing the group velocity of that frequency component [10]. A square shaped pulse will broaden over transmission distance and overlap with neighbouring logical ones or logical zeros causing what is referred to as inter-symbol interference (ISI). Such broadening introduces errors and places limits on the capabilities of modern optical communication systems known as the Bandwidth-Distance Product and has three prime sources [10]:

Chromatic Dispersion: Intrinsic properties of the material through which the light is travelling govern whether high or low frequency components of the pulse will travel faster. In particular, the frequency dependence of the group velocity, which is the speed at which energy and information travel, determines the extent of the dispersion.

Modal Dispersion: The propagation constant of different optical modes depends on the refractive index profile of a multi-mode fibre as they experience different confinement factors in the fibre core and cladding.

Polarisation Mode Dispersion: This is a special case of modal dispersion where the orthogonal polarization modes have two different, albeit

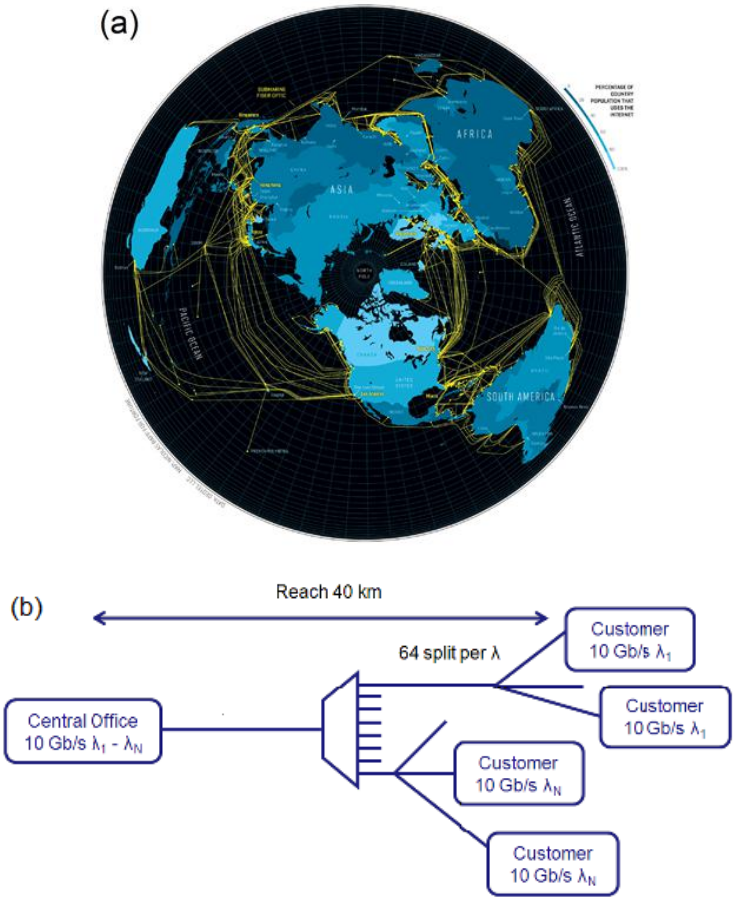

Figure 1.6: (a) An overview of the long haul under-sea optical fibres which form the backbone of the internet. Image taken from nicolasrapp.com (b) The outline of a Passive Optical Network which could be used to deliver network access to a metropolitan area. A directly modulated long wavelength VCSEL could be used as the optical source at the customer's location

very close, propagation constants. Internal and external stresses, such as physical bends, introduce a birefringence into a theoretically polarisation degenerate SMF creating a fast and a slow axis.

Unfortunately due to the relationship between the refractive index and the carrier density, the output of a directly modulated semiconductor laser is composed of multiple frequencies so the pulse will suffer from dispersion effects. In contrast, continuous wave light which is externally modulated by a Mach-Zehnder, for example, is not greatly effected by dispersion. Standard Silica optical fibre demonstrates zero dispersion at approx. 1310 nm but normally a longer wavelength region near 1550 nm is used for transmission as that is an absorption minimum and Erbium Doped Fibre Amplifiers (EDFAs) operate in that spectral range. There are four general approaches to dealing with chromatic dispersion from directly modulated lasers:

1. By pre-chirping, or distorting, the optical signal before transmission to use the known chromatic dispersion constructively.

2. By replacing some of the standard single mode fibre with an appropriate length of dispersion-compensating fibre (DCF).

3. By using various error detection methods in the electronics domain at the receiver end on order to correct for the dispersion.

4. By injection locking the laser to pin the carrier level so that the frequency chirp is greatly reduced.

The work in this thesis relates to the final two options. In chapter 5, error free transmission at 10 Gbit/s is demonstrated by using Electronic Dispersion Compensation (EDC) to compensate for the chirp during optical transmission.

Under certain configurations, the modulation response of an optically injected semiconductor laser can be greatly enhanced relative to the free running case with increases in the resonance frequencies up to 107 GHz

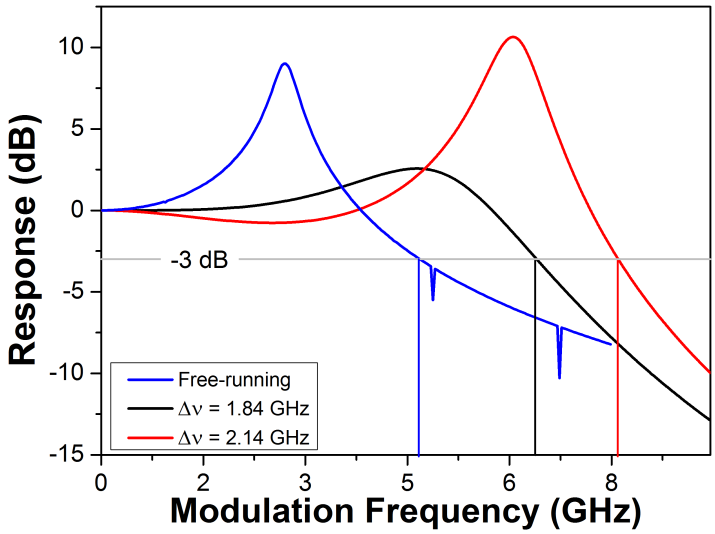

Figure 1.7: Optical injection locking can greatly affect the modulation frequency response of a laser. Frequency responses for two sample detunings are shown here which extend the 3 dB modulation frequency relative to the free running case by altering the resonance frequency, damping rate and parasitic pole. These are calculated by applying a sinusoidal perturbation to the bias current in eqs. (1.1) to (1.3) with an injection ratio of $R = -20\,\mathrm{dB}$.

recorded [32]. This is a cost effective method of increasing the transmission properties of low-cost lasers. Figure 1.7 presents sample modulation frequency responses for two sample detunings for an injection ratio of $-20\,\mathrm{dB}$ and for the same laser in free running mode. The $-3\,\mathrm{dB}$ bandwidth is increased from 4.95 GHz to 6.78 GHz and 8.06 GHz as the resonance frequency increases from 2.84 GHz to 4.95 GHz and 6.42 GHz. Note these are linear frequencies rather than the angular frequencies used in [32]. The studies of the voltage response in chapters 3 and 4 can be used to remotely identify the optimum injection configuration necessary to achieve the desired frequency response profile.

1.4 Thesis organisation

As optical fibres begin to replace slower copper based transmission lines at the consumer end of the network, low cost lasers will be needed for the

electro-optical conversion. Optically injected, long wavelength VCSELs are an attractive option. While these systems are impressive in the laboratory, they require significant expertise and equipment to implement which may restrict commercial adoption. This thesis addresses this issue by removing some of the experimental barriers to achieving performance increases through remote optical injection.

The work presented here is ordered in terms of increasing applicability, starting with a review of long wavelength VCSEL development and some of the major contributions to field of optical injection locking. Even in a relatively mature field of study, areas which have not yet been fully explored are identified. Focusing on these openings, a purely theoretical investigation into the variation of the locked phase during stable injection locking as a function of injection strength, detuning and linewidth enhancement factor is presented in chapter 3 and includes a new diagnostic method to determine the operating state of an injected semiconductor laser based on the carrier number. This diagnostic method is experimentally investigated in chapter 4 where it is shown that the locked state of an injected long wavelength VCSEL can be inferred by just a voltage measurement, eliminating the need for equipment such as optical or electrical spectrum analyzers and their operators. This generates the possibility of remotely injecting a semiconductor laser with confidence that the laser is in the desired operating state. Finally, real world applications for VCSELs are explored. It is shown in chapter 5 that state of the art fixed wavelength and tuneable wavelength VCSELs are promising candidates for high speed and colourless PON components respectively. A brief discussion on the main results and the future investigative and developmental opportunities conclude the main body of this thesis.

Chapter 2

Literature Review

This thesis is comprised of three essential elements: optical injection, VCSELs and their use in telecoms applications. An overview of important relevant topics is presented here to help put the novel work of this thesis into context. This review discusses the initial problems which had to be solved to realize room temperature continuous wave operation of long wavelength (LW) VCSELs, device design and performance improvements up to the current state of the art. An interest in creating tuneable long wavelength VCSELs exists worldwide. Two of the primary tuneable VCSEL structures in concurrent development over the last decade, one of which is used in an application in chapter 5, are compared. Following that, the background of optical injection locking, incorporating some of the seminal papers on the topic, is examined prior to focusing on the interesting physics and dynamics recorded in long wavelength VCSELs which are subject to optical injection. The use of VCSELs as sources for optical transmission and their main technical drawback, which is limited transmission distance due to frequency chirping are also considered. Finally, all of the previous areas are briefly combined to show that optically injection locked long wavelength VCSELs can provide superior performance relative to free running VCSELs, making them highly attractive sources for Long Reach PONs up to 100 km and a valid and important current research topic.

2.1 Long wavelength VCSELs

Following the proposal and successful development of the initial VCSEL concept in the 1970s and 80s [33], rapid progress was made on 650 nm and 850 nm surface emitters. This shorter wavelength technology matured quickly, mainly due to a relatively simple device structure and well established materials [34]. At 1550 nm, it took until the mid-1990s before room temperature pulsed [35] and continuous wave (CW) [36] laser action was achieved. Two prime obstacles to achieving room temperature lasing existed: the poor thermal conductivities and the low refractive index differences between the ternary (AlInAs) and quaternary (InGaAsP and AlInGaAs) alloys lattice matched to InP, required for the active regions and DBR mirror stacks. In particular, passing current though the *p*-doped layers generated an excess of heat, mainly because of lower hole mobility relative to *n*-doped layers. To overcome these issues, the use of a tunnel junction was introduced [37] in 1999 which permitted the use of *n*-doped materials on both sides of the active region. The diameter of the tunnel junction of this bottom emitting device was defined via proton implantation which also provided current confinement. The DBRs used were two 50 pair *n*-GaAs/AlAs and *n*-InGaAsP/InP stacks.

Concurrently, another long wavelength VCSEL design based around a tunnel junction was in development and was reported in 2000 by researchers from the Technische Universität München (TUM) [38]. This design was a substantial re-think of the traditional VCSEL structure. After the epitaxial growth of the mirror and active region, the tunnel junction was structured using standard lithographic techniques before an *n*-InP heat spreading layer was grown over the tunnel junction in a second MBE session. The second DBR was dielectric instead of epitaxial and consisted of 3.5 pairs of CaF_2/α-Si. The assembly was then covered with electro deposited gold for both mechanical and thermal stability before the original InP substrate was completely removed. An image and further discussion on a variation of this design, which is used in this thesis, is included in chapter 1. Dielectric DBRs had been used in VCSEL development previously by Baba *et al.* [39].

The integration of the tunnel junction deeply into the middle of the device generated the moniker of Buried Tunnel Junction (BTJ) VCSEL. The BTJ provides both current and optical confinement so that the resulting VCSELs have low threshold currents and single mode operation with high side mode suppression ratios. Index guiding occurs as an effective refractive index difference of up to 1% between the junction and surrounding semiconductor is possible [40].

There were, of course, other parties interested in developing LW VCSELs thus alternative device designs employing wafer fusion techniques [41], fully monolithic growth [42] or antimonide based material systems [43] were reported.

Applications for long wavelength VCSELs include telecommunications and gas sensing with others being continually developed such as medical imaging [44]. One of the major advantages of the TUM VCSEL design is that the general device structure can be maintained right across the emission wavelength range of the AlInGaAs material system (1.2 to 2.3 µm) used for the active region [45]. This feature makes the main telecom bands at 1.31 µm and 1.55 µm readily accessible [12], [14] but also important gas sensing ranges around 2.0 µm [46], [47], [48]. When it comes to optical communications, direct modulation of the optical sources at high speeds is desirable in terms of cost efficiencies and network simplification. Early demonstrations proved that VCSELs were suitable for 10 Gbit/s transmission [49]. However, a re-design of the devices in 2006 [50] which included an optimization of the doping profiles to reduce the dynamical resistance and device capacitances resulted in 22 Gbit/s back-to-back transmission in 2009 [51]. Further evidence to the flexibility of the TUM design is that a single mode output power of 6.7 mW [8] was achieved with an almost identical design to the one with a very high resonance frequency above 17 GHz [13], with the only difference being the design of the strain in the active region. These output powers have been exactly matched by wafer fused VCSELs [52]. Based on very recent understandings, adjustments to the relative widths of the contact ring on the dielectric side and to the diameter of the tunnel junction have enhanced the amount of gain available to only the fundamental mode by minimizing spatial

hole burning. Such finely tuned devices have demonstrated a record 8 mW of single mode output power with a 50 dB SMSR at room temperature [9]. As there is no possibility to increase the Indium content in the AlInGaAs further than 100%, VCSEL emission at longer wavelengths requires a change of material to a GaSb based system which has been used to show CW operation up to 75 °C at 2.3 µm [53]. This electrically pumped design is different to that for 1.55 µm as the substrate is not removed during processing and the dielectric mirror is not over-coated in gold. As the 1550 nm VCSELs incorporate an efficient, internal heat dissipation mechanism, they can be arrayed in order to achieve very high output powers. In fact, arrays of up to 1000 VCSELs have been manufactured and successfully CW operated generating output powers of up to 3 W [54]. Monolithic arrays with a predictable wavelength variation due to high contrast grating geometries were also developed [55].

Due to the circular symmetries, the polarization of the output light is dependent on local stress gradients in the active region which will vary across a wafer leading to unpredictable polarization properties. There have been several successful attempts to incorporate a polarization selective element into VCSEL cavities in order to set and maintain the emission polarization over the entire operating current range. These methods included structuring the tunnel junction into an ellipse [56] to create a gain anisotropy but the most successful approaches were those which utilized the revolutionary sub-wavelength grating mirror developed in the University of California at Berkeley (UCB) in 2004 [57], [58]. A thin grating with a large refractive index contrast between the composition materials is capable of reflectivities greater than 99.9% across a wide wavelength range for one polarization with substantially less reflectivity, approximately 60%, for the orthogonal one. The origin of this near unity reflectivity is dependent on both the dimensions and the materials of the grating. First, the refractive index difference is chosen so that only two modes are excited in the waveguide upon illumination with light. Secondly, the thickness of the grating is selected such that destructive interference of these modes happens at the opposite side of the grating, fully suppressing the transmitted mode, resulting in near complete power transfer back into the reflected mode. A detailed explanation of the physics involved

and design rules for high contrast SWGs were presented by Karagodsky *et al.* [59], [60]. The first 850 nm VCSEL realized with a SWG replacing all except the first 4 pairs of the top DBR mirror was reported in 2007 [61]. In 2010 two long wavelength equivalents were presented [62], [63]. Ortsiefer *et al.* successfully integrated a SWG into the dielectric mirror of their 1625 nm VCSEL providing stable and predictable output polarization properties [64].

2.2 MEMS-VCSELs

At the time long wavelength VCSELs first appeared, work on tuneable short wavelength VCSELs using Micro-Electro-Mechanical-Systems (MEMS) was already in progress [65]. With the light emitting technology established, the focus turned towards emitters which were broadly tuneable around 1550 nm. Two main competitive tuneable VCSEL designs, each of which replaces the top fixed DBR with a high reflectivity equivalent on a form of movable platform which could be used to change the length of the optical cavity and hence vary the emission wavelength. The group of Prof. Chang Hasnain at UCB adapted and developed their short wavelength design which consisted of a mirror on a counter balanced cantilever [66], [67] while a European consortium led by the Technical University of Darmstadt (TUD) decided on a semi-confocal cavity approach by placing the DBR on a four legged membrane which could be flexed via electro thermal or electrostatic forces [68].

Work on a similar technology, although optically instead of electrically pumped, was also reported [15]. Other attempts at electrically pumped tuneable long wavelength VCSELs of alternative designs appeared occasionally [69].

The TUD membrane design has gone through a significant evolution. Initially, the VCSEL and the DBR membrane were developed separately in a 'two chip' process [16]. The lower half VCSEL, already established at TUM, was effectively a standard VCSEL structure without the top DBR. The membrane DBR was fabricated at TUD. Both parts were combined in an active alignment step where the half VCSEL was biased and the position

of the membrane was adjusted until maximum lasing power was achieved before being fixed in place with a UV active epoxy [70]. The mirror was made of either semiconductor (GaAs/AlGaAs, [71]) or dielectric (SiO2/SiN , [72]) and single mode tuning ranges of 76 nm and output powers up to 1.3 mW with threshold currents in the 4 mA range were achieved. The half VCSEL and the membrane have to be designed in tandem so that the radius of curvature of the mirror, which was implemented through mechanical stress in the membrane material, and the BTJ diameter both support the same fundamental mode, otherwise a stable resonator is not created. The membrane had different radii of curvature along its two major axes to help with polarization selectivity. This two-chip design was intrinsically wasteful as while the mirror section of the membrane was only 200 µm in diameter the entire chip (mirror, beams, electrical contacts) had dimensions on the order of 1 mm approximately. This meant that for every one tuneable VCSEL created, the on-wafer surface area for 9 or more half VCSELs was needed. This inefficiency was eliminated in 2011 with the introduction of a monolithic growth approach where the membrane materials (SiO_2/SiN) were deposited directly onto the half VCSELs. This eliminated the requirement for manual alignment as all the process steps now utilized only standard lithography techniques making the entire process, in principle, scalable to an industrial level. Record single mode tuning ranges of 102 nm with over 2 mW of fibre coupled power were achieved [73]. MEMS-VCSELs of this design are used later in this thesis.

Further refinements of the tuneable VCSEL designs from UCB included replacing the cantilever actuator with a piezo electro system and the DBR with a SWG [74], initially operating at 850 nm and later 1550 nm. Recently, a SWG was implemented into the membrane in order to achieve polarisation stability and predictability for the membrane style MEMS-VCSEL [75].

2.3 Optical injection of semiconductor lasers

The effect of injected light on laser has been the subject of global research for over forty years. The physics of coupled electrical oscillators was studied

by Adler as early as the 1940s [76]. Following the development of the fundamental laser principles in the late 1950s [77], [78] and first demonstration of a ruby based optical laser by Theodore Maiman in the early 1960s [79], it took less than 2 years before Robert Hall published the first reports of a semiconductor laser, a GaAs based device emitting at 850 nm [80]. Within a few years the initial investigations in the area on optical injection into gas [81] and semiconductor lasers [82] were published. The 1980s were a crucial time in the development of the theories of external optical injection and feedback with several seminal works laying down the fundamentals of the field. The basic mathematical description of the problem was originally derived for time delayed optical feedback [18] and introduced terms into the standard single mode laser rate equations accounting for the back reflected light. These are now referred to as the Lang-Kobayashi equations and they include the coupling between the carrier density and the refractive index which has a major bearing on the complexity of the injected system. The effect of this phase-amplitude coupling on the linewidth of the laser was later uncovered by Henry [83]. The asymmetries in the stable locking range, the changes in carrier density and in the output powers as functions of detuning were all first described during the early 1980s [84], [85]. Of particular importance to this work was the derivation of the analytical conditions for locking based on the limits of the phase [7]. First accounts of the reduction of frequency chirp under direct modulation while injected [86], the effects on the relaxation oscillations frequencies and damping factors [87], as well as using injection based methods to determine the value of the linewidth enhancement factor for different lasers all also appeared at this time [88]. Numerous other works provided valuable contributions also such as the early studies of optically injected VCSELs [89], [90]. The use of power spectra and spectral analysis to study the locking and unlocking mechanism were the elementary experimental steps toward the application of bifurcation theory to optically injected lasers. Bifurcation theory first appeared in the 1880s and developed into an extensive set of analytical tools through which the discrete changes that a system of differential equations can under-go based on a continuous change of one of the system parameters could be explained. An excellent

report by Wieczorek *et al.* combines much of the available knowledge on the multiple layers of complexity hidden within the optically injected single mode rate equations. Information on the origin and relationship between the various stable and unstable states and the transition between them are thoroughly discussed [91], [92]. Impressive agreements between theoretical and experimental studies are included. Other works on the single mode rate equations also increased the common understanding of the dynamics of injected lasers [93].

These powerful tools have allowed researchers to examine more exotic systems such as injection into two colour lasers [94] and mutually coupled lasers [95], [17]. Novel applications of injected locked lasers include all optical memory and signal processing. Most of the early experimental work on injected long wavelength lasers was necessarily performed using Fabry-Perot [96] or DFBs [88] as VCSELs weren't yet developed. These cavities inherently support multiple longitudinal modes which, while useful in some applications such as wide tunablity [97], imposed experimental restrictions. Long wavelength VCSELs on the other hand have large longitudinal mode separation due to their short optical cavities, enabling wide frequency detunings under strong injection to be investigated without hops or coupling between modes. Of course the orthogonal polarisation mode is always present and contributes to the dynamics under certain conditions. There has been some consistent contributors to the area of optical injection of long wavelength VCSELs over the last 20 years. Prof. Chang-Hasnain's electrical engineering group in Berkeley have worked on maximizing the resonance frequencies of the injected VCSELs through a variety of different methods. With stronger injection strength into faster VCSELs, resonance frequencies of 28 GHz [98], 50 GHz [99] and 107 GHz [32] were achieved. A novel method of increasing the resonance frequency involving a series of cascaded modulated VCSELs which are all injection locked by the same master laser was developed.

The physical mechanism for this resonance frequency enhancement was earlier investigated by Simpson *et al.* who suggested it was due to the beat frequency between the injected frequency and the frequency to which the

cavity resonance has shifted due to the associated carrier change during locking [100]. In 2003, Murakami *et al.* reported that the increase is due to the beat between the transient cavity mode and the injected mode [20]. There is also an added effect due to non-linear gain where the low frequency relaxation side band experiences a preferential gain when it overlaps with the cavity mode [101]. Successful decreases in VCSEL Relative Intensity Noise and in the frequency chirp during direct modulation due to optical injection were also reported [102], [103].

VCSEL-by-VCSEL locking at 1.3 µm was also investigated by Hayat *et al.* who injected the first order transverse mode and showed a three-fold increase in the resonance frequencies. A good review on injection locking of VCSELs by the same authors is available [104]. An in-depth account of the modulation characteristics on injection locked lasers is also recommended reading [6].

Meanwhile other groups focused more on investigating and understanding the physics of the dynamics during optical injection. A major step forward in the understanding of the polarisation dynamics in VCSELs was made with the development of the spin-flip mode (SFM) by M. San Miguel *et al.* in 1995 [105]. The spin flip model describes the polarization modes in a VCSEL as being the result of the combined influence of the unique cavity effects, such as gain or geometry anisotropies, and the angular momentum and associated selection rules of the allowed electronic transitions between the quantum well states created in active region layers by the material properties and dimensions. In particular, two transitions relating to right- and left-circularly polarized light are allowed. A decomposition of these circular emission states into their orthogonal linear components and a stability analysis of the subsequent rate equation model show that linearly polarized emission, which occurs when both transitions have the same intensity, is stable. In addition, while elliptically polarized states where the intensity of the allowed quantum transitions are different can in principle occur, due to stricter stability conditions they are not usually observed [106].

Sciamanna and Panajotov expanded the model proposed by Regalado by investigating the dynamics induced by orthogonal injection and the associated bifurcations. Via intensity traces for each mode, complex oscillations

and even two mode locking under some configurations, referred to as an elliptically polarized injection locked state, were identified [107]. Experimental papers released the following year demonstrated some of the observed dynamics and bistabilities in an injected 850 nm laser using polarization mode powers and optical spectra [108], [109]. Bifurcation maps including a period doubling route to chaos were also presented. In 2006, an analysis of the same model was published where numerical continuation methods allowed the authors to follow bifurcation curves and identify nested regions of dynamics including the bistablity between the elliptical state and the conventionally locked state for the orthogonal mode [110].

The research interests of the Adams group at the University of Essex has focused also on the bistabilities between polarization switches in long wavelength VCSELs when subject to both parallel and orthogonally polarized injection. In work published in a series of Journal of Selected Topics in Quantum Electronics articles the group explored the SFM as a way to describe the dynamics of polarised injection. In 2008, non-linear, bistable and butterfly shaped hysteresis in the output power curves during orthogonal injection at a constant detuning was first presented [111]. A year later, the stability maps for polarized injection were reported with a model based on a Fabry-Perot cavity rather than rate equations used for theoretical analysis [112]. Further publications in 2009 demonstrated polarisation switching and bistability when the linearly polarized injection was not necessarily aligned perpendicular or parallel to either of the VCSEL modes but at a discrete angle to both [113]. It was conjectured that the induced dynamics were related to the amount of light coupled into each VCSEL mode. In 2011, a SFM rate equation based description for these dynamics was published focusing only on perpendicular and orthogonally polarized injection. Experimental stability maps were accurately reproduced using the Lynapunov exponent as a discriminator between various oscillation states [5]. Finally, in 2013, the model was expanded to include the effect of injected light regardless of polarization properties, be it linear, circular or elliptically polarized. A sophisticated analysis of the effects of the elliptical polarisation, both theoretically and experimentally, on two VCSELs with different polarization mode

spacings showed that the angle of the polarization and the mode separation have a greater effect on the induced dynamics than the ellipticity does [114].

Earlier, in 2006, the same research group had published a paper in which they discussed the correlation of the carrier changes with frequency detuning and the voltage variation under weak injection [4]. Results compatible with the initial papers on the topic by van Exter *et al.* [115] and Hui *et al.* [88] were reported where a positive and negative voltage variation across the locked region was observed. While a limited discussion on mode pulling in conjunction with measured optical spectra is included, the information which could be extracted from the dynamics outside the locking range was not investigated.

Van Exter continued his study under very weak injection with a preliminary investigation into the voltage changes outside the locked region. Optical spectra were used to illustrate a reduction in the damping of the relaxation oscillations [116]. The shape of the voltage change outside the locked region is attributed to four wave mixing for which a theoretical basis was presented in a separate publication [117].

Hui *et al.* introduced a method to extract the linewidth enhancement factor, α, using the voltage across an injected semiconductor laser. When considering just the stable locking boundaries no asymmetry in the locking range can be detected. However, the amplitude of the carrier response across the region is asymmetric and can be used to determine α. This concept is further discussed in chapter 3 of this thesis. The authors used the voltage response of an injected laser as an investigative tool again in 1993 except this time the injected laser was biased below threshold, so it acted as a resonant amplifier, in a study of the linewidth variation at currents near threshold [118].

The phase limits of the stable locking region are often mentioned but as of yet have not been thoroughly investigated. In the single mode model they can be derived analytically for weak injection [7], [6] and found asymptotically for strong injection [119]. The extensive intermediate injection strength region, which is the most accessible experimentally, is largely neglected in this respect despite several works operating in this regime but continuing to use the limits

for the weak regime regardless [120]. A lack of clarity in this area partially motivated the focus of this thesis.

2.4 Optical communications

Modern optical communications networks are truly massive in scope and scale requiring carefully designed components over an impressive 14 orders of magnitudes ranging from nanometer control of quantum well thicknesses to optical fibres which can be up to 100 km long.

As noted in chapter 1, the frequency chirping under direct modulation is a major obstacle to the widespread adoption of VCSELS as transmitters in PONs and other long reach networks. Hofmann and Amann have demonstrated error free transmission at 10 Gbit/s using three different fibre based methods. Specifically, transmission over 29 km of SMF followed by appropriate length of dispersion compensating fibre (DCF) at room temperature and over 10 km of SMF with DCF at 85 °C were demonstrated [121]. Separately, reports of transmission over 22 km of dispersion shifted fibre (DSF) and 10 km of non-zero (NZ) DSF, were published showing that these devices could be used as uncooled transmitters in PONs [122]. With improving resonance frequencies and reduced parasitics VCSELs capable of 20 Gbit/s were developed and have demonstrated error free transmission over 6.5 km of SMF at this speed [123].

Operating at the 1.3 µm dispersion minimum Gatto *et al.* successfully transmitted at 12.5 Gbit/s and 10.3 Gbit/s over distances of 20 km and 40 km respectively while operating up to 70 °C using a VCSEL in a TOSA style package [124]. Recently, the milestone of 10 Gbit/s transmission over 100 km was passed using a long wavelength VCSEL and a precisely configured DCF and SMF combination [125].

A novel method to greatly improve the reach of a directly modulated VCSEL in a DWDM PON architecture, with only a relatively small power penalty, was recently reported [126]. By offsetting the center VCSEL wavelength relative to the midpoint of the AWG channel passband, the authors used the variable absorption in the channel to reshape the transmitted pulse

and extend the 10 Gbit/s error free transmission up to 23.6 km without any form of dispersion compensation and labelled this technique as dispersion mitigation. Other demonstrations of free running, long wavelength VCSELs used in transmission experiments included 10 Gbit/s over 10 km at 85 °C at both 1.3 µm and 1.5 µm with the longer wavelength device also capable of 40 km using Electronic Dispersion Compensation (EDC) at 25 °C [127].

Hybrid networks which combine both SMF for the long haul parts and MMF for the access portions of the networks have also been successfully investigated with 2.5 Gbit/s over 25 km of SMF and 2.2 km of MMF without any dispersion compensation scheme [128]. Over these distances, dispersion becomes a critical issue only in the 10 Gbit/s bandwidth regime.

Chirp control, by pinning the VCSEL carrier number via optical injection, has also been reported on several occasions with specific configurations for different applications. Initially, VCSEL-by-VCSEL injection locking was reported where decreased pulse timing jitter indicated a reduction in chirp to allow 2.5 Gbit/s operation over 50 km [129]. Later, in 2006, Wong *et al.* describe a directly modulated VCSEL at 2.5 Gbit/s as an upstream transmitter over 25 km of SMF which is injection locked by the data carrying downstream light wave [130]. The difficulties in achieving locking and in finding optimal conditions are discussed and implementation of a look up table is recommended. The use of the junction voltage as a diagnostic tool is mentioned very briefly but not elaborated on. It is likely that the authors noticed the voltage of the injected VCSEL change during the experiment without performing a deeper investigation. The methods proposed in chapter 5 of this thesis would greatly help in overcoming some of the problems faced by these researchers in this regard.

An injected VCSEL was demonstrated to be capable of acting as both a transmitter and a receiver at the same time by monitoring the voltage variation across the pads during the injection of a modulated signal [131]. The photodetecting ability of the device is a function of detuning which is strongly related to some of the ideas emphasized in this thesis.

Further improvements in the field of VCSEL-by-VCSEL locking were presented in 2009. Control over the chirp of the modulated VCSEL via changes

in the bias conditions, injection strength and frequency detuning facilitated 10 Gbit/s transmission over 40 km [132]. The impact of having a low cost VCSEL rather than an ECL or DFB as the master laser in these set-ups strongly motivates the investigations of VCSEL-by-VCSEL locking applications.

Other advanced modulation formats have also benefited from the decreased chirp and increased resonance frequencies of optically injected VCSELs such as the 60 GHz radio over fibre scheme based on an injected and directly modulated VCSEL reported in 2010 [133].

Infra-red VCSELs have also been demonstrated as viable options for long reach transmission. One noteworthy result is a recent report of 105 Gbit/s over 960 km using a three level phase modulation combined with polarization multiplexing and a coherent detection method [134].

2.5 Conclusions

This chapter reviewed some of the major developments in the area of long wavelength VCSELs including optical injection of VCSELs and optical communications using these devices as the light source. The output powers and direct modulation bandwidths achievable from these VCSELs have placed them as realistic transmitters for many access and metro range applications.

It has been shown that their Achilles' heel, the strong wavelength chirping under direct modulation caused by their sensitivity to heat, can be engineered out of the network using a variety of different approaches. Some of these solutions are not flexible and would require dedicated portions of dispersion compensation fibre to be permanently installed. Others, such as VCSEL-by-VCSEL injection locking, could be eventually integrated onto the semiconductor die as part of a photonic integrated circuit, as is being currently developed using edge emitting lasers [135]. Other major advantages include resonance frequencies significantly above 10 GHz at 80 °C, 'colourless' tuneable variations and the ability to be easily integrated into two dimensional arrays. Most importantly however, with increasing interest and up-scaling of manufacturing activities, these devices have the potential to become very low cost similar to their shorter wavelength counterparts which dominate the

optical mice market. As injection locking to achieve high resonance frequencies or low chirp requires very specific configurations of injection ratio and detuning, it is not trivial to translate the results presented in this chapter to real work applications. The techniques developed in this thesis contribute significantly to removing some of the barriers preventing this lab-to-life leap.

Chapter 3

The phase of an optically injected laser

Several authors have studied single mode optical injection of a semiconductor laser [7], [20], [91]. This is unsurprising as it is theoretically engaging, rich with unusual dynamics and yet relatively easy to test in the laboratory.

In practice, nearly all works represent the measured or calculated dynamics on a plane with axes describing the injection ratio/strength and the frequency detuning. This is a natural approach as these parameters are the most easily accessible. With such a well studied system another point of view is required in order to gain fresh insights and in this chapter such an alternative approach is presented. Rather than the frequency detuning, it is the phase difference between the injection laser and the locked injected laser (or simply just the phase of the system) that is taken as the free parameter. The terms master and slave are often used to refer to the injection and injected lasers respectively.

To date a complete analysis of the phase over the entire injection ratio range has not been performed. Such an investigation is performed in this chapter. First, combinations of the numerical and steady state solutions to the rate equations are used to harmonize the variations of the photon and carrier numbers both inside and outside the stable locking range [136].

Then, based on their numerical stability, the phase limits are shown not

to be fixed but to vary non-linearly with injection ratio and are studied in detail for an α parameter value of 2. This value is chosen as, while values up to 5 are reported for long wavelength VCSELs [24], $\alpha = 2$ keeps the physics discussed in this chapter clear without the loss of any details.

The change in these limits as a function of α is shown along with the various bifurcation points so that the three distinct regions of the phase-injection strength plane can be identified.

Finally the detuning of lines of constant phase values is characterised. In particular $\phi = 0$ is discussed as it is a critical value in terms of carrier and photon number changes, α parameter measurements and small signal frequency response. A method to estimate the coupling efficiency, k, is described before the values of the various modulation response parameters across the locking range and their interactions at $\phi = 0$ are presented.

3.1 Photon and carrier number changes with detuning

The long term behaviour of the system introduced in section 1.3 can be determined by numerically or, within the stable locking region at least, by a steady state analysis. Numerical integration of the rate equations gives the variation of S, ϕ and N with time for a given injection ratio and the calculated final S and N values as functions of detuning are presented using grey dots for $R = -27$ dB in fig. 3.1. The relevant *Mathematica* code can be found in appendix B. For detunings less than -6 GHz and greater than 0 GHz, these data points are scattered and disjoint as the laser is not in a stable locking state. Between -6 GHz and 0 GHz they form a continuous curve. This smooth region is associated with the laser being in a stable locking configuration where the values of S and N remain constant in time. During stable locking the carrier number is generally lower than when free running while the photon number conversely increases as the laser acts as a regenerative amplifier of the input light [137]. In the unstable regions the laser oscillates at one or more frequencies which are non-linearly dependent on

the detuning. The non-continuous nature of the data points in these regions can be accounted for by the fact that the time series is necessarily calculated only for a finite period of time (200 ns) with only the final value displayed. While these regions are often discussed from a dynamical perspective the effect on S and N is rarely reported.

The maximum and minimum values of the oscillations in S and N in the unstable regions measured after the timescale for relaxation oscillations, 40 ns , are also plotted in fig. 3.1 using blue and green lines respectively. The average value calculated over the full oscillation cycle, not just the mean of the max and min curves, is shown in black and corresponds to the measured DC voltage across the device [23]. These maximum and minimum bounds converge smoothly at the positive edge of the stable locking range as the amplitude of the oscillation shrinks. The average carrier number is reduced below the free running value but note that this is not sufficient to indicate a stable locked state. The negative edge of the SL region is abrupt due to a different mechanism governing the oscillations at this boundary, see section 3.2. Distinct peaks and troughs near -7.5 GHz indicate that the laser enters and exits several areas of different higher order dynamics within a small detuning span.

Equations (1.1) to (1.3) have steady state solutions that satisfy the following implicit relations, see appendix A:

$$S = \frac{I/q - \gamma_n N}{G_0(N - N_{tr})} \tag{3.1}$$

$$\phi = \arcsin\left(\frac{-2\pi\Delta\nu}{k\sqrt{1+\alpha^2}}\sqrt{\frac{S}{S_{inj}}}\right) - \arctan(\alpha) \tag{3.2}$$

$$N = N_{tr} + \frac{\gamma_p}{G_0} - \frac{2k}{G_0}\sqrt{\frac{S_{inj}}{S}}\cos(\phi) \tag{3.3}$$

These can be solved algebraically to try and determine which phases and more usefully which frequency detunings will result in a stable locked state. The phase limits can be found by considering the range of the principal values

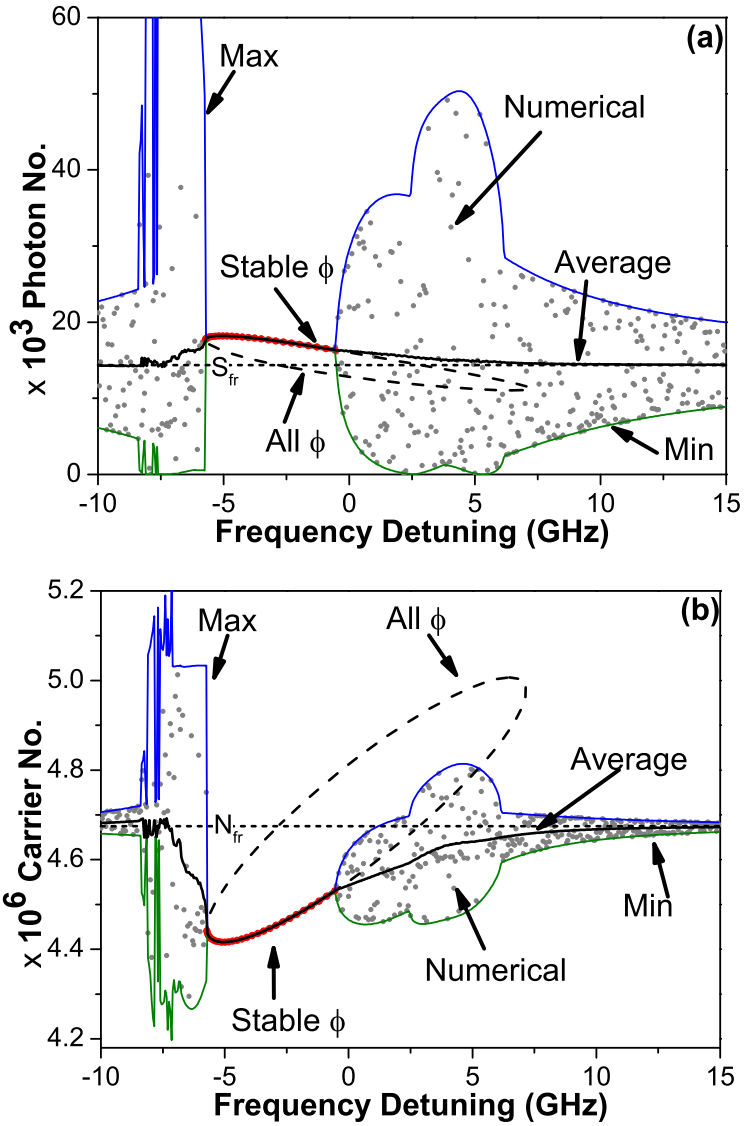

Figure 3.1: (a) Photon number, S, and (b) carrier number, N, as functions of frequency detuning from the free running cavity resonance for an injection ratio of -27 dB after numerical integration. The end points of the selected time series signals at each detuning are indicated by grey dots while the maximum, minimum and average of those time series are shown using blue, green and black solid lines respectively. All possible allowed values of S and N as calculated from the stationary analysis are traced out by a dashed line with stable points marked with red dots. S_{fr} and N_{fr} are the free running values of S and N respectively.

of the *arcsine* function, [7], appendix A which is $-\pi/2 \leq \phi \leq \pi/2$ suggesting that at all injection ratios the stable locking range is bounded by phases of

$$-\frac{\pi}{2} - \arctan(\alpha) \leq \phi \leq \frac{\pi}{2} - \arctan(\alpha). \tag{3.4}$$

For $\alpha = 2$ this corresponds to a stable phase range of

$$-2.678 \leq \phi \leq 0.464. \tag{3.5}$$

These limits do not adequately describe the system as a whole however and are only valid under weak injection. Instead by setting the phase to discrete values between $-\pi$ and π eqs. (3.1) and (3.3) can be solved simultaneously generating a set of all the possible (S, ϕ, N) steady state solutions, referred to as fixed points, which can be either stable or unstable. Most of the fixed points calculated here are unstable and so are not observed experimentally. Their values are overlaid on the numerical integration results in fig. 3.1 using dashed lines tracing out an elliptical region. Those that are calculated to be stable in section 3.2 below are shown with red dots which could be observed experimentally as stable locking. In contrast, the system will not settle on an unstable fixed point or trajectory but will instead switch to another stable fixed point or oscillation. For example, a detuning of $-2.5\,\mathrm{GHz}$ cuts the ellipse in fig. 3.1(b) at two points with one being stable (red dots) and the other one unstable (dashed line). This means that at this detuning the system will tend to the stable fixed point at $N \simeq 4.45 \times 10^6$. At higher values of α there are regions of multistability where two stable attractors can coexist but are not discussed here. Extensive discussions on fixed points, stability and bifurcations can be found in [91].

3.2 Stability analysis

The stability of the fixed points of a dynamical system can be determined by a method which involves linearization of the rate equations [6], [138]. Applying this method to all the possible steady state solutions determines

limits as to which phases are actually stable, namely ϕ_{lower} and ϕ_{upper}. These phase limits can be broken into three separate regions depending on the injection ratio namely S1, S2 and S3, fig. 3.2(a). Under weak injection (S1) the phase limits are those expected from the steady state solution of eq. (3.2), $\phi_{lower} = -\pi/2 - \arctan(\alpha)$ and $\phi_{upper} = \pi/2 - \arctan(\alpha)$. Under medium strength injection (S2) the limits vary non-linearly with injection ratio and no simple analytical expressions for them exist but they depend strongly on α. In the strong injection regime (S3) the limits reach $\phi_{lower/upper} = \mp\pi/2$. These phase boundaries in the limit of strong injection were previously pointed out in [139].

At most injection ratios the stable locking region is bound by a single $(\phi_{lower}, \phi_{upper})$ pair marked by red triangles and black dots, respectively, in fig. 3.2. However, injection ratios between -52 dB and -50 dB show two disjoint areas of stable phases, fig. 3.2(b). At low and high injection ratios (S1, S3) there is an absolute difference of π radians between the locking limits while in S2 the difference varies with injection ratio reaching a minimum for these parameters of approx. $5\pi/8 - \arctan(\alpha) = 0.856\,\text{rad}$ at R=-36 dB.

Given steady state values for S, N and ϕ the corresponding linear frequency detuning $\Delta\nu$ can be calculated for that fixed point using (3.2) and a map of the stable locking region in $(R, \Delta\nu)$ space can be generated. The stable injection limits are indicated using black dots in fig. 3.5 and are shown across two graphs to highlight features at different injection ratio scales. For the α value used here, fixed points change stability through two different mechanisms: Hopf bifurcations (HB) and Saddle-Node (SN) bifurcations which are summarized in appendix C. A description of the mathematics involved in the stability tests is included in appendix A but briefly the bifurcation through which the fixed point loses stability can be identified via the three complex eigenvalues, λ, of the Jacobian matrix for the system eqs. (1.1) to (1.3). A HB occurs when the real part of one of the eigenvalues becomes zero and a SN occurs when the complex part of two eigenvalues becomes zero as a pair. Plots of the real and complex parts of the calculated eigenvalues as functions of phase and frequency detuning for an injection ratio of $-27\,\text{dB}$ are shown in figs. 3.3 and 3.4 respectively. For each value of the phase there

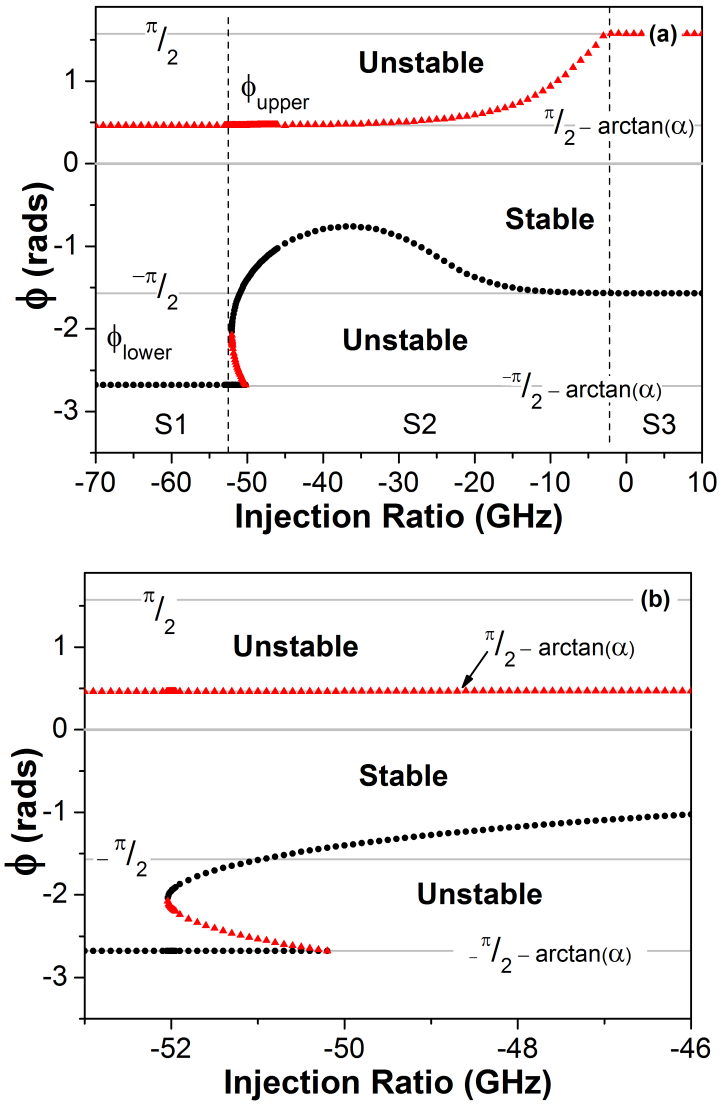

Figure 3.2: (a) The range of stable phases as determined from a stability analysis. Under weak injection the stable phase is limited by $\pm\pi/2 - \arctan(\alpha)$ whereas at high injection ratios it is limited by $\pm\pi/2$. Two separate regions of stable phase occur near -51 dB. The minimum phase span is approx. $5\pi/8 - \arctan(\alpha)$ and occurs near -36 dB. (b) A zoom of the region near -51 dB which has two separate areas of stable phase.

are two corresponding detunings which account for the closed loop nature observed. The detunings at which the Hopf and Saddle Node bifurcations occur are highlighted.

The blue and red lines in fig. 3.2 represent the HB and SN lines respectively as generated using the bifurcation software AUTO [140] on a normalised version of eqs. (1.1) to (1.3), see appendix A, and match the limits generated through the phase analysis. The shape of the positive detuning SN and HB curves near -50 dB reflects the splitting of the range of stable phases as shown in fig. 3.2(b). A large portion of the detunings within the stable locking region, in particular in S1 and S2, correspond to multiple fixed points. However only one of those fixed points results in stable locking, see fig. 3.1. This is further discussed in section 3.3. The points marked with red crosses are cusp bifurcation points (labelled C) and codimension-two Fold-Hopf, also known as Zero-Hopf, bifurcation points (labelled FH) [91]. At these FH points the HB and SN curves are tangent to each other and, in this example, there is a change in stability of each curve. Considering the ZH point near $(-2.5, -50)$ in fig. 3.5 (b) crossing the lower section of the HB curve from negative to positive detunings at injection ratios less than ZH results in the birth of unstable fixed points whereas at higher injection ratios a stable fixed point is created. The frequency detuning as a function of injection ratio for selected values of ϕ are plotted in fig. 3.5. At very low injection ratios, fig. 3.5 (a), $\phi = \pm\pi/2 - \arctan(\alpha)$ form the locking boundaries (SN) while at high injection ratios, fig. 3.5 (b), $\phi = \pm\pi/2$ are the locking boundaries (HB) as identified in fig. 3.2 (b). At intermediate injection ratios, the positive boundary is the HB curve and the negative boundary is the SN curve.

3.2.1 Phase limits at other values of α

The shape of the stable region strongly depends on the value of α. Inspection of eq. (3.2) shows that α amplifies the effect of the change in carrier number under optical injection in terms of the phase difference between the injected and injection fields. This is because α quantifies the amount a change

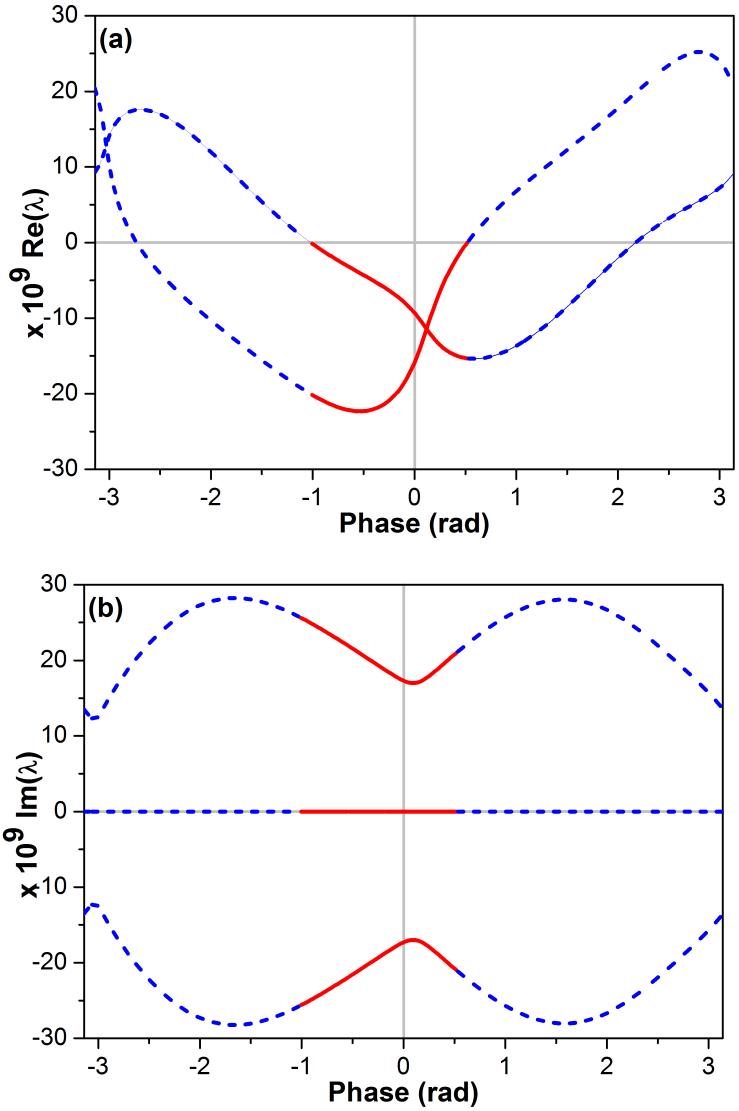

Figure 3.3: (a) The real part and (b) the imaginary part of the complex eigenvalues of the Jacobian as functions of phase for $R = -27\,\mathrm{dB}$. The real parts of two of the eigenvalues are the same. This overlap is indicated in (a) using a thin blue line.

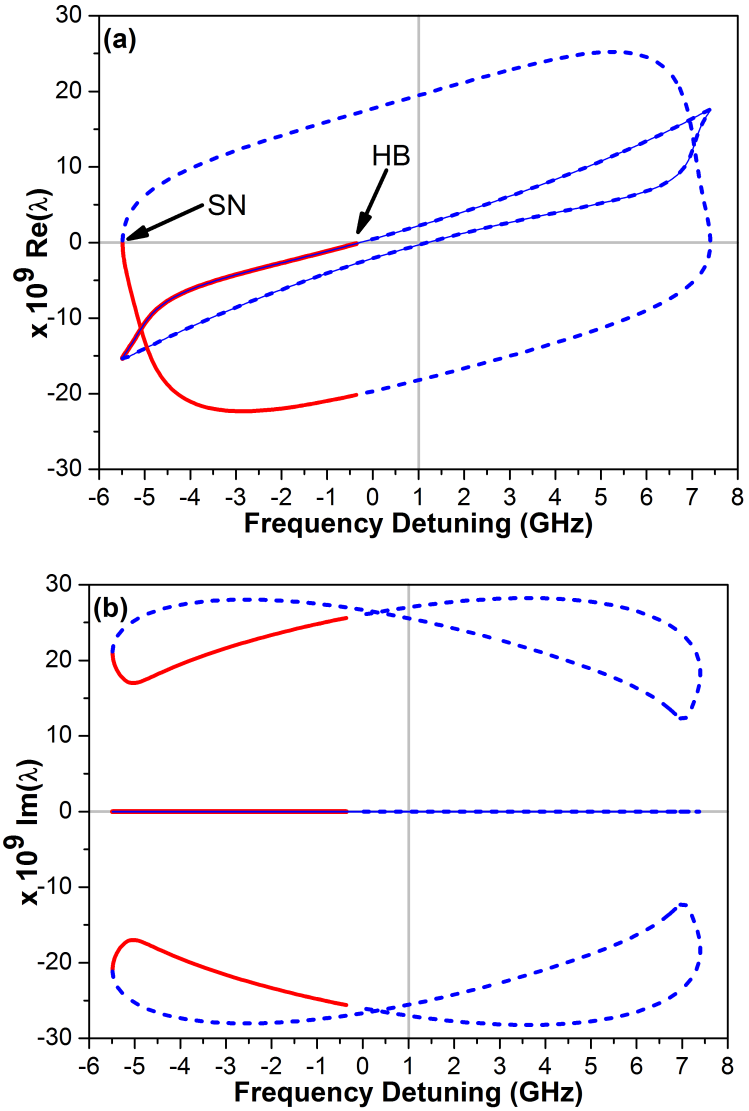

Figure 3.4: (a) The real part and (b) the imaginary part of the complex eigenvalues of the Jacobian as functions of detuning for $R = -27\,\mathrm{dB}$. At several detunings, the eigenvalues are double valued with the overlap indicated using a thin blue line. The characteristic crossings of the x-axis indicating HB and SN bifurcations are marked in both plots.

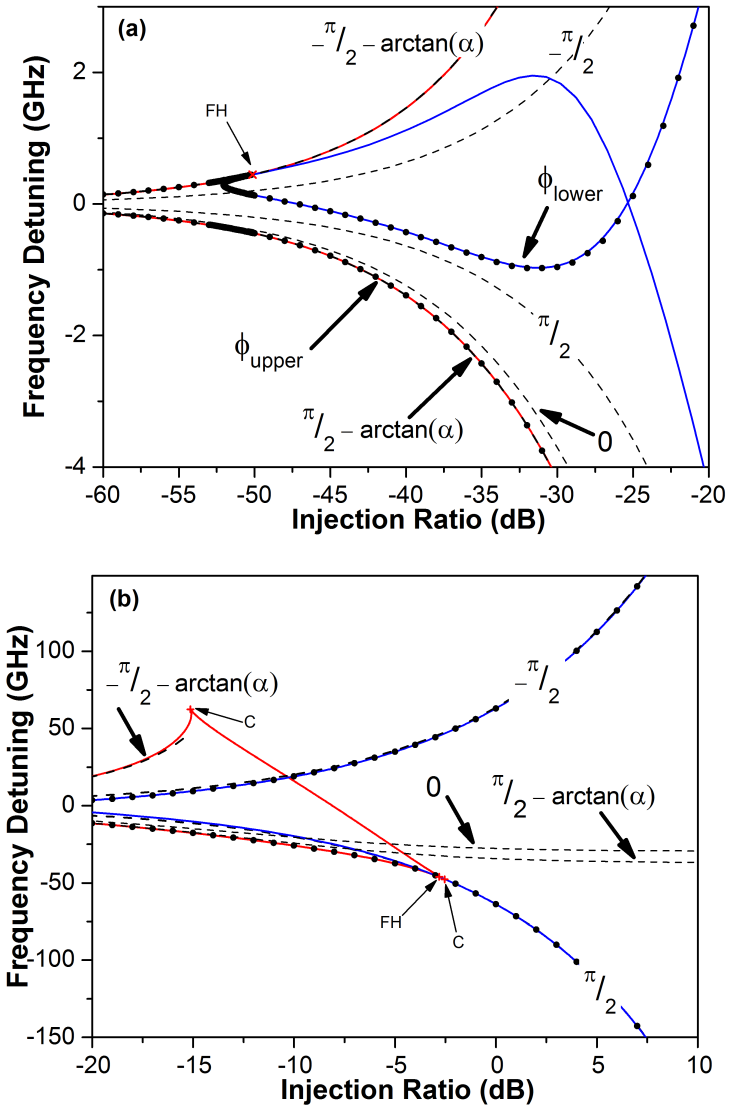

Figure 3.5: (a) Frequency detuning of fixed values of ϕ with injection ratio for selected phases. The limits of the stable locking area (black dots) are calculated through the stability analysis. Hopf (HB) and Saddle-Node (SN) lines are shown in blue and red respectively. (a) At low injection ratios the SL region is limited by $\pm\pi/2 - \arctan(\alpha)$. (b) Detuning under stronger injection. The phase condition at the boundaries changes with injection until eventually the SL region is bounded by the $\pm\pi/2$ line. Other phase curves stop varying in the detuning ordinate.The points marked with red crosses are cusp bifurcation points (labelled C) and codimension-two Fold-Hopf, also known as Zero-Hopf, bifurcation points (labelled FH).

in inversion causes a change in refractive index which in turn changes the resonance frequency of the laser as discussed in section 1.3. Having a non-zero value of α allows the resonant frequency to shift when there is a change in inversion. This phenomenon is characteristic of semiconductor lasers and facilitates the complex dynamics which have been recorded [141]. As in general, but not always, optical injection causes a reduction in carrier number the refractive index will increase forcing a red-shift in the resonance altering the frequency and phase difference with respect to the injected light.

In order to demonstrate this dependance the phase and frequency limits have been calculated using $\alpha = 0, 0.1, 0.2, 0.5, 1, 3, 4$ and 8 and are presented in figs. 3.6 to 3.14. Qualitatively these diagrams show that the phase limits have a similar structure at all values to that of $\alpha = 2$, fig. 3.2. At low injection ratios the limits are consistently given by $\pi/2 - \arctan(\alpha)$ and the high injection ratio limits are also fixed at $\pm\pi/2$.

At low values of α the frequency limits are generally symmetric reflecting the near symmetry in the phase curves. In the special case of $\alpha = 0$, $\pi/2 - \arctan(\alpha) \equiv \pi/2$ as $\arctan(0) = 0$ and the majority of the ϕ_{upper} and ϕ_{lower} curves lie on $\phi = \pm\pi/2$. The exceptions being two small areas centered on the FH points at $R = -30\,\mathrm{dB}$ which pull the curves to slightly higher and lower phase values respectively across a span of a few deciBels. The origin of this feature where the stability of each curve changes is not yet fully understood.

With increasing α an asymmetry develops as the injection ratios at which the FH point on ϕ_{upper} and ϕ_{lower} move to higher and lower injection ratios respectively. These points are marked explicitly in figs. 3.6 and 3.12. An interesting divergence now occurs as the FH point on ϕ_{lower} remains at $\phi = -\pi/2 - \arctan(\alpha)$ for all injection ratios whereas the FH on ϕ_{upper} remains at $\phi = \pi/2$. In the frequency domain this is observed as a saddle-node curve distorting into a twisted triangular shape. The positive detuning FH point remains at small positive detunings for all α, starting near $\Delta\nu = 2\,\mathrm{GHz}$ and reaching $\Delta\nu = 0.75\,\mathrm{GHz}$ at $\alpha = 4$ but the negative detuning FH grows to $\Delta\nu = -92\,\mathrm{GHz}$. At this value of α the maximum value of $\phi_{lower} = -0.43\,\mathrm{rad}$ compared to $-1.15\,\mathrm{rad}$ when $\alpha = 1$.

The ratio that the phase limits enter the S1 region also decreases of

course. For low values of α the S1/S2 boundary is delimited by the FH point on ϕ_{lower}. Above $\alpha = 2$ the boundary point changes as ϕ_{lower} reaches back to lower injection ratios where the stable phase range splits near $R = -52\,\text{dB}$ in fig. 3.11. The stable phase range does not split into two for injection ratios near the positive detuning zero-Hopf point for α less than 1.5 approximately.

The system enters the S3 region at the FH point on ϕ_{upper} as both phase limits have reached their final value of $\pm\pi/2$. The ϕ_{lower} boundary always reaches this value at lower injection ratios as the negative detuning (ϕ_{upper}) FH point gets shifted to larger R values with increasing α, for example at $R = 5\,\text{dB}$ for $\alpha = 4$. Not shown in these graphs is that the level of complexity of the non-linear dynamics near the Zero-Hopf birfurcation increases dramatically with α.

3.2.2 Measuring α in S1

The results in section 3.2 show that the phase limits set by eq. (3.4) are only valid at very low injection ratio (S1). There, the stable locking region is symmetrical with respect to detuning but the carrier and photon number are not so. For example, the asymmetry in N is shown in fig. 3.15 (a) where N is plotted against detuning for several injection ratios near the S1/S2 border at approx -52 dB. For ratios in S1, $N > N_{fr}$ at detunings near the positive locking boundary. In S2 the locking range loses any symmetric properties it had as it splits into two and the separated positive region shrinks and disappears.

Experimental determination of the linewidth enhancement factor using optical injection methods has been reported on multiple occasions. Some works [120, 142] incorrectly use the asymmetry of the stable locking boundaries in the S2 region to calculate α. Others more appropriately use power [143] and voltage [88, 115] variations in the S1 region. In general agreement with those works the expression required for this measurement is explicitly derived and discussed. Furthermore it is shown how the coupling rate, k, can be estimated in the same measurement. Estimates for k between 36×10^9 s^{-1} and 1500×10^9 s^{-1} have been used with some justifications [7, 89]. The cou-

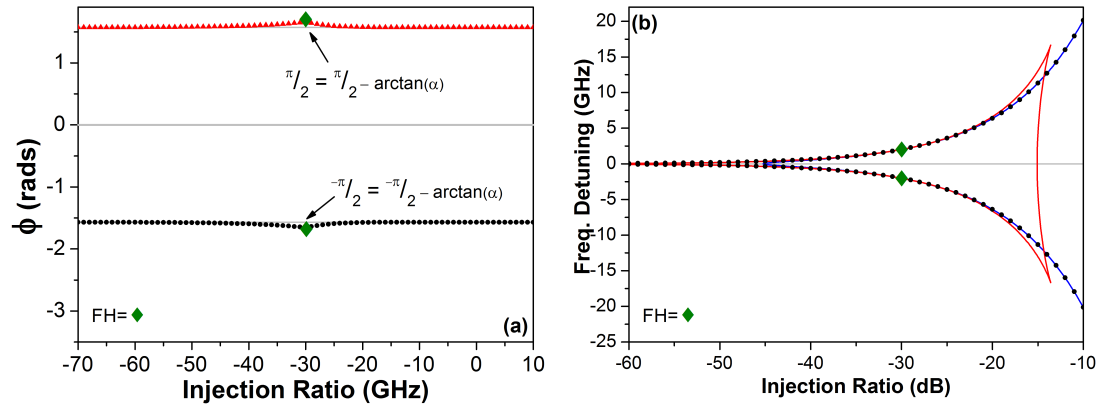

Figure 3.6: (a) Phase limits and (b) frequency limits for the stable locking region when $\alpha = 0$. FH indicates the position of the Fold-Hopf points.

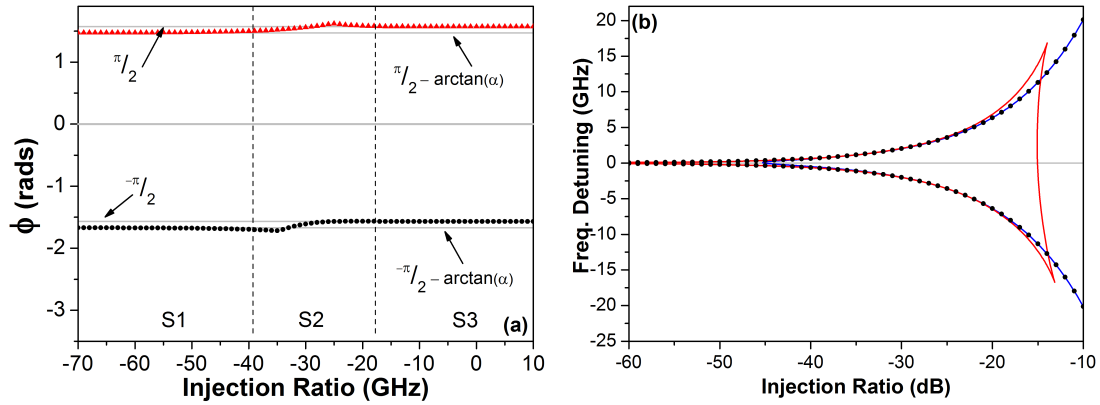

Figure 3.7: (a) Phase limits and (b) frequency limits for the stable locking region when $\alpha = 0.1$.

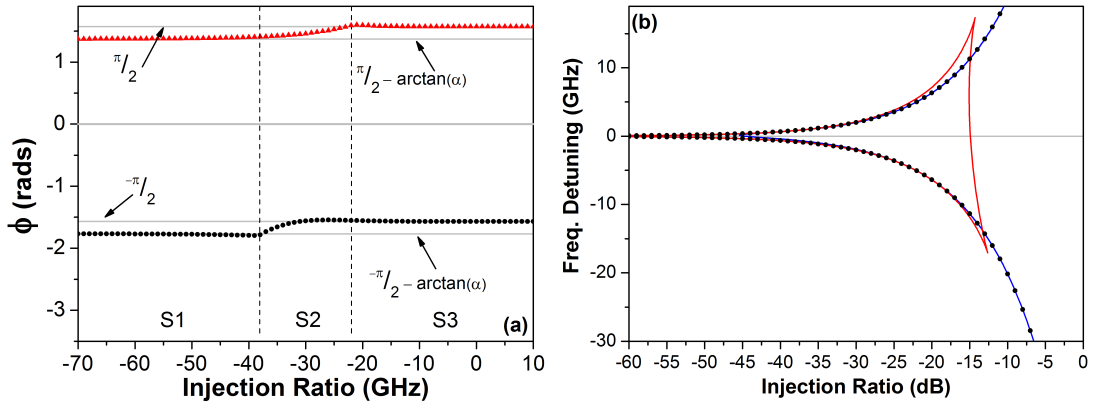

Figure 3.8: (a) Phase limits and (b) frequency limits for the stable locking region when $\alpha = 0.2$.

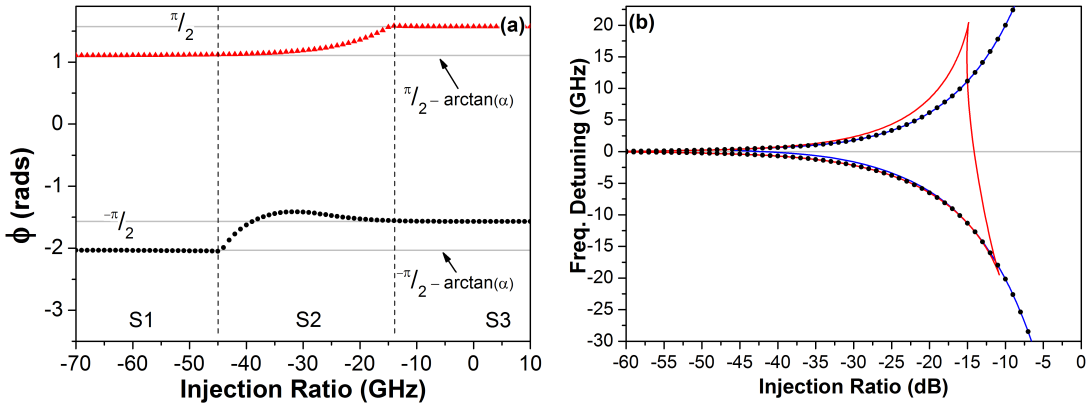

Figure 3.9: (a) Phase limits and (b) frequency limits for the stable locking region when $\alpha = 0.5$.

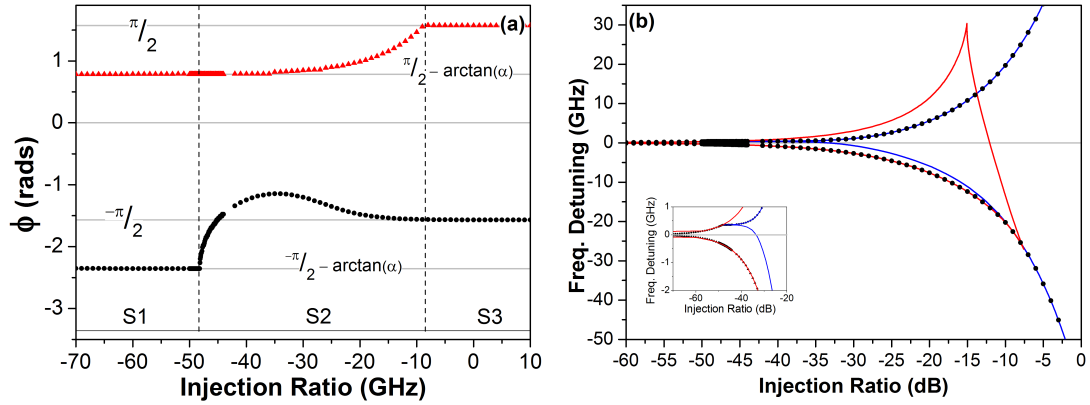

Figure 3.10: (a) Phase limits and (b) frequency limits for the stable locking region when $\alpha = 1$.

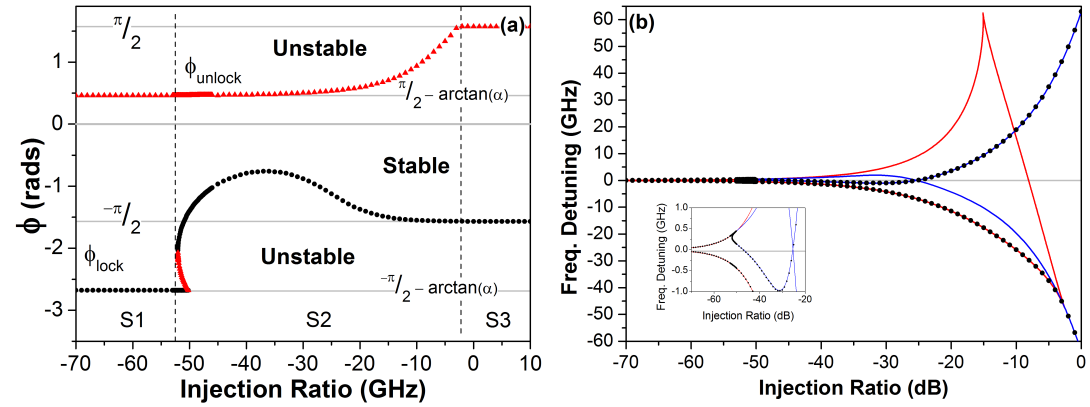

Figure 3.11: (a) Phase limits and (b) frequency limits for the stable locking region when $\alpha = 2$.

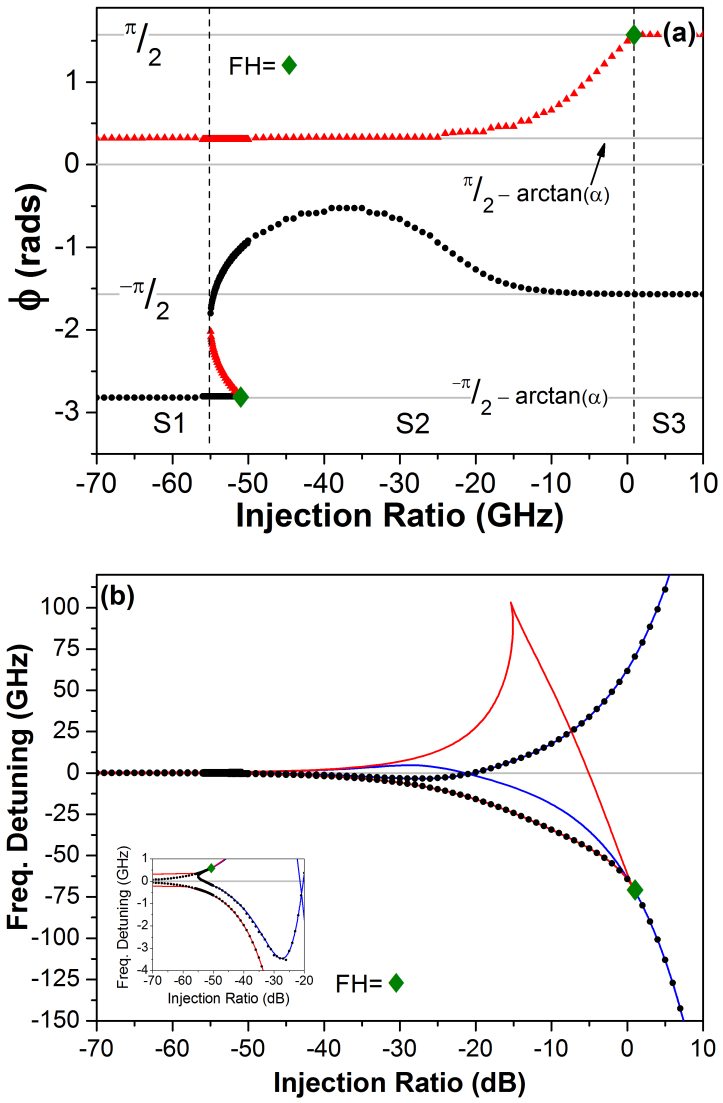

Figure 3.12: (a) Phase limits and (b) frequency limits for the stable locking region when $\alpha = 3$. FH indicates the position of the Fold-Hopf points.

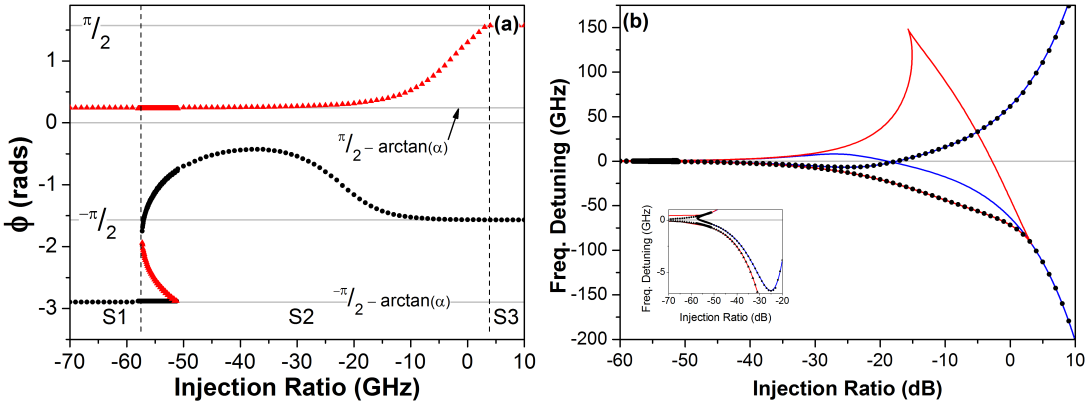

Figure 3.13: (a) Phase limits and (b) frequency limits for the stable locking region when $\alpha = 4$.

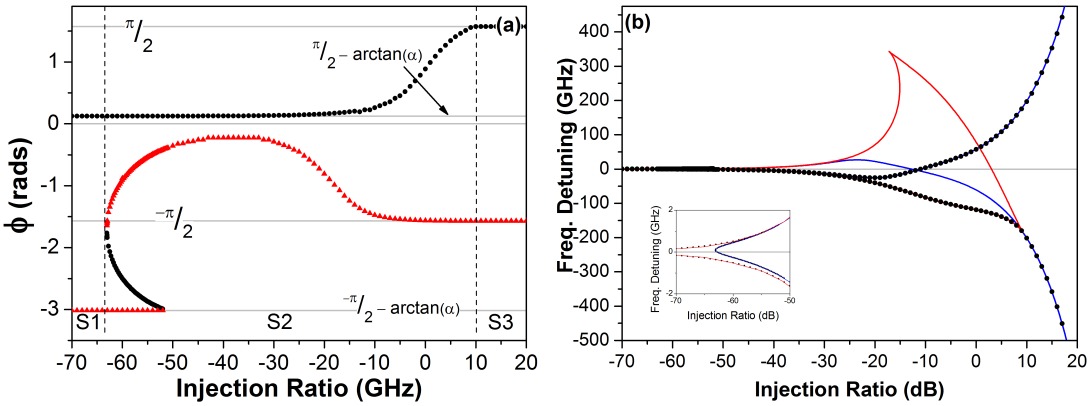

Figure 3.14: (a) Phase limits and (b) frequency limits for the stable locking region when $\alpha = 8$.

pling rate is an important experimental parameter needed to relate observed dynamics to theoretical maps where the injection strength is usually non-dimensionalised [91] and has been used as a free parameter to fit experimental data to theory [4]. The value of $k = 400 \times 10^9$ s^{-1} used here was derived on a similar basis [23]. Discussions on the upper limits of the validity of eqs. (3.1) to (3.3) in terms of injection strength usually focus on the injection ratio but must necessarily also include k which is often overlooked. A low coupling rate with strong injection can have a similar net effect to a high coupling rate with medium injection as it is always the product $k\sqrt{S_{inj}}$ which appears in the eqs. (3.1) to (3.3). For instance, these equations were used to successfully model cavity responses at an experimental injection ratio of +8 dB [144] which is close to the maximum value of +12 dB considered in this work validating the use of these equations in a regime with numerically high injection powers. Figure 3.15(a) shows that in the S1 region the locking range is symmetric and that the carrier number can experience both a positive and negative deviation from N_{fr}. Inspection of eq. (3.3) shows that N will be equal to N_{fr} only for $\cos(\phi) = 0$. Following from fig. 3.2(a) the only stable phase inside the locking range which satisfies this is $\phi = -\pi/2$. At this phase eq. (3.2) reduces to

$$\Delta\nu_0 = \frac{k}{2\pi}\sqrt{\frac{S_{inj}}{S_{fr}}} \tag{3.6}$$

where S_{fr} is the steady state photon value at this detuning equal to the free running value and measurable in the absence of injection. On the negative locking boundary $\phi = \pi/2 - \arctan(\alpha)$ so eq. (3.2) now reduces to

$$\begin{aligned}\Delta\nu_- &= -\frac{k}{2\pi}\sqrt{\frac{S_{inj}}{S_-}}\sqrt{1+\alpha^2} \\ &\simeq -\Delta\nu_0\sqrt{1+\alpha^2}\end{aligned} \tag{3.7}$$

where S_- is the steady state photon value. As the photon number increases with negative detuning the assumption $S_{fr} = S_-$ is not strictly correct. However, as the difference is small for injection ratios in S1 the approximation

holds to within a small error in α . The lower the injection ratio at which the measurement is performed the more accurate this assertion is. Combining eqs. (3.6) and (3.7) gives the expression for α [88]:

$$\alpha = \sqrt{\left(\frac{\Delta\nu_-}{\Delta\nu_0}\right)^2 - 1}. \tag{3.8}$$

Note that $\Delta\nu_-$ is the entire negative locking width and not half the difference between the maximum and the minimum of the voltage change as suggested in [115] which can introduce an error of approx. 10% in the estimated value of α. Figure 3.15(b) shows the injection ratios for which $|\Delta\nu_-/\Delta\nu_0| = \sqrt{1+\alpha^2}$ is approximately valid for increasing values of α with all other parameters kept constant. In a real device the expected change of parameters including α with N would also influence the accuracy of this expression.

In particular in the -25 dB to -10 dB region of fig. 3.5(a) and (b) it is clear that due to the shape of the HB line there will be a sweet spot where the expected ratio appears to exist. It is possible to verify experimentally that the system is operating in the correct regime for using this technique to determine α. Firstly, the locking range should be symmetric and continuous. If the stable locking range is split like the -52 dB curve or asymmetric like the -49 dB curve in fig. 3.15(a) the injected power needs to be reduced. Secondly, analysis of the unlocking mechanisms at the stable locking boundaries should determine Saddle Node bifurcations at both positive and negative detunings, rather than one Hopf and one Saddle Node, if not then the injection ratio is too high. If both of these conditions are met, measurement of α using the ratios of the locking widths with a relatively reduced carrier number, measurable as an operating voltage less than the free running voltage, should be successful. In principle the measurement could be made if once the carrier curve is continuous across the $N = N_{fr}$ level as in the case of $R = -52\,\mathrm{dB}$ in fig. 3.15 (a), stability would be lost and then regained through two Hopf bifurcations before being lost again through a SN bifurcation.

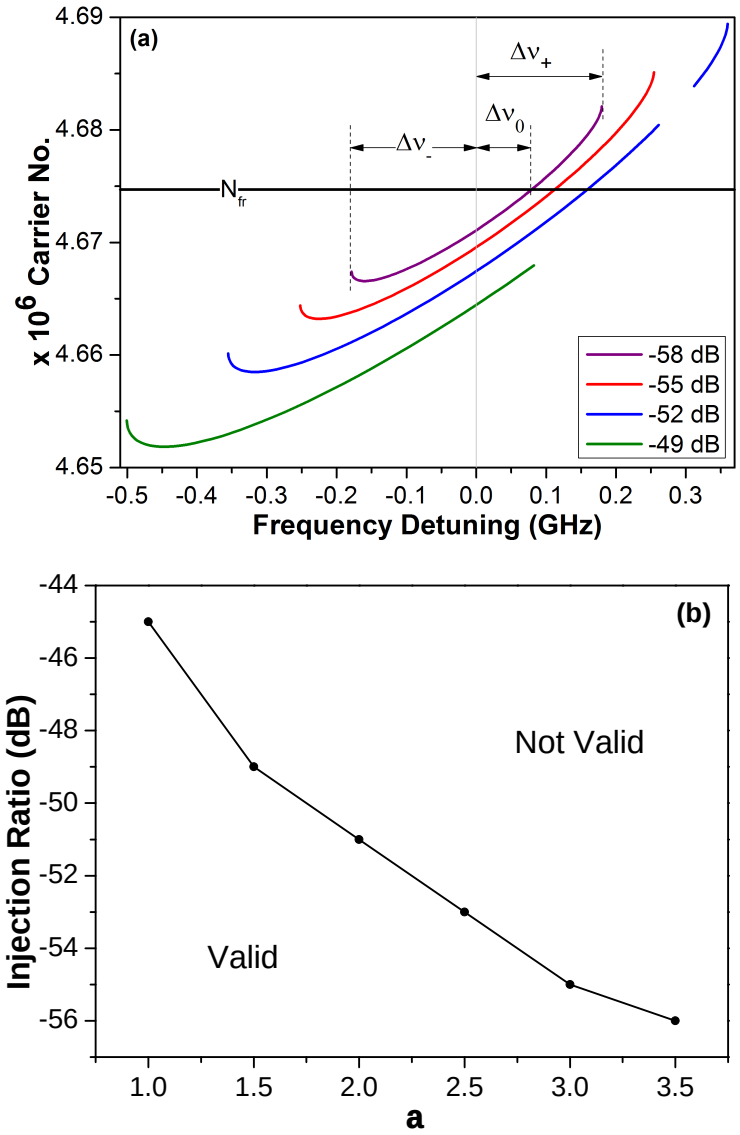

Figure 3.15: (a) Variation in the carrier number with detuning at low injection ratios. The positive, $\Delta\nu_+$, and negative, $\Delta\nu_-$, locking widths as well as detuning at which the carrier number equals the free running carrier number, $\Delta\nu_0$, are highlighted for an injection ratio of -58 dB and $\alpha = 2$. (b) Testing the correctness of $|\Delta\nu_-/\Delta\nu_0| = \sqrt{1+\alpha^2}$ for $\alpha = 0$ to 3.5. This asymmetry is valid only for injection ratios in the S1 region for each α, as shown in fig. 3.2(a) for $\alpha = 2$.

3.3 The special case of $\phi = 0$

The detuning with injection ratio for phase values between $-\pi/2 - \arctan(\alpha)$ and $\pi/2$ are plotted in fig. 3.16. The plotted difference in phase is non-linear with the smallest step sizes near $\pm\,\pi/2$. The stability of the phase at each injection ratio is not indicated but it varies with injection strength as expected from fig. 3.2. For injection ratios between -30 dB and -5 dB, the phase condition on the negative detuning SN line (negative locking boundary) adjusts to allow the smooth graduation in phase to $\pi/2$ radians as depicted in the lower inset to fig. 3.16. The evolution of a particular phase ($\phi = 1.178\,\text{rad}$) is highlighted to show how, at low R, it represents an unstable phase before gaining stability as it becomes tangent to the SN curve and remains stable at higher injection ratios. Note a similar change happens on the positive detuning SN curve which has a phase of $-\pi/2 - \arctan(\alpha)$ over most of its length but decreases towards $-\pi$ near the cusp marked C in fig. 3.5(b). The positive and negative detuning SN lines are joined together by a curve which crosses the stable locking region whose phase condition is not discussed here.

Under strong injection the majority of the π phase change across the locking region occurs within a narrow detuning range offset to negative detuning as shown in the upper inset of fig. 3.16 for an injection ration of $+8$ dB. The detuning at which $\phi = 0$ is always stable and converges to value of ~ -25 GHz for the parameters used here (thick black line). Setting $\phi = 0$ in eq. (3.2) gives an expression for the detuning in terms of the steady state photon number:

$$\Delta\nu_{\phi 0} = -\frac{\alpha k}{2\pi}\sqrt{\frac{S_{inj}}{S}} \tag{3.9}$$

Equation (3.3) shows that at all injection ratios, the zero phase point corresponds to the maximum deviation in the photon and carrier numbers from their free running values. The reduced N during stable locking, fig. 3.1(b), becomes the threshold carrier number and the addition of the injection term in the photon number rate equation can be considered as a phase dependent reduction in the cavity losses, γ_p, it being a positive carrier independent term which is proportional to a photon number ($\sqrt{S_{inj}S}$). The phase and carrier

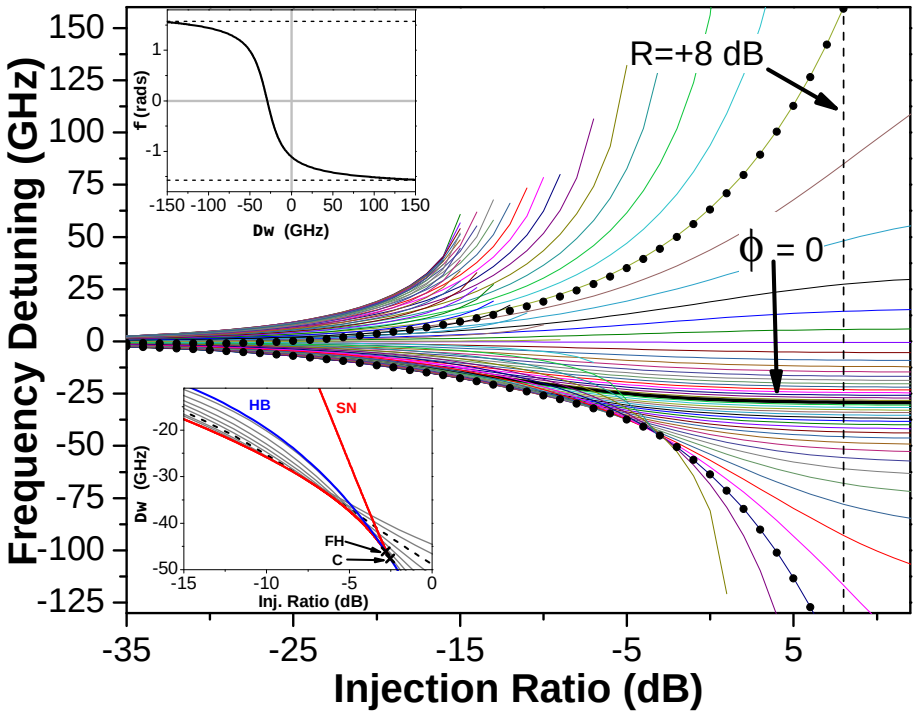

Figure 3.16: (a) Frequency detuning with injection ratio for fixed ϕ between $-\pi/2-\arctan(\alpha)$ and $\pi/2$ where the phase difference between the chosen ϕ is non-linear. The black dots show the stable locking boundaries. The cross section at +8 dB (upper inset) shows that, under strong injection, the majority of the π phase change happens near the $\phi = 0$ point near -25 GHz. The lower inset shows the phase condition on the Saddle Node line smoothly changing from $\pi/2 - \arctan(\alpha)$ to $\pi/2$ as phase lines of increasing value become tangent to it. The trajectory of one curve is highlighted by dashing.

number dependence on detuning for several injection ratios are shown in fig. 3.17 with the zero phase point marked on each curve. Under weak injection, the zero phase point is at the negative detuning boundary but tends to a more central position in the stable locking region as the injection strength increases. Thus, at any injection ratio, an absolute reference phase ($\phi = 0$) can be found using just a DC voltage measurement as a function of detuning which could be relevant to transmission applications based on phase modulation [145]. Applying the same $S \simeq S_{fr}$ approximation in S1 the coupling rate can be estimated using the detuning of the minimum of the carrier variation:

$$k = -\frac{\alpha}{2\pi}\frac{1}{\Delta\nu_{\phi 0}}\sqrt{\frac{S_{inj}}{S_{fr}}} \tag{3.10}$$

where α could be using eq. (3.8) with the same experimental setup. If the output power from the injected laser can be accurately measured this technique can be used to study if there is a change in coupling rate with increasing injection assuming a constant coupling efficiency.

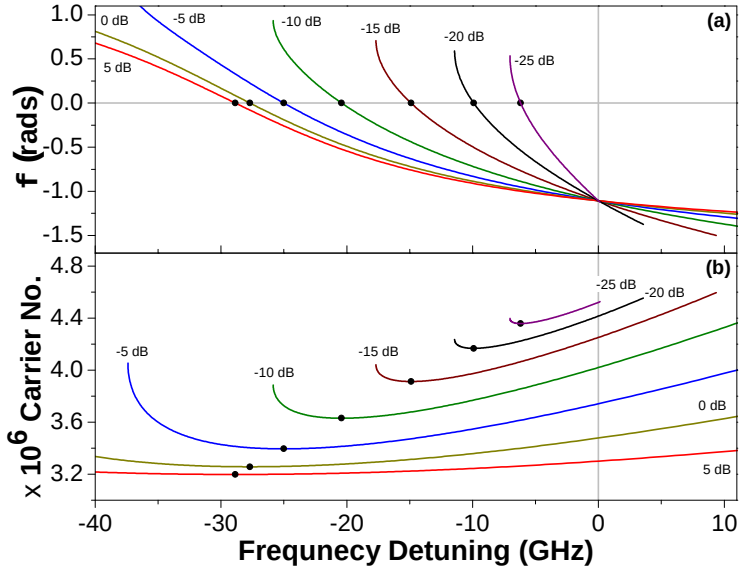

Figure 3.17: Plots of (a) phase and (b) carrier number with detuning for multiple injection ratios. The points at which $\phi = 0$ are marked with black dots in both plots and always correspond to the minimum of the carrier number.

The phase solution as a function of detuning is plotted in fig. 3.18 for injection ratios of $-55\,\mathrm{dB}$, $-25\,\mathrm{dB}$ and $5\,\mathrm{dB}$ where dashed lines indicate instability and a solid line indicates stable locking. Note the varying detuning scale. At low injection ratios the phase curve loops around repeating the same $\Delta\nu$ at different phases resulting in the closed ellipses plotted for the S and N curves in fig. 3.1 but opens up with increasing injection ratio. A plot of the photon number as a function of detuning for such an open phase state is shown in fig. 3.18 (d) with the same colour coding as in fig. 3.1.

3.4 Small signal frequency response at $\phi = 0$

Under unstable optical injection light will be emitted at both the injected frequency and the resonance frequency of the optical cavity. Once locked, emission will be solely at the injected frequency but the resonance of the cavity still remains. Generally during stable locking, there will be a reduction in the carrier number in the active region, increasing the refractive index. The optical path length in turn increases leading to a red shift in the cavity resonance frequency. The extent of the linear frequency red shift can be quantified as $\Delta\nu_{cav} = \alpha G_0(N - N_{th})/4\pi$ where N_{th} is the threshold carrier number. This effect on the phase of the laser is included in the rate equations by the first term on the right hand side of eq. (1.2).

The natural resonance of a free running laser is due to the coupling of the carriers and the photons as the system settles to its steady state. The frequency of these relaxation oscillations can be calculated to be $f_r^0 = \omega_r^0/2\pi = \sqrt{G_0\gamma_p S_{fr}/4\pi^2} \simeq 2.9\,\mathrm{GHz}$ for the current parameters. The overall relaxation rate is influenced by the introduction of a second resonance at a frequency related to the difference between the frequencies of the shifted cavity resonance and the injected light, $|\delta f_{res}|$ [20]. Due to the non-linear change in N across the stable locking region, this difference frequency also changes non-linearly. This model for the resonance frequency under injection has been expanded upon by taking carrier pulsations [141] and non-linear gain into account [101].The non-linear gain term influences the resonance frequency through the amplification of the relaxation oscillation sidebands around the

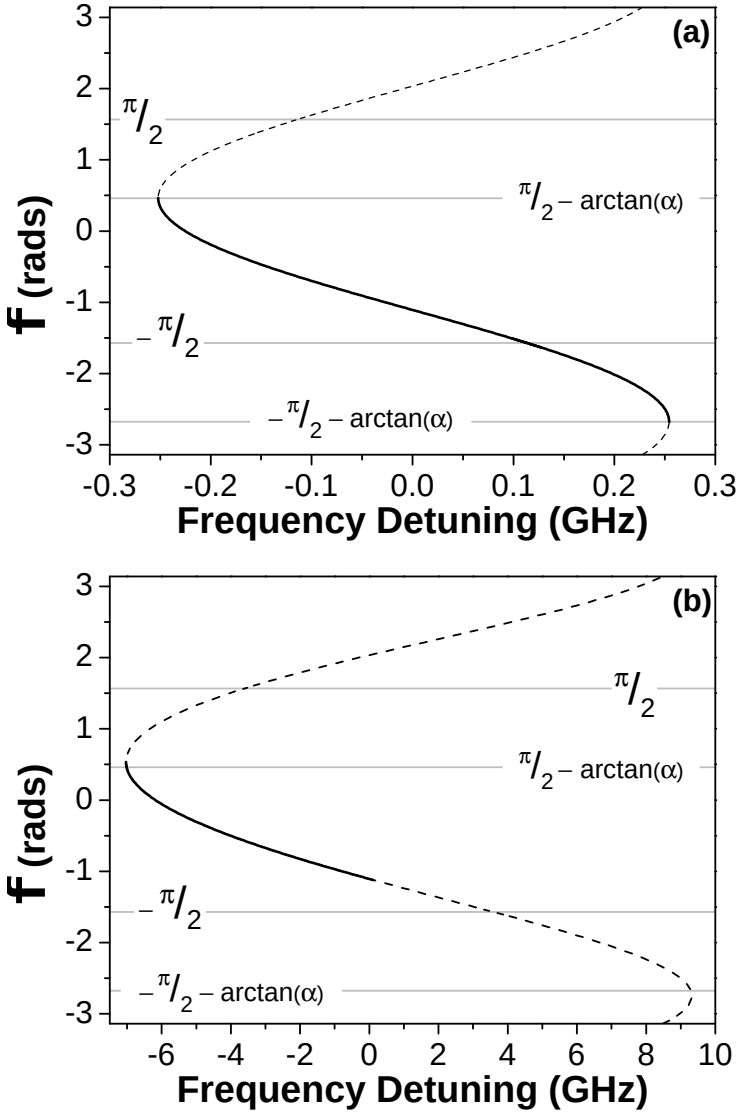

Figure 3.18: Phase curves at different injection ratios (a)−55 dB (b)−25 dB and (c) 5 dB. Solid lines indicate stability, dashed line indicate instability. (d) The maximum, minimum and average photon number variation at −12 dB overlaid with stable (red dots) and unstable (dashed line) analytically calculated values as in fig. 3.1.

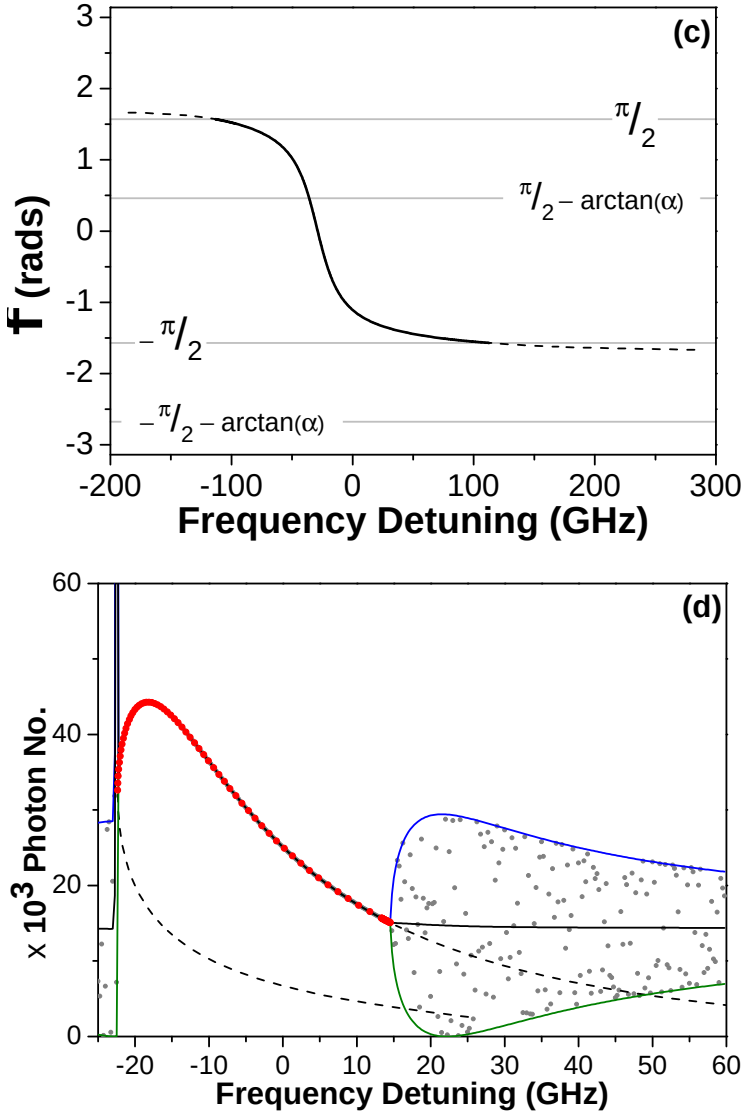

Figure 3.18: Phase curves at different injection ratios (a)−55 dB (b)−25 dB and (c) 5 dB. Solid lines indicate stability, dashed line indicate instability. (d) The maximum, minimum and average photon number variation at −12 dB overlaid with stable (red dots) and unstable (dashed line) analytically calculated values as in fig. 3.1.

shifted cavity resonance. In particular the sideband at lower frequencies relative to the emission peak is seen to experience preferential gain, depending on the detuning and the injection strength, which influences the overall resonance response. For the purposes of this discussion which focuses on the qualitative changes around the zero phase point these non-linear terms are not considered. A graphical method to understand the behaviour of the cavity resonance was recently proposed in [144].

Using the method outlined in [138] the resonance frequency, f_r, of the system under a small signal perturbation to the bias current can be calculated at each steady state point. At frequency detunings very close to the negative locking boundary these perturbations can cause the laser to pulsate rather than oscillate. The variation of f_r as a function of detuning is plotted with solid lines for injection ratios of -35 dB, -24 dB and -13 dB in fig. 3.19. The minimum of f_r occurs near the zero phase point and decreases in magnitude with increasing injection strength. The highest values for f_r are calculated at the positive detuning boundary where very low damping rates (not shown) are also found. Injection at these detunings lead to isolated, high amplitude peaks in the frequency response. However, both resonance frequency and damping rate need to be relatively high in order to achieve a wide modulation bandwidth [141].

The resonance frequency due to the optical injection, calculated using the *sin* term in eq. (1.2), is plotted as a function of detuning using dashed lines in fig. 3.19. At each injection ratio this frequency is zero at the zero phase point as the cavity resonance has red-shifted to exactly match the frequency of the injected light. However it is clear that $|\delta f_{res}|$ only matches the actual resonance frequency f_r under stronger injection conditions. The value of f_r at the zero phase point with increasing injection strength is shown in fig. 3.20(a). Under weak injection the resonance frequency of the laser at this detuning is due to the intrinsic photon/carrier interaction. At an injection ratio ($\simeq -35$ dB) the resonance frequency begins to decrease as the injection effect becomes dominant and is zero by -16 dB. Unexpectedly, at a small span of higher injection ratios ($2-5$ dB) f_r becomes non-zero again. A more detailed picture is found by examining the behaviour of all the roots of

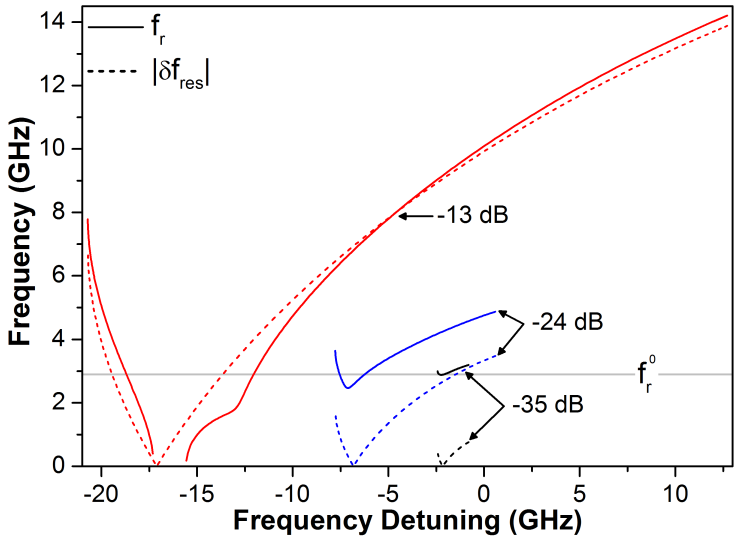

Figure 3.19: The resonance frequency, f_r, of the optically injected laser calculated using a numerical analysis of the system and the frequency difference between the cavity resonance and injected light, $|\delta f_{res}|$, at injection ratios of -35 dB, -24 dB and -13 dB. The estimate of f_r from $|\delta f_{res}|$ becomes more accurate with increasing injection strength as the effect of the optical injection becomes stronger than the intrinsic carrier/photon resonance. The value of the free running resonance frequency f_r^0 is indicated.

the determinant of the Jacobian matrix of the system after the small-signal perturbation, see appendix A. These usually have the form of two complex roots, $0.5\gamma \pm if_r$, where γ is the damping rate and one real root, f_p, known as the real pole. Once f_r becomes zero the damping of the oscillations can no longer exist so the three roots will be referred to as the triple real poles.

Values of f_r, 0.5γ, f_p and the triple real poles at the zero phase point are plotted as a function of injection ratio in fig. 3.20(b). It is 0.5γ which is plotted here as that is what appears in the root of the determinant. Once the resonance frequency goes to zero near -16 dB two new real poles branch away from the damping curve before coming back together as the resonance frequency becomes non-zero again. In this regime the single real pole increases in value until it begins to saturate at approx. 15 GHz. Above 6 dB the damping rate breaks into two again with one branch increasing to large values while the other converges to the value of the single real pole.

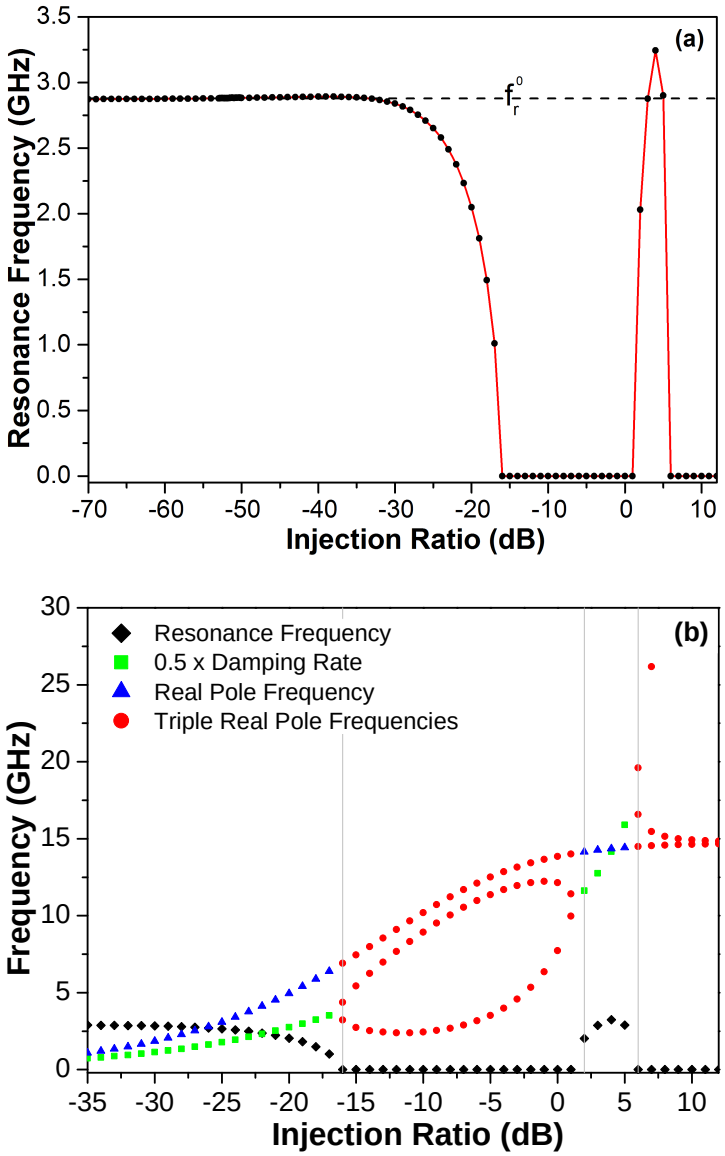

Figure 3.20: (a) The resonance frequency at the zero phase point as a function of injection ratio. At ratios < -35 dB the system retains a resonance at f_r^0. As injection strength increases that resonance drops in frequency to 0 GHz except for a region around 3 dB where it returns approximately to f_r. (b) The various modulation parameters at the zero phase point as a function of injection ratio. Where the resonance frequency has gone to 0 GHz the damping rate no longer exists and instead splits into extra two real poles. These branch apart and then recombine at 2 dB where the resonance becomes non-zero again. At higher ratios one of the extra real poles gets very large while the other converges to the frequency of the conventional real pole.

The link between the 0.5γ and f_p curves around the zero phase point is best illustrated by plotting all of the small signal parameters versus frequency detuning at selected injected ratios in fig. 3.21. At -13 dB, fig. 3.21(a), the triple real poles smoothly join the four disconnected ends of the 0.5γ and f_p curves while at -5 dB, fig. 3.21(b), the two curves are isolated from each other with two of the real poles branching from and returning to the 0.5γ curve. The transition between the two configurations is smooth. Figure 3.21(c) shows the situation at 3 dB where the non-zero resonance frequency and the other curves remain continuous across the zero phase point.

The shape of the frequency response is highly dependent on all of the modulation parameters at a given detuning. For a wide modulation bandwidth, a flat frequency response curve with a high resonance frequency is desirable. In general it is difficult to achieve both of these as a flat response curve needs a high γ. The damping rate is maximum around the zero phase point where the resonance frequency is obviously lowest while it is minimized at the positive locking boundary where the resonance frequency can grow to very large values. This leads to frequency responses which are either flat but without a high resonance frequency or responses which quickly roll off in amplitude to below the -3 dB level but then feature an intense but solitary resonance peak for detunings near the positive locking boundary.

It is also important to consider the effect of the real pole which will cause a drop in the frequency response near its characteristic frequency. A real pole frequency near 0 GHz will reduce the DC value of the response which is used to determine the -3 dB point while a high real pole frequency could reduce the maximum achievable bandwidth. A median value is desirable where the resonance and the real pole are suitably offset so that the attenuation is compensated for by the resonance and the response remains flat. Such an optimization by varying the injection ratio and frequency detuning has been discussed [146] where the dip due to the real pole is minimized to -3 dB of the DC response in order to maximize the modulation bandwidth. No large resonance peak is recorded at this configuration as the damping rate must be large enough that the peak due to the resonance is sufficiently wide and intense to compensate for the real pole attenuation.

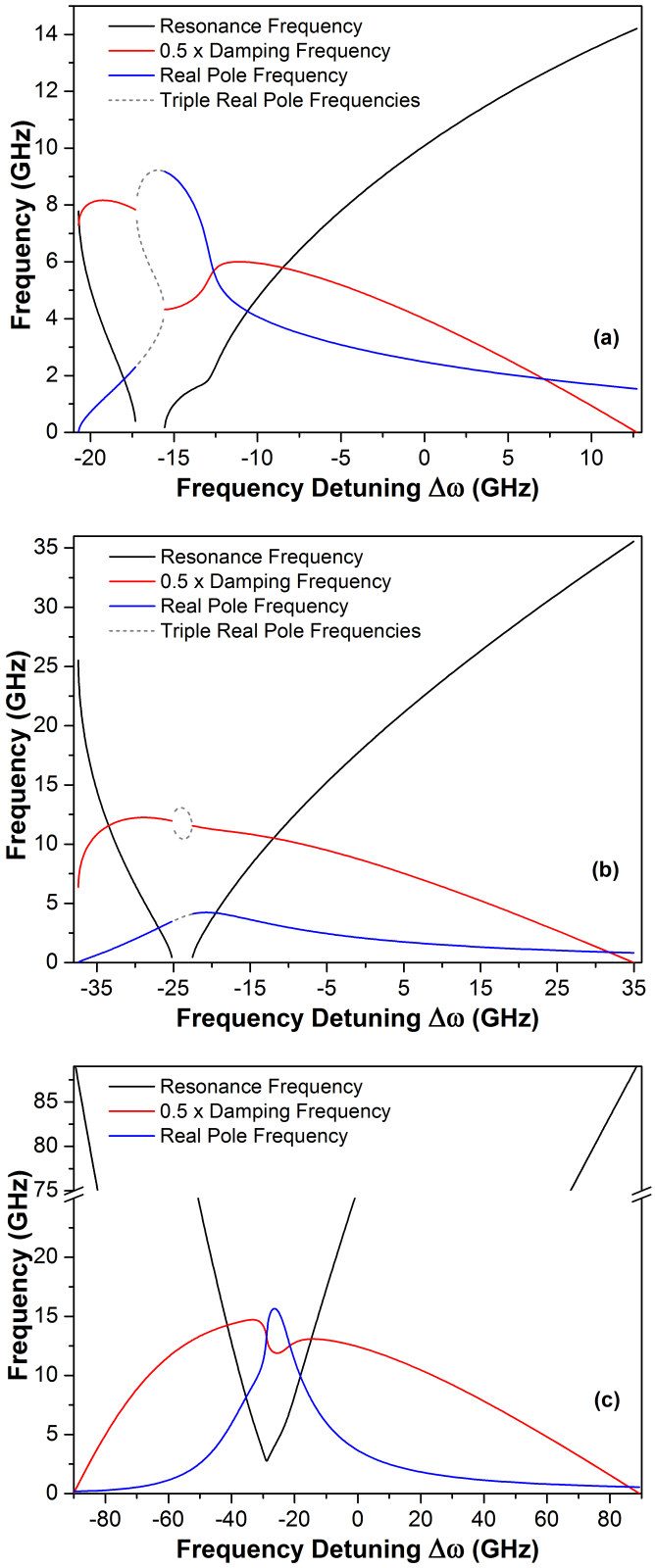

Figure 3.21: The modulation response parameters as functions of detuning for injection ratios of (a) -13 dB, (b) -5 dB and (c) 3 dB emphasizing different configurations of the poles at $\phi = 0$. (a) The triple real poles smoothly link the damping and single real pole curves. (b) The curves no longer join. Two of the real poles branch away from the damping curve while the third continues as a single real pole as at detunings away from the zero phase point. (c) The resonance frequency is non-zero so the damping and real pole curves are continuous and single-valued.

3.4.1 Small signal response parameters at other α

In general increasing the α-factor leads to an increase in complexity in the dynamics of semiconductor lasers. In terms of the small signal response it can be seen to drastically increase the asymmetry of the response in accordance with eq. (3.9) which shows that the zero phase point will be at $\Delta\nu = 0$ only for $\alpha = 0$ and tends to negative detuning with increasing α. The modulation parameters are calculated for injection ratios of $-13\,\mathrm{dB}$, $-5\,\mathrm{dB}$ and $3\,\mathrm{dB}$ for fig. 3.21 which show some qualitatively different responses. The frequency detunings for which the system is in a stable locking state and at which it is possible to compute these parameters differ with injection ratio and the values of f_r, γ and f_p obviously differ as well. Given the large effect of α a surprising result is found that, for a given injection ratio, at the zero phase point the values of these three parameters is independent of the value of α. That is to say that regardless of the value of α used in the simulation plots of the $3\,\mathrm{dB}$ parameters at the zero phase point all look identical to fig. 3.20 (b). At this specific detuning frequency the modulation response to the effects due to α must be completely balanced by the effects of the optical injection. Further confirmation of this matching is seen in fig. 3.22 where the frequency response of the optically injected laser is numerically calculated. The continuous curves show the response at the zero phase point ($\Delta\nu = 0$) at various injection ratios for $\alpha = 0$. The dots plot the response of the system with $\alpha = 4$ when injected at the zero phase point for two of the same injection ratios. The reponses are identical to the $\alpha = 0$ case.

3.5 Conclusions

The locked phase of an optically injection locked semiconductor laser was analysed in-depth to reveal three qualitatively different behaviours as a function of injection ratio. In each region different phase limits apply at the stable locking boundaries with analytical expressions available for weak and strong injection. Under medium strength injection the phase limits vary in a non-linear way and no closed forms for the limits were found. The frequency

detuning of lines of fixed values of the phase also vary non-linearly but a quasi-static distribution is found under strong injection. Frequency detunings at which the phase is zero are of particular interest and correspond to the maximum change in photon and carrier number. Simultaneous determination of the coupling rate and the linewidth enhancement factor from a single measurement of the voltage as a function of detuning under weak injection was discussed. Regularly considered a fitting parameter, the importance of the coupling rate can often be overlooked but it is necessary for accurate comparison of theoretical and experimental studies. The method suggested here allows a good estimate for k and facilitates better fitting of other experimental parameters which are harder to measure. The response to a small signal bias modulation at the zero phase detuning is different to the rest of the locking range and includes interconnected damping and real pole curves and both zero and non-zero resonance frequencies. The relationship between these response parameters at the zero phase point has also been presented and discussed.

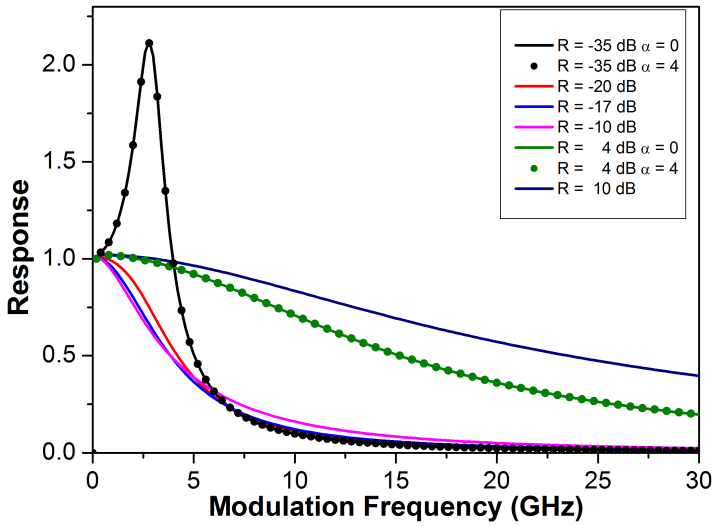

Figure 3.22: Numerically calculated frequency responses at $\phi = 0$ for $\alpha = 0$ and $\alpha = 4$ showing matching curves at injection ratios of $R = -35\,\mathrm{dB}$ and $R = 4\,\mathrm{dB}$.

Chapter 4

Voltage Spectroscopy of Long Wavelength VCSELs

Following from the theory developed in chapter 3 it is noted that the carriers in a semiconductor laser during detuned optical injection can be used as an indicator of the induced dynamics. The most obvious of these is that there is a reduction in carrier number during stable locking with the minimum of the carrier number always a stable state with zero locked phase.

In reality, measuring the carrier number during laser operation is not an easy task. Instead by monitoring the voltage across the device, which is related to the logarithm of the carrier number ($\log N$), it is possible to establish the trends and qualitative changes in N.

Currently, a large array of high end laboratory instruments and significant operator expertise are required to identify which dynamics are occurring in the laser. Based on the output of electrical spectrum analyzers, optical spectrum analyzers and oscilloscopes it is possible to build up a picture of whether the laser is locked or oscillating.

In this chapter, the voltage responses of injected long wavelength VCSELs are experimentally characterised and linked to spectral and temporal characteristics providing a mechanism to identify the induced dynamics which can be performed remotely and automatically.

The optical spectra of a short cavity VCSEL during parallel- and orthogonally-

polarised injection are recorded and correlated with the voltage change to identify characteristic features. Alterations in the voltage response at different injection ratios are recorded and an estimate for the carrier number change during injection is given. Two dimensional voltage vs injection maps are generated to illustrate corresponding behaviours. Following this, the electrical spectra of an injected VCSEL with a longer cavity are correlated with its voltage response. Maps of the measured oscillation frequencies in the VCSEL output and the voltage are presented and the various bifurcations which occur are discussed.

4.1 Spectral properties of optically injected VCSELs

There are two measurement domains in this injection experiment; Optical spectrum analysis and the voltage required to maintain a constant current through the VCSEL. Sample responses from both domains will be discussed individually and then combined to provide new insights.

The laser used in this experiment was an unpackaged, high power, single longitudinal mode VCSEL with similar design to the record output power long wavelength VCSEL [8] developed at the Technische Universität München as described in section 1.2. In the case of the particular device used here, the BTJ has a diameter of 5.5 µm. Basic device characterisation shows room temperature output power of approx. 2 mW with single mode emission recorded for bias currents less than thermal rollover. The Side Mode Suppression Ratio and Polarisation Mode Suppression Ratio are greater than 50 dB and 15 dB respectively. The fibre coupled power-voltage-current (LVI) characteristics and a sample spectrum is shown in fig. 4.1. Figure 4.1 (b) also includes spectra measured through a linear polarizer showing two polarisation modes explicitly. Both polarisation modes appear to have equal intensity in this plot due to a poor couping efficiency during the measurement for the parallel mode. The polarisation mode separation is approx. 0.07 nm or 8.75 GHz with the short wavelength being the dominant lasing mode. Structuring the

burried tunnel junction in the shape of a low eccentricity ellipse provides favorable gain conditions for one of the polarisation modes, however the polarisation properties of the device are more dependent on intrinsic dichroism in the crystal lattice. Polarisation selective elements, such as a sub wavelength grating, have also been used to provide preferential gain conditions to one polarisation relative to the other [64].

4.1.1 Experimental set-up for optical injection

Optical injection into the VCSEL was performed using linearly polarised light from an Agilent 81600B series tuneable laser through a polarisation controller and a three port circulator as depicted in fig. 4.2. This laser could tune between 1440 nm and 1640 nm with a typical linewidth of 100 kHz. The output was linearly polarised with a side mode suppression ration of 60 dB. Coupling to the VCSEL was via a lens ended single mode fibre with an anti-reflection coating specifically designed for optimum coupling to the devices used in these experiments. The output from the VCSELs was routed through a 90%/10% splitter into a powermeter and an ANDO AQ6317B Optical Spectrum Analyzer (OSA). The VCSEL is electrically contacted using Ground-Signal probe and the voltage necessary to maintain a constant current in the device was recorded as the injected light from the tuneable laser was swept in discrete steps of 0.001 nm from positive to negative frequency detuning around the VCSEL's free running lasing wavelength. The OSA trace at each injection point was recorded and later analyzed in a post-processing step in order to determine the dynamical state of the VCSEL.

The experiment was performed with the polarisation of the injection light aligned with the unperturbed VCSEL main (parallel) lasing mode and subsequently rotated to align with the orthogonal mode. Alignment with each polarisation mode under injection was determined by adjusting the polarisation rotator and manually scanning the injected wavelength in proximity to the cavity mode under investigation until a maximum voltage decrease was observed.

The injection ratio, R, was determined through the proportion of inci-

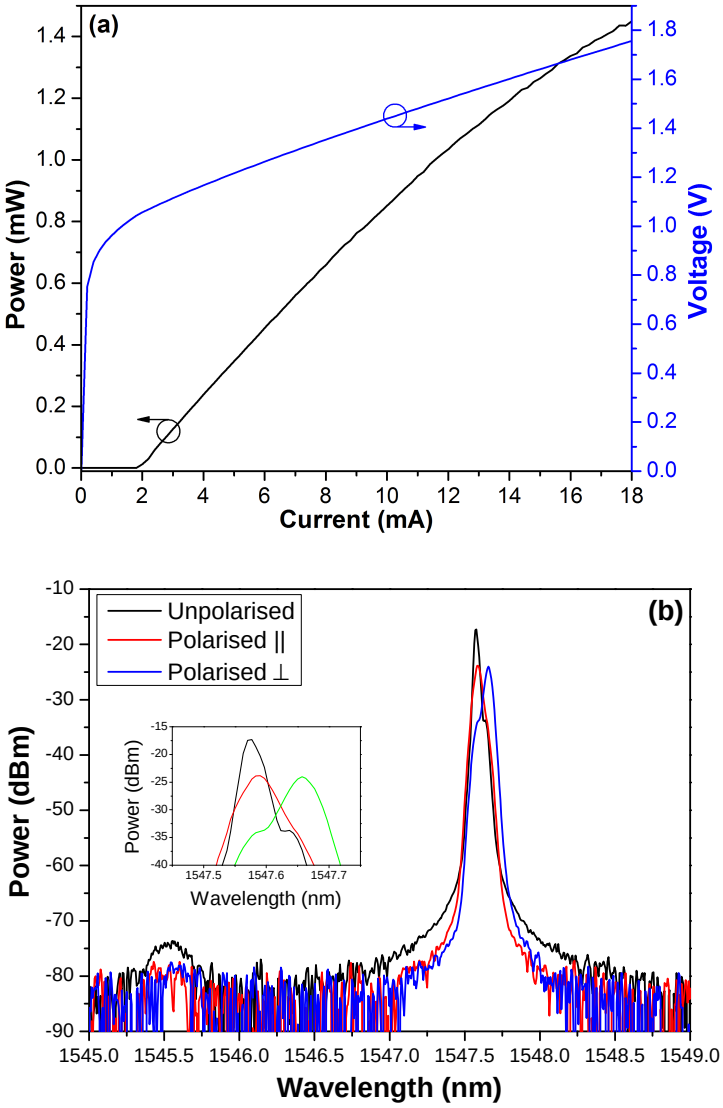

Figure 4.1: Basic VCSEL characteristics. (a) Power-Voltage-Current curves showing threshold is approx. 1.8 mA. (b) Optical spectrum at 2.5 mA. The spectrum is shown three times. The black curve is recorded without a polariser and the red and blue curves are measured with a polariser aligned with the parallel and orthogonal modes respectively. The spacing to the first order mode is approximately -2.1 nm.

dent power to total power emitted from the free running VCSEL. This ratio dynamically changes with detuning due to induced effects as discussed in chapter 3. The incident power was measured as the product of the total power out of the fibre and the coupling efficiency with the VCSEL (45%). This efficiency was estimated as the ratio of the fibre power at optimum coupling to that collected by a broad area detector. Not all of the light incident onto the VCSEL will contribute to the injection effects. For instance, there will be some light reflected from the top mirror and any mis-match between the injected and cavity mode would also reduce the real injection ratio. As these effects are difficult to quantify and can vary with injected wavelength, the definition of the injection ratio used here was chosen as it offers a good overall measure of the trends regarding the injection strength.

The VCSEL under test was biased at 2.5 mA ($1.4^{*}I_{th}$) with a Keithley 2602A low noise current source while being thermally maintained at $25 \pm 0.1\,^{\circ}\mathrm{C}$. The coupling efficiency is believed to be constant as the fibre position manipulation stages were sturdy and the set-up was isolated from air currents by cardboard shielding. Previous experience using high resolution spectral methods aided in the positioning of the optical fibre in order to avoid unwanted optical feedback. Some of the possible effects of optical feedback on the spectrum are discussed in appendix D.

4.1.2 Experimental results

Optical domain

Five qualitatively different types of optical spectra recorded during this experiment are detailed in table 4.1. This list is not exhaustive, for instance the spectrum of a chaotic laser is not included. The types of dynamics which can be expected will vary with injection strength and the most complex dynamics will, in general, be observed in the −50 dB to −30 dB region of fig. 3.5. The results in the next sections suggest we are operating in the −20 dB to −10 dB region of that figure. Each of the different spectral responses are detailed in table 4.1.

Table 4.1: Sample spectra and descriptions of the corresponding dynamics under parallel injection at $R = 0.45$

Description	Optical Spectrum
No Dynamics (ND) There are no interactions between the injection laser and the VCSEL visible on the optical spectrum	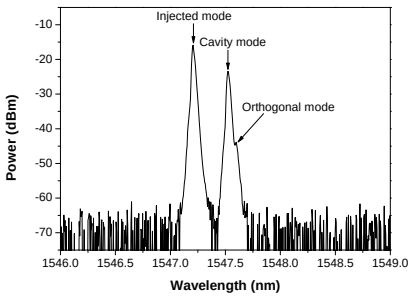
Four Wave Mixing (FWM) The energy in the main VCSEL lasing mode is steadily decreased. There are still two distinct peaks and sideband peaks appear at the beating frequency	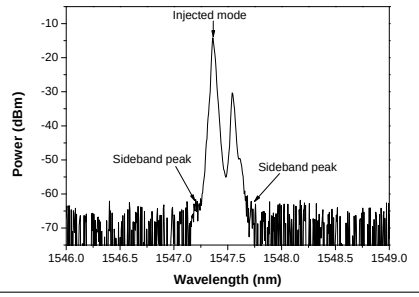
Stable Injection Locking (SIL) There is only a single peak in the optical spectrum which is at the frequency of the injected light	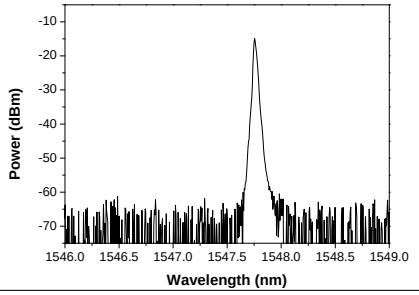
Orthogonal Mode Lasing (OML) The VCSEL has a lasing component in its orthogonal mode which is at its free running wavelength. The normally dominant parallel mode is suppressed	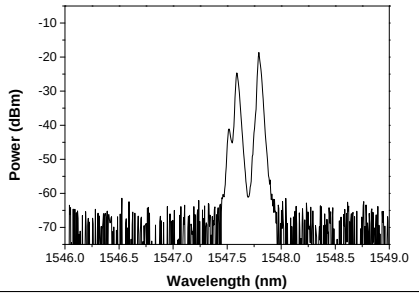
Polarisation Mode Competition (PMC) Both polarisation modes in the VCSEL are competing to lase with approximately equal intensity at their respective free running wavelengths. Rather than both modes lasing simultaneously, there may be fast mode hopping occurring which is averaged out in the DC OSA measurement.	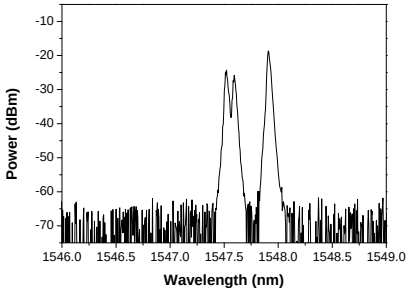

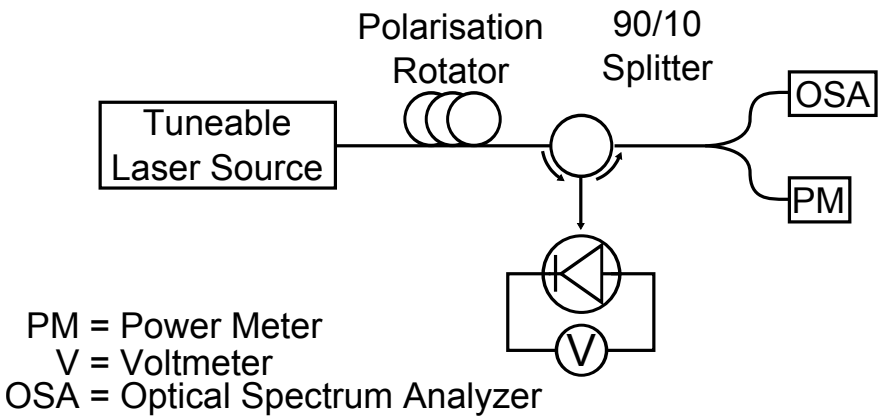

Figure 4.2: The experimental setup used to investigate the correlation between the dynamical state of an injected laser and the voltage required to operate it in a constant current configuration. There is negligible leakage through the circulator ($-48\,\mathrm{dB}$) and minimal back reflections from the antireflection coated tip of the lens ended fibre.

Voltage domain

The fluctuations in the voltage across the device directly reflect the changes in the carrier number in the active region both inside and outside the stable locking range, a theoretical example of which is shown in fig. 3.1 (b). The voltages measured as functions of injected wavelength for injection ratios of $R = 0.04, 0.34$, and 0.68 are shown in fig. 4.3 with the vertical line indicating the wavelength of the free running VCSEL's parallel mode, λ_{fr} and the horizontal line marking the free running voltage, V_{fr}. In these examples the linearly polarized injection light is aligned parallel to the main VCSEL lasing mode. The spectral width where the voltage changes from the uninjected value grows with increasing injection strength. The voltage initially is at the free running level although a slight decrease is observed with increasing injection strength at positive frequency detunings. The free running value is recovered at larger positive frequency detunings.

With decreased detuning a drop in voltage is measured. At low injection strength ($R = 0.04$) the voltage shows a non-linear change with injected wavelength starting at approximately $1546.9\,\mathrm{nm}$. The voltage decrease becomes linear with detuning at $1547.05\,\mathrm{nm}$. Under stronger injec-

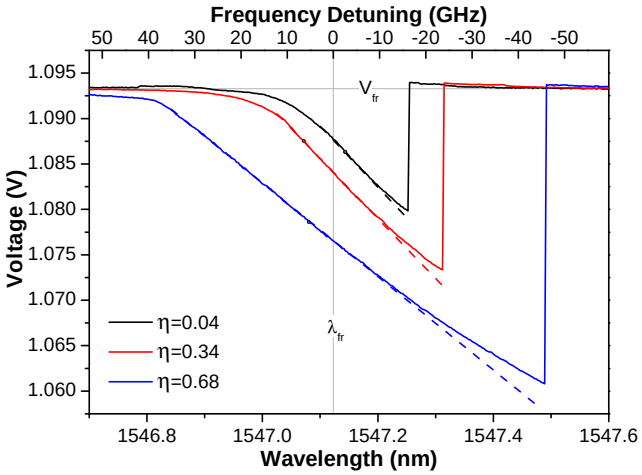

Figure 4.3: Sample voltage responses as functions of injected wavelength for several injection ratios which show common features such as the linear voltage decrease and sharp change to a voltage slightly higher than the free running voltage on the long wavelength side. The vertical and horizontal lines mark the position of the free running parallel wavelength and voltage respectively.

tion ($R = 0.68$) the voltage at large positive frequency detunings is reduced relative to the free running value and transitions to a linear decrease with detunng at 1546.82 nm. On the negative frequency side of the free running wavelength the voltage change becomes sub-linear. This deviation from linear changes is highlighted for all three examples by extending the linear portion with a dashed line. The voltage decrease eventually ends with a sharp increase back to near the free running voltage at 1547.255 nm for $R = 0.04$. The detuning of this feature is also injection strength dependant (1547.5 nm for $R = 0.68$) but always on the long wavelength side of the free running VCSEL mode. The voltage is slightly increased relative to the free running value ($\Delta V \simeq 1$ mV) for a small span of detuning wavelengths in this area before returning back down to V_{fr}. Maximum voltage drops of 13.4 mV for $R = 0.04$ and 32.5 mV for $R = 0.68$ are recorded. The slopes of the dashed lines in fig. 4.3, m_l, and linear approximations to each curve near the voltage minimum, m_{sub}, are noted in table 4.2 showing the change near the voltage minimum. In the next section, variations in the slope of the voltage response with wavelength will be used to identify when the VCSEL is injection locked.

Injection Ratio	$\underline{m_l}$ mV/nm	$\underline{m_{sub}}$ mV/nm
0.04	-67.36	-50.00
0.34	-66.36	-42.49
0.68	-51.20	-37.87

Table 4.2: Slope of the voltage response with injected wavelength in the linear portion, m_l, and near the voltage minimum, m_{sub}.

The homogeneous responses above are not a full set of all measured responses. Voltage responses containing a series of new features that were recorded for another injected VCSEL of a similar design at lower injection ratios are shown in fig. 4.4 (a). Figure 4.4 (a) illustrates the entire data set of which the curves in fig. 4.3 are only a select sample. Under the weakest injection in (a) two peaks in the measured signal occur at 1546.14 nm and 1546.19 nm as indicated by the arrows. These decline in magnitude with increasing injection strength. Under the strongest injection considered in this graph the maximum voltage change is 17.8 mV and the response has evolved so that the shorter wavelength peak is much smaller but still observable while the longer wavelength peak has disappeared entirely into a smooth region near the voltage minimum indicated by the red bracket. There is an noticeable kink at the interface between these two parts. The voltage responses show a clear continuity with regards to increasing injection strength.

Similar features are observed under weak injection in fig. 4.4 (b) which fade in magnitude with increasing injection until they are no longer observable. The change in slope is the only remaining indicator of the weak injection non-linearities. The source of the peaks, the smooth region near the voltage minimum and the other features are discussed in section 4.2. The free running voltage in (b) is lower than (a) as a higher bias current was used in (a) to increase the output power and reduce the relative injection strength. This could be achieved by simply changing the position of the optical fibre however it is best kept at the optimum position for coupling in order to minimize back reflections. A maximum voltage drop of 35 mV is measured.

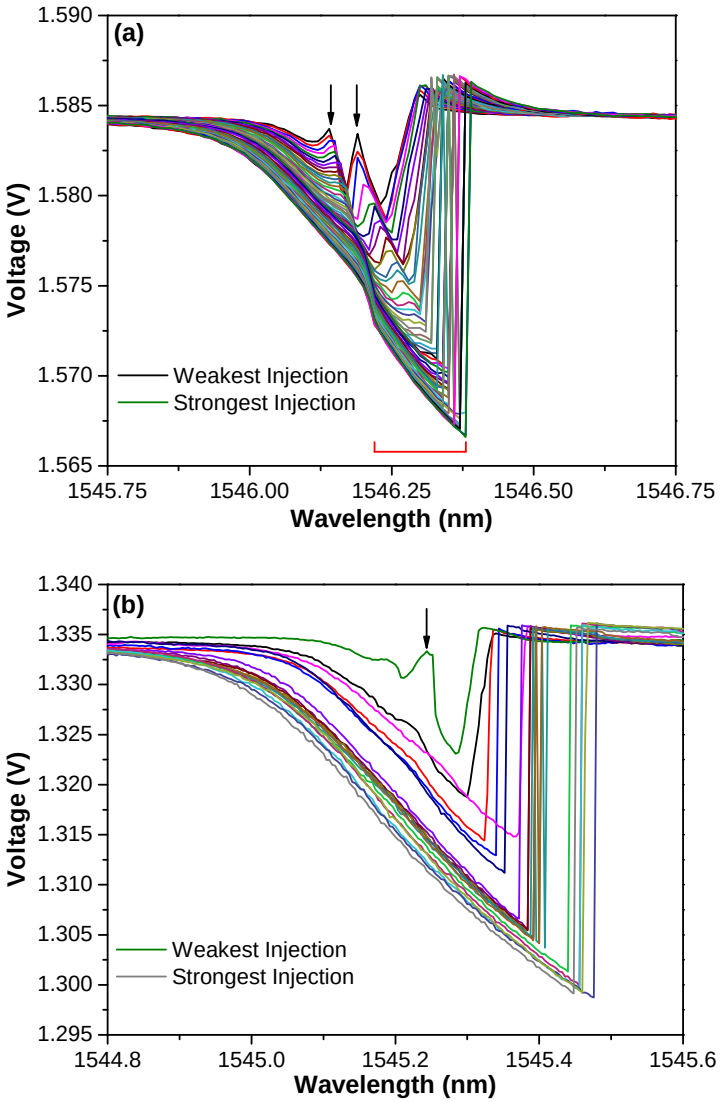

Figure 4.4: Voltage responses for two VCSELs of similar design as functions of injection strength and detuning. The injection regime in (b) is stronger than in (a) where more non-linear behaviour is observed. The free running voltage in (a) is higher than (b) as a higher bias current was used to reduce the injection strength. The arrows in each plot indicate features in the response which decrease in magnitude with increasing injection strength.

Combined Optical and Voltage responses for a single injection ratio

The spectral and voltage responses must contain complementary information for the same experiment. To understand this, Figure 4.5 combines three different data types into a single plot:

1. the voltage required for constant current operation;
2. the dynamical state as determined from the optical spectrum;
3. the peak wavelength of the VCSEL emission.

In this figure, the polarisation of the injected light is parallel and perpendicular to the free running VCSEL mode in (a) and (b) respectively. The injection ratios are measured as $R_{\parallel} = 0.45$ and $R_{\perp} = 0.425$ relative to the free-running 'parallel' mode power. Under parallel injection, the optical spectra show that there are several distinct responses present that correspond to different regions of the voltage response and are delineated by dashed vertical lines.

In detail, the parallel response in fig. 4.5 (a) shows that at smaller positive frequency detunings to the initial No Dynamics (ND) region, where no interaction features are observed on the optical spectrum analyzer, there is a Four Wave Mixing (FWM) region where the optical power from the unlocked VCSEL cavity mode transfers to the injected mode and FWM signals are present in the optical spectra. The transition to stable locking is deemed to have occurred when the light output at the VCSEL's cavity resonance has reduced to amplified spontaneous emission (ASE) with no modal features. A Hopf bifurcation is expected at this point which would lead to undamped relaxation oscillations in the unlocked region. If this does occur, the evidence of increased amplitude relaxation oscillation side bands is hidden beneath the noise floor. Stable injection locking (SIL) is obtained at a detuning of approximately $\Delta\nu_{+} = 10.1\,\text{GHz}$ from the parallel free-running mode. As the frequency offset is further decreased, the locked VCSEL adjusts its lasing frequency to match. The reduction in voltage can be explained physically, see chapter 3, by the VCSEL adjusting the optical length of the cavity through

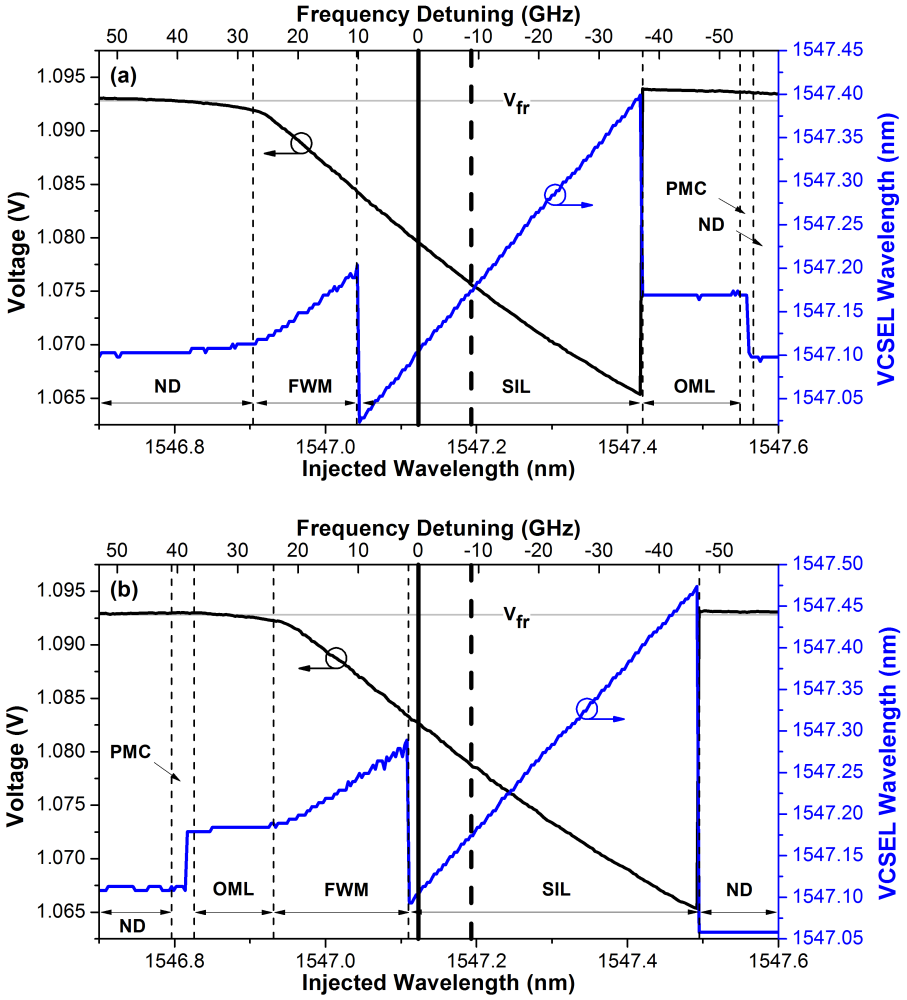

Figure 4.5: Voltage response curves and VCSEL cavity wavelength during injection showing the zones of different optical states for (a) parallel injection at an injection ratio $R = 0.45$ and (b) orthogonal injection at $R = 0.425$. ND = No Dynamics, FWM = Four Wave Mixing, SIL =Stable Injection Locking, OML = Orthogonal Mode Lasing, PMC = Polarisation Mode Competition. The heavy solid (dashed) line at 1547.123 nm (1547.193 nm) shows the position of the free running parallel (orthogonal) mode. The free running voltage is indicated by a dash horizontal line.

a carrier density change which results in a shift in the standing optical wave and a possible gain change. Additionally it can be viewed as a reduction in the cavity losses as the injected light adds constructively to the cavity field with a dependence on the phase, at least across the stable locking region.

The unlocking at negative detuning is at $\Delta\nu_{-} = -36.7\,\text{GHz}$ and is correlated with the sharp return to a nearly free running voltage. At this injection ratio the locking bandwidth and maximum voltage drop are approx. 42 GHz and 28 mV respectively. The slight voltage increase of approx. 0.45 mV measured at these detunings corresponds to the VCSEL lasing in the orthogonal mode in a stable manner (OML). Even though the polarisation of the injected light is aligned to the parallel mode and offset by $-50\,\text{GHz}$ from the free-running VCSEL frequency it nevertheless induces a stable polarisation switch. The voltage increase reflects a rise in the carrier density in the active region so that the orthogonal mode experiences higher optical gain than usual. Typically, a fixed output polarisation exists due to asymmetries unique to each VCSEL such as stresses and strains in the active region but, given the right conditions as in this work, the normally suppressed mode can lase. Complex dynamics, instead of a stable polarisation switch, could also occur as discussed in chapter 3 but they are not observed in this device. Models incorporating both polarisation modes indicate the possibility of such stable switches [110], [114]. Eventually, at a frequency detuning of $-55\,\text{GHz}$, the injected light is no longer able to maintain this switching effect as the detuning limit of this feature has been reached. The two polarization modes briefly compete for the available gain (PMC) before the VCSEL returns to its free running configuration, reflected by a free running voltage. The magnitude of the voltage increase measured during OML should be dependent on the polarisation mode separation. As the optical spectrum measurement takes several seconds, there is no information on the high speed dynamics which might be occurring. In the PMC region, the two modes might not be lasing at the same time but rather there might be fast switching between the two or else a two mode limit cycle might exist [147]. The excitation of such dynamics suggests that the injected light, while linearly polarised, might demonstrate a polarisation rotation as a function of wavelength.

In the ND region on the long wavelength side the system has not returned identically to its original state, see fig. 4.6 which shows OSA traces at five detunings from the ND region on either side of stable locking. On the short wavelength side, the power levels in the cavity mode are slightly increased and the power in the injection mode slightly reduced compared to the ND region on the blue side. It is speculated that energy lost from the injected mode must be going to pump the orthogonal VCSEL mode to some small extent as the Polarisation Mode Suppression Ratio (PMSR) is only 14.5 dB compared to 20 dB. The parallel VCSEL wavelength is also slightly blue shifted.

Some information on the interband transitions can be extracted from these plots. Injection on the short wavelength side of the cavity mode implies that photons are entering the cavity with energies larger than that of the electronic transition pumping the lasing mode. Tuning the injected wavelength across the stable locking region eventually results in the energy of the injected light being less than the free running light. When the negative frequency detuning boundary is crossed the injected light can no longer cause resonant absorption or stimulation for the parallel mode but is now closer to the resonance energies for the longer wavelength orthogonal mode. The injected light now inefficiently pumps the orthogonal mode but the parallel mode sees no reduction in output powers as the bias current pumps that mode just as in the free running case. This mechanism contributes to explaining the disparity between the ND regions on the opposite sides of SIL as indicated in fig. 4.6 (b).

A broadly similar result is found for orthogonally polarised injection. The primary difference is that the orthogonal mode is induced into lasing on the positive frequency side of locking (approx. 24 GHz from parallel mode) as shown in fig. 4.5 (b). Correspondingly, it is the intensity of the orthogonal mode which is being reduced in the Four Wave Mixing region. The locking bandwidth and maximum voltage drop are approx. 43 GHz and approx. 28 mV which is comparable with those values for parallel injection.

The decrease in the average carrier number increases the refractive index of the active region resulting in the VCSEL lasing at longer wavelengths as

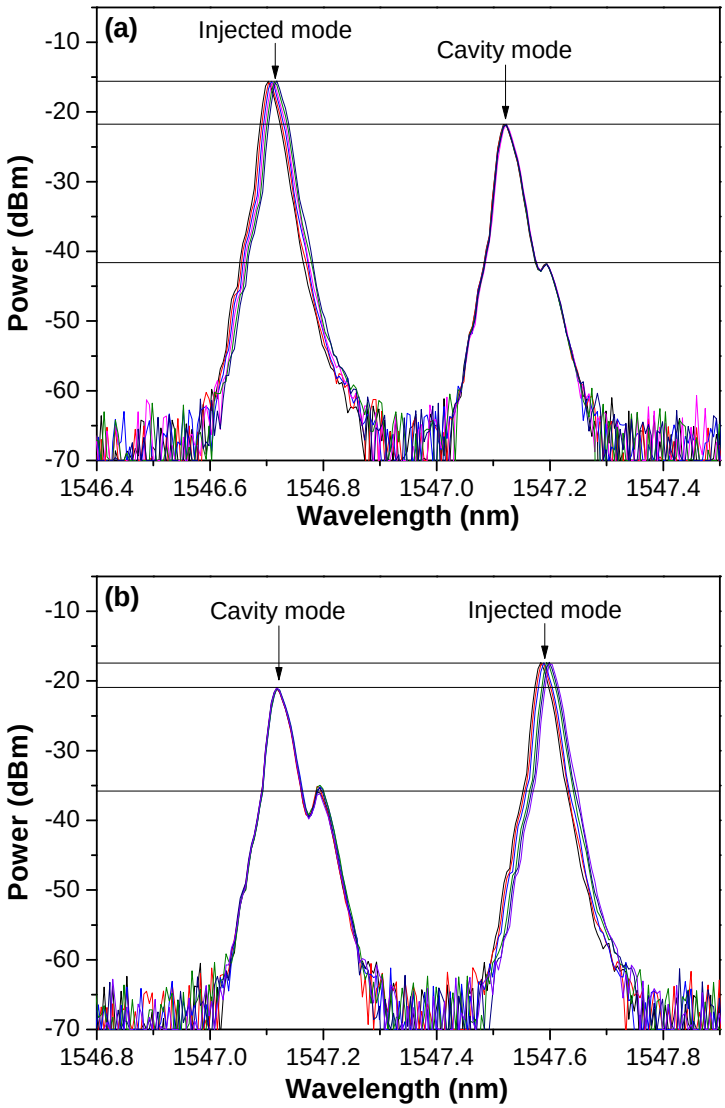

Figure 4.6: Optical spectra in the ND region for an injection ratio of $R = 0.425$ on the (a) positive (53 GHz to 51 GHz) and (b) negative frequency detunings (-57 GHz to -60 GHz). The non-lasing polarisation mode is more intense on the negative side while the injection mode is less intense compared to the positive frequency side.

verified by comparing the traces for the voltage (black) and cavity wavelength (blue) in the FWM region of fig. 4.5 (a). As expected, there are discontinuous wavelength jumps at the locking and unlocking boundaries and also halfway through the area of Polarisation Mode Competition as the VCSEL changes from one polarisation mode to the other. Four sample optical spectra are presented in fig. 4.7 to highlight the changes in VCSEL output with frequency detuning. The peak of the injected light is marked with a black dot and the VCSEL cavity output indicated by a black square. With decreased frequency detuning the VCSEL cavity mode simultaneously shifts to longer wavelengths and reduces in intensity despite the constant pump current. At the same time the intensity at the injected wavelength increases even though the amount of external light being injected remains constant. This shows that the number of photons generated in the VCSEL active region and going into the injected mode rather than the cavity mode increases with decreased frequency detuning. The PMSR drops as the injected mode becomes the dominant mode in the cavity showing that, at these detunings, the injected mode has only a weak effect on the orthogonal polarisation.

The change in the spectral position of the VCSEL cavity referred to as the cavity resonance shift, $\Delta\omega_{cav}$, with a change in carrier number, ΔN, can be calculated using [20]:

$$\Delta\omega_{cav} = |\frac{\alpha}{2}\Gamma v_g g_0 \Delta N| \tag{4.1}$$

where v_g, g, Γ and α are the group velocity, differential gain, longitudinal confinement factor and linewidth enhancement factor respectively. The cavity resonance shift measured across the FWM region is 0.1 nm. An estimate using ΔN is given in the discussion later in this chapter.

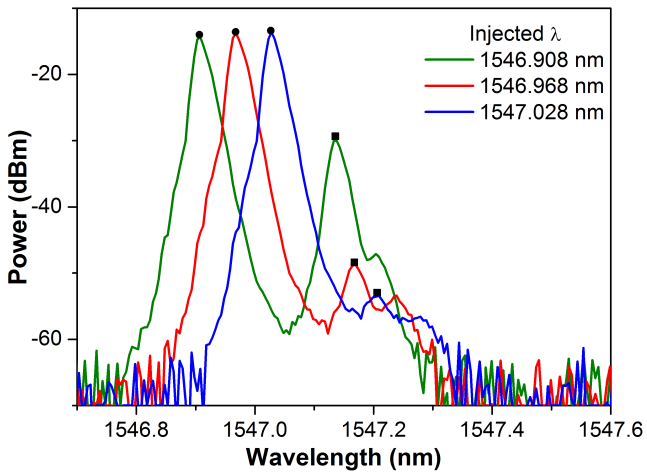

Figure 4.7: Optical spectra for injection at several wavelengths on the positive frequency detuning side of the locking region with $R = 0.425$. As the injected peak (black dots) approaches the VCSEL peak (black squares) the VCSEL peak is red-shifted due to the change in carrier number in the active region altering the refractive index. A power decrease (increase) in the cavity (injection) mode is observed as the VCSEL begins to emit at the injected frequency more than at its cavity resonance.

Injection ratio dependence of voltage and dynamical response

Spectral and voltage data for the individual injection ratios can be complied into two dimensional maps, presented in fig. 4.8 (a) and (b) for the case of parallel injection with calculated ratios between 0.08 and 0.82. To assist in interpreting the plots, the boundaries between the different optical responses are overlaid onto the voltage maps. An immediate conclusion which can be drawn from these maps is that the region with the largest voltage decrease is also the area of stable locking. This is true for both polarizations, see also fig. 4.10.

The locking boundary on the negative frequency side can be identified in the voltage map at all injection ratios by a discontinuity in the voltage across the boundary. This can be up to 30 mV as measured near -50 GHz for an injection ratio of 0.8.

At the positive frequency locking boundary, a smooth decrease in voltage with no easily distinguishable feature is observed. This lack of a clear

boundary corresponds to the difficulty of determining stable locking based purely on an optical spectrum although it is reasonable to state that the positive frequency locking boundary is correct to within a few GigaHertz. In fact, it is the smooth responses at these injection ratios which make it difficult to accurately determine the negative frequency locking boundaries. For example, referring back to fig. 4.4 (a), where the injection is weaker than in fig. 4.8, it is now easy to pick out the stable locked regions as the smooth pseudo-linear portions of each voltage trace featuring the lowest voltage and the sharp return to almost free running values indicated by the red bracket. Other features present in these traces such as those marked by the arrows can now be attributed to oscillations occurring. There is a clear change in slope at the short wavelength locking boundary. This is exemplified in fig. 4.9 where the voltage response for the strongest injection ratio and its derivative are plotted as functions of injection wavelength. There, a local trough and a local peak in the derivative trace are visible at wavelengths corresponding to the short and long wavelength stable locking boundaries respectively.

Returning to fig. 4.8, on the negative frequency detuning side of the stable locking region there is a band where the polarisation has switched and the orthogonal mode is lasing (OML). The spectral width of this band grows, in general, with increasing injection strength. At the negative frequency side of the PML region, a narrow spectral window where both polarisations are lasing with similar intensity is found. The width of this region is also proportional to the injection strength. Again, there may be fast dynamics such as polarisation switching or a two mode limit cycle occurring here but this information cannot be recorded by the slow OSA measurement. At positive frequency detunings a Four Wave Mixing (FWM) band is recorded with a spectral width similar to the stable locking width. The boundary between SIL and FMW is measured as being approx. 5 GHz for injection ratios greater than $R = 0.25$. For weaker injection ratios an average locking detuning of 0 GHz is recorded. The spectral widths of all the different regions (FMW, SIL, OML, PMC) reach a minimum at $R = 0.25$. The origin of this feature is still under investigation but it appears in both the optical and voltage responses. An abrupt change in the coupling efficiency can be ruled

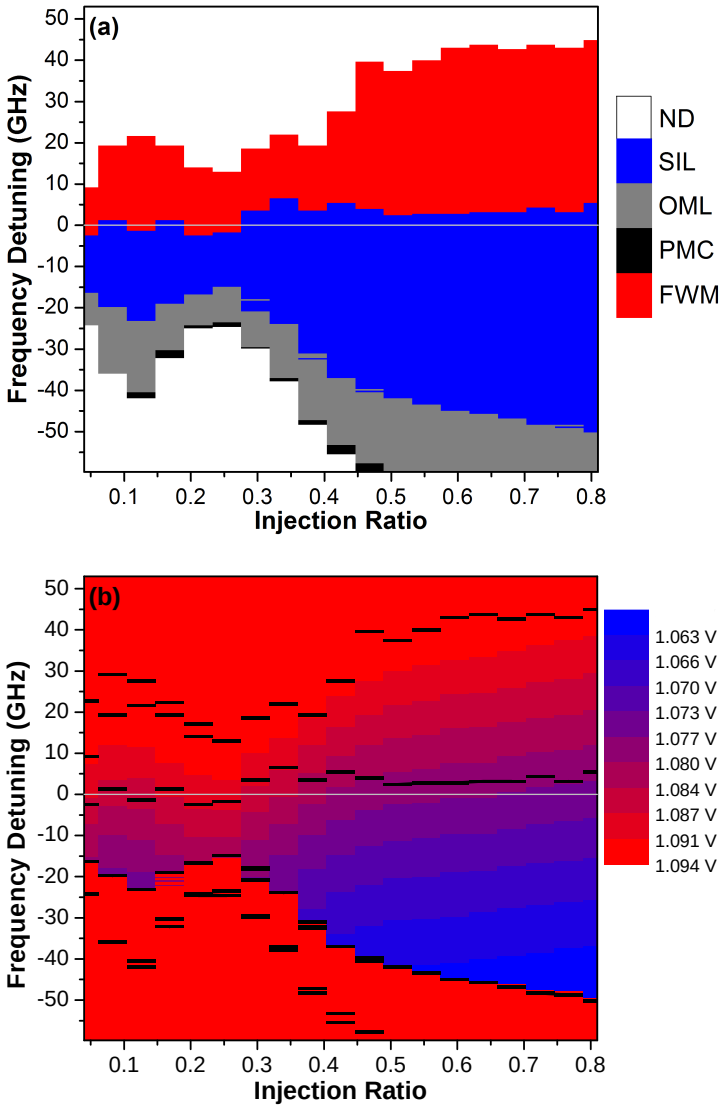

Figure 4.8: (a) The dynamical state of the injected VCSEL during parallel injection as determined via the optical spectrum as a function of injection ratio and frequency detuning. ND = No Dynamics, FWM = Four Wave Mixing, SIL =Stable Injection Locking, OML = Orthogonal Mode Lasing, PMC = Polarisation Mode Competition. (b) The voltage response as a function of injection ratio and frequency detuning.

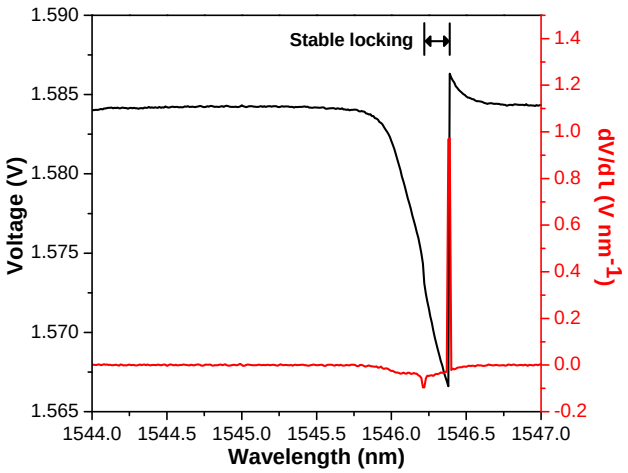

Figure 4.9: The voltage response of the VCSEL and its derivative as functions of injected wavelength. The derivative shows local extrema at the locking and unlocking boundaries. The response studied here is that for the strongest injection depicted in fig. 4.4 (a) with $R = 0.01$.

out as there is a smooth gradient in spectral widths on both sides of $R = 0.25$.

The two dimensional maps for the case of orthogonal injection are shown in fig. 4.10. The injection ratios are still quantified relative to the free running intensity of the parallel mode while the detunings are given with respect to the orthogonal mode.

At all injection strengths the VCSEL switches to the orthogonal mode on the positive frequency side of locking before entering a FWM region with increasing frequency detuning. As with parallel injection, the spectral widths of the stable locking and FWM regions grow in proportion to the injection strength. The width of the OML region remains approximately constant (3 GHz) at all injection ratios. At the lowest ratio considered, however, an anomaly occurs in that after the VCSEL switches to the orthogonal mode there is a region where both polarisation modes lase instead of Four Wave Mixing occurring. The positive detuning stable locking boundary remains approx. -5 GHz over the entire injection ratio range considered. At negative detunings greater than the negative locking boundary no other features are recorded in the optical domain. There, the VCSEL returns to lasing in its parallel mode.

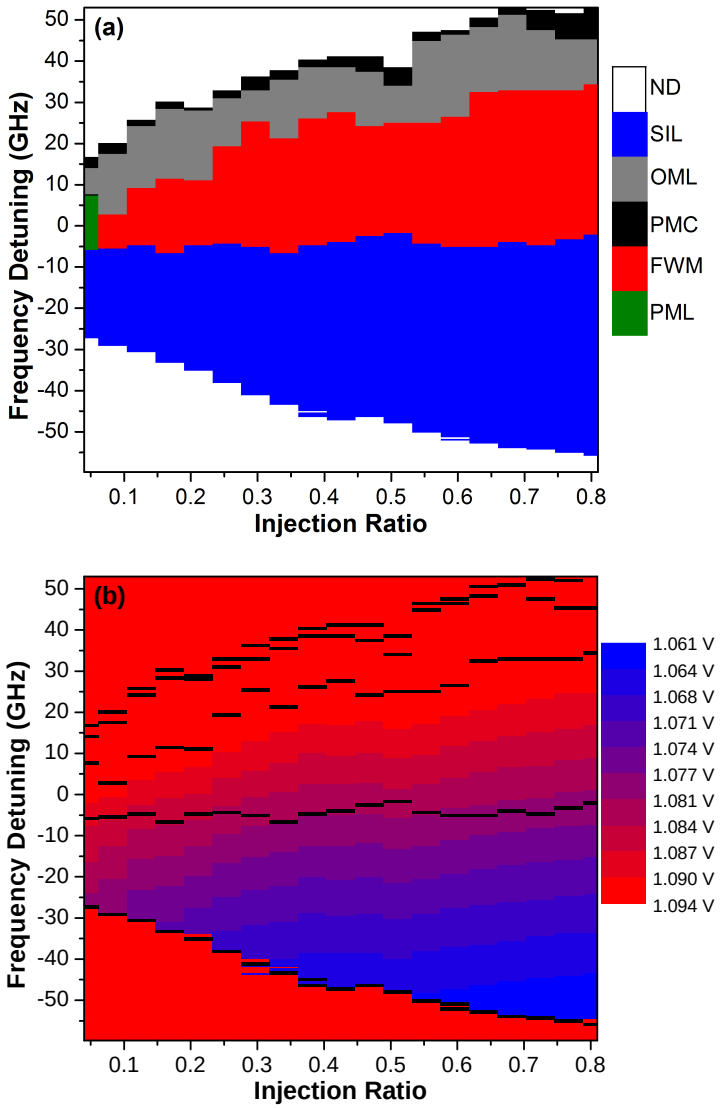

Figure 4.10: (a) The dynamical state of the VCSEL during othogonal injection determined via the optical spectrum as a function of injection ratio and frequency detuning. The detuning is given relative to the parallel mode. (b) The voltage response as a function of injection ratio and frequency detuning.

4.1.3 Discussion

A significant discrepancy between the behaviour suggested by the theory and the experimental results is the occurence of a stable switch to lasing in the orthogonal mode when injecting parallel light at larger negative frequency detunings than the stable locking region. A Saddle-Node bifurcation is expected to take place at this boundary, resulting in the birth of a limit cycle, but no characteristic traits of an oscillation are seen experimentally. This is likely due to the difference between the single mode model used and the actual polarization properties of the device. In order to maximise the performance of these VCSELs considerable attention is directed towards the design of the optical cavity including controlling the possible optical modes which can be sustained in the cavity as mentioned in section 1.2. Discussion on models which include electric field terms for both polarisations can be found in [106], [112] and [109].

Nevertheless,the model used in this work, which neglects a second polarisation mode, can still provide a reasonable explanation of the observed behaviour. Solving the optical injection locking rate equations with a combination of fixed parameters and using the differential gain, g, the linewidth enhancement factor, α and the coupling rate, k as free parameters for fitting results produces carrier density curves which reproduce the measured voltage responses over the entire detuning range. The exact parameters used can be found in table 1.1 and the details of the integration method can be found in appendix B. The simulation is done in the frequency domain but has been normalised to the same wavelength scales as the experimental data for ease of comparison. The simulated characteristics are shown in fig. 4.11 and compared to the voltage response for parallel injection from fig. 4.5.

In the unlocked region, sinusoidal oscillations of varying frequencies related to the beat frequency between the injected frequency and the shifted cavity mode are calculated. The maximum and minimum values of the time traces are extracted and their envelopes plotted in fig. 4.11(a). These maximum and minimum curves coalesce at the point of locking ($\Delta\nu_- = -37.3\,\mathrm{GHz}$) in a Hopf bifurcation and split apart again at the unlocking de-

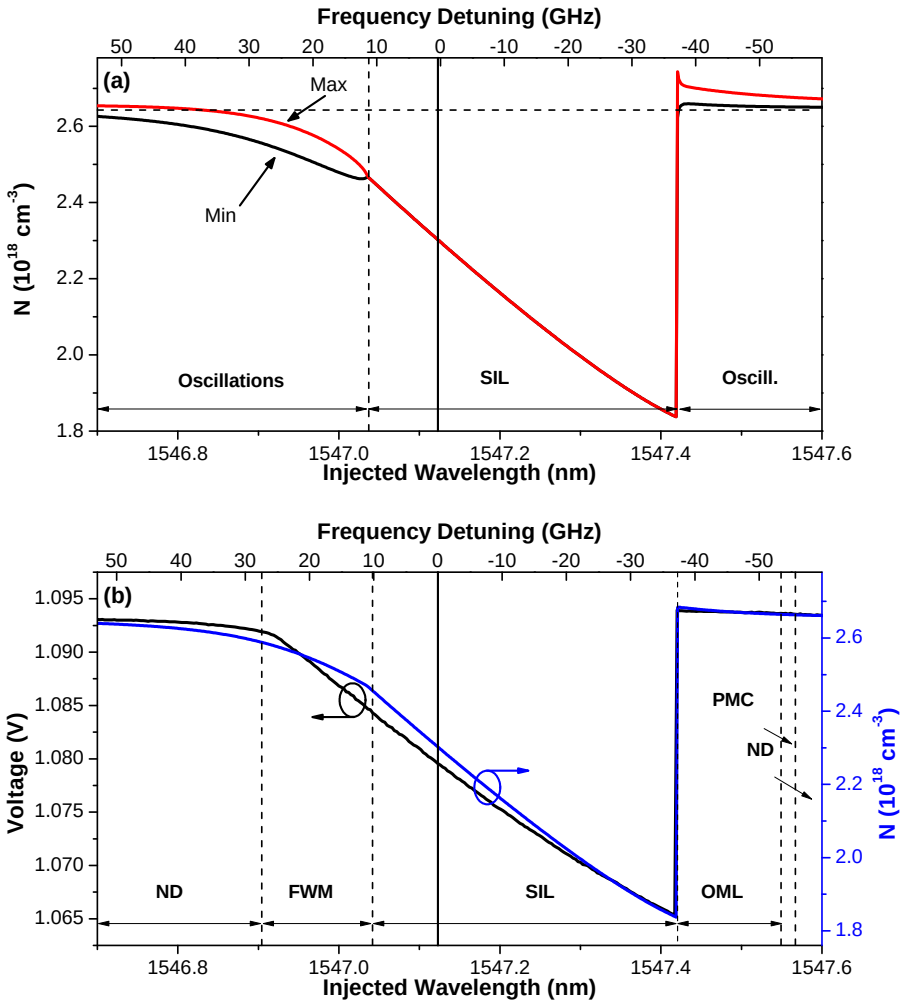

Figure 4.11: Simulated carrier density variation (N) during optical injection. The maximum and minimum envelopes of induced oscillations are shown in (a) with the mean of these compared to the experimental voltage data (black curve) for parallel injection in (b). The free running carrier density is indicated by a horizontal line and the different optical zones are marked as in fig. 4.5 (a). The injection ratio was set at $-4\,\mathrm{dB}$ and a coupling rate of $220 \times 10^9\ \mathrm{s}^{-1}$ was used to provide the best fit.

tuning at $\Delta\nu_+ = 10.8\,\text{GHz}$ through a saddle-node bifurcation, as the system returns to an oscillatory state. Figure 4.11 (b) compares the mean of carrier density in fig. 4.11 (a) with the experimental data for the parallel injection case. The various regions are delineated as in fig. 4.5 (a).

A good qualitative match between the simulated carrier density and measured voltage response is achieved over the entire detuning region but in particular on the negative frequency detuning side of locking. There, the carrier density is higher than the free running value. Experimentally, an increased voltage in this region is observed in this OML region.

The example considered in detail here has a continuous behaviour across the locking boundary on the positive detuning side making it difficult to locate the boundary based on the value of the voltage or its derivative. In order to ensure the VCSEL is in a locked state based purely on the voltage, it is necessary to maintain detunings near the negative frequency locking boundary.

Depending on the injection ratio and detuning, either an increase or decrease in carrier number is expected during stable locking, fig. 3.15. Under medium to strong injection only a drop in carrier number will be observed and this drop will not be from the free running carrier number but rather an already reduced value due to the asymmetry in the stable locking range with respect to detuning. The carrier change during locking can be estimated via the experimental voltage measurement by utilising the quasi-linear change in voltage with injected wavelength during the Four Wave Mixing region on the positive frequency of the locked region. The changes in carriers, ΔN, and in wavelength of the VCSEL cavity mode, are related through (4.1) which can be expressed in terms of wavelength as:

$$\Delta\lambda_{cav} = -\frac{\alpha\lambda^2}{4\pi c}\Gamma v_g g_0 \Delta N \tag{4.2}$$

where λ is the free running wavelength. Figure 4.5 (a) shows that, across the FWM region, the cavity mode red shifts from 1547.1 nm to 1547.2 nm resulting in a calculated carrier density change of:

$$\Delta N_{\mathrm{FMW}} = \frac{4\pi c}{\alpha\lambda^2}\frac{\Delta\lambda}{\Gamma v_g g_0} = -2.43 \times 10^{16}\ \mathrm{cm}^{-3}. \tag{4.3}$$

As the voltage variation is quasi-linear through the FWM and SIL regions in fig. 4.5 (a) the carrier change across the locked region can then be estimated through the ratio of the voltage changes in the FWM region ($\Delta V_{\mathrm{FMW}} = 7.08\,\mathrm{mV}$) and the locked region ($\Delta V_{\mathrm{SIL}} = 18.95\,\mathrm{mV}$) to be

$$\Delta N_{\mathrm{SIL}} = \frac{\Delta V_{\mathrm{SIL}}}{\Delta V_{\mathrm{FWM}}}\Delta N_{\mathrm{FWM}} = -6.5 \times 10^{17}\,\mathrm{cm}^{-3}. \tag{4.4}$$

The carrier density change across the stable locking region of $6.3 \times 10^{17}\,\mathrm{cm}^{-3}$ estimated theoretically in fig. 4.11 (b) is in good agreement with the experimental estimate calculated here using eq. (4.4). The accuracy of these calculations is reliant on several fitting parameters so independent verification of the various quantities, such as determining α using the method proposed in chapter 3, would be beneficial. These checks were not performed due to damage to the devices being investigated and time constraints prohibiting repeating the entire set of measurements.

4.2 Dynamical properties of optically injected VCSELs

In addition to the fundamental oscillation at $\sim 193\,\mathrm{THz}$ slower oscillations, due to the injection, modulating this primary signal will occur. These frequencies, on the order of GigaHertz, are detectable and are a good indicator of the temporal dynamics in the laser.

Based on this knowledge, a second class of experiments was performed where the OSA in the experimental set-up was replaced with a New Focus Model 1014, 45 GHz IR photodetector and an Agilent 4407E Electrical Spectrum Analyser (ESA) with a bandwidth of 26.5 GHz as shown in fig. 4.12. The ESA decomposes the electrical output from the photodiode into its constituent frequencies and displays their relative intensities. The resulting trace is effectively the Fourier Transform of the time series of the induced oscil-

lations. More information on electrical and optical spectra can be found in [91], [20] and appendix A.

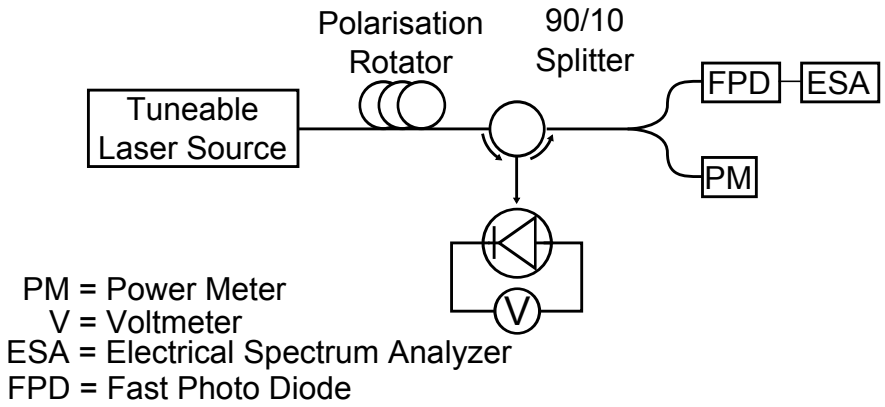

Figure 4.12: Injection locking set-up using a high speed photodiode and Electrical Spectrum Analyzer to determine the temporal dynamics of the VCSEL.

The devices studied in these particuar experiments were provided by Vertilas GmbH and have a similar physical structure to the TUM VCSELs in that they also use a Buried Tunnel Junction to achieve good temperature characteristics but employ a semiconductor rather than dielectric top DBR leading to a longer effective cavity length. The VCSELs were packaged on TO-46 headers without any covering cap so close positioning of the lensed fibre to the output aperture was still possible. The pins of the TO-46 header were connected with home-made sockets, in comparison with the TUM VCSELs which were directly contacted with high quality Ground-Signal probes. While being thermally controlled at 25 °C, the laser is biased at $2.2 * I_{th} = 3.4\,mA$ during the experiment. At this current the optical spectrum emitted in a single longitudinal mode at 1542.07 nm with an orthogonally polarised mode at 1542.598 nm. This polarisation mode separation is almost 8 times larger than for the TUM VCSEL. The PMSR is around 40 dB. A first order transverse mode is suppressed by around 60 dB with a wavelength separation of approx. $-2.5\,nm$ (312 GHz). Basic device characteristics are presented in fig. 4.14.

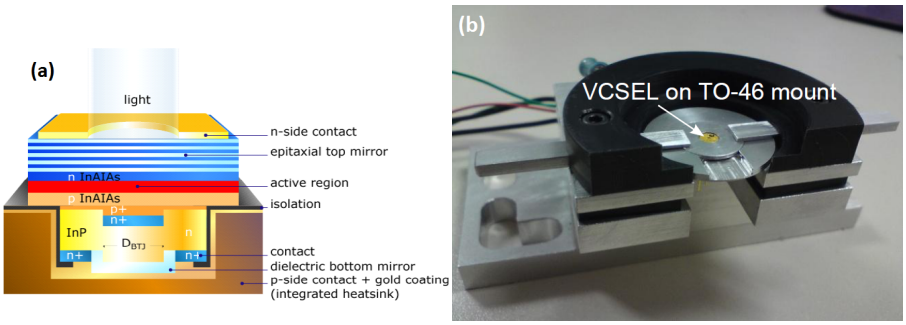

Figure 4.13: (a) Schematic structure for Vertilas long wavelength VCSEL. Image taken from http://www.vertilas.com (b) VCSEL on a TO-46 header mounted in a home-made measurement structure.

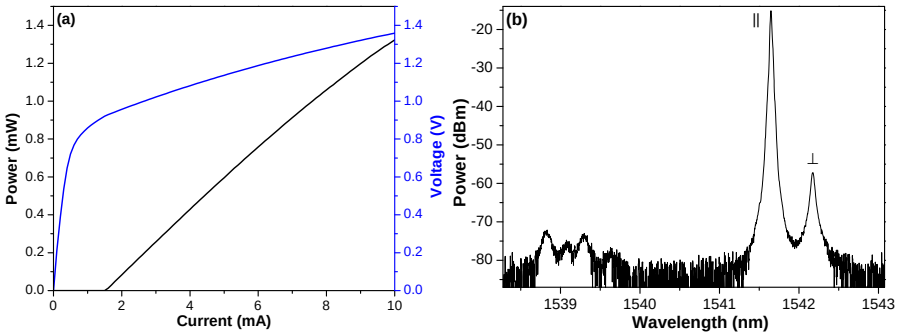

Figure 4.14: Basic VCSEL characteristics for the Vertilas device. (a) Power-Voltage-Current curves at a heat sink temperature of 25 °C showing threshold of approx. 1.6 mA. (b) Optical spectrum at 3.4 mA indicates the short wavelength polarisation mode is the free running mode.

4.2.1 Experimental results

In this section, detuned linearly polarised light from the same laser described in section 4.1.1 was injected around both polarisation modes separately. First, parallel light was injected around the free running mode then orthogonally polarised light was injected around the orthogonal mode and the voltage and ESA responses in each case were recorded.

Electrical domain

Table 4.3 shows sample electrical spectra measured for regions of stable locking, single period dynamics, period doubled dynamics and when the laser operates in a chaotic manner. A summary of their qualitative features is also given.

The spectrum for stable locking contains no peaks or features making it easier to identify both edges of the stable locking region using an ESA compared with the OSA. No features are seen on the trace if the dynamics are faster than the bandwidth of the measurement system. The ESA is only capable of 26 GHz so it is this, rather than the 40 GHz photodiode, which is the bandwidth limiting element.

Voltage domain

The corresponding voltage responses under detuned injection are, in principle, similar to those recorded in section 4.1.2 for the TUM short cavity VCSELs. The voltage when the VCSEL is driven at constant current changes from free running values by a few milliVolts at different detunings. While the same output powers from the tuneable laser were used as in section 4.1 (nominally these are 0.1 mW to 1.8 mW), and similar fibre-coupling efficiencies were achieved, the voltage responses of the VCSEL demonstrated significantly more non-linear features, characteristic of a lower injection strength. One possible reason for this could be a lower coupling rate for these VCSELs vis-a-vis the TUM devices. Different Linewidth Enhancement Factors will also influence the extent of non-linear behaviour as was discussed in sec-

Table 4.3: Sample electrical spectra and descriptions of the corresponding dynamics recorded at $R = 0.3$.

Description	Electrical Spectrum
No Dynamics (ND) No features in the ESA trace. This is generally because the beating of the injected light and the VCSEL light occurs at a frequency beyond the measurement capabilities of the system.	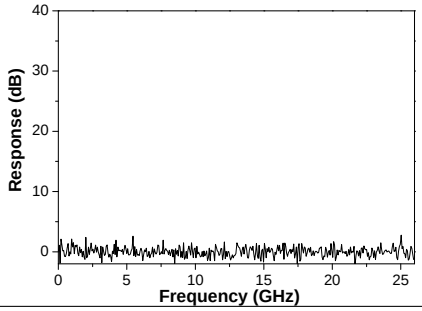
Single Period Oscillation (P1) The fundamental frequency, f, of the oscillation is recorded as a single intense peak. Less intense peaks at multiples of f appear due to an imperfect sinusoidal fundamental oscillation.	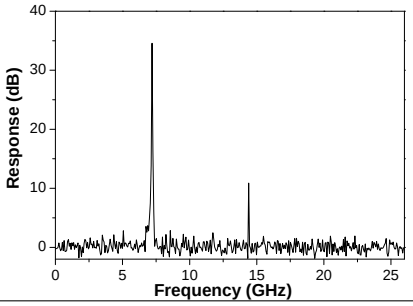
Period Doubled Oscillation (P2) After a period doubling bifurcation frequency components at half the fundamental frequency are present. Subsequent period doublings will lead to components at $f/4$, $f/8$ etc. along with sum and difference frequencies.	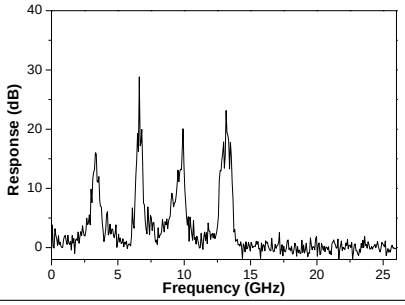
Stable Injection Locking (SIL) A flat response is recorded in the case of stable locking as there are no oscillations present on the output light. This can be distinguished from ND by the spectral position of the locked region.	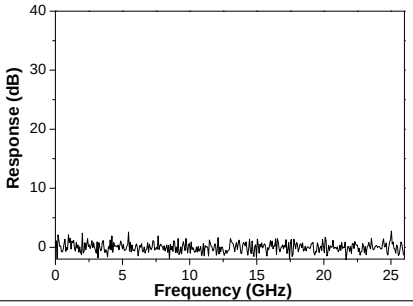
Chaos (CH) Dynamical features at a continuum of frequencies are present in the output light so that the electric spectrum loses its descrete nature. Chaotic behaviour arises through a period doubling cascade.	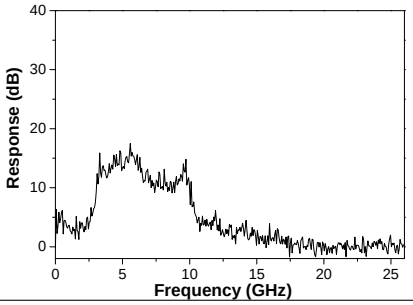

tion 3.2.1. The detuning range over which dynamics were measured for these VCSELs was smaller than the devices in section 4.1 and, in general, the voltage responses were also nosier but the relative difference in the magnitude of the voltage changes probably also contributes to this effect. Other factors like poor electrical contacts could also be a source of voltage noise.

A voltage drop followed by a return to approx. free running values is measured for both injected polarisations as a function of frequency detuning. Under weak injection, increases of $1-2\,\mathrm{mV}$ are recorded on the positive frequency detuning side of the free running cavity mode for parallel injection which are not present for orthogonal injection. The magnitude of these features is a function of injection ratio and they diminish with increasing injection strength as the voltage responses tend toward the responses observed under the strongest injection in fig. 4.4 (b). Maximum voltage drops of $\Delta V = 4.5\,\mathrm{mV}$ and $\Delta V = 5\,\mathrm{mV}$ for parallel injection and orthogonal injection respectively are measured at $R = 0.8$ in agreement with the hypothesis that the experiments are at relatively weaker injection ratios than section 4.1.2 which shows far larger voltage reductions.

Combined Electrical and Voltage Results

An efficient way to visualise the dynamics is to array all of the ESA spectra and plot them alongside the voltage reponses. This allows easy comparison of the changes in each domain. This type of plot is presented for two injection ratios for each polarisation. Figure 4.15 shows the response for parallel injection at $R = 0.29$ and 0.52 while the orthogonal response for $R = 0.28$ and 0.52 is presented in fig. 4.16. A strong correspondence between the different non-linear dynamics and the voltage response is revealed. The area of stable injection locking again corresponds to the area of lowest voltage next to a sharp change on the negative frequency detuning side to approximately free-running voltage. This transition is not always as sharp as in section 4.1.2 for the TUM VCSELs and this may be related to the weaker injection regime under consideration.

Detunings where the voltage increases generally correspond to higher

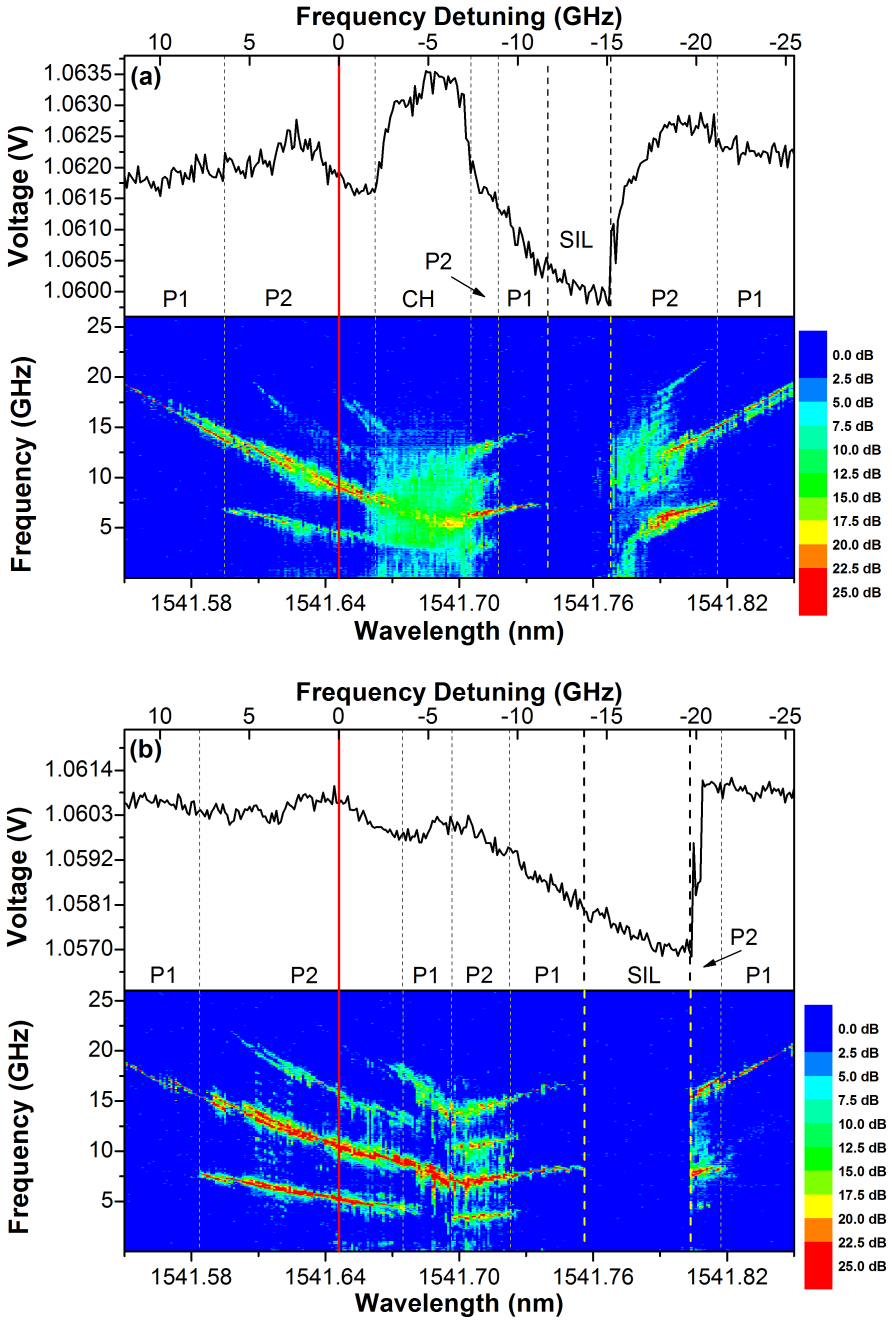

Figure 4.15: Combined voltage response and intensity plots of the electrical spectrum during parallel optical injection of the Vertilas device at injection ratios of (a) $R = 0.29$ and (b) $R = 0.52$

.

order dynamics. For instance, in fig. 4.15 (a) the voltage increase near 1541.68 nm is a region where a continuum of frequencies in the ESA response is observed indicating complicated oscillations and chaotic behaviour. With longer wavelength injection near 1541.70 nm the ESA shows the oscillation simplifies to P1 though a cascade of reverse period doubling (or period halving) bifurcations before stable locking is achieved near 1541.725 nm. The width of the stable locking region at this injection ratio ($R = 0.29$) is only 3.5 GHz and yet is still easily identifiable from the voltage trace. Under weak injection, as in this example, the return of the voltage to its free running value is not as sharp as under stronger injection. Here, it takes a relatively wide frequency detuning band of 1.8 GHz to achieve this. The ESA response in the unlocked zone near 1541.78 nm smoothly tends to zero in frequency just on the edge of the locking zone. These characteristics suggest a Saddle-Node on a Limit Cycle bifurcation at the negative frequency locking boundary where the period of the limit cycle in the unlocked region goes to infinity as the detuning reaches the locking boundary before the birth of two fixed points, one of which results in stable locking [27]. The dynamics in this region are complicated and could possibly be broken down into smaller sections, regardless the region as a whole is designated as P2. There is a voltage increase at negative detunings beyond the SIL region where higher order oscillations are observed rather than the polarisation switch seen in TUM devices (fig. 4.5). Regions of high order dynamics are usually surrounded by regions of Period 1 and Period 2 dynamics. These sections can be missed due to a combination of measurement resolution and experimental noise. As expected, the stronger the injection strength, the greater the voltage decrease to the locking region and the sharper the increase at the negative frequency detuning locking boundary. The linear regions to the positive frequency detuning side of the minimum voltage on both traces again match the stable locking region.

Far fewer features are measured in the ESA response for the case of perpendicular injection. As seen in the examples for $R = 0.28$ and $R = 0.52$ in fig. 4.16, with the exception of stable locking the only dynamical response measured was Period 1. All of the observed P1 oscillations had frequencies in the region of 7 GHz which suggests the relaxation oscillation

frequency plays an important role. Stable locking is achieved through a Hopf bifurcation. This can be inferred from the change in fig. 4.16 (b) at 1541.24 nm where, with decreasing frequency detuning the single peak at 10 GHz decreases in intensity until it completely disappears at the stable locking boundary. This is characteristic of a Hopf bifurcation where a stable limit cycle shrinks and loses stability while simultaneously a fixed point gains stability. The SIL region matches the minimum voltage with a near-linear variation with wavelength detuning.

Under weaker injection, the frequency of the oscillations on the negative frequency side of the stable locking region goes to 0 GHz, as with parallel injection, suggesting a Saddle-Node on a Limit Cycle. There is a small voltage increase above the free running value at these detunings. This voltage increase is not measured under stronger injection where the temporal response suggests a Saddle Node on a Limit Cycle. This can be deduced from fig. 4.16 (b) at 1542.325 nm where an intense P1 dynamic appears abruptly rather than growing from a smaller amplitude. This corresponds to the stability of the fixed point being lost through annihilation with an unstable fixed point and the VCSEL switching to a stable limit cycle.

Figure 4.17 shows the optical spectra under orthogonal injection at an injection ratio of $R = 0.517$ when the VCSEL is (a) locked and (b) unlocked. When locked, the parallel mode is suppressed by 50 dB and the cavity output is in the orthogonal polarisation mode at the injected wavelength. The parallel mode is re-established upon unlocking as seen in (b) but the parallel mode displays significant broadening. The bias current for this demonstration is 4.7 mA rather than 2.5 mA which was the bias for the general study.

In a similar manner to fig. 4.8, the measured voltage dynamical response can be plotted in two dimensions as functions of injection ratio and detuning. The maps for parallel injection are shown in fig. 4.18. Comparing the two measurement domains at all injection ratios, the negative detuning unlocking boundary is easily identifiable due to the dramatic voltage change. The voltage increase near -5 GHz, which extends along nearly the entire injection ratio range, matches the white chaotic region in the dynamical response map. This suggests voltage increases correspond to regions of higher order

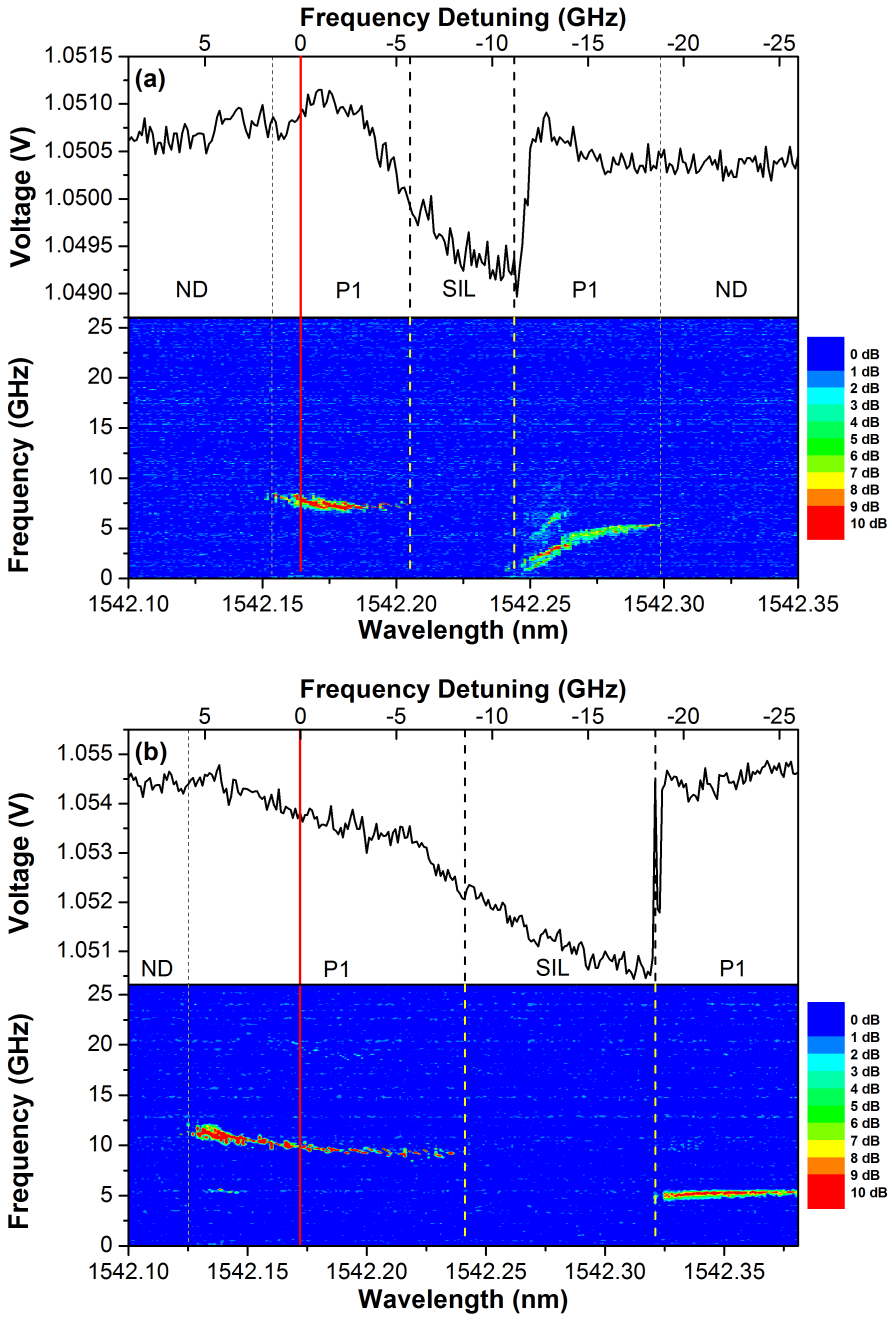

Figure 4.16: Combined voltage response and intensity plots of the electrical spectrum during orthogonal optical injection of the Vertilas device at injection ratios of (a) $R = 0.28$ and (b) $R = 0.52$

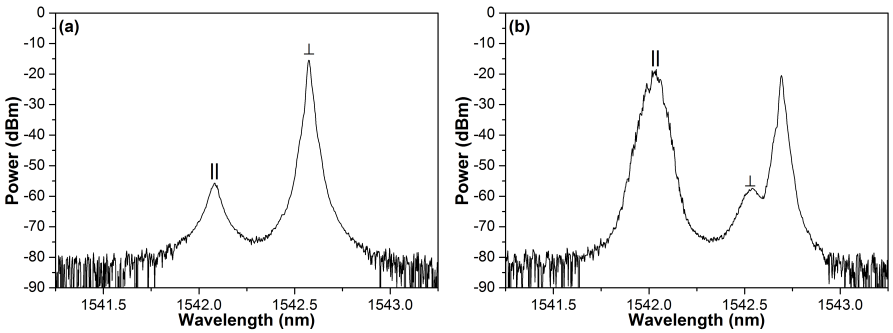

Figure 4.17: Optical spectra during orthogonal injection showing the parallel mode being suppressed during stable locking (a) but becomes dominant again when unlocked (b). The bias current is 4.7 mA in these examples.

dynamics.

For orthogonal injection, fig. 4.19, the frequency detuning is given relative to the free running orthogonal mode but the injection ratio is relative to the free running parallel mode. Period 1 dynamics and stable locking are the only dynamics measured. The shape of the locked region is accurately reflected in the voltage map.

4.2.2 Discussion

The results presented in this section demonstrate a strong correspondence between the operating voltage of the VCSEL and the induced temporal dynamics. However, multiple features need further discussion and clarification.

The voltage response between −5 GHz and −15 GHz for weak parallel injection, fig. 4.15 (a), is similar to the theoretical curve for −58 dB produced in fig. 3.15 for SIL in the S1 region only. Erroneous understanding of the shape of the voltage response could lead to errors in judging the stable locking limits if the voltage is being used to estimate the linewidth enhancement factor. One difference between the two cases is that the entire experimental spectral region being discussed is on the negative detuning side of the free running wavelength. However without a prior characterisation and temperature control of the VCSEL it is not possible to determine the position of the features relative to the free running wavelength.

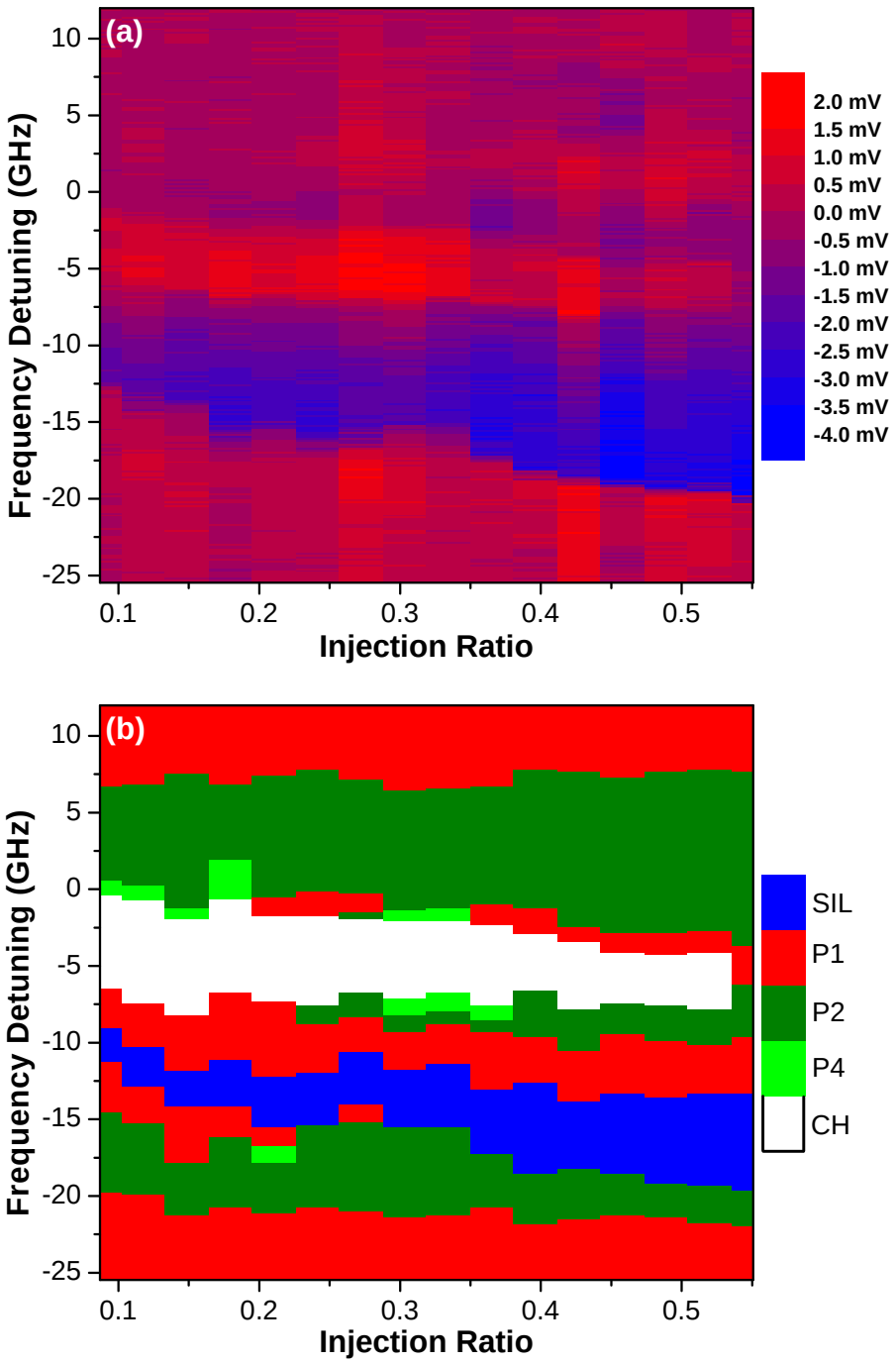

Figure 4.18: (a) Voltage and (b) electrical responses partitioned into the measured dynamics plotted as functions of wavelength detuning and injection strength for parallel optical injection. The maximum voltage drop corresponds to the stable locking region and the areas of voltage increase correspond to regions of higher order dynamics. SIL = Stable Injection Locking, P1 = Period 1 dynamics, P2 = Period 2 dynamics, P4 = P4 dynamics, CH = Chaos

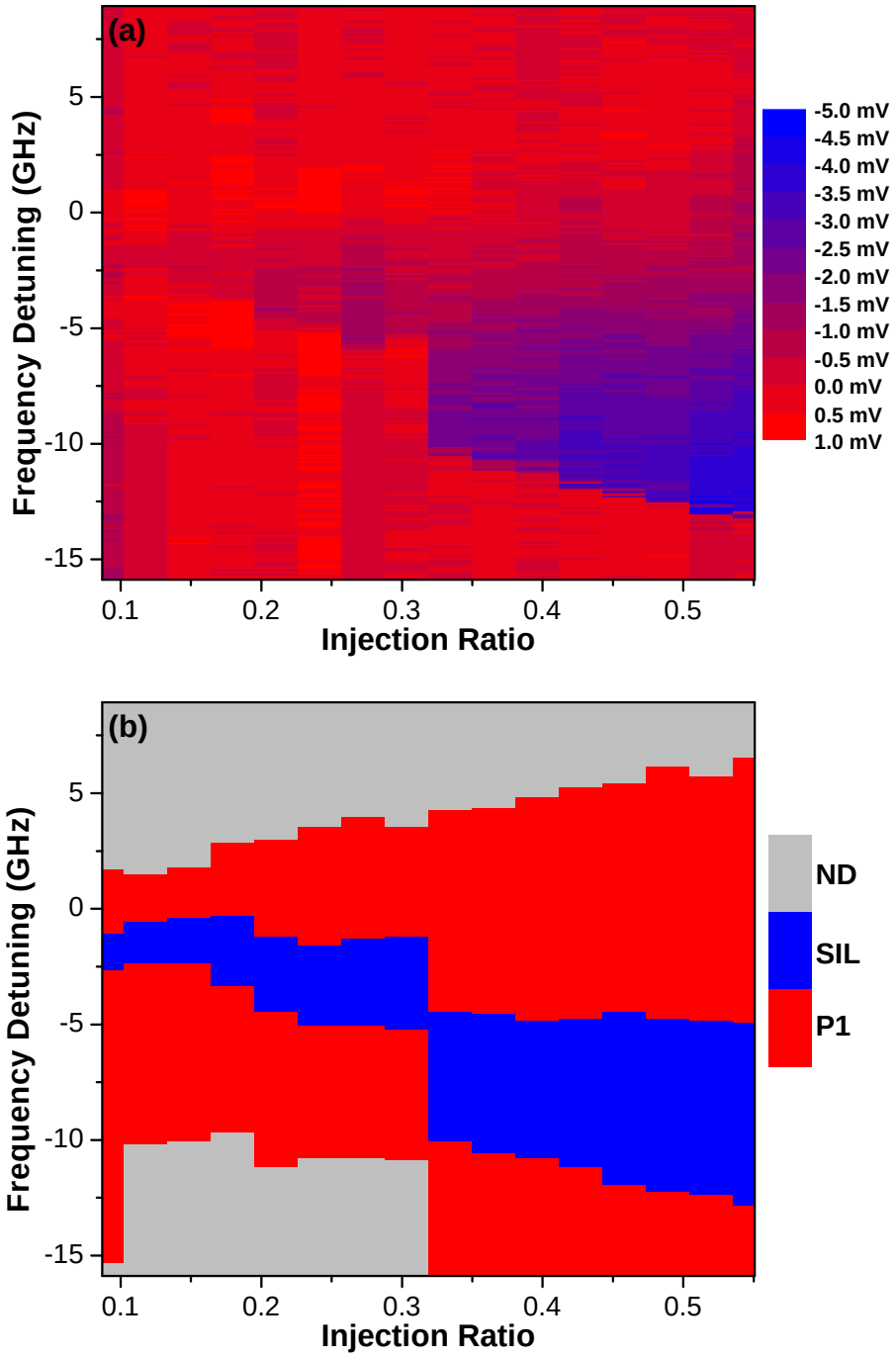

Figure 4.19: (a) Voltage and (b) electrical responses partitioned into the measured dynamics plotted as a function of wavelength detuning and injection strength for orthogonal optical injection.

Another distinguishing feature is that where the theoretical curve shows a smooth variation from carrier number reduction to elevated carrier number across the locking range, the experimental voltage trace clearly shows non-differentiable slope changes at the interfaces between the different dynamics. Assuming a sufficiently low noise voltage response, the derivative of the voltage across the stable locking region should not have any large peaks whereas they would exist at the boundaries between different dynamics, see fig. 4.9 where the derivative for the SIL region is smooth but there are discrete extrema at the locking and unlocking detunings.

Figure 4.18 (b) shows that all of the measured dynamics occur within a window bounded approximately by 7 GHz and −20 GHz. In comparison to fig. 3.5 which features a logarithmic scale, here only a small region of the entire injection plane is being studied experimentally. Despite that, a less rectilinear boundary was expected. It is possible that there is a device specific property that limits the spectral width which is capable of supporting the possible non-linear dynamics.

The two dimensional maps for orthogonal injection, fig. 4.19, feature a discontinunity around $R = 0.325$ where both locking boundaries shift by approx. −5 GHz. It is not known whether this feature is due to a sharp change in injection strength due to a change in the alignment of the fibre with the VCSEL aperture or if it is a real feature of the injection map. The former seems the more likely explanation as no theoretical feature exists to explain it but the positive detuning boundary for the P1 region does remain continuous across this injection ratio region suggesting this is not the origin. In any case, the voltage response also features this dramatic delineation.

Theoretical modelling, based on eqs. (1.1) to (1.3), was performed to further validate the conclusions from the experimental voltage and electrical responses. A sample theoretical study of the average carrier number and the frequencies of all the oscillations occurring at each detuning is presented in fig. 4.20. This plot shows many features observed in the experiments such as carrier increases where higher order dynamics and chaos are observed (−7 GHz and 4 GHz); reverse period doublings on the way to locking on the positive frequency side (2.5 GHz to −2 GHz) and the frequency of the oscilla-

tions going to zero at the negative locking boundary indicating a saddle-node on a limit cycle (−3 GHz).

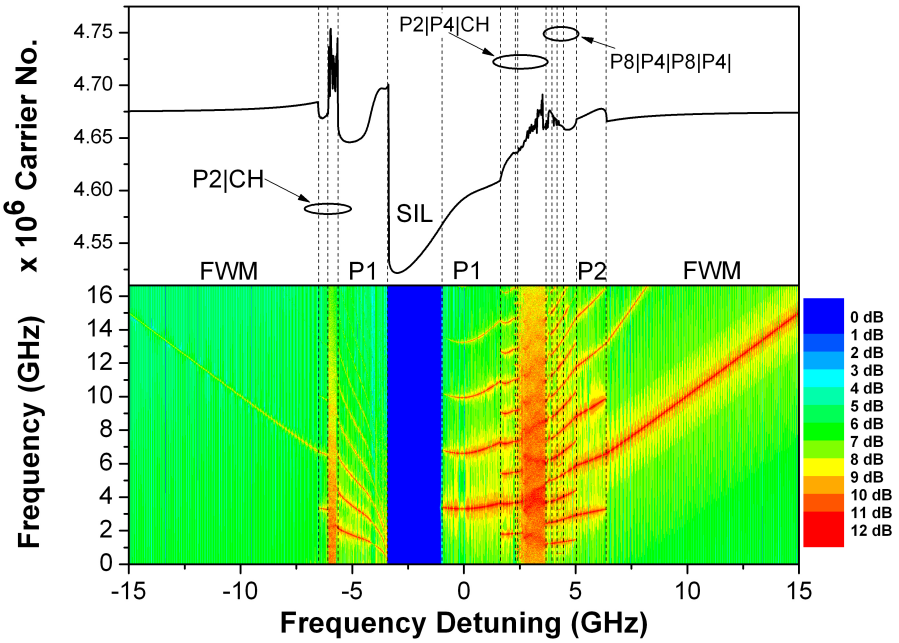

Figure 4.20: Modelled carrier response during injection which has been partitioned using the corresponding electrical spectra at each frequency detuning. The various experimental features observed such as SIL, P1 and chaotic oscillations and the associated carrier changes are well reproduced with this model.

4.3 Conclusions

A comprehensive study of the voltage response of a long wavelength VCSEL during tuned optical injection and its optical state has been performed. Two different VCSELs were investigated. One has a short effective cavity length and a small polarisation mode splitting. The other has a longer effective cavity and a much larger polarisation mode separation. Detailed measurements as functions of frequency detuning, polarisation and injection strength show a strong correspondence between the induced dynamics and the voltage. In particular, the response of one VCSEL was investigated in the optical domain while the other was studied in the electrical domain. Large

locking bandwidths and voltage changes are observed as well as stable polarization switching at large frequency offsets. Higher order oscillations are also detected in the voltage measurements.

The prime result of this chapter is that the region of near-linear voltage response which has the maximum voltage reduction matches the stable locking region. This has been confirmed in each of the investigations using both diagnostic methods. Theoretical calculations are also performed for both measurement domains to validate the experimental findings. The results are in general agreement. Future investigations could include the use of a bias-T to monitor the high speed response of the carrier number during injection in real time which should be highly correlated with the output intensity of the VCSEL.

The investigative method pioneered in this chapter introduces a new and cost efficient way of characterising an injected laser. These techniques could facilitate remote tuning of the VCSEL wavelength to match an injected reference signal without the use of expensive resources such as optical and electrical spectral analyzers, power meters or an experienced operator. In a real system, the choice of VCSEL and current driver would be important considerations. As features in the derivative indicate the locking and unlocking boundaries, a low noise voltage response provides a significant advantage in terms of accurately and easily identifying these detunings.

Chapter 5

Optical Transmission using Fixed and Tuneable Wavelength VCSELs

Current and future communication networks will require optical sources which are capable of fast transfer speeds but which also satisfy reconfigurability requirements. The required bandwidths of $10 - 40\,\text{Gbit/s}$ over long distances are beyond the capabilities of copper wires. In this chapter, the application of both fixed wavelength and tuneable wavelength VCSELs in optical transmission networks is demonstrated.

One such application is in Passive Optical Networks (PONs) which can operate in a mixed Wavelength Division Multiplexing and Time Division Multiple Access configuration such as described in section 1.3.4. VCSELs are ideal sources for PONs given their high coupling efficiency to optical fibres, their capability for high speed direct modulation and, crucially, their low cost potential. A consequence of altering the bias current of a semiconductor laser is a change in the emission wavelength as the path length in the optical cavity adjusts with the current density. This can lead to transmission errors due to chromatic dispersion in the fibre, section 1.3.4. To overcome this, a form of Electronic Dispersion Compensation (EDC) is used to achieve error-free transmission at 10 Gbit/s over 40 km of single mode fibre.

Table 5.1: Common abbreviations relating to optical transmission networks.

Abbreviation	Meaning
ED	Error Detector
EDC	Electronic Dispersion Compensation
PG	Pattern Generator
PON	Passive Optical Network
VOA	Variable Optical Attenuator
BER	Bit Error Rate
ONU	Optical Network Unit
WDM	Wavelength Division Multiplexing
TDMA	Time division Multiple Access

'Colourless' devices such as the MEMS-VCSEL introduced in chapter 1 allow Internet Service Providers (ISPs) to take advantage of complex transmission schemes as well as reducing inventory levels of wavelength specific parts. Demonstration of the colourless properties of these devices is performed here when error free transmission over 50 km is measured while externally modulated at 10 Gbit/s. This is achieved across a record 30 nm wavelength span which is limited by the experimental set-up and not the device itself.

One of the challenges of colourless sources is selecting the emission wavelength to the one desired in a given application. One approach is to create a map of the wavelength as a function of the tuning variable which is usually either the bias current or the heat sink temperature. There is no guarantee that those maps will stay valid outside of the characterisation lab as external factors such as ambient temperature variations or internal factors such as current annealing could change the gain properties. By combining the results of the previous two chapters a new method to identify and thus fix the lasing wavelength of a MEMS-VCSEL is presented and discussed via both theory and experiment. This method utilises a sharp change in the device voltage to easily determine when the MEMS-VCSEL is emitting at the desired wavelength as set by an externally injected reference signal. A list of the abreviations used in this chapter is given in table 5.1.

5.1 Direct modulated VCSEL at 10 Gb/s

In this section the basic characteristics of the 1550 nm VCSEL used for transmision are presented with an emphasis on the possible effects of the different types of dispersion and the methods used to overcome the associated limits. Then, experimental results showing error free transmission at 10 Gbit/s over 40 km at 30 °C using EDC are discussed. Error free transmission at 60 °C is achieved over 20 km and all performances are qualified relative to a narrow linewidth external cavity laser in the same experimental set up.

5.1.1 VCSEL characteristics

The VCSEL used in this experiment is of the same short cavity design as described in section 1.2 and fibre-coupled properties at room temperature are shown in fig. 5.1 (a) and (b) which includes a maximum output power of 2.5 mW. The VCSEL is voltage driven with the logical 'on' and logical 'off' voltages and their corresponding bias currents highlighted.

Sample spectra at several bias currents show single mode operation on the longer polarisation mode at all bias points with a PMSR $\simeq$ 40 dB. The first order transverse mode exists 2.81 nm to the short wavelength side of the main peak with an SMSR$\simeq$ 60 dB for the bias currents of interest. Due to these high suppression ratios, it can be anticipated that chromatic dispersion rather than polarisation or modal dispersion will be the main dispersion related problem during transmission. The VCSEL peak wavelength changes by approximately 0.25 nm/mA due to gain changes with bias and thermal effects. This effect is intrinsic to semiconductor lasers but is particularly strong in VCSELs as they experience strong Joule heating due to small active volumes. The Buried Tunnel Junction design employed in these long wavelength VCSELs which confines the current in the same way that ion implantation or an oxide aperture does for 650 nm or 850 nm devices also helps reduce the amount of internal heat generation by facilitating the use of n-doped rather than p-doped materials on the p side of the active region.

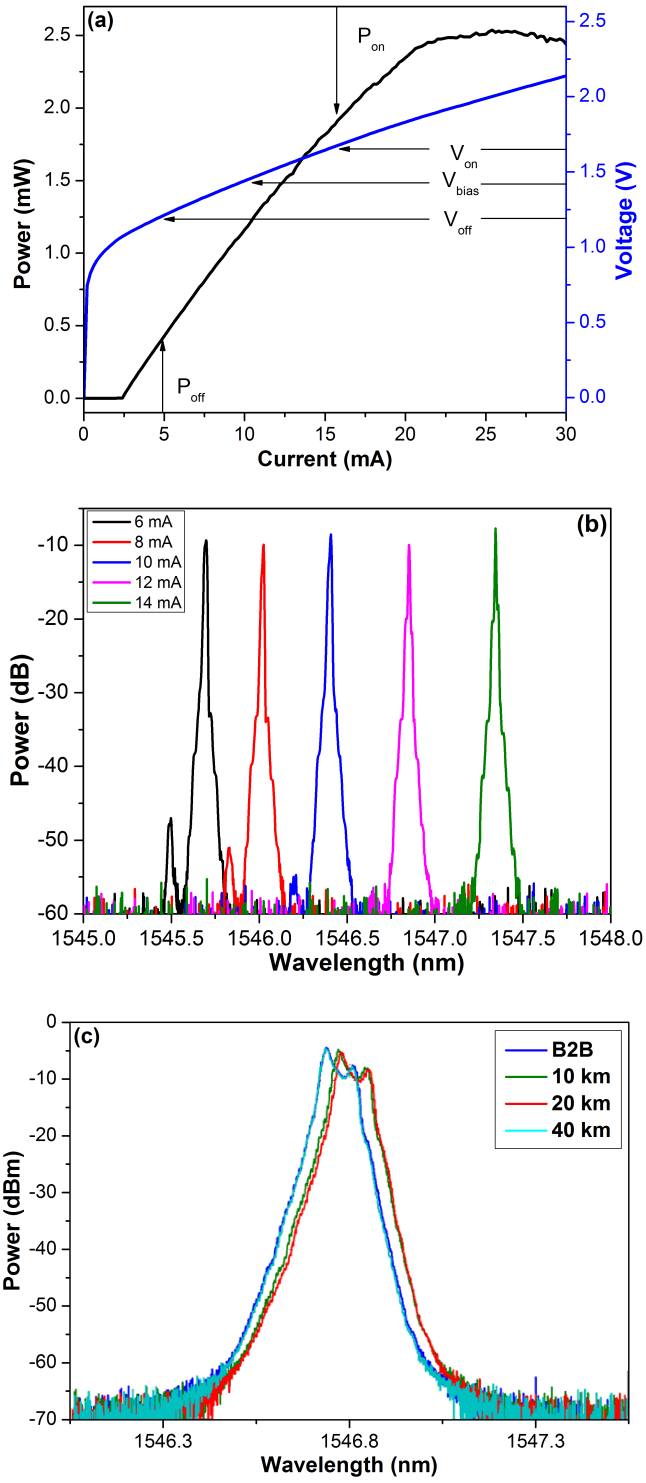

Figure 5.1: (a) LI and VI curves for the VCSEL used for transmission experiments. The high and low voltage biases and the associated current equivalents are shown. (b) Optical spectra from the VCSEL under DC bias at points on the linear portion of the LI. The smaller peak is the orthogonal polarisation mode. The first order transverse mode is at 2.81 nm to the short wavelength side of the main peak. (c) Spectra of the VCSEL under 10 Gbit/s modulation as recorded at different distances in the fibre. The shift in center wavelength is due to a change in ambient temperature as the air conditioning in the laboratory became operational for a short period.

The spectrum under modulation at 10 Gbit/s for different transmission distances at room temperature is presented in fig. 5.1 (c) and is centered at 1546.75 nm which is equal to the wavelength at the DC bias point. Spectral broadening is seen due to the wavelength chirp between the bias points but there are no significant differences in the spectra measured over longer transmission distances. This is because the spectrum can only measure average values and not high speed effects. The slight shift in center wavelength is due to a change in ambient temperature during the measurement as the air conditioning in the laboratory became operational for a short period. The splitting between the two peaks approximately matches that between the polarisation modes. As the PMSR is large, it is unlikely that the orthogonal mode is being excited and that this value is simply coincidental. The wavelength shift under modulation will not be 2.5 nm as expected from fig. 5.1 (b) as the active region does not get as hot as when DC biased. Nevertheless assuming a wavelength change of 0.2 nm under modulation and given a dispersion parameter value of $D_\lambda = 18\,\mathrm{ps\,nm^{-1}\,km^{-1}}$ for the SMF there is a difference in propagation speed of 3.6 ps/km. At a bit rate of 10 Gbit/s each logical bit has a width of approximately 100 ps so after transmission over 15 km consecutive 1 and 0 pulses will interfere by approx. 54 ps, closing the optical eye and highlighting the need for a dispersion compensation scheme to recover the data.

5.1.2 Experimental setup for direct modulation experiments

An experimental set-up was designed to qualitatively match a PON as shown in section 1.3.4. In a real system the optical circuit would also include an Arrayed Waveguide Grating (AWG) to implement a WDM scheme but was omitted here. Our set-up is shown in fig. 5.2 and consisted of a Pattern Generator (PG) applying a non-return-to-zero (NRZ) pseudo random bit sequence (PRBS) with a $2^{31} - 1$ word length to a Bias-T with a DC bias of 1.42 V which is close to mid-way up the linear part of the LI curve as shown in fig. 5.1 (a). The exact DC bias and the peak to peak voltage of the RF portion

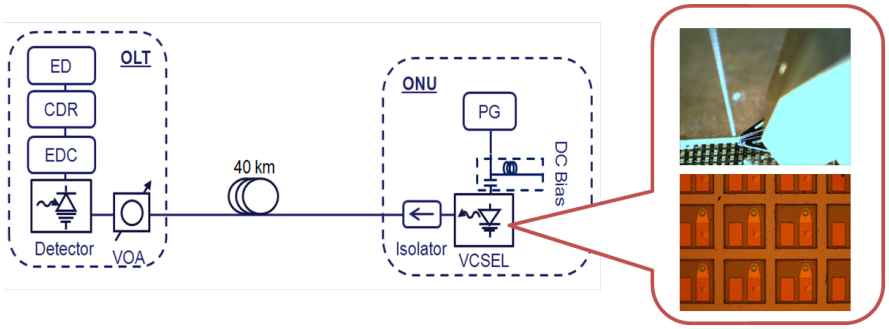

Figure 5.2: Experimental set-up used to simulate a VCSEL in use at an Optical Network Unit (ONU) in a Passive Optical Network (PON).

(460 mV) of the bias was determined by a manual optimisation routine in order to maximise the extinction ratio without reducing the current to below the lasing threshold value. This time-varying voltage was delivered to the temperature controlled (either 30 °C or 60 °C) VCSEL using high speed cables and a Picosecond GSG probe which had a bandwidth up to 40 GHz. The probe had K type connectors but most of the connections in the system were done with SMA type connectors which are limited to 18 GHz. A data rate of 10 Gbit/s was chosen as the target speed for downstream data rates for PONs, the target for upstream data rates is significantly slower at 2.5 Gbit/s [148]. The patterned light was coupled into a lens-ended single mode fibre (SMF) with an anti-reflection coating before being passed through an in-line optical isolator. The optical spectrum was checked to ensure no signs of optical feedback were present. The data was then transmitted over a set length of SMF before reaching the receiver end of the network (Rx). A 90/10 splitter and power meter combination (not shown) was used in order to monitor the coupling efficiency with the light in the 90% channel coupled to a variable optical attenuator (VOA) in order to simulate loss in the system.

Next, the light was optically amplified and then detected by a New Focus 1554-B-50 high speed photodetector with transimpedance amplifier which can operate up to 12 GHz. The resulting signals are routed to a Vitesse Electronic Dispersion Compensation (EDC) board capable of eliminating the effects of ISI [149]. By implementing methods which are effective up to at least 40 Gbit/s such as Feed Forward Equalisation (FFE), which uses previously

detected logical bits to adjust the current bit, and Decision Feedback Equalisation (DFE), which alters the decision threshold level, this EDC board can successfully open up optical eyes which have been severely distorted due to chromatic dispersion [150].

A clock recovery module was used to synchronise the received data to the patterning time and a bit-wise comparison was done to detect the differences between them using a Bit Error Rate Tester or an Error Detector (ED) for short. Error measurements were performed over distances of 0 km, 10 km, 20 km and 40 km at 30 °C and over 20 km at 60 °C. The 0 km is also referred to as a Back-to-Back (B2B) configuration. In order to quantify the optimum receiver sensitivity a tuneable external cavity laser from CIP in the UK [151] was externally intensity modulated using a Reflective Electro-Absorption Modulator Semiconductor Optical Amplifier (R-EAM-SOA). This device was a late stage development product not yet ready for full commercialisation and so has no official data sheet. However, it was characterised as having 14 dB optical gain, a 9 dB extinction ratio under 10 Gbit/s modulation and a 3 dB small signal RF bandwidth of 18 GHz.

5.1.3 Results and discussion

Results from all the error rate measurements are presented in figs. 5.3 and 5.4. Figure 5.3 (a) shows the BER curves measured at 30 °C over various distances with and without the EDC and also a reference curve with the optimum reciever sensitivity determined using a narrow linewidth External Cavity Laser (ECL). Compared to the back-to-back reference the directly modulated VCSEL introduces an average power penalty of 3.3 dB after EDC. Without compensating for the dispersion this power penalty increases by 1.3 dB. The discrepancy is greater over 10 km where a difference of 3.4 dB is measured at a BER of 10^{-9}. At the same error rate, power penalties of 2.2 dB, 2.5 dB and 3.4 dB were measured relative to B2B with the EDC for 10 km, 20 km and 40 km respectively. The slope of the BER curves with EDC decreases with transmission distance indicating these power penalties are not constant over all error rates. For distances over 10 km it was not possible

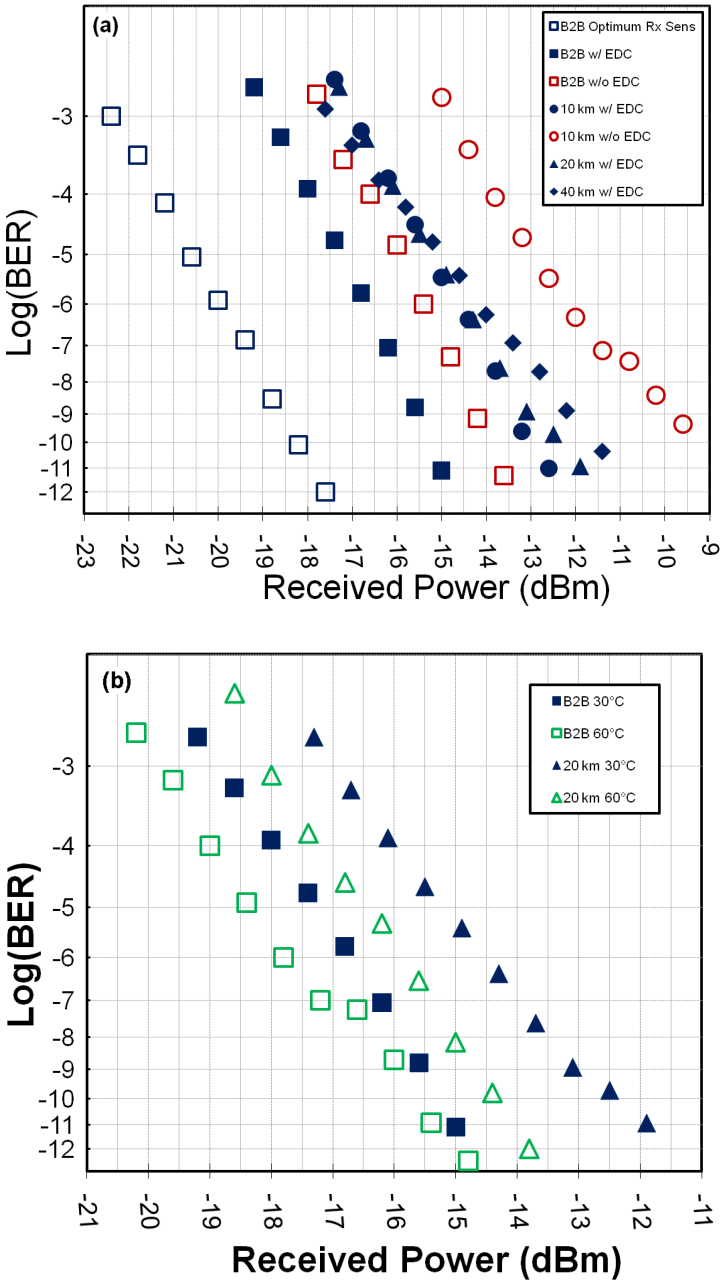

Figure 5.3: Bit Error Rate measurements for the directly modulated VCSEL compared to the optimum reciever sensitivity determined using a reference narrow linewidth laser (a) over several distances up to 40 km with and without Electronic Dispersion Compensation (EDC) and (b) at 30 °C and 60 °C with EDC measured Back-to-Back and over 20 km.

to recover the transmitted data without the use of the EDC as the clock recovery could not hold the synchronisation for more than a few seconds due to the chromatic dispersion even with improving signal to noise ratios.

BER measurements over 10 km and 20 km at 30 °C and 60 °C are compared in fig. 5.3 (b). In general, the received power requirement for error free transmission is less at 60 °C than at 30 °C due to a larger extinction ratio at the higher temperature. At this elevated heat sink temperature, more power was available at the higher bias level as these VCSELs were designed for high power applications up to 80 °C rather than high speed applications. Devices of similar design have been shown to be capable of operation up to 90 °C if the epitaxial structure is grown with a sufficient offset between the photoluminescence peak of the active region and the resonance wavelength of the optical cavity [8]. In particular, the differences in the received power necessary for error free transmission between the two temperatures are 0.6 dB B2B and 1.5 dB over 20 km of SMF respectively. Unfortunately, the device under test was damaged during the preparation for the 40 km measurement so no data for that distance at 60 °C was recorded.

Finally, the recovered optical eye diagrams post-EDC are presented in fig. 5.4 for the different distances. The most distorted eye is measured at 20 km.

In summary, a state-of-the-art long wavelength VCSEL is successfully directly modulated at 10 Gbit/s demonstrating more than acceptable qualities as an upstream transmitter when used in conjunction with electronic dispersion compensation to mitigate the VCSEL chirp. In particular, error-free (BER$< 10^{-9}$) performance following transmission of a 9.953 28 Gbit/s NRZ PRBS of length $(2^{31} - 1)$ over 40 km of SMF (640 ps/nm) following EDC was recorded. At lower bit rates, increased transmission distance would be achievable both with and without EDC. These devices provide a good alternative to ECLs especially considering their size, low power budget and potential price.

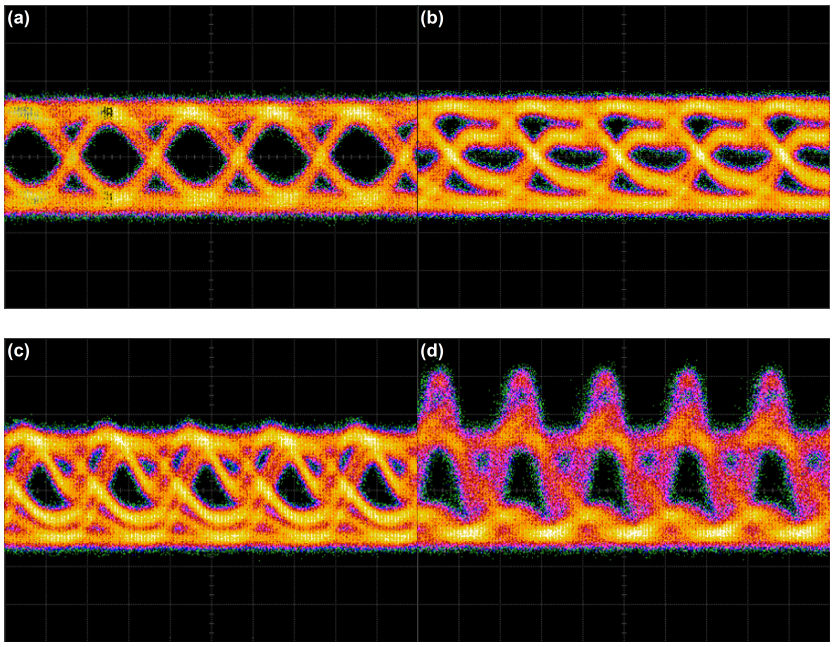

Figure 5.4: Optical eyes for the directly modulated VCSEL over (a) B2B (b)10 km (c) 20 km and (d)40 km

5.2 Externally modulated MEMS-VCSEL

Tuneable VCSELs based on Micro Electro Mechanical Systems (MEMS) mirrors are an attractive solution for optical source components in Long Reach-PON [30] and in gas sensing [46] applications. Recently VCSELs fabricated with a semi-monolithically integrated MEMS mirror per device [73] have shown a record continuous tuning range over 100 m with a centre wavelength of 1550 nm and are capable of meeting the performance criteria for a PON colourless source. The MEMS mirror concept is in principle wavelength agnostic and depends on the availability of compatible materials and fabrication technologies. For instance, similar MEMS technology has been applied to VCSELs with an emission wavelength near 850 nm with great success [74]. By tailoring the emission properties of the active region and using a broadband back DBR the tuning ranges could be shifted to center on regions of the infrared spectrum where important industrial gases have molecular vibrational and rotational absorption lines. VCSEL active regions emitting

around 1.3 µm [14], 1.55 µm [49], 1.8 µm [47], 2.0 µm [48] and 2.3 µm [56] have already been demonstrated. Fully monolithic MEMS-VCSELs incorporating a high contrast sub wavelength grating instead of a dielectric DBR are also in advanced stages of development [152], [153].

Previously, direct modulation of tuneable VCSELs was limited to 2.5 Gbit/s [154] while an externally modulated tuneable VCSEL with 24 nm tuning achieved 2.5 Gbit/s over 300 m of single mode fibre (SMF) [155]. In this section, error free transmission at 10 Gbit/s over 50 km of single mode fibre using external modulation across a 30 nm tuning range is demonstrated [156]. An average power penalty of just 0.2 dB is measured when compared to transmission using an ECL. The wavelength span measured was limited by the experimental apparatus rather than the device under test.

5.2.1 MEMS-VCSEL characteristics

The tuneable MEMS-VCSEL is described in detail in [73]. Briefly the devices are fabricated in two distinct parts where first a half VCSEL consisting of an AlInGaAs based quantum well active region with a buried tunnel junction and dielectric DBR is processed and embedded in a gold electroplated pseudo substrate before the InP substrate is removed similar to as described in section 1.2. Next a second dielectric DBR is deposited on top of the wafer using low temperature Plasma Enhanced Chemical Vapour Deposition (PECVD) which assumes a concave shape after etching of a sacrificial layer beneath the mirror thanks to tailored strain gradients within the DBR. The radius of curvature of the DBR is designed in conjunction with the diameter of the BTJ to create a stable semi-confocal laser cavity which supports only a single longitudinal mode. Wavelength adjustment is achieved via current induced heating of the membrane which deflects and changes the length of the airgap cavity between the concave mirror and the half VCSEL. Figure 5.5 shows a schematic of the fabricated device and a Scanning Electron Microscope image of the top surface of the VCSEL. The contacts, suspension beams and mirror are coated in gold to facilitate the heating and tuning but there is a central aperture to allow light emission.

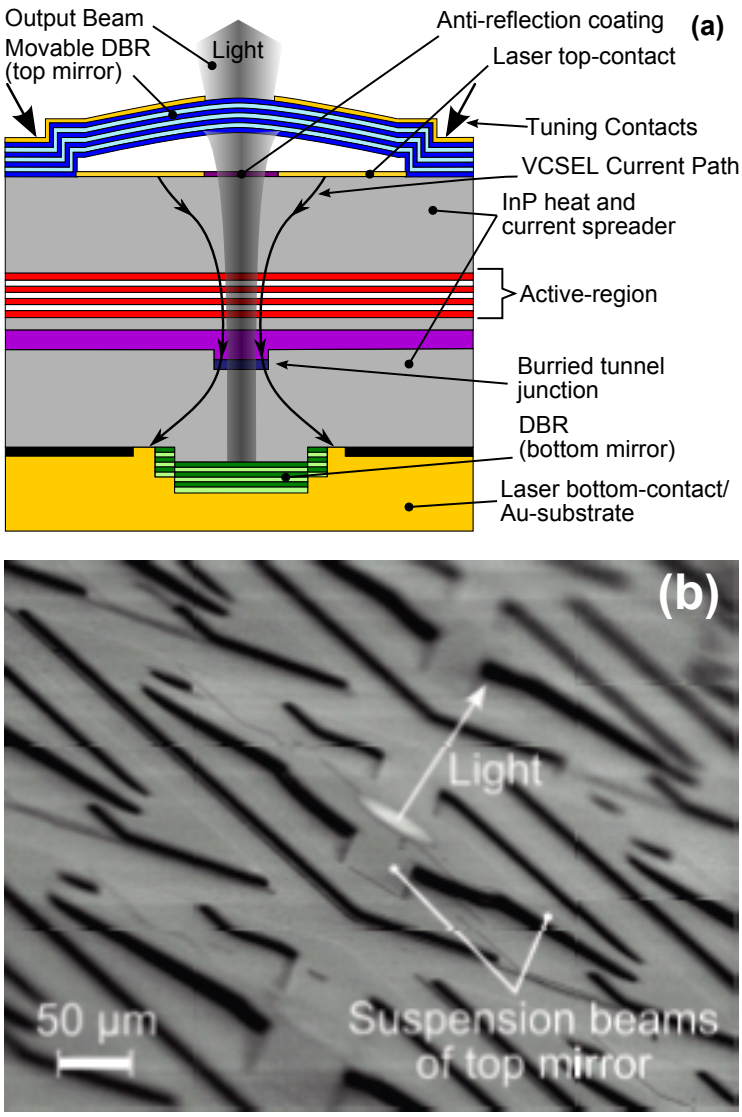

Figure 5.5: (a) Schematic structure of the MEMS-VCSEL and (b) Scanning Electron Microscope image of the flexible membrane which facilitates the wavelength tuning. Image credit: Dr.-Ing. Christian Gierl, Technische Universität Darmstadt.

The VCSEL threshold current and the maximum output power are dependent on the deflection of the membrane as this changes the gain conditions [71]. This is because the relative overlap of the antinode of the electric field with the quantum wells in the active region is dependent on the actual mode supported by the optical cavity at that mirror deflection.

Fibre-coupled LVI curves for a MEMS-VCSEL at different tuning currents are presented in fig. 5.6(a). For this device, laser action could not be achieved for MEMS currents less than 13 mA. With increasing tuning current, the VCSEL threshold current drops from $I_{th} = 10$ mA to a minimum of $I_{th} = 6$ mA for $I_{MEMS} = 23$ mA. At this optimum mirror deflection a maximum (un-coupled) output power of 1.2 mW was recorded. The voltages across the VCSEL for all MEMS currents are indistinguisable on this scale.

For this data transmission experiment, the continuous-wave light is externally modulated with the VCSEL bias current set at 16 mA as this current offered a good compromise between output power and tuning range. Two sample spectra at $I_{MEMS} = 22$ mA and 26 mA are shown in fig. 5.6(b). Under these conditions the MEMS-VCSEL lased when the tuning current was varied between 11 mA and 35 mA. This resulted in a single mode tuning range of 55 nm (approx. 1530 nm - 1585 nm) as shown in fig. 5.7(a). Large continuous tuning ranges are possible due to the large spectral range in a VCSEL. First and second order transverse modes occur with an SMSR of approx. 60 dB. The orthogonal polarisation mode exists on the longer wavelength side of the main peak with a PSMR of over 30 dB.

The tuning rate is proportional to the square of the tuning current as the mirror deflection is achieved through thermal expansion membrane support beams as shown in main figure and inset of fig. 5.7 (b).

The unpackaged VCSEL exhibited wavelength instabilities on two timescales: a steady drift to longer wavelengths on the order of minutes and sub-second oscillations around the lasing wavelength as depicted by the black curve in fig. 5.8(a). These variations have multiple sources including (a) resonance oscillations from residual air currents (b) release of material stress and (c) significant mechanical vibrations passing through the contact probe tips. Environmental reverberations can severely impact on device operation creating

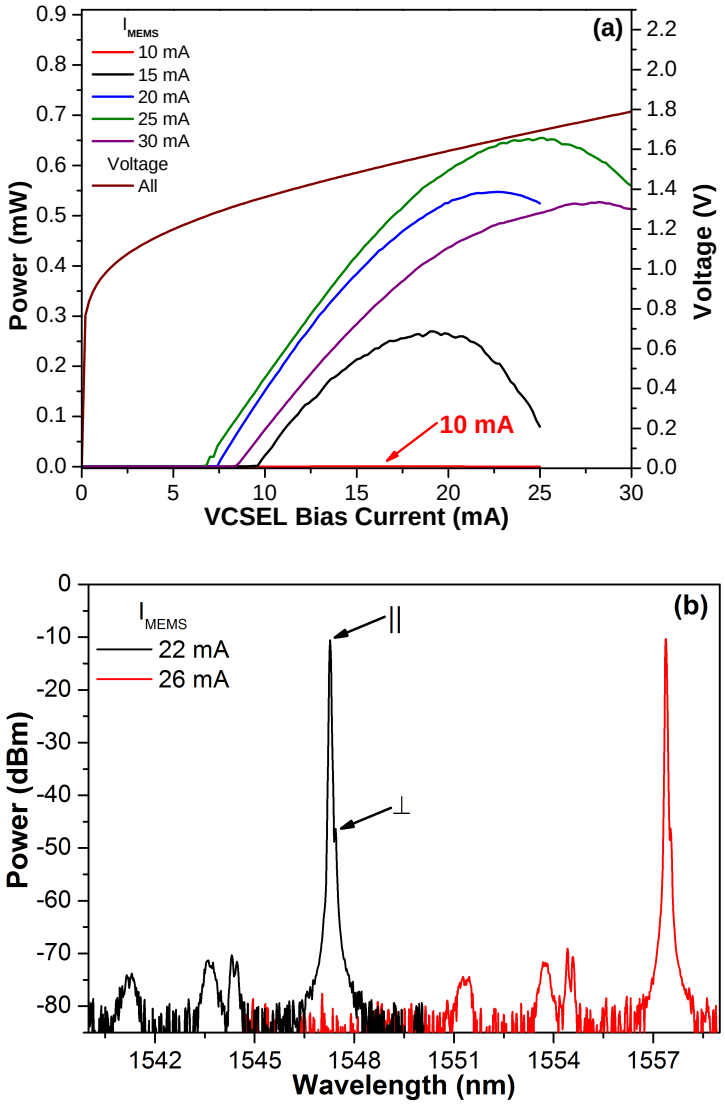

Figure 5.6: (a) LI curves for the MEMS-VCSEL with different membrane currents showing a variation in threshold current due to the dependence of the gain on the mirror position. The polarisation modes are indicated. (b) Sample spectra at two membrane currents for the same bias current, 18 mA.

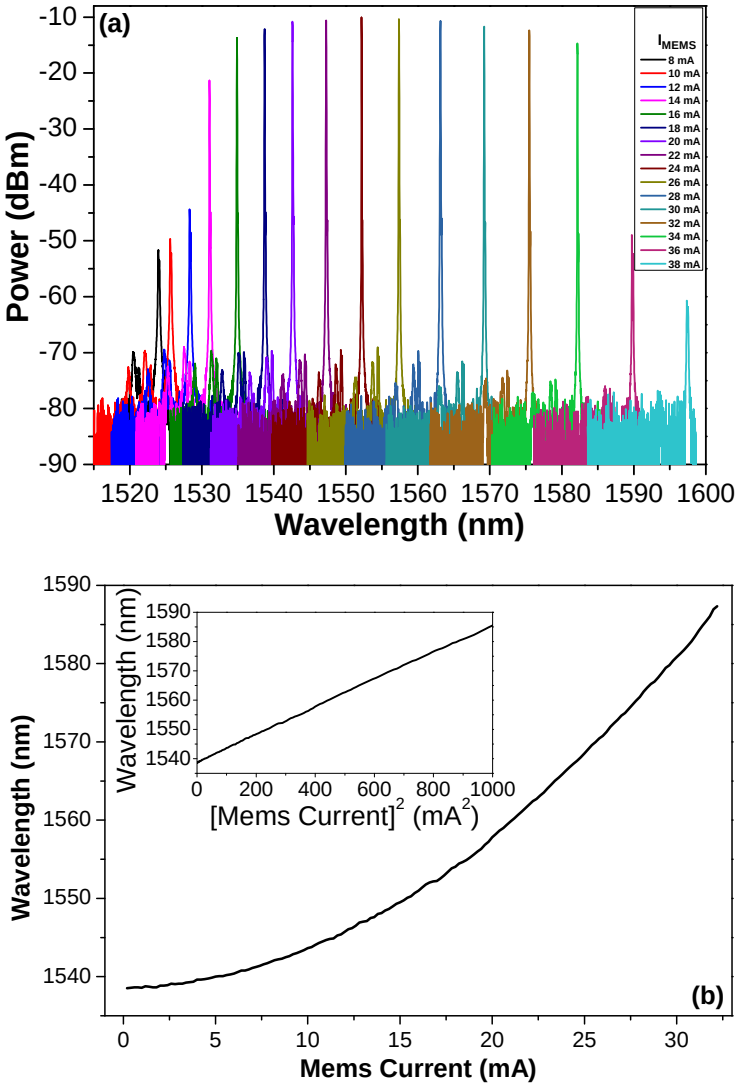

Figure 5.7: (a) Spectra across the tuning range when VCSEL is biased at 16 mA showing continuous single mode operation throughout and (b) the peak wavelength as a function of membrane current showing linear behaviour as a function of the square of the tuning range.

an effect referred to as 'optical microphoning'. For wide wavelength tunability the mirror needs a large displacement range (on the order of microns) necessitating a certain amount of flexibility in the beams. The lower the stiffness the more the beams flex upon heating and the greater the change in the length of the optical cavity. Changing the beam stiffness to reduce these instabilities would be possible with material design considerations done on a per-application basis. In many applications, such as the PIEMAN PON architecture [29], such large tuning ranges are not required. PIEMAN proposes delivery of 10 Gbit/s both upstream and down stream to every customer unit in the network by implementing a hybrid Dense Wavelength Division Multiplexing (DWDM) and Time Division Multiple Access (TDMA) protocol. The upstream wavelength band consists of 32 channel grid each of width 50 GHz centered at 1535 nm. This arrangement is ideally suited to the MEMS-VCSEL reported on here as a colourless source. Proper packaging using wire bonds to deliver the current and packaging of the devices in a fibre coupled configuration would be a significant step to aid stability.

As the tuning depends on heating, there is the possibility of thermal coupling between the membrane and the half VCSEL which could effect wavelength stability. While a detailed study has not been done, evidence that this coupling does not happen can be gathered from devices which can tune across more than one free spectral range. This characteristic allows for two possible tuning currents corresponding to shortest possible emission wavelength. Experimentally it is measured that this wavelength is the same for both of the tuning currents [73]. If there was thermal coupling, the heat from the membrane would cause a red-shift in this wavelength for the higher tuning current relative to the lower one, at the same bias current, as the optical path length would increase due to the refractive index dependence of the semiconductors on temperature. The likelihood of thermal coupling between the individual devices in an array of MEMS-VCSELs is small given that there is no observed thermal coupling in arrays of fixed wavelength lasers.

The magnitudes of the wavelength shifts correspond to membrane movements of approx. 5 nm. To compensate for the wavelength drift a feedback

loop consisting of an Optical Spectrum Analyzer (OSA) and a PC/labVIEW controlled algorithm was implemented which monitored the current emission wavelength and adjusted the tuning current to keep the peak within a predefined 0.3 nm = 37 GHz channel. The channel width was chosen to be narrower than the 50 GHz ITU grid but variations still occurred within this channel. A similar control loop based on a wavelength locker instead of an OSA would lead to faster feedback and more accurate control [157]. The temporal wavelength variation with the stability loop is compared to the case without the loop in fig. 5.8(a) and the changes in tuning current required to maintain the wavelength within the channel is shown in fig. 5.8 (b).

5.2.2 Transmission measurements

The tuneable continuous wave VCSEL light was intensity modulated using a Reflective-Electro Absorption Modulator-Semiconductor Optical Amplifier (R-EAM-SOA), see end section 5.1.2, while being temperature controlled to $25 \pm 0.1\,^{\circ}\mathrm{C}$ as shown in fig. 5.9. The optical output was coupled into a lens-ended SMF with an antireflection coating and then divided using a 90/10 splitter. The 10% tap was used to control the wavelength stability as discussed previously. The input power was optimised for the R-EAM-SOA which had a net on-chip gain of approximately +14 dB, to avoid the generation of overshoots and unwanted patterning on the optical eye. Using an Agilent N4901B Serial Bit Error Rate Tester (BERT) the R-EAM-SOA was modulated at 10.3 Gbit/s using a $2^7 - 1$ PRBS superimposed on a DC bias while the error detection was carried out using the internal clock recovery. The optimum decision threshold and delay with respect to the optical eye were found at each measurement step. As the optimum DC bias for the R-EAM depends on both the wavelength used and on the transmission distance, the bias applied was adjusted for both Back to Back (B2B) and 50 km transmission in order to optimise the chirp and achieve the minimum BER. An ANDO AQ8201-13 External Cavity Laser (ECL) was used to determine the optimum bias at the chosen test wavelengths in the B2B case as well as for 50 km transmission. This ECL was also used to provide a reference for

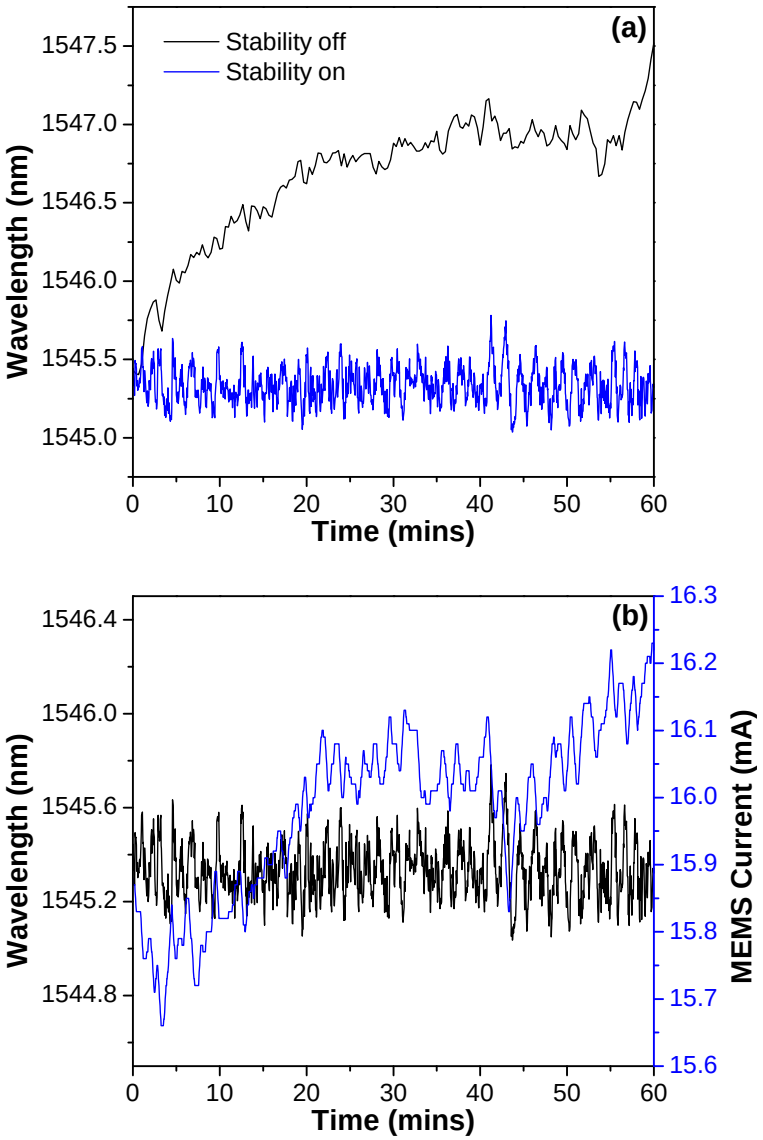

Figure 5.8: Analysis of the VCSEL wavelength variation with time. (a) Comparison of the drift with and without the stability loop active. (b) Change in tuning current required to keep the VCSEL within the set channel of width 0.3 nm centered around 1545.4 nm over 1 hour

comparison with a MEMS tuneable VCSEL.

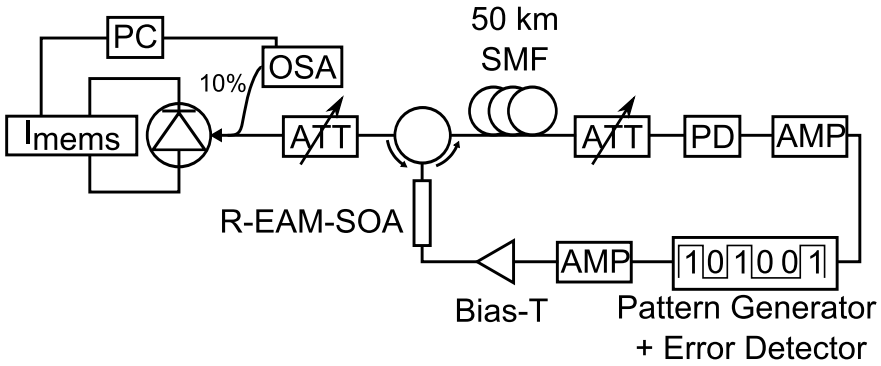

Figure 5.9: Experimental setup used to demonstrate the capability of the MEMS-VCSEL as a colourless component in an optical network.

5.2.3 Results and discussion

The externally modulated MEMS-VCSEL consistently achieved bit error rates less than 10^{-9} across a 30 nm wavelength tuning range with only a small average receiver penalty of approximately 0.2 dB between the VCSEL and the ECL in both the back to back and 50 km cases. Figure 5.10 (a) and (b) show that the VCSEL data has a slight scatter around the fit. In order to maximize the transmission distance, the amount of power incident onto the R-EAM-SOA was set to just below the gain saturation level. However, there were unpredictable changes in the output associated with wavelength changes due to the vibrations of the membrane. These power changes were amplified by different amounts, as the SOA itself has a wavelength dependent gain spectrum, and propagated through the system to the extent that the power at the receiver end varied from the original set value by up to 0.5 dB. The observed power changes are the source of the scatter around the linear fit for the MEMS-VCSEL data in fig. 5.10 compared to the more ideal continuous wave source. Nevertheless, the variation is not large enough to prevent successful 10.3 Gbit/s transmission.

The optical eyes as measured B2B and after 50 km are shown in fig. 5.10. The 50 km eye is significantly less open than the B2B case. The extinction

ratio is reduced and there is timing jitter present. Also shown is a B2B optical eye when the bias on the R-EAM-SOA is not optimum and oscillations are present all along the logical 'on' level. This should be compared with (a) where the overshoots are minimized.

The entire tuning range has similar optical characteristics but the wavelengths for which error free transmission could be demonstrated were limited by the specifications of the modulator available at the time of the experiments.

5.3 Wavelength referencing by optical injection of MEMS-VCSEL

Colourless PON components need to be able to be selectively adjusted to particular wavelengths when required. Conventional multi-section tuneable lasers have an associated map of the emission wavelength as a discrete function of the current. This is time consuming and resource intensive lowering manufacturing through-put and affecting yield numbers. Some network architectures used a R-EAM to pattern data onto light which has been sent downstream within the allocated wavelength spacing from the central office [158]. A similar principle could be used to set the wavelength of a MEMS-VCSEL to the centre of the desired grid spacing using the voltage changes investigated in chapter 4.

In this section, the principles of using a voltage change to reference the wavelength are demonstrated. First, the effect on the carrier number of a fixed wavelength laser as a function of bias current under constant optical injection is theoretically investigated and a characteristic voltage change associated with locking is identified. Next, this characteristic voltage feature is measured experimentally in a tuneable MEMS-VCSEL under constant optical injection. Finally, a demonstration of this technique is presented where the MEMS-VCSEL is automatically tuned to an emission wavelength specified via optically injected light.

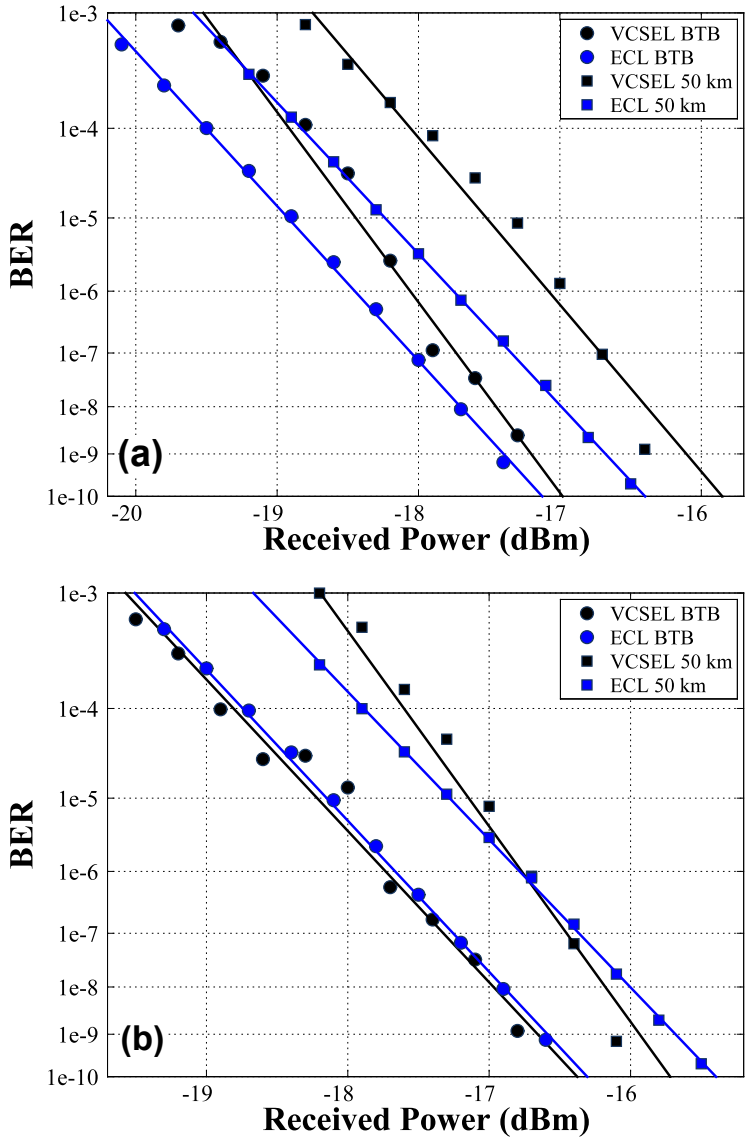

Figure 5.10: Bit Error Rate measurement results for the externally modulated MEMS-VCSEL compared to a reference ECL both Back-to-Back and over 50 km at a wavelength of (a)1540 nm and (b)1570 nm.

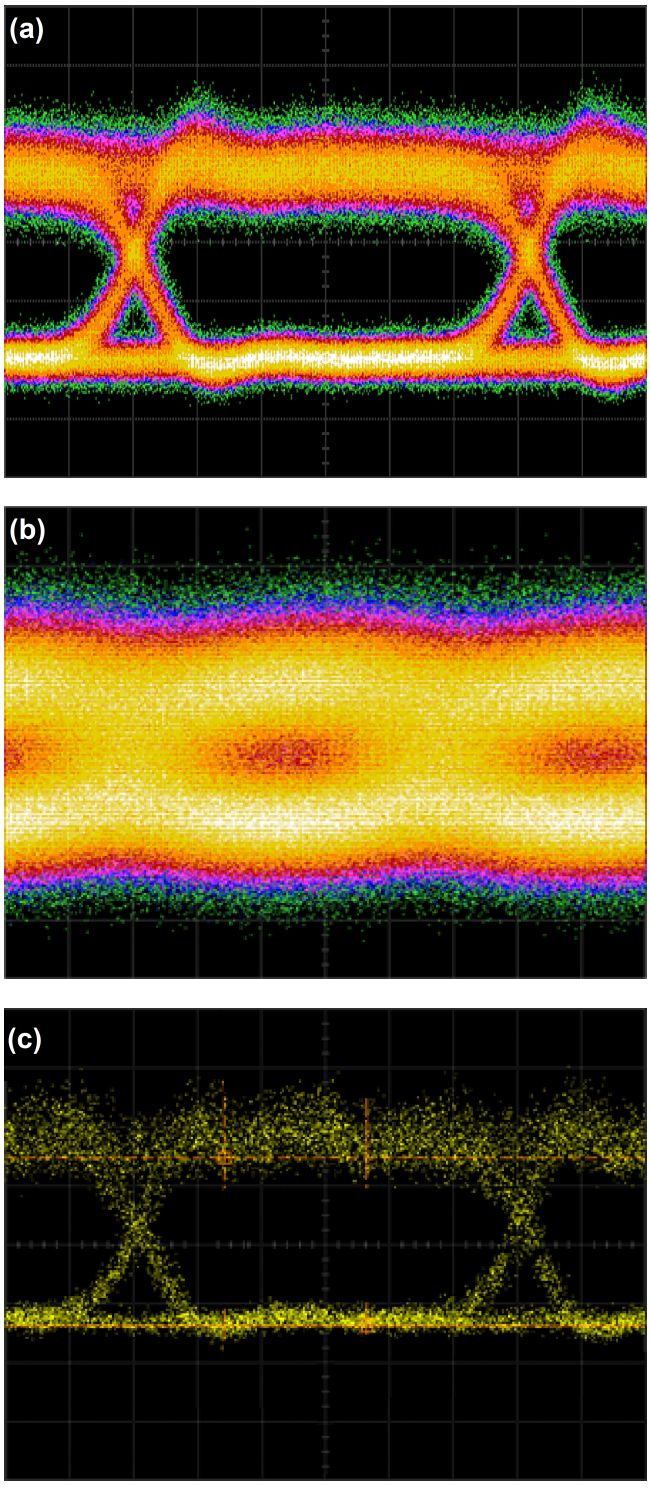

Figure 5.11: Optical eyes for the externally modulated MEMS VCSEL (a) B2B and (b) over 50 km. (c) The B2B eye at non-optimum bias of the R-EAM-SOA showing patterning on the top rail.

5.3.1 Carrier number response to bias change under constant injection

In general, the refractive indices of semiconductors increase with temperature so that heat generated by increasing the bias current will cause an associated change in the optical path length. In turn, this causes the cavity resonance and hence the lasing wavelength to change also. Above threshold, this wavelength change can be linearly approximated by:

$$\lambda(\Delta I) = \lambda_0 + \frac{\partial \lambda}{\partial I}\Delta I \tag{5.1}$$

where λ is the emission wavelength, λ_0 is the wavelength at which the change in bias current, ΔI, from some initial current, I_0, is zero and $\partial\lambda/\partial I$ is the change in wavelength with current. Rewriting in terms of normalised frequency ν_0 gives:

$$\nu(\Delta I) = \nu_0 + \frac{\partial \nu}{\partial I}\Delta I \tag{5.2}$$

where

$$\frac{\partial \nu}{\partial I} = -\frac{c}{\lambda_0^2}\frac{\partial \lambda}{\partial I}. \tag{5.3}$$

The detuning, $\delta\nu$, between the free running VCSEL output frequency and a constant injection frequency, ν_I, also depends on the bias and can be written as

$$\delta\nu(\Delta I) = \nu(\Delta I) - \nu_I. \tag{5.4}$$

Using the same parameters as table 1.1 and eqs. (1.1) to (1.3) with $k = 0$ a threshold current of 0.38 mA is calculated. Normalising $\Delta I = 0$ mA and $\nu_0 = 0$ GHz at a bias of $I_0 = 0.8$ mA and using $\partial\lambda/\partial I = 0.25$ nm/mA which was estimated using the shift in the peak wavelength with current in fig. 5.1 (a) gives a realistic approximation. This allows the OIL equations to be re-stated using the change in bias current relative to I_0 as the free parameter instead

of detuning.

$$\frac{dS}{dt} = [G_0(N - N_{tr}) - \gamma_p]S + 2k\sqrt{S_{inj}S}\cos(\phi) \tag{5.5}$$

$$\frac{d\phi}{dt} = \frac{\alpha}{2}(G_0(N - N_{tr}) - \gamma_p) - 2\pi\delta\nu(\Delta I) - k\sqrt{\frac{S_{inj}}{S}}\sin(\phi) \tag{5.6}$$

$$\frac{dN}{dt} = \frac{I_0 + \Delta I}{q} - \gamma_n N - G_0(N - N_{tr})S. \tag{5.7}$$

If the injected and lasing wavelengths are sufficiently detuned from each other the average carrier number remains near the free running value although low amplitude oscillations will exist. Decreased relative detuning will excite non-linear dynamics such as higher order oscillations or pulsations but stable locking will be achieved for a small frequency span. As in chapter 3 there will be a minimum of the average carrier number in the SIL configuration which will appear in the voltage trace and can be used to remotely and algorithmically identify the locked region [23]. As the VCSEL output power increases with bias the injection ratio is lowered due to the fixed injected photon number. In this model, the carrier number clamps at N_{th} above threshold but in a real device the voltage does not clamp in a similar manner. Instead it increases approximately linearly due to the series resistance so that voltage drops due to the injection would decrease in magnitude. Sweeping the bias current to find a turning point of the voltage and another defining characteristic such as the increase at the unlocking point could be readily implemented to identify the stable locking range. Figure 5.12 (a) shows a plot of the maximum, minimum and average carrier number as functions of laser bias current at a fixed injection frequency of $-24.5\,\mathrm{GHz}$ relative to the free running frequency normalised to $0\,\mathrm{GHz}$ at $I = 0.8\,\mathrm{mA}$ with the stable locking range indicated which includes a minimum of the average carrier number (black curve). Lower carrier numbers are found at the minimum of the oscillations in the unstable locking regions but these would not be observed in a DC voltage measurement. A map of the average carrier number vs detuning and bias current is presented in fig. 5.12(b) where the SIL region

is bordered by dashed lines clearly showing a notable carrier drop when locked. Increased average carrier numbers are observed outside the locking range. The percentage drop in carrier number is larger when small relative detuning occurs at low bias currents, locking ranges are also largest there due to the increased injection strength relative to higher bias points.

If injection is ceased the VCSEL wavelength will return to its free running value for that bias current. By maintaining a weak injection strength the change will be minimal, well below the 50 GHz or 100 GHz grid spacing used in WDM applications. For instance, from these calculations a locked region 0.05 mA in width in terms of current converts to a locking width of only 1.5 GHz in frequency space. Given that the minimum of the carrier number is always on the long wavelength side of the free running peak simply increasing the bias current by a factor inversely proportional to the bias at unlocking would push the free running wavelength to the exactly required value. Alternatively maintaining the injection could be used to boost the VCSEL frequency response as discussed in chapter 1 or else to reduce the frequency chirp.

5.3.2 Characteristic voltage change of an injected MEMS-VCSEL

Wavelength tuning of the MEMS-VCSEL is via a current through the mirror. With a fixed bias current on the VCSEL there is a smooth voltage variation due to changes in gain conditions with mirror deflection. This can be seen in fig. 5.13 (a) and (b) where the voltage variation with a tuning current change but constant half-VCSEL bias is presented. In (a) the current is linearly changed from 0 mA to 13 mA and back again. Simultaneously, light at a fixed frequency from the same Agilent 86100B tuneable Laser Source described in section 4.1.1 with a wavelength stability of less that 1 pm variation per 24 hours was injected.

At the two bias currents near 10 mA on both sides of the graph there are sharp dips in the voltage corresponding to when the relative detuning between the injected and cavity modes was sufficiently small for locking to

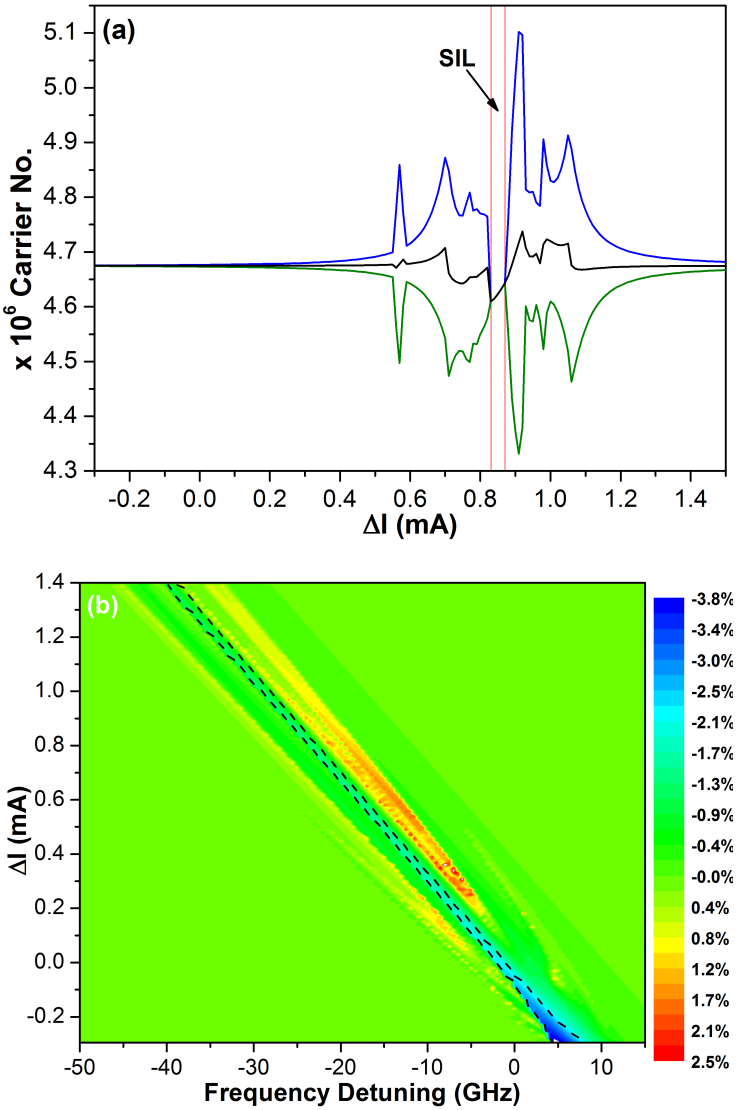

Figure 5.12: (a) Maximum (blue), minimum (green) and average (black) of the carrier number vs. bias current with a fixed injected frequency ($-24.5\,\mathrm{GHz}$) and photon number. The dashed line shows the level of the free running carrier number and the stable locking region is indicated by SIL. (b) Two dimensional map of the carrier number against frequency detuning and bias current at a fixed injected photon number showing how the locking range for a set detuning can be located through a bias change. The frequency detuning is set with regards to a free-running wavelength (i.e. $0\,\mathrm{GHz}$ at a bias current of $0.8\,\mathrm{mA}$).

occur. Under stable locking conditions the injected photons lower the required threshold gain causing the characteristic drop in carrier number that has been observed multiple times in this work and create a unique and easily identifiable indicator of when, at least under weak injection, the wavelength of the widely tuneable MEMS-VCSEL and the injected light are at small relative detunings to each other.

Figure 5.13 (b) shows the result of a similar experiment but with the tuning currents restricted to between 11 mA and 12 mA for an injected wavelength slightly longer than in (a) to highlight the repeatability and symmetry of the voltage drop. A similar change in the current at which the voltage drop occurs for a constant injected wavelength might be expected if the experiment was repeated several hours after the initial measurement due to the wavelength drift from the mechanical instability shown in fig. 5.8. The magnitude and shape of the feature is independent of the direction of the mirror movement. Depending on the injection ratio some interesting physics such as bi-stability could be present in the system. Unfortunately these investigations were not possible due to all the available devices being damaged. The most common cause of device damage was current surges though the active regions due to unstable electrical contacts. The laser and mirror were contacted using probe needles which, despite precautions being taken, occasionally lost physical contact with the electrical contact pads due to mechanical vibrations through the optical bench. Another failure mechanism was distortion of the membrane mirror around the output aperture due to resistive heating effects at high tuning currents.

Estimating the maximum tuning rate from fig. 5.7 (b) as 2.6 nm/mA and ascribing a current range of 0.05 mA to the voltage minimum in fig. 5.13 (b) means that the emission wavelength can be localised to within 0.13 nm or 16 GHz of the desired value as set by the injection.

5.3.3 Remote tuning of MEMS-VCSEL

To demonstrate the effectiveness of this technique explicitly an experiment was performed to show that it is possible to automatically tune a

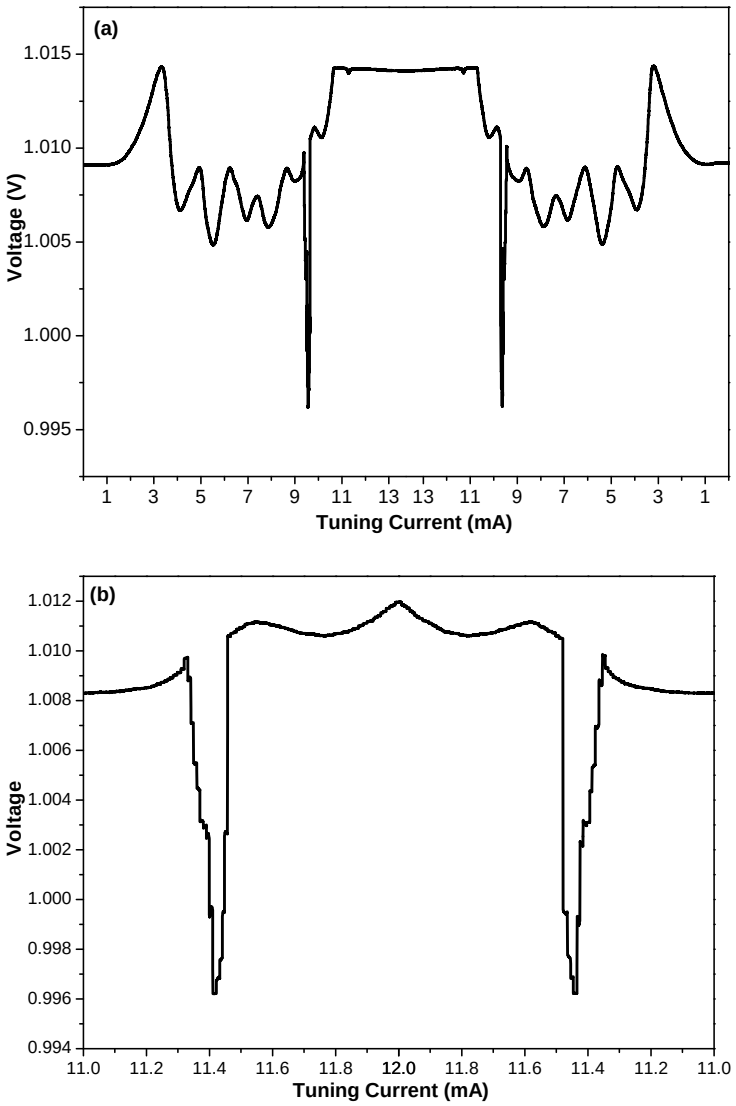

Figure 5.13: Change in the operating voltage of a MEMS-VCSEL with increasing and then decreasing membrane current while light from an external laser at a fixed wavelength is injected. In (a) the current is varied from 0 mA to 13 mA and back again while in (b) the variation is between 11 mA and 12 mA with a longer injected wavelength than in (a). Sharp drops are observed once the wavelength of the MEMS-VCSEL and injected wavelength are relatively detuned so that stable locking occurs.

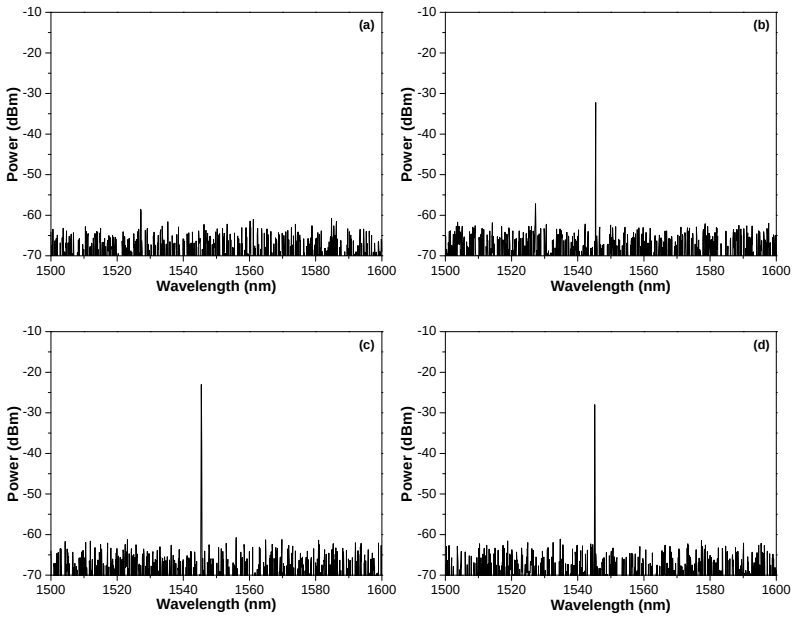

Figure 5.14: Demonstration of the wavelength locking algorithm based on the voltage drop. Spectrum for (a) Membrane current: 0 mA and no injection, (b) Membrane current: 0 mA and injection at 1545 nm, (c) Membrane current tuned to voltage drop and injection at 1545 nm and (d) Injection off and MEMS-VCSEL emission wavelength is 1545 nm.

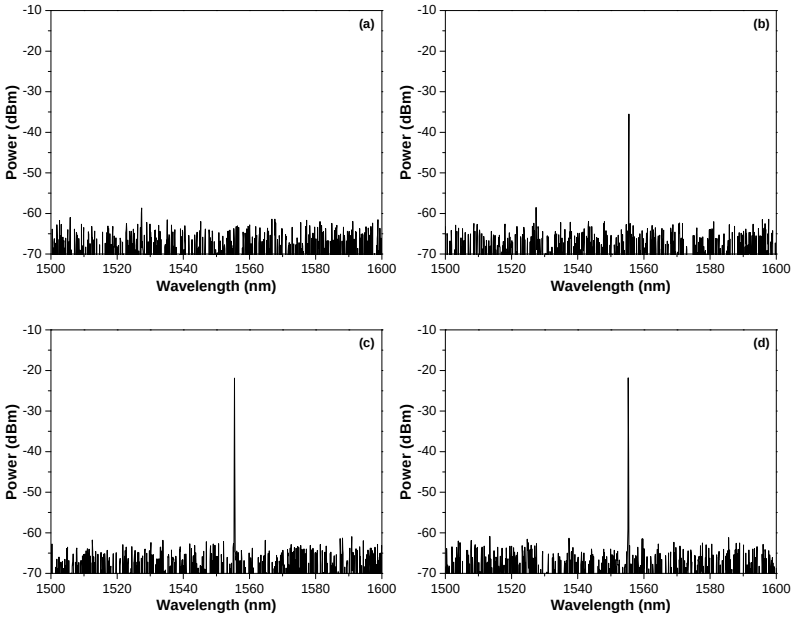

Figure 5.15: Demonstration of the locking algorithm for an injection wavelength of 1555 nm.

MEMS-VCSEL to the wavelength injected by an external tuneable laser. With the VCSEL biased at 7 mA, a labVIEW program increases the MEMS tuning current until a predetermined voltage decrease is detected at which point the VCSEL is assumed to be emitting at the injected wavelength. The injected light is then turned off and the correct MEMS-VCSEL emission wavelength verified. Setting another injection wavelength causes the program to sweep the tuning current (within limits) until the voltage drop is detected again. The time between wavelength set and successful tuning is on the order of a second for this configuration. The detection method could be either observing a sharp change in slope of the voltage versus tuning current curve or simply setting a minimum voltage change such as 5 mV/mA in fig. 5.13 and finding the local minimum. This procedure is demonstrated for injection wavelengths of 1545 nm and 1555 nm in fig. 5.14 and fig. 5.15. Each figure consists of four plots which show the optical spectrum when (a) the tuning current is 0 mA (a peak near 1530 nm can be seen), (b) there is external injection at the set wavelength with 0 mA tuning current, (c) the tuning current has been adjusted to match the wavelengths using the algorithm discussed above and (d) the MEMS-VCSEL spectrum when the injection has been turned off showing the requested wavelength. This approach takes external factors such as ambient temperature into account and does not rely on a prior knowledge of the wavelength tuning characteristics other than a maximum tuning current. It does require the VCSEL to be lasing for the required mirror deflection at the bias current however in order to achieve stable locking.

5.4 Conclusions

In this chapter several results demonstrating the use of VCSELs in high performance optical transmission systems have been presented. First, a cost-effective transmitter capable of error free transmission at 10 Gbit/s under direct modulation over 40 km at 30 °C and over 20 km at 60 °C was described. An Electronic Dispersion Compensation scheme was used to overcome the wavelength chirp intrinsic to directly modulated VCSELs. These devices

would be suitable for use in a Passive Optical Network.

Next, a widely tuneable MEMS-VCSEL was introduced and characterised. Error free transmission at 10 Gbit/s over 50 km of single mode fibre across a modulator limited 30 nm tuning range using external modulation was demonstrated for the first time. As the device was unpackaged, an elementary wavelength locking scheme was implemented to provide wavelength stability in a practical application. High quality packaging with an integrated wavelength locker will provide tighter control. Future generations of bottom half-VCSELs will incorporate high speed contacts and transmission lines to allow direct modulation creating a true colourless, high bandwidth, low energy optical source.

Finally, a method for remotely setting the wavelength of a MEMS-VCSEL based on knowledge developed in earlier parts of this thesis is developed and demonstrated. This approach uses a measurable voltage drop once the VCSEL and injected wavelength are narrowly detuned to fix the correct tuning current for the desired wavelength.

Chapter 6

Conclusions and Future Work

The prime goal of this dissertation was to identify interesting and unanswered questions relating to optically injected VCSELs in order to uncover new physical insights through a comprehensive, scientific study. One such question was "what are the stable locking phase limits as a function of injection strength and other parameters?". This query initially arose after failed attempts to estimate the linewidth enhancement factor of a VCSEL using optical injection techniques as part of a separate study. A literature search indicated contrasting beliefs on whether the stable locking phase limits under moderate strength injection remain constant even though the frequency detuning limits vary non-linearly.

In order to establish the facts of this matter, numerical simulations based on the single mode optically injected rate equations were performed. Through these calculations, three separate regions of the phase limits vs injection strength plane were identified, These regions, denoted as S1, S2 and S3 in fig. 3.2, can be associated with the weak, intermediate and strong injection strength regimes respectively. Analytical expressions exist for the weak and strong regimes. Under intermediate strength injection, the phase limits were found to change in a non-linear way with a strong but predictable dependence on the linewidth enhancement factor. A novel method to evaluate the coupling rate, k, was proposed. As it is often used as a fitting parameter, a good estimate for k will assist in more accurate determination of other

parameters in optically injected systems. A special case was identified where detunings with zero locked phase were found to always be the detunings with a maximum reduction in carrier number. Strong interlinkage between the modulation response parameters at these detunings was also observed.

These numerical studies also suggested that change in carrier number with detuning, which should be reflected in the device voltage, was indicative of the unstable dynamics present in the laser cavity. An extensive and comprehensive experimental study of the voltage response of two long wavelength VCSELs during tuned optical injection verified this assertion. Independently, dynamics inferred by the optical response and by the electrical response of the injected VCSELs were correlated with the voltage changes as functions of polarisation and injection strength. These results demonstrated that the stable locking region could be reliably identified based on a voltage measurement and the derivative of the voltage with respect to the frequency detuning. The identification procedure developed in this work is cheap, easy to implement and robust to changes in operating conditions.

One of the motivating ideas behind exploring the possibilites of voltage spectroscopy was to facilitate remote tuning of the VCSEL wavelength to match an injected reference signal. As optical fibres gradually replace the copper wires, customer units such as homes, offices and apartment blocks will each eventually need their own high speed optical source to access Passive Optical Networks. Long wavelength VCSELs are attractive candidates for these sources due to their potential low cost and ability to be directly modulated at high speed. To support this claim, error free transmission over 40 km using a state of the art VCSEL 10 Gbit/s was demonstrated using Electronic Dispersion Compensation to mitigate penalties due to frequency chirp.

With the implementation of Dense Wavelength Division Multiplexing systems, wavelength restrictions are placed on the individual sources which must maintain emission wavelengths within specific 50 GHz wide grids. However, stock piling a large amount of wavelength specific or 'coloured' components is not efficient for network operators who would prefer a 'colourless' solution which could be fixed, on command, to a given grid spacing. In response, the transmission properties of a state of the art, monolithic, tuneable, long

wavelength MEMS-VCSEL based on a flexible membrane were investigated. These devices can have single mode tuning ranges over 100 nm. The output light was externally modulated as the MEMS-VCSEL was not optimised for high speed. Error free transmission at 10 Gbit/s over 50 km of single mode fibre across a modulator limited 30 nm tuning range up to 60 °C was demonstrated for the first time. Future devices will be capable of direct modulation.

Combining the locking detection method developed in this work with the widely tuneable MEMS-VCSELs is a significant step towards generating a true 'colourless' component. It is necessary that the desired wavelength is injected into the MEMS-VCSEL from the central office. As the VCSEL tuning is free of mode hops, sweeping the emission wavelength across the available range guarantees a small enough relative frequency detuning between the MEMS-VCSEL and the injected light for stable locking to occur. At this point, a sharp drop in the operating voltage is observed. This is the indicator that the MEMS-VCSEL is emitting at the correct 'colour'.

While the work performed in this thesis is relevant and contributes to active research fields it is, naturally, incomplete and imperfect. For instance, all of the theoretical work has been performed using a model which only considers a single polarisation mode. As VCSELs are capable of polarisation switches, this may seem like a serious oversight but, for this work, it was considered that more intuitive conclusions could be drawn from the single mode model while still providing a realistic explanation of the experimental observations. The spin flip rate equation model is more descriptive but also generally less accessible. Due to time constraints, the proposed method for measuring k and α using the shape of the voltage response under detuned injection has not been performed but would be a practical way to compare the theoretical description used here with experimental realities.

Another method to investigate the high speed correlations between the dynamics and voltage/carrier response is available but was not explored in this work. If the DC current to the VCSELs is delivered through a bias-T, a high speed voltage variation in response to unstable injection should exist at the RF port of the bias-T and be observable on an oscilloscope in real time.

A host of related and interesting experiments exist which could also be

performed such as an equivalent study of injected short wavelength VCSELs. Wafer-fused or monolithic long wavelength VCSELs might show generally similar responses yet have design specific features. Additional studies into the effect of different cavity lengths and finesses could also be instructive.

Less obvious experiments are also worthy of consideration. A VCSEL emits the same output power at two different bias points: one on either side of the thermal rollover. The result of optical injection with the same strength and detuning for both bias currents is not predictable with the current model as different gain conditions exist. Detuned injection on edge emitters would have more complicated responses due to the smaller free spectral range. Each new piece of evidence would assist in confidently identifying the different dynamics and would provide further insights into the physics involved.

The MEMS-VCSEL used in this work is a highly advanced piece of technology but there is always scope for improvement. Currently, the two main impediments to further transmission milestones are the severe mechanical instabilities, which had to be overcome in chapter 5, and the need for external modulation. If remote optical injection could be employed to first fix the desired wavelength, as demonstrated here, and then to reduce the frequency chirp under modulation, a powerful element for future low cost, high speed communication networks will have been cultivated. It should be possible to engineer out the instabilities in the device through proper packaging, thermal controls, wavelength lockers and low noise current sources.

By its nature, every endeavour employing the scientific method requires a significant amount of effort. This thesis is no different but having the privilege of contributing to the body of human knowledge easily justifies the toil involved.

Hopefully, others will acknowledge the merits of the ideas proposed in this thesis and be engaged enough to continue this work. It would be particularly pleasing to see voltage spectroscopy applied in real world, commercial devices helping to deliver universal, high speed Internet access.

This work was supported by the European Union (Grant FP7-ICT 40530), by Science Foundation Ireland (Grant SFI 10/CE/I1853 CTVR II) and by a European Space Agency project on VCSEL reliability for space applications.

Appendix A

Optical Injection Rate Equations

A.1 Derivation

The rate of change of the amplitude of a laser's complex electric field will be proportional to the intensity of the field itself with the constant of proportionality equal to the difference between the stimulated emission and the cavity loss rates.

$$\begin{aligned} \frac{d|\mathbf{E}|^2}{dt} &= (G(N) - \gamma_p)|\mathbf{E}|^2 \\ 2|E|\frac{d|\mathbf{E}|}{dt} &= (G(N) - \gamma_p)|\mathbf{E}|^2 \\ \frac{d|\mathbf{E}|}{dt} &= \frac{1}{2}(G(N) - \gamma_p)|\mathbf{E}| \end{aligned} \tag{A.1}$$

In the linear gain approximation:

$$\begin{aligned} G(N) &= G(N_{th}) + \frac{\partial G}{\partial N}(N - N_{th}) \\ &= G(N_{th}) + G_0(N - N_{th}) \end{aligned} \tag{A.2}$$

so eq. (A.1) becomes:

$$\frac{d|\mathbf{E}|}{dt} = \frac{1}{2}(G(N_{th}) + G_0(N - N_{th}) - \gamma_p)|\mathbf{E}| \tag{A.3}$$

In the steady state $N = N_{th}$ and $\frac{d|\mathbf{E}|}{dt} = 0$ so $G(N_{th}) = \gamma_p$. This produces the rate equation for the complex electric field amplitude.

$$\frac{d|\mathbf{E}|}{dt} = \frac{1}{2}G_0(N - N_{th})|\mathbf{E}| \tag{A.4}$$

The rate of change of the phase of the complex electric field, ϕ, will be proportional to the carrier dependent change in the refractive index, $n(N)$, above threshold.

$$\begin{aligned} \frac{d\phi}{dt} &\propto n(N) \\ \frac{d\phi}{dt} &= b(N - N_{th}) \end{aligned} \tag{A.5}$$

where $b = \frac{\partial n}{\partial N}$. Since the complex electric field $\mathbf{E} = |\mathbf{E}|e^{i\phi}$

$$\begin{aligned} \frac{d\mathbf{E}}{dt} &= \frac{d|\mathbf{E}|}{dt}e^{i\phi} + |\mathbf{E}|\frac{de^{i\phi}}{dt} \\ &= e^{i\phi}(\frac{d|\mathbf{E}|}{dt} + i|\mathbf{E}|\frac{d\phi}{dt}) \end{aligned} \tag{A.6}$$

Combining eqs. (A.4) to (A.6) gives

$$\frac{d\mathbf{E}}{dt} = (\frac{1}{2}G_0 + ib)(N - N_{th})\mathbf{E} \tag{A.7}$$

Rewriting and identifying $\frac{2b}{G_0} = 2\frac{\partial n}{\partial N}/\frac{\partial G}{\partial N}$ is the linewidth enhancement factor, α, completes the complex electric field rate equation.

$$\frac{d\mathbf{E}}{dt} = \frac{1}{2}(1 + i\alpha)G_0(N - N_{th})\mathbf{E} \tag{A.8}$$

The rate equation for the carriers can be phenomenologically determined by recognising that the carriers will change at a rate equal to the difference

between the electronic pumping rate and the combined carrier loss rate due to spontaneous and stimulated emission.

$$\frac{dN}{dt} = \frac{I}{q} - \gamma_N N - G_0(N - N_{th})E \tag{A.9}$$

Optical injection is modelled as the addition of an external electric field term in eq. (A.8).

$$\frac{d\mathbf{E}}{dt} = \frac{1}{2}(1 + i\alpha)G_0(N - N_{th})\mathbf{E} + k\mathbf{E_{inj}} \tag{A.10}$$

where k is the coupling rate. Both complex electric fields can be decomposed into their amplitude and phase components including the information on their frequencies.

$$\mathbf{E} = |\mathbf{E}|e^{j(\omega_0 t + \phi_0(t))}$$
$$\mathbf{E_{inj}} = |\mathbf{E_{inj}}|e^{j(\omega_1 t + \phi_1(t))}$$

Inserting these expressions into eq. (A.10) and expanding all the derivatives generates a complex expression. Equating the real and imaginary parts separately gives

$$\frac{d|\mathbf{E}|}{dt} = \frac{1}{2}G_0(N - N_{th})|\mathbf{E}| + k|\mathbf{E_{inj}}|\cos(\Delta\omega t + \phi_1(t) - \phi_0(t)) \tag{A.11}$$

$$\frac{d\phi_0}{dt} + \omega_0 = \frac{1}{2}\alpha G_0(N - N_{th}) + k\frac{|\mathbf{E_{inj}}|}{|\mathbf{E}|}\sin(\Delta\omega t + \phi_1(t) - \phi_0(t)) \tag{A.12}$$

where $\Delta\omega$ is the relative frequency detuning. The phase difference between the laser and injected light can be defined as $\phi = \phi_0(t) - \Delta\omega t - \phi_1(t)$. Inserting this new definition into eq. (A.12), normalising the free running frequency ω_0 to zero and setting the time derivative of the phase of the injected light to zero without loss of generality produces

$$\frac{d|\mathbf{E}|}{dt} = \frac{1}{2}G_0(N - N_{th})|\mathbf{E}| + k|\mathbf{E_{inj}}|\cos(\phi) \tag{A.13}$$

$$\frac{d\phi}{dt} = \frac{1}{2}\alpha G_0(N - N_{th}) - \Delta\omega - k\frac{|\mathbf{E_{inj}}|}{|\mathbf{E}|}\sin(\phi) \tag{A.14}$$

The intensity of the electric field can be equated with the photon number, S:

$$|\mathbf{E}|^{\mathbf{2}} = S$$

$$\frac{d|\mathbf{E}|}{dt} = \frac{1}{2}\frac{1}{\sqrt{S}}\frac{dS}{dt}$$

Substituting this expression into eqs. (A.13) and (A.14), converting from angular to linear frequency ν and observing that $G_0(N - N_{th}) = G_0(N - N_{tr}) - \gamma_p$, the final form of the rate equations used in this thesis is reached.

$$\frac{dS}{dt} = [G_0(N - N_{tr}) - \gamma_p]S + 2k\sqrt{SS_{inj}}\cos(\phi) \tag{A.15}$$

$$\frac{d\phi}{dt} = \frac{1}{2}\alpha[G_0(N - N_{tr}) - \gamma_p] - 2\pi\Delta\nu - k\sqrt{\frac{S_{inj}}{S}}\sin(\phi) \tag{A.16}$$

$$\frac{dN}{dt} = \frac{I}{q} - \gamma_N N - G_0(N - N_{th})S \tag{A.17}$$

A.2 Steady state solution relations

The steady state solutions to eqs. (A.15) to (A.17) can be found by setting the time derivatives equal to zero. In particular the photon number equation becomes

$$(G_0(N - N_{tr}) - \gamma_p)S + 2k\sqrt{SS_{inj}}cos(\phi) = 0$$

Reorganization of the terms gives the steady state carrier number as

$$\boxed{N = N_{tr} + \frac{\gamma_p}{G_0} - \frac{2k}{G_0}\sqrt{\frac{S_{inj}}{S}}\cos(\phi)} \tag{A.18}$$

Substituting eq. (A.18) into the steady state form of eq. (A.16) gives

$$-\frac{\alpha}{2}2k\sqrt{\frac{S_{inj}}{S}}\cos(\phi)-2\pi\Delta\nu-k\sqrt{\frac{S_{inj}}{S}}sin(\phi)=0$$

Isolating $\Delta\nu$:

$$2\pi\Delta\nu=-k\sqrt{\frac{S_{inj}}{S}}(\sin(\phi)+\alpha\cos(\phi)) \tag{A.19}$$

A trigonometric expansion of eq. (A.19), facilitates a re-write into the form

$$2\pi\Delta\nu=-k\sqrt{\frac{S_{inj}}{S}}\sqrt{1+\alpha^2}\sin(\phi+\arctan\alpha) \tag{A.20}$$

This gives an expression relating the stable phase difference to the frequency detuning.

$$\boxed{\phi=\arcsin\left(\frac{-2\pi\Delta\nu}{k\sqrt{1+\alpha^2}}\sqrt{\frac{S}{S_{inj}}}\right)-\arctan(\alpha)} \tag{A.21}$$

The steady state photon number is trivially solved by setting eq. (A.17)= 0 and solving for S:

$$\boxed{S=\frac{I/q-\gamma_n N}{G_0(N-N_{th})}} \tag{A.22}$$

The stable locking phase limits under weak injection can be derived by considering the principle limits of the arcsin function in eq. (A.21)

$$-\frac{\pi}{2}-\arctan(\alpha)\leq\phi\leq\frac{\pi}{2}-\arctan(\alpha) \tag{A.23}$$

Inserting these limits into eq. (A.20) determines the stable locking frequency limits under weak injection.

$$\boxed{-k\sqrt{\frac{S_{inj}}{S}}\sqrt{1+\alpha^2}\leq 2\pi\Delta\nu\leq k\sqrt{\frac{S_{inj}}{S}}} \tag{A.24}$$

A.3 Non-dimensionalisation

A non-dimensional form of eqs. (A.15) to (A.17) can be found by introducing scaling factors and noting that the carriers and photons will operate on different timescales.

$$\begin{aligned} S &\to s_c\chi \quad t \to \tau_p t_p \text{ (photons)} \\ N &\to n_c\eta \quad t \to \tau_c t_c \text{ (carriers)} \end{aligned}$$

Separate time derivatives replace the single time scale of the original equations

$$\begin{aligned} \frac{d}{dt} &\to \frac{1}{\tau_c}\frac{d}{dt_c} \text{ (carriers)} \\ \frac{d}{dt} &\to \frac{1}{\tau_p}\frac{d}{dt_p} \text{ (photons)} \end{aligned}$$

Each of eqs. (A.15) to (A.17) can now be transformed as follows:

$$\begin{aligned} \textit{eq. (A.15)} : \frac{1}{t_p}\frac{ds_c\chi}{d\tau_p} &= [G_0(n_c\eta - N_{tr}) - \gamma_p]sc\chi + 2k\sqrt{S_{inj}s_c\chi}\cos(\phi) \\ \frac{d\chi}{d\tau_p} &= [G_0 n_c t_p(\eta - \frac{N_{tr}}{n_c}) - \gamma_p t_p]\chi + 2kt_p\sqrt{\frac{S_{inj}}{s_c}}\sqrt{\chi}\cos(\phi) \end{aligned} \tag{A.25}$$

$$\begin{aligned} \textit{eq. (A.16)} : \frac{1}{t_p}\frac{d\phi}{d\tau_p} &= \frac{\alpha}{2}[G_0(n_c\eta - N_{tr}) - \gamma_p] - 2\pi\Delta\nu - k\sqrt{\frac{S_{inj}}{s_c\chi}}\sin(\phi) \\ \frac{d\phi}{d\tau_p} &= \frac{\alpha}{2}[G_0 n_c t_p(\eta - \frac{N_{tr}}{n_c}) - \gamma_p t_p] - 2\pi\Delta\nu t_p - kt_p\sqrt{\frac{S_{inj}}{s_c}}\frac{1}{\sqrt{\chi}}\sin(\phi) \end{aligned} \tag{A.26}$$

$$\begin{aligned} \textit{eq. (A.17)} : \frac{1}{t_c}\frac{dn_c\eta}{d\tau_c} &= \frac{I}{q} - \gamma_n n_c\eta - G_0(n_c\eta - N_{tr})s_c\chi \\ \frac{d\eta}{d\tau_c} &= \frac{It_c}{qn_c} - \gamma_n\eta t_c - G_0 t_c s_c(\eta - \frac{N_{tr}}{n_c})\chi \end{aligned} \tag{A.27}$$

An exchange of derivatives can be done to place all three equations back on the same time scale.

$$\begin{aligned} t &= t \\ \tau_p t_p &= \tau_c t_c \\ \frac{1}{t_p}\frac{d}{d\tau_p} &= \frac{1}{t_c}\frac{d}{d\tau_c} \\ \Rightarrow \frac{d}{d\tau_c} &= \frac{t_c}{t_p}\frac{d}{d\tau_p} \end{aligned} \tag{A.28}$$

so eq. (A.27) becomes

$$\frac{d\eta}{d\tau_c} = \frac{It_p}{qn_c} - \gamma_n t_p \eta - G_0 s_c t_p (\eta - \frac{N_{tr}}{n_c})\chi \tag{A.29}$$

By observation choosing the scaling factors in the following way simplifies the system

$$\begin{aligned} s_c &\to S_{inj} \\ n_c &\to N_{tr}\eta \\ t_p &\to \frac{1}{\gamma_p} \\ t_c &\to \frac{1}{\gamma_n} \end{aligned}$$

eqs. (A.25) to (A.27) now take the non-dimensional form

$$\frac{d\chi}{d\tau} = [G(\eta - 1) - 1]\chi + 2\kappa\chi^{\frac{1}{2}}\cos(\phi) \tag{A.30}$$

$$\frac{d\phi}{d\tau} = \frac{\alpha}{2}[G(\eta - 1) - 1]\chi - \delta - \kappa\chi^{-\frac{1}{2}}\sin(\phi) \tag{A.31}$$

$$\frac{d\eta}{d\tau} = P - T\eta - Q(\eta - 1)\chi \tag{A.32}$$

where

$$\begin{aligned} G &= \frac{G_0 N_{tr}}{\gamma_p} \\ P &= \frac{I}{qN_{tr}\gamma_p} \\ T &= \frac{\gamma_n}{\gamma_p} \\ Q &= \frac{G_0 S_{inj}}{\gamma_p} \end{aligned} \tag{A.33}$$

and the bifurcation parameters $\Delta\nu$ and k have been rescaled by γ_p so that

$$\begin{aligned} \delta &= \frac{\Delta\nu}{2\pi\gamma_p} \\ \kappa &= \frac{k}{\gamma_p} \end{aligned} \tag{A.34}$$

A.4 Stability

At each steady state phase value a fixed point $(S_{inj}, \phi, S, N, \Delta\nu)$ is calculated. A general approach to determine the stability of a fixed point is to analyze the eigenvalues of the system Jacobian, J. This Jacobian is the matrix of the partial derivatives of the system and measures the local stability around the fixed point.

$$J = \begin{pmatrix} \rho - \gamma_p + \kappa\cos(\phi) & -2\kappa S\sin(\phi) & G_0 S \\ -\frac{\kappa}{2S}\sin(\phi) & \kappa\cos\phi & \frac{\alpha}{2}G_0 \\ -\rho & 0 & -\gamma_n - G_0 S \end{pmatrix} \tag{A.35}$$

where $\rho = G_0(N - N_{tr})$ and $\kappa = k\sqrt{S_{inj}/S}$. The eigenvalues of this matrix are λ such that $J - \lambda\mathbb{I}_3 = 0$. Each of the three eigenvalues must have a negative

real part for the fixed point to be stable. The system can lose stability through the birth of a limit cycle from the fixed point at a Hopf boundary or the collision of two fixed points at a Saddle Node boundary.

A.5 Small single response

The response of the system, ΔS, to small sinusoidal perturbations to the bias current of amplitude ΔI and frequency ω can be analysed with the following matrix equation:

$$i\omega\mathbb{I}_3 - J = \begin{pmatrix} 0 \\ 0 \\ \Delta I \end{pmatrix} \tag{A.36}$$

where $\mathbb{I}_3$ is a 3×3 identity matrix and $i = \sqrt{-1}$. The transfer function $H(\omega)$ which describes the photon number response to the frequency of the perturbation is given by

$$H(\omega) = \frac{\Delta S}{\Delta I} = C_1 \left(\frac{i\omega + C_2}{(i\omega)^3 + C_3(i\omega)^2 + C_4(i\omega) + C_5} \right) \tag{A.37}$$

Where $C_1 = J_{13}$, $C_2 = -J_{22} + J_{12}J_{23}/J_{13}$, $C_3 = -(J_{11} + J_{22} + J_{33})$, $C_4 = J_{11}J_{22} + J_{11}J_{33} + J_{22}J_{33} - J_{12}J_{21} - J_{13}J_{31}$ and $C_5 = J_{12}J_{21}J_{33} + J_{13}J_{31}J_{22} - J_{11}J_{22}J_{33} - J_{12}J_{23}J_{31}$. J_{xy} is the x^{th} element of the y^{th} column of J evaluated at the steady state point.

The small signal response is given by $|H(\omega)|^2$. In this work, it is the poles of the transfer function which are investigated. The analytical roots to the polynomial in the denominator of the transfer function are not easily expressible but the transfer function is still assumed to be that of a damped oscillator so the denominator of (A.37) can be factored with one real root and two complex conjugate roots. The complex roots are taken to have the form $0.5\,\gamma \pm if_r$ where γ and f_r are the damping and resonance frequencies. The root is a pole, f_p, which causes a drop off in response at nearby frequencies [6].

A.6 Electrical and Optical Spectra

The electrical and optical spectra of a free running or optically injected laser result from the intensity oscillations in the internal electric field. Using eqs. (A.15) to (A.17), the complex electric field $\mathbf{E}$ is constructed as

$$\mathbf{E}(t) = E_x(t) + iE_y(t) \tag{A.38}$$

$$= S(t)\cos(\phi(t)) + iS(t)\sin(\phi(t)) \tag{A.39}$$

where $i = \sqrt{-1}$. The intensity of the electric field, I, is given by

$$I(t) = |\mathbf{E}(t)|^2 \tag{A.40}$$

$$= \mathbf{E}(t)\overline{\mathbf{E}}(t) \tag{A.41}$$

where $\overline{\mathbf{E}}(t)$ represents the complex conjugate of $\mathbf{E}(t)$.

While the electrical spectrum is given by the Fourier transform of the intensity, the optical spectrum of the laser is given by the Fourier transform of the autocorrelation of the complex electric field.

$$L(\omega) = \int_{-\infty}^{\infty} \langle \mathbf{E}(t)\overline{\mathbf{E}}(t-\tau)\rangle e^{-2\pi i\omega t}\, d\tau \tag{A.42}$$

The definition for L is strictly for an infinitely long, continuous time series. In the case of a truncated time series as in this work the limits of the integration are reduced to within the domain for which $\mathbf{E}$ has been calculated. Some other representations which can be used to identify laser dynamics are:

Phase portraits: Plots of (E_x, E_y, N) exist in what is referred to as *phase space*. These traces may form single dots, closed curves or more complex structures. Projections of (E_x, E_y) onto the *phase plane* gives information of the boundedness of the phase.

Poincaré cuts: Plane intersections of the phase space curves at $N = N_{fr}$. The Poincaré cut gives quantifable data on the dynamics.

Appendix B

Mathematica code

Optically Injection Locked VCSELs

Parameter Definitions

```
(*Note: in this code Δω represents the linear frequency detuning*)
τn = 2 × 10^-9;          γn = 1/τn;
τp = 5.4 × 10^-12;       γp = 1/τp;
a0 = 8 × 10^-20;
cc = 3 × 10^8;
n = 3.703;               vg = cc/n;
Lact = 42 × 10^-9;
Lcav = 2.1 × 10^-6;
mesarad = 4 × 10^-6;
Amesa = π mesarad^2;
Vact = Lact Amesa;
Γ = 2 Lact / Lcav;
α = 2.0;
q = 1.6 × 10^-19 ;
β = 1 × 10^-4;
B = 1 × 10^-16;
G0 = Γ a0 vg / Vact;
Islave = 0.8 × 10^-3;
rateeqnsfree = {
   S'[t] == G0 (Nn[t] - Ntr) S[t] - γp S[t] + B β / Vact Nn[t]^2,
   ϕ'[t] == α/2 ( G0 (Nn[t] - Nth) / (*1+ϵ S[t]*)1 ),
   Nn'[t] == Iswap/q - γn Nn[t] - G0 (Nn[t] - Ntr) S[t]};
initialconsfree = {S[0] == 0, ϕ[0] == 0, Nn[0] == 0};
fulleqnsfree = Flatten[Join[rateeqnsfree, initialconsfree]];
```

Slave Nth and Ntr Calculation

```
Ndata = {};
gaindatacurrent = {};
gaindatacarrier = {};
Sdata = {};
timel = 30 × 10^-9;
For[h = 0.0, h ≤ 1.2, h += 0.005, {Iset = h 10^-3, solsl = NDSolve[{S'[t] == G0 (Nn[t] - Ntr) S[t] - γp S[t] + (B β)/Vact Nn[t]^2,
    Nn'[t] == Iset/q - γn Nn[t] - G0 (Nn[t] - Ntr) S[t], S[0] == 0, Nn[0] == 0}, {S, Nn}, {t, 0, timel}, Method → "Automatic",
   MaxSteps → 200000], AppendTo[Ndata, {h, Nn[timel] /. solsl[[1]]}], AppendTo[Sdata, {h, S[timel] /. solsl[[1]]}],
  AppendTo[gaindatacurrent, {h, Nn[timel] - Ntr /. solsl[[1]] (*+Log[Nn[timel]/.solsl[[1]]/Ntr]*)}]}]
freerunningcarrierdens = Ndata[[-1, 2]]/Vact2 10^-6;
dataTH = Drop[Sdata, Round[0.9 Length[Sdata]]];
fitparasTH = Fit[dataTH, {1, x}, x];
fitfuncTH[x_] := fitparasTH[[1]] + fitparasTH[[2, 1]] x
IThresholdvalue = Round[Root[Fit[dataTH, {1, x}, x], 1], 0.005]
Nth = Ndata[[Position[Round[Transpose[Ndata][[1]], 0.005], IThresholdvalue][[1, 1]], 2]]
```

Free Running VCSEL

```
timefree = 20 × 10^-9;
Ssolsfree = NDSolve[Evaluate[fulleqnsfree /. Iswap → Islave],
   {S, ϕ, Nn}, {t, 0, timefree}, Method → "Automatic", MaxSteps → 200000];
Print["Final S is " <> ToString[S[timefree] /. Ssolsfree[[1]], TraditionalForm]]
Print["Final S density is " <> ToString[S[timefree] 10^-6/Vact /. Ssolsfree[[1]], TraditionalForm]]
Print["Final ϕ is " <> ToString[ϕ[timefree] /. Ssolsfree[[1]], TraditionalForm]];
Print["Final N is " <> ToString[Nn[timefree] /. Ssolsfree[[1]], TraditionalForm]];
Print["Final N density is " <> ToString[Nn[timefree] 10^-6/Vact /. Ssolsfree[[1]], TraditionalForm]];
p1 = Plot[S[t] /. Ssolsfree, {t, 0, timefree}, PlotRange → All, PlotLabel → "Slave Free Running Photon Number"]
p2 = Plot[Nn[t] /. Ssolsfree, {t, 0, timefree}, PlotRange → All, PlotLabel → "Slave Free Running Carrier Number"]
p3 = Plot[ϕ[t] /. Ssolsfree, {t, 0, timefree}, PlotRange → All, PlotLabel → "Slave Free Running Phase"]

Nfr = Nn[timefree] /. Ssolsfree[[1]]
Sfr = S[timefree] /. Ssolsfree[[1]]
```

Optically Injected VCSEL Numerical Solutions

- OIL solution at a single frequency detuning

```
S0 = S[timefree] /. Ssolsfree[[1]];
ϕ0 = 0 * 32.98; (*ϕ[timefree]/.Ssolsfree[[1]]*);
N0 = Nn[timefree] /. Ssolsfree[[1]];
k = 400 × 10^9;(*Hz*)
injrat = -25;
Sinjsing = 10^(injrat/10) S[timefree] /. Ssolsfree[[1]];;
Δωdet = -3.6 10^9; (*Hz*)
timesingle = (6 + 0 × 250) 10^-9; solsinjsingle =
 NDSolve[{S'[t] == G0 (Nn[t] - Ntr) S[t] - γp S[t] + 0 × 1 (B β)/Vact Nn[t]^2 + 2 k Sqrt[S[t] Sinjsing] Cos[ϕ[t] (*-ϕoff-ϕslope t*)],
   ϕ'[t] == α/2 (G0 (Nn[t] - Ntr) - γp) - 2 π Δωdet - k Sqrt[Sinjsing/S[t]] Sin[ϕ[t] (*-ϕoff-ϕslope t*)],
   Nn'[t] == Islave/q - γn Nn[t] - G0 (Nn[t] - Ntr) S[t], S[0] == S0, ϕ[0] == ϕ0, Nn[0] == N0},
  {S, ϕ, Nn}, {t, 0, timesingle}, Method → "Automatic", MaxSteps → ∞];
pOIL1 = Plot[S[t] /. solsinjsingle, {t, 0 timesingle, timesingle}, PlotRange → All,
  PlotLabel → "Slave Injection Locked Photon Number"]
pOIL2 = Plot[Nn[t] /. solsinjsingle, {t, 0, timesingle}, PlotRange → All,
  PlotLabel → "Slave Injection Locked Carrier Number", Epilog → Line[{{0, Nfr}, {timesingle, Nfr}}]]
pOIL3 = Plot[{ϕ[t] /. solsinjsingle}, {t, 0. timesingle, timesingle},
  PlotRange → All, PlotLabel → "Slave Injection Locked Phase"]
```

```
Nex = Table[{t, Nn[t] /. solsinjsingle[[1]]}, {t, 0.45 timesingle, 0.48 timesingle, 0.03 timesingle / 10 000}];

Sex = Table[{t, S[t] /. solsinjsingle[[1]]}, {t, 0.45 timesingle, 0.48 timesingle, 0.03 timesingle / 10 000}];

ϕex = Table[{t, ϕ[t] /. solsinjsingle[[1]]}, {t, 0.45 timesingle, 0.48 timesingle, 0.03 timesingle / 10 000}];

d10 = Table[{(S[t] /. solsinjsingle[[1]]) (Cos[ϕ[t]] /. solsinjsingle[[1]]),
    (S[t] /. solsinjsingle[[1]]) (Sin[ϕ[t]] /. solsinjsingle[[1]])}, {t, 0.8 timesingle, 1.0 timesingle, 0.2 timesingle / 5000}];

d8 = Table[{(S[t] /. solsinjsingle[[1]]) (Cos[ϕ[t]] /. solsinjsingle[[1]]), (S[t] /. solsinjsingle[[1]])
     (Sin[ϕ[t]] /. solsinjsingle[[1]]), Nn[t] /. solsinjsingle[[1]]}, {t, 0.2 timesingle, 0.8 timesingle, 0.6 timesingle / 1 000 000}];
```

■ Poincaré cuts

```
zeroCrossings[l_List] := Module[{t, u, v}, t = {Sign[l], Range[Length[l]]} // Transpose; (*List of-1,
  0,1 only*)u = Select[t, First[#] ≠ 0 &]; (*Ignore zeros*)v = Split[u, First[#1] == First[#2] &];
  (*Group into runs of+and-values*){Most[Max[#[[All, 2]]] & /@ v], Rest[Min[#[[All, 2]]] & /@ v]} // Transpose]
clusters[pts_, dist_] := Gather[pts, EuclideanDistance[##] < dist &];
dt = d8;
zcross = zeroCrossings[Last /@ dt - Nfr];

NfrsExEy = Partition[Riffle[dt[[zcross[[All, 1]]]][[All, 1]], dt[[zcross[[All, 1]]]][[All, 2]]], 2];
meanZcross = Mean /@ clusters[NfrsExEy, 1000];
ListPlot[NfrsExEy, PlotRange → All, PlotStyle -> PointSize[0.01], Epilog → {PointSize[0.01], Red, Point[meanZcross]}]
```

■ Generate the optical spectrum

```
Ex[t_] := (S[t] /. solsinjsingle[[1]]) (Cos[ϕ[t]] /. solsinjsingle[[1]]);
Ey[t_] := (S[t] /. solsinjsingle[[1]]) (Sin[ϕ[t]] /. solsinjsingle[[1]]);

ExExport = Table[{t, Ex[t]}, {t, (0.45) timesingle, 0.48 timesingle, 0.03 timesingle / 10 000}];
EyExport = Table[{t, Ey[t]}, {t, (0.45) timesingle, 0.48 timesingle, 0.03 timesingle / 10 000}];

Inten = Table[{t, (Ex[t] + i Ey[t]) Conjugate[Ex[t] + i Ey[t]]},
   {t, (0.45) timesingle, 0.48 timesingle, 0.03 timesingle / 10 000}];

fr1 = ListLinePlot[ExExport];
fr2 = ListLinePlot[EyExport];
fr3 = ListLinePlot[Inten];
GraphicsGrid[{{fr1, fr2, fr3}}]

lc = {};
deltarange = 200;
deltastep = 0.2;
STF = 0.3;(*sampletimesfactor*)
tT = deltarange / 1000 (2 STF + 0 × 2 0.4) timesingle;
Nsamp = deltarange / deltastep;

{a = Table[Ex[t] + i Ey[t], {t, (0.5 - STF) timesingle, (0.5 + STF) timesingle, timesingle / 1000}];
    delay = # / 1000 (STF + 0 × 2 0.4) timesingle;
    b = Table[Conjugate[Ex[t - delay] + i Ey[t - delay]],
      {t, (0.5 - STF) timesingle, (0.5 + STF) timesingle, timesingle / 1000}];
    AppendTo[lc, {delay, ListCorrelate[a, b][[1]]}]} & /@ Range[-deltarange, deltarange, deltastep];

amps = Abs[Fourier[lc[[All, 2]]]];
ampsRot = RotateRight[Abs[Fourier[lc[[All, 2]]]], 0.5 deltarange / deltastep];

freqs = Table[kl / tT, {kl, 1, Nsamp, 1}];

freqsRot = Table[kl / tT, {kl, 0.5 Nsamp, -0.5 Nsamp, -1}];

psd = Table[{freqs[[th]] 10^-9, amps[[th]]}, {th, 1, Length[freqs], 1}];
OSA = Table[{freqsRot[[th]] 10^-9, ampsRot[[th]]}, {th, 1, Length[freqs], 1}];

ListLinePlot[Drop[psd, 0], PlotRange → All, AxesOrigin → {0, 0}]
ListLinePlot[Drop[OSA, 0], PlotRange → All, AxesOrigin → {0, 0}, Axes → {True, False}]
```

ω and ϕ Boundaries of the SIL Region

- **Generate analytical solutions for the cinq - tuplets (ratio, ω, N, S, ϕ) by looping through all phases.**

```
Clear[phasestepdensity];(*Define a function to adjust the phase step
 size as at the edges a tiny phase change accounts for a huge detuning change*)
phasestepdensity[ϕ_ /; -π ≤ ϕ < -1.04 π/2] := 1/20 π/2;
phasestepdensity[ϕ_ /; -1.04 π/2 ≤ ϕ ≤ -0.96 π/2] := 1/1000 π/2;
phasestepdensity[ϕ_ /; -0.96 π/2 < ϕ < 0.96 π/2] := 1/20 π/2;
phasestepdensity[ϕ_ /; 0.96 π/2 ≤ ϕ ≤ 1.04 π/2] := 1/1000 π/2;
phasestepdensity[ϕ_ /; 1.04 π/2 < ϕ ≤ π] := 1/20 π/2;

Timing[NsolfRAT = {}; SsolfRAT = {}; NsolfωRAT = {}; SsolfωRAT = {}; ϕsolfωRAT = {}; locksolfωRAT = {};
 For[currentRAT = -20, currentRAT ≤ -20, currentRAT += 30, {Nsolfloop = {}; Ssolfloop = {}; Nsolfωloop = {};
   Ssolfωloop = {}; ϕsolfωloop = {}; locksolfωloop = {}; For[ϕdif = -π, ϕdif ≤ π, ϕdif += phasestepdensity[ϕdif],
    {sols = NSolve[{S == (Islave/q - γn (Nn))/(G0 (Nn - Ntr)), Nn == Ntr + (γp - 2 k Sqrt[(10^(currentRAT/10) S0a)/S] Cos[ϕdif])/G0}, {Nn, S}, Reals],
     If[Length[sols] == 0, Null, AppendTo[Nsolfloop, {ϕdif, sols[[1, 1, 2]]}]; AppendTo[Ssolfloop, {ϕdif, sols[[1, 2, 2]]}];
      AppendTo[Nsolfωloop, {10^-9/(-2 π) (k Sqrt[(10^(currentRAT/10) S0a)/sols[[1, 2, 2]]] Sin[ϕdif] - α/2 (G0 (sols[[1, 1, 2]] - Ntr) - γp)), sols[[1, 1, 2]]}];
      AppendTo[Ssolfωloop, {10^-9/(-2 π) (k Sqrt[(10^(currentRAT/10) S0a)/sols[[1, 2, 2]]] Sin[ϕdif] - α/2 (G0 (sols[[1, 1, 2]] - Ntr) - γp)), sols[[1, 2, 2]]}];
      AppendTo[ϕsolfωloop, {10^-9/(-2 π) (k Sqrt[(10^(currentRAT/10) S0a)/sols[[1, 2, 2]]] Sin[ϕdif] - α/2 (G0 (sols[[1, 1, 2]] - Ntr) - γp)), ϕdif}];
      AppendTo[locksolfωloop, {10^-9/(-2 π) (k Sqrt[(10^(currentRAT/10) S0a)/sols[[1, 2, 2]]] Sin[ϕdif] - α/2 (G0 (sols[[1, 1, 2]] - Ntr) - γp)), 1}]]]},
   AppendTo[NsolfRAT, {currentRAT, Nsolfloop}], AppendTo[NsolfωRAT, {currentRAT, Nsolfωloop}],
   AppendTo[SsolfRAT, {currentRAT, Ssolfloop}], AppendTo[SsolfωRAT, {currentRAT, Ssolfωloop}],
   AppendTo[ϕsolfωRAT, {currentRAT, ϕsolfωloop}],
   AppendTo[locksolfωRAT, {currentRAT, locksolfωloop}], PrintTemporary[currentRAT]}]]

allcinq = Table[
   Table[{NsolfωRAT[[ratvar, 1]], NsolfωRAT[[ratvar, 2, we, 1]], NsolfωRAT[[ratvar, 2, we, 2]], SsolfωRAT[[ratvar, 2, we, 2]],
     ϕsolfωRAT[[ratvar, 2, we, 2]]}, {we, 1, Length[SsolfωRAT[[ratvar, 2]]], 1}], {ratvar, 1, Length[NsolfRAT], 1}];
```

■ **Generate the eigenvalues from the Jacobian and test which ones satisfy Re$[\lambda_i] < 0$**

```
Timing[stabNdata = {};
 stabSdata = {};
 stabϕdata = {};
 stabilityRAT = {};
 For[wq = 1 , wq ≤ Length[allcinq], wq ++, {stabilityindex = {};
   For[kk = 1, kk ≤ Length[allcinq[[wq]]], kk ++, {
     matcinq =
      {{(G0 (allcinq[[wq, kk, 3]] - Ntr) - γp) + k Sqrt[(10^(allcinq[[wq,kk,1]]/10) S0a)/allcinq[[wq,kk,4]]] Cos[allcinq[[wq, kk, 5]]]   -2 k Sqrt[10^(allcinq[[wq,kk,1]]/10) S0a allcinq[[wq,
        k/(2 allcinq[[wq,kk,4]]) Sqrt[(10^(allcinq[[wq,kk,1]]/10) S0a)/allcinq[[wq,kk,4]]] Sin[allcinq[[wq, kk, 5]]]   -k Sqrt[(10^(allcinq[[wq,kk,1]]/10) S0a)/allcinq[[wq,kk,4]]] Cos
        G0 (Ntr - allcinq[[wq, kk, 3]])   0}};
     mateigs = Eigenvalues[matcinq];
     If[Re[mateigs[[1]]] < 0 && Re[mateigs[[2]]] < 0 && Re[mateigs[[3]]] < 0, AppendTo[stabilityindex, kk], Null]}];
   thisstabN = Map[{allcinq[[wq, #, 2]], allcinq[[wq, #, 3]]} &, stabilityindex];
   AppendTo[stabNdata, {allcinq[[wq, 1, 1]], thisstabN}];
   thisstabS = Map[{allcinq[[wq, #, 2]], allcinq[[wq, #, 4]]} &, stabilityindex];
   AppendTo[stabSdata, {allcinq[[wq, 1, 1]], thisstabS}];
   thisstabϕ = Map[{allcinq[[wq, #, 2]], allcinq[[wq, #, 5]]} &, stabilityindex];
   AppendTo[stabϕdata, {allcinq[[wq, 1, 1]], thisstabϕ}],
   AppendTo[stabilityRAT, {allcinq[[wq, 1, 1]], stabilityindex}], PrintTemporary[allcinq[[wq, 1, 1]]]}]]
```

■ **Analytically calculated stable phase limits**

```
(*Determine which injection ratios have two sections of locking - around hopf SN interface*)
splitRATs = {};
For[rt = 1, rt ≤ Length[stabilityRAT], rt ++, {
   parttemp = {};
   For[i = 1, i ≤ Length[stabilityRAT[[rt, 2]]] - 1, i ++, {If[stabilityRAT[[rt, 2, i]] + 1 == stabilityRAT[[rt, 2, i + 1]],
      AppendTo[parttemp, {i, 0}], AppendTo[parttemp, {i, 1}]]}], If[Length[Position[Transpose[parttemp][[2]], 1]] == 1,
    AppendTo[splitRATs, {stabilityRAT[[rt, 1]], 1, Position[Transpose[parttemp][[2]], 1][[1, 1]]}],
    AppendTo[splitRATs, {stabilityRAT[[rt, 1]], 0}]]}];

phaseneglimits = {};
phaseposlimits = {};
For[temp = 1, temp ≤ Length[stabϕdata], temp ++, {
  If[splitRATs[[temp, 2]] == 0, AppendTo[phaseneglimits, {stabϕdata[[temp, 1]], Transpose[stabϕdata[[temp, 2]]][[2, 1]]}],
   {AppendTo[phaseneglimits, {stabϕdata[[temp, 1]], Transpose[stabϕdata[[temp, 2]]][[2, 1]]}],
    AppendTo[phaseneglimits, {stabϕdata[[temp, 1]], stabϕdata[[temp, 2, splitRATs[[temp, 3]] + 1, 2]]}]}],
  If[splitRATs[[temp, 2]] == 0, AppendTo[phaseposlimits, {stabϕdata[[temp, 1]], Transpose[stabϕdata[[temp, 2]]][[2, -1]]}],
   {AppendTo[phaseposlimits, {stabϕdata[[temp, 1]], Transpose[stabϕdata[[temp, 2]]][[2, -1]]}],
    AppendTo[phaseposlimits, {stabϕdata[[temp, 1]], stabϕdata[[temp, 2, splitRATs[[temp, 3]], 2]]}]}]}]
```

■ **Analytically calculated stable detuning limits**

```
omeganeglimits = {};
omegaposlimits = {};
For[temp = 1, temp ≤ Length[stabϕdata], temp ++, {
  If[splitRATs[[temp, 2]] == 0, AppendTo[omegaposlimits, {stabϕdata[[temp, 1]], Transpose[stabϕdata[[temp, 2]]][[1, 1]]}],
   {AppendTo[omegaposlimits, {stabϕdata[[temp, 1]], Transpose[stabϕdata[[temp, 2]]][[1, 1]]}],
    AppendTo[omegaposlimits, {stabϕdata[[temp, 1]], stabϕdata[[temp, 2, splitRATs[[temp, 3]] + 1, 1]]}]}],
  If[splitRATs[[temp, 2]] == 0, AppendTo[omeganeglimits, {stabϕdata[[temp, 1]], Transpose[stabϕdata[[temp, 2]]][[1, -1]]}],
   {AppendTo[omeganeglimits, {stabϕdata[[temp, 1]], Transpose[stabϕdata[[temp, 2]]][[1, -1]]}],
    AppendTo[omeganeglimits, {stabϕdata[[temp, 1]], stabϕdata[[temp, 2, splitRATs[[temp, 3]], 1]]}]}]}]
```

■ **Extracting frequency response parameters**

```
Timing[wqind = Range[Length[allcinq]];
 (*allpolesRAT={};*)
 realpolesRAT = {}; dampsRAT = {}; realtripsRAT = {}; resfreqsRAT = {};
 {wq = #;
    realpolesind = {}; dampsind = {}; resfreqsind = {}; realtripsind = {};
    stabind = Range[Position[Transpose[allcinq[[wq]]][[5]], stabϕdata[[wq, 2, 1, 2]]][[1, 1]],
      Position[Transpose[allcinq[[wq]]][[5]], stabϕdata[[wq, 2, -1, 2]]][[1, 1]]];
    { kk = #;
       newmat =
          ( iω - G0 (allcinq[[wq, kk, 3]] - Ntr) + γp - k Sqrt[10^(allcinq[[wq,kk,1]]/10) S0a / allcinq[[wq,kk,4]]] Cos[allcinq[[wq, kk, 5]]]   2 k Sqrt[10^(allcinq[[wq,kk,1]]/10) S0a allcinq
                -k / (2 allcinq[[wq,kk,4]]) Sqrt[10^(allcinq[[wq,kk,1]]/10) S0a / allcinq[[wq,kk,4]]] Sin[allcinq[[wq, kk, 5]]]                                iω + k Sqrt[10^(allcinq[[wq,kk,1]]/10) S
                                G0 (allcinq[[wq, kk, 3]] - Ntr)
          );
       matdetsol = Solve[Det[newmat] == 0];

       sola = matdetsol[[1, 1, 2]] i; solb = matdetsol[[2, 1, 2]] i; solc = matdetsol[[3, 1, 2]] i;
       reals = Select[{sola, solb, solc}, Im[#] == 0 &];
       comps = Select[{sola, solb, solc}, Im[#] ≠ 0 &];

       realpole = Abs[reals[[1]]]; damp = 2 Abs[Re[comps[[1]]]]; resfreq = Abs[Im[comps[[1]]]];

       If[Length[reals] == 3, AppendTo[realtripsind, {{allcinq[[wq, kk, 1]], allcinq[[wq, kk, 2]], 2 Abs[reals[[2]]]},
          {allcinq[[wq, kk, 1]], allcinq[[wq, kk, 2]], 2 Abs[reals[[3]]]}}], Null];

       AppendTo[realpolesind, {allcinq[[wq, kk, 1]], allcinq[[wq, kk, 2]], realpole}];
       AppendTo[dampsind, {allcinq[[wq, kk, 1]], allcinq[[wq, kk, 2]], damp}];
       AppendTo[resfreqsind, {allcinq[[wq, kk, 1]], allcinq[[wq, kk, 2]], resfreq}];
     } & /@ stabind;

   AppendTo[realpolesRAT, realpolesind]; AppendTo[dampsRAT, dampsind];
   AppendTo[resfreqsRAT, resfreqsind]; AppendTo[realtripsRAT, realtripsind]} & /@ wqind;]
```

Appendix C

Bifurcations

The two bifurcations of most interest to this work are the Hopf bifurcation (HB) and the Saddle-Node bifurcation (SN). These bifurcations are methods by which the stability of a fixed point and of an oscillation can discretely change as a parameter of the system undergoes a small continuous change.

C.1 Hopf bifurcation

A Hopf bifurcation typically occurs when a conjugate pair of eigenvalues of the Jacobian matrix eq. (A.35) for a fixed point cross the real axis and become purely imaginary. The fixed point now becomes an unstable rather than stable focus so that nearby orbits are no longer attractive but rather tend away from the point. As this bifurcation is a local one, orbits far away from the bifurcation might still be tending towards to the origin of the Hopf bifurcation. A stable periodic orbit will be created where the local and far orbits interact. Initially, the stable orbit will be small in amplitude but, in general, as the bifurcation parameter is varied away from the bifurcation value, the size of the orbit will increase. The Hopf bifurcation is illustrated using the model for a Van der Pol oscillator where varying the bifurcation parameter μ from -0.5 to $+0.5$ results in a stable fixed point losing stability and the birth of a stable limit cycle:

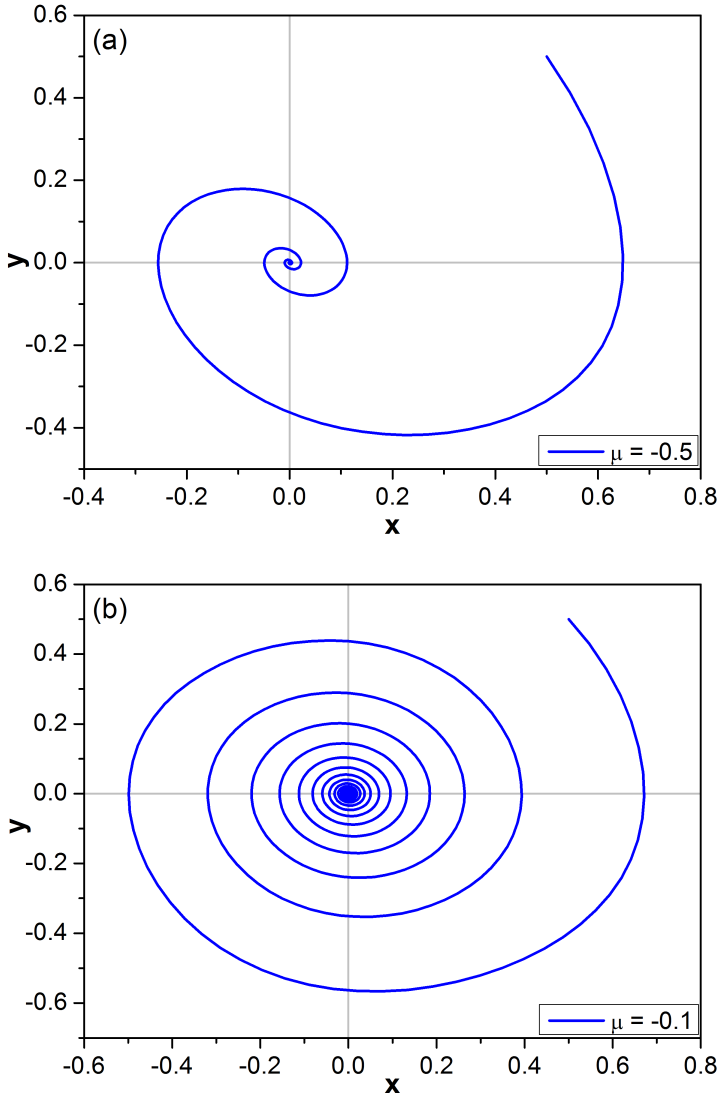

Figure C.1: Demonstration of a Hopf bifurcation using the Van Der Pol oscillator model. (a) At $\mu = -0.5$ a strongly attractive fixed point exists. (b) Increasing μ to $\mu = -0.1$ shows that the fixed point becoming less attractive.

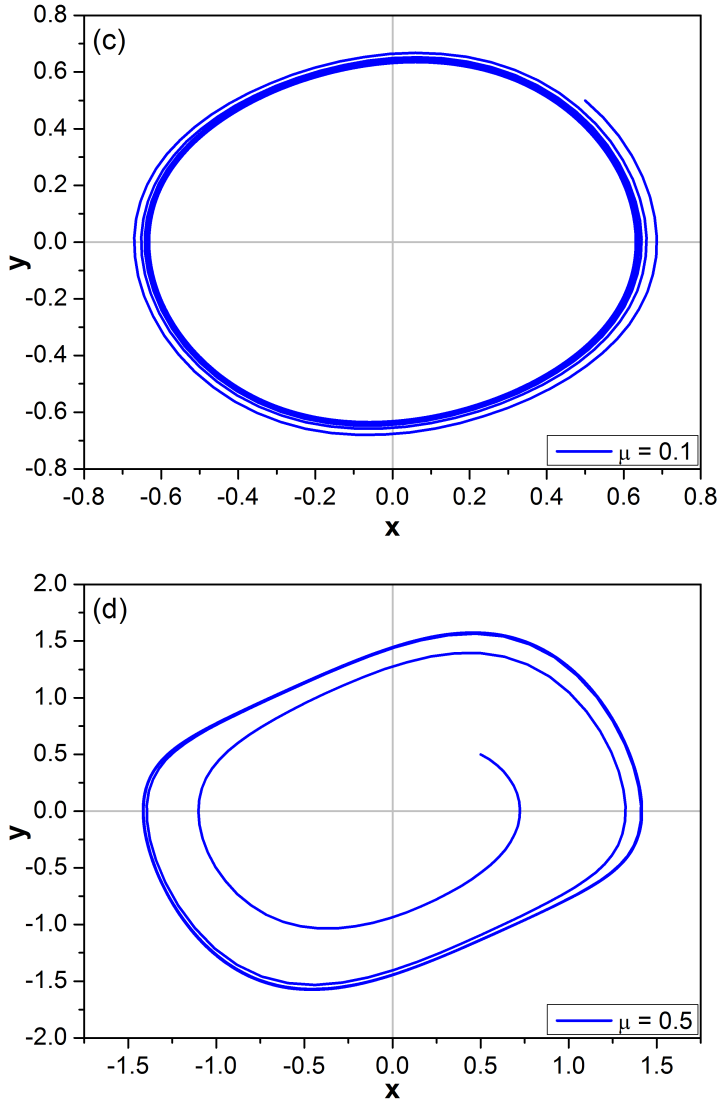

Figure C.1: Demonstration of a Hopf bifurcation using the Van Der Pol oscillator model. A Hopf bifurcation occurs at $\mu = 0$ where the fixed point loses stability and a stable limit cycle is born and the limit cycle grows larger at (c) $\mu = 0.1$ and (d) $\mu = 0.5$.

$$\dot{x} = \mu(x - \frac{1}{3}x^3 - y) \tag{C.1}$$

$$\dot{y} = \frac{1}{\mu}x \tag{C.2}$$

The mechanism of the Hopf is depicted in fig. C.1. At $\mu = -0.5$ a strongly attractive fixed point exists (a) which becomes less attractive as μ is increased to $\mu = -0.1$, (b). This is shown by the trajectory taking longer to reach the fixed point from the same initial condition. A Hopf bifurcation occurs at $\mu = 0$ where the fixed point loses stability and a stable limit cycle is born. With $\mu = 0.1$ the limit cycle is circular in shape and the orbit spirals into it to become a period orbit, (c). Finally, with $\mu = 0.5$, the orbit has grown so that it is further from the origin of the Hopf bifurcation and the trajectory now must spiral outwards to reach the periodic orbit, (d).

C.2 Saddle-Node

Whereas the Hopf bifurcation relates to the change of stability of a fixed point and the birth of a limit cycle, a Saddle-Node relates to the creation or destruction of two fixed points. In the creation process, the fixed points appear suddenly and without arising from another feature in the system. One of the fixed points will be stable, the other unstable. The Saddle-Node bifurcation is illustrated using the one dimensional normal form:

$$x' = r - x^2 \tag{C.3}$$

where the bifurcation parameter is r. For values of $r < 0$, no fixed points exist for the system. This is shown in fig. C.2 (a) where x' is plotted as a function of x for r between -1 and 2. A fixed point exists when the curve cuts the y-axis (red dots) but does not occur for $r < 0$. At $r = 0$, a single fixed point appears at $x = 0$. This is the Saddle-Node bifurcation where two fixed points appear suddenly on the variation of a parameter, both of which are at $x = 0$ here. With increasing r the two fixed points ($= \pm\sqrt{r}$) diverge. The fixed

points at negative x are unstable while those at positive x are stable. This is better represented in the bifurcation diagram, fig. C.2 (b), which shows the fixed points appearing at $r = 0$ and diverging with increasing r. The Saddle-Node bifurcation can also occur in reverse where a stable and unstable fixed point collide and annihilate each other. Under very weak injection, the stable locking region of the optically injected system eqs. (1.1) to (1.3) is bounded at positive and negative frequency detuning by Saddle-Node bifurcations.

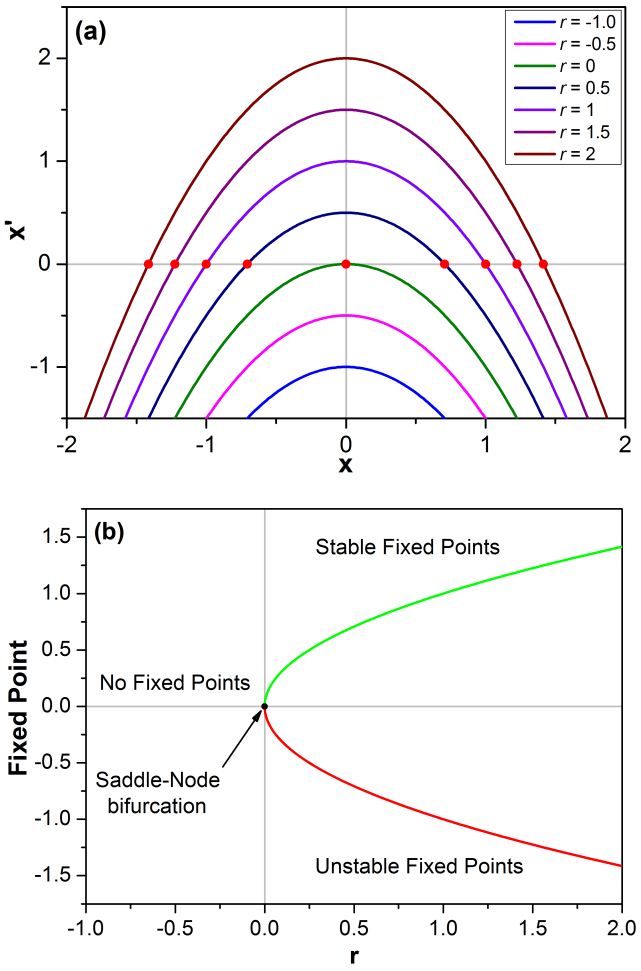

Figure C.2: A Saddle-Node bifurcation showing the sudden appearance of two fixed points, one stable and one unstable. These are created as the curve crosses the x-axis with increasing bifurcation parameter r. These are indicated by the red dots and don't exist for $r < 2.31$. In reverse, the Saddle-Node bifurcation results in the annihilation and disappearance of the two fixed points.

Appendix D

Effects of optical feedback

The sensitivity of semiconductor lasers to optical back reflections is examined through the lineshape of the VCSELs described in chapter 1 as a function of the position of a lensed fibre. Even though the fibre has been designed specifically for these VCSELs and includes an anti-reflection coating, non-optimal positioning of the fibre results in severe output distortion.

The lineshapes recorded here were measured using a dynamic linewidth characterization method based on an optical quadrature front end [159]. These experiments were done with Mr. Tam N. Huynh at the Radio and Optical Communication Laboratory under the supervision of Prof. Liam Barry at the Rince Institute, Dublin City University, Ireland.

First, the VCSEL lineshapes at various bias currents from below to above lasing threshold wee observed with no detrimental effects due to feedback, fig. D.1. The measured lineshapes are smooth and change in a continuous manner. Threshold current is approx 6.5 mA above which the peak increases in intensity and reduces in width. Relaxation oscillation side bands are seen.

Next, at a bias current of 8 mA, the position of the fibre is adjusted to achieve maximum destruction of the lineshape, fig. D.2 (a) where features related to the presence of extended cavity effects are observed. From there, slight adjustments to the fibre reduce the distortion (b), (c) and (d) before the eventual recovery of the expected lineshape, (e). A total fibre movement of just a few microns highlights the importance of fibre positioning.

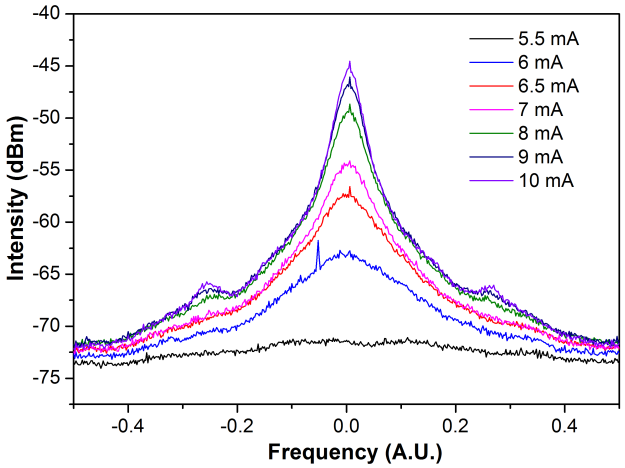

Figure D.1: The lineshape of the VCSEL as a function of bias current. Threshold current is approx 6.5 mA above which the peak increases in intensity and reduces in width. Relaxation oscillation side bands are observed.

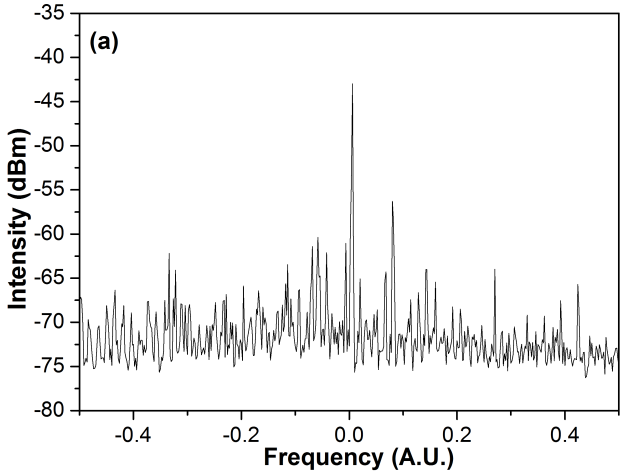

Figure D.2: The position of an optical fibre over a VCSEL aperture can distort the optical spectrum through back reflections and extended cavity effects. As the fibre is moved from (a) a position of maximum distortion to (e) an optimum position with no feedback, the expected lineshape is recovered. The total fibre movement is just a few microns.

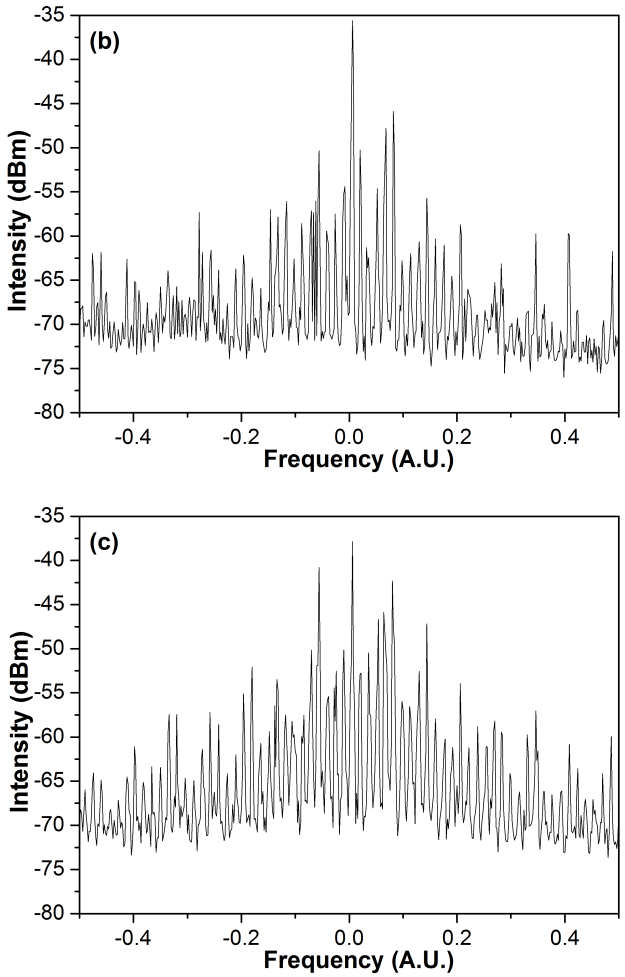

Figure D.2: The position of an optical fibre over a VCSEL aperture can distort the optical spectrum through back reflections and extended cavity effects. As the fibre is moved from (a) a position of maximum distortion to (e) an optimum position with no feedback, the expected lineshape is recovered. The total fibre movement is just a few microns.

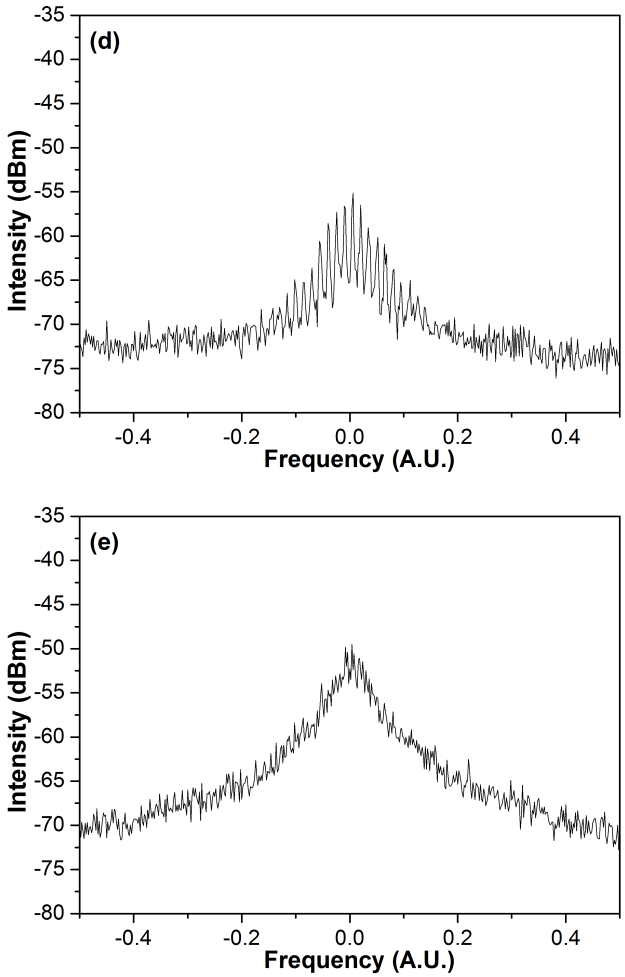

Figure D.2: The position of an optical fibre over a VCSEL aperture can distort the optical spectrum through back reflections and extended cavity effects. As the fibre is moved from (a) a position of maximum distortion to (e) an optimum position with no feedback, the expected lineshape is recovered. The total fibre movement is just a few microns.

Bibliography

[1] C. Degen, W. Elsaber, and I. Fischer, "Transverse modes in oxide confined vcsels: Influence of pump profile, spatial hole burning and thermal effects," *Optics Express*, vol. 5, no. 3, pp. 38–47, 1999.

[2] M. A. Bandres, J. C. Gutiérrez-Vega, *et al.*, "Ince-Gaussian modes of the paraxial wave equation and stable resonators," *Optical Society of America A, Journal of*, vol. 21, no. 5, pp. 873–880, 2004.

[3] M. Müller, W. Hofmann, G. Bohm, and M.-C. Amann, "Short-Cavity Long-Wavelength VCSELs With Modulation Bandwidths in Excess of 15 GHz," *Photonics Technology Letters, IEEE*, vol. 21, pp. 1615–1617, Nov 2009.

[4] N. M. Al-Hosiny, I. Henning, and M. Adams, "Correlation of electron density changes with optical frequency shifts in optically injected semiconductor lasers," *Quantum Electronics, IEEE Journal of*, vol. 42, no. 6, pp. 570–580, 2006.

[5] R. Al-Seyab, K. Schires, N. Khan, A. Hurtado, I. Henning, and M. Adams, "Dynamics of Polarized Optical Injection in 1550 nm VCSELs: Theory and Experiments," *Selected Topics in Quantum Electronics, IEEE Journal of*, vol. 17, no. 5, pp. 1242–1249, 2011.

[6] E. Lau, L. J. Wong, and M. Wu, "Enhanced modulation characteristics of optical injection-locked lasers: A tutorial," *Selected Topics in Quantum Electronics, IEEE Journal of*, vol. 15, no. 3, pp. 618–633, 2009.

[7] F. Mogensen, H. Olesen, and G. Jacobsen, "Locking conditions and stability properties for a semiconductor laser with external light injection," *Quantum Electronics, IEEE Journal of*, vol. 21, no. 7, pp. 784–793, 1985.

[8] T. Gruendl, M. Mueller, K. Geiger, C. Grasse, G. Boehm, R. Meyer, and M.-C. Amann, "High-power BCB encapsulated VCSELs based on InP," in *Lasers and Electro-Optics (CLEO), 2011 Conference on*, pp. 1–2, 2011.

[9] T. Gründl, P. Debernardi, M. Muller, C. Grasse, P. Ebert, K. Geiger, M. Ortsiefer, G. Bohm, R. Meyer, and M.-C. Amann, "Record Single-Mode, High-Power VCSELs by Inhibition of Spatial Hole Burning," *Selected Topics in Quantum Electronics, IEEE Journal of*, vol. 19, no. 4, pp. 1700913–1700913, 2013.

[10] J. Liu, *Photonic Devices*. Cambridge University Press, 2005.

[11] M. Raja, S. Brueck, M. Osinski, C. Schaus, J. McInerney, T. Brennan, and B. Hammons, "Resonant periodic gain surface-emitting semiconductor lasers," *Quantum Electronics, IEEE Journal of*, vol. 25, no. 6, pp. 1500–1512, 1989.

[12] M. Ortsiefer, S. Baydar, K. Windhorn, G. Bohm, J. Rosskopf, R. Shau, E. Ronneberg, W. Hofmann, and M.-C. Amann, "2.5 mW single-mode operation of 1.55 μm buried tunnel junction VCSELs," *Photonics Technology Letters, IEEE*, vol. 17, no. 8, pp. 1596–1598, 2005.

[13] M. Muller, W. Hofmann, T. Gründl, M. Horn, P. Wolf, R. Nagel, E. Ronneberg, G. Bohm, D. Bimberg, and M.-C. Amann, "1550 nm High-Speed Short-Cavity VCSELs," *Selected Topics in Quantum Electronics, IEEE Journal of*, vol. 17, no. 5, pp. 1158–1166, 2011.

[14] M.-C. Amann and M. Ortsiefer, "Long-wavelength ($\lambda \geq 1.3$ μm) InGaAlAs/InP vertical-cavity surface-emitting lasers for applications in optical communication and sensing," *physica status solidi (a)*, vol. 203, no. 14, pp. 3538–3544, 2006.

[15] A. Tarraf, F. Riemenschneider, M. Strassner, J. Daleiden, S. Irmer, H. Halbritterort, H. Hillmer, and P. Meissner, "Continuously tunable 1.55 μm VCSEL implemented by precisely curved dielectric top DBR involving tailored stress," *Photonics Technology Letters, IEEE*, vol. 16, no. 3, pp. 720–722, 2004.

[16] M. Maute, B. Kogel, G. Bohm, P. Meissner, and M.-C. Amann, "MEMS-tunable 1.55 μm VCSEL with extended tuning range incorporating a buried tunnel junction," *Photonics Technology Letters, IEEE*, vol. 18, no. 5, pp. 688–690, 2006.

[17] E. Clerkin, S. O'Brien, and A. Amann, "Multi-stabilities and symmetry-broken one-colour and two-colour states in closely coupled single-mode lasers," *ArXiv e-prints*, Aug. 2013.

[18] R. Lang and K. Kobayashi, "External optical feedback effects on semiconductor injection laser properties," *Quantum Electronics, IEEE Journal of*, vol. 16, no. 3, pp. 347–355, 1980.

[19] C. Henry, N. Olsson, and N. Dutta, "Locking range and stability of injection locked 1.54 μm InGaAsP semiconductor lasers," *Quantum Electronics, IEEE Journal of*, vol. 21, pp. 1152–1156, Aug. 1985.

[20] A. Murakami, K. Kawashima, and K. Atsuki, "Cavity resonance shift and bandwidth enhancement in semiconductor lasers with strong light injection," *Quantum Electronics, IEEE Journal of*, vol. 39, no. 10, pp. 1196–1204, 2003.

[21] N. Schunk and K. Petermann, "Noise analysis of injection-locked semiconductor injection lasers," *Quantum Electronics, IEEE Journal of*, vol. 22, no. 5, pp. 642–650, 1986.

[22] L. Chrostowski, *Optical Injection Locking of Vertical Cavity Surface Emitting Lasers*. PhD thesis, University of Caifornia at Berkeley, Berkeley, California, USA, Mar. 2004.

[23] A. Daly, T. Gründl, S. Huber, M. Müller, B. Roycroft, M. Amann, and B. Corbett, "Voltage spectroscopy and the operating state of an optically injected long wavelength VCSEL," *Photonics Technology Letters, IEEE*, vol. 24, pp. 1245–1247, July 2012.

[24] Y. Yu, G. Giuliani, and S. Donati, "Measurement of the linewidth enhancement factor of semiconductor lasers based on the optical feedback self-mixing effect," *Photonics Technology Letters, IEEE*, vol. 16, no. 4, pp. 990–992, 2004.

[25] G. P. Agrawal and R. Roy, "Effect of injection-current fluctuations on the spectral linewidth of semiconductor lasers," *Physical Review A*, vol. 37, no. 7, p. 2495, 1988.

[26] "Wolfram mathematica computatuonal software." http://www.wolfram.com.

[27] Y. A. Kuznetsov, *Elements of applied bifurcation theory*. Springer, 2004.

[28] M. Virte, K. Panajotov, H. Thienpont, and M. Sciamanna, "Deterministic polarization chaos from a laser diode," *Nature Photonics*, 2012.

[29] S. Smolorz, H. Rohde, P. Ossieur, C. Antony, P. Townsend, T. De Ridder, B. Baekelandt, X. Qiu, S. Appathurai, H.-G. Krimmel, D. Smith, and A. Poustie, "Next generation access networks: Pieman and beyond," in *Photonics in Switching, 2009. PS '09. International Conference on*, pp. 1–4, 2009.

[30] P. Ossieur, C. Antony, A. Clarke, A. Naughton, H.-G. Krimmel, Y. Chang, C. Ford, A. Borghesani, D. Moodie, A. Poustie, R. Wyatt, B. Harmon, I. Lealman, G. Maxwell, D. Rogers, D. Smith, D. Nesset, R. Davey, and P. Townsend, "A 135-km 8192-Split Carrier Distributed DWDM-TDMA PON With 2 × 32 × 10 Gb/s Capacity," *Lightwave Technology, Journal of*, vol. 29, no. 4, pp. 463–474, 2011.

[31] J. S. Malhotra, M. Kumar, and A. K. Sharma, "Performance Comparison of PS-QPSK and PM-QPSK Modulation Schemes in High Capacity Long Haul DWDM Optical Communication Link," *International Journal of Engineering*, vol. 2, no. 5, pp. 154–159, 2013.

[32] X. Zhao, E. K. Lau, D. Parekh, H.-K. Sung, W. Hofmann, M. C. Amann, M. C. Wu, and C. J. Chang-Hasnain, "107 GHz Resonance Frequency of 1.55 μm VCSELs under Ultra-High Optical Injection Locking," in *Conference on Lasers and Electro-Optics/Quantum Electronics and Laser Science Conference and Photonic Applications Systems Technologies*, p. CMW4, Optical Society of America, 2008.

[33] K. Iga, "Surface-emitting laser-its birth and generation of new optoelectronics field," *Selected Topics in Quantum Electronics, IEEE Journal of*, vol. 6, no. 6, pp. 1201–1215, 2000.

[34] R. Jager, M. Grabherr, C. Jung, R. Michalzik, G. Reiner, B. Weigl, and K. Ebeling, "57% wallplug efficiency oxide-confined 850 nm wavelength GaAs VCSELs," *Electronics Letters*, vol. 33, no. 4, pp. 330–331, 1997.

[35] T. Tadokoro, H. Okamoto, Y. Kohama, T. Kawakami, and T. Kurokawa, "Room-temperature pulsed operation of a 1.5 μm GaInAsP/InP vertical cavity surface emitting laser," *Electron Devices, IEEE Transactions on*, vol. 39, no. 11, pp. 2651–2652, 1992.

[36] D. I. Babic, K. Streubel, R. Mirin, N. Margalit, J. Bowers, E. L. Hu, D. E. Mars, L. Yang, and K. Carey, "Room-temperature continuous-wave operation of 1.54 μm vertical-cavity lasers," *Photonics Technology Letters, IEEE*, vol. 7, no. 11, pp. 1225–1227, 1995.

[37] J. Boucart, C. Starck, F. Gaborit, A. Plais, N. Bouche, E. Derouin, J. C. Remy, J. Bonnet-Gamard, L. Goldstein, C. Fortin, D. Carpentier, P. Salet, F. Brillouet, and J. Jacquet, "Metamorphic DBR and tunnel-junction injection. A CW RT monolithic long-wavelength VCSEL," *Selected Topics in Quantum Electronics, IEEE Journal of*, vol. 5, no. 3, pp. 520–529, 1999.

[38] M. Ortsiefer, R. Shau, G. Bohm, F. Kohler, and M.-C. Amann, "Low-threshold index-guided 1.5 μm long-wavelength vertical-cavity surface-emitting laser with high efficiency," *Applied Physics Letters*, vol. 76, no. 16, pp. 2179–2181, 2000.

[39] T. Baba, Y. Yogo, K. Suzuki, F. Koyama, and K. Iga, "Near room temperature continuous wave lasing characteristics of GaInAsP/InP surface emitting laser," *Electronics Letters*, vol. 29, no. 10, pp. 913–914, 1993.

[40] G. Hadley, K. Lear, M. Warren, K. Choquette, J. Scott, and S. Corzine, "Comprehensive numerical modeling of vertical-cavity surface-emitting lasers," *Quantum Electronics, IEEE Journal of*, vol. 32, pp. 607–616, Apr 1996.

[41] A. Syrbu, V. Iakovlev, C.-A. Berseth, O. Dehaese, A. Rudra, E. Kapon, J. Jacquet, J. Boucart, C. Stark, F. Gaborit, I. Sagnes, J. C. Harmand, and R. Raj, "30°C CW operation of 1.52 μm InGaAsP/AlGaAs vertical cavity lasers with in situ built-in lateral current confinement by localised fusion," *Electronics Letters*, vol. 34, no. 18, pp. 1744–1745, 1998.

[42] M.-R. Park, O. K. Kwon, W. Han, K.-H. Lee, S.-J. Park, and B.-S. Yoo, "All-epitaxial InAlGaAs-InP VCSELs in the 1.3-1.6 μm wavelength range for CWDM band applications," *Photonics Technology Letters, IEEE*, vol. 18, no. 16, pp. 1717–1719, 2006.

[43] O. Ostinelli, E. Gini, M. Ebnother, G. Almuneau, M. Haiml, R. Grange, U. Keller, and W. Bachtold, "Metalorganic vapor-phase epitaxy of antimonide for application to 1.55 μm VCSELs on InP substrates," in *Indium Phosphide and Related Materials, 2005. International Conference on*, pp. 594–597, 2005.

[44] V. Jayaraman, G. Cole, M. Robertson, C. Burgner, D. John, A. Uddin, and A. Cable, "Rapidly swept, ultra-widely-tunable 1060 nm MEMS-VCSELs," *Electronics Letters*, vol. 48, no. 21, pp. 1331–1333, 2012.

[45] M. Ortsiefer, G. Bohm, M. Grau, K. Windhorn, E. Ronneberg, J. Rosskopf, R. Shau, O. Dier, and M.-C. Amann, "Electrically pumped room temperature CW VCSELs with 2.3 μm emission wavelength," *Electronics Letters*, vol. 42, no. 11, pp. 640–641, 2006.

[46] B. Kogel, H. Halbritter, S. Jatta, M. Maute, G. Bohm, M.-C. Amann, M. Lackner, M. Schwarzott, F. Winter, and P. Meissner, "Simultaneous Spectroscopy of NH_3 and CO Using a 50 nm Continuously Tunable MEMS-VCSEL," *Sensors Journal, IEEE*, vol. 7, no. 11, pp. 1483–1489, 2007.

[47] G. Totschnig, M. Lackner, R. Shau, M. Ortsiefer, J. Rosskopf, M.-C. Amann, and F. Winter, "1.8 μm vertical-cavity surface-emitting laser absorption measurements of HCl, H_2O and CH_4," *Measurement Science and Technology*, vol. 14, no. 4, p. 472, 2003.

[48] C. Lauer, M. Ortsiefer, R. Shau, J. Rosskopf, G. Bohm, M. Maute, E. Kohler, and M.-C. Amann, "Electrically pumped room temperature CW-VCSELs with emission wavelength of 2 μm," *Electronics Letters*, vol. 39, no. 1, pp. 57–58, 2003.

[49] M. Ortsiefer, R. Shau, F. Mederer, R. Michalzik, J. Rosskopf, G. Bohm, F. Kohler, C. Lauer, M. Maute, and M.-C. Amann, "High-speed modulation up to 10 Gbit/s with 1.55 μm wavelength InGaAlAs VCSELs," *Electronics Letters*, vol. 38, no. 20, pp. 1180–1181, 2002.

[50] W. Hofmann, N. Zhu, M. Ortsiefer, G. Böhm, Y. Liu, and M.-C. Amann, "High speed ($>$ 11 GHz) modulation of BCB-passivated 1.55 μm InGaAlAs-InP VCSELs," *Electronics Letters*, vol. 42, no. 17, pp. 976–978, 2006.

[51] W. Hofmann, M. Müller, A. Nadtochiy, C. Meltzer, A. Mutig, G. Böhm, J. Rosskopf, D. Bimberg, M.-C. Amann, and C. Chang-Hasnain, "22 Gb/s Long Wavelength VCSELs," *Optics Express*, vol. 17, pp. 17547–17554, Sep 2009.

[52] A. Caliman, A. Mereuta, G. Suruceanu, V. Iakovlev, A. Sirbu, and E. Kapon, "8 mW fundamental mode output of wafer-fused VCSELs emitting in the 1550 nm band," *Optics Express*, vol. 19, pp. 16996–17001, Aug 2011.

[53] A. Bachmann, T. Lim, K. Kashani-Shirazi, O. Dier, C. Lauer, and M.-C. Amann, "Electrically Pumped GaSb-Based VCSEL with Buried Tunnel Junction," in *Conference on Lasers and Electro-Optics/Quantum Electronics and Laser Science Conference and Photonic Applications Systems Technologies*, pp. 1,2,4–9, Optical Society of America, 2008.

[54] W. Hofmann, E. Wong, G. Bohm, M. Ortsiefer, N. Zhu, and M.-C. Amann, "1.55 μm VCSEL Arrays for High-Bandwidth WDM-PONs," *Photonics Technology Letters, IEEE*, vol. 20, no. 4, pp. 291–293, 2008.

[55] V. Karagodsky, B. Pesala, C. Chase, W. Hofmann, F. Koyama, and C. J. Chang-Hasnain, "Monolithically integrated multi-wavelength VCSEL arrays using high-contrast gratings," *Optics Express*, vol. 18, pp. 694–699, Jan 2010.

[56] A. Bachmann, K. Kashani-Shirazi, S. Arafin, and M.-C. Amann, "GaSb-Based VCSEL With Buried Tunnel Junction for Emission Around 2.3 μm," *Selected Topics in Quantum Electronics, IEEE Journal of*, vol. 15, no. 3, pp. 933–940, 2009.

[57] C. F. R. Mateus, M. Huang, Y. Deng, A. R. Neureuther, and C. Chang-Hasnain, "Ultrabroadband mirror using low-index cladded subwavelength grating," *Photonics Technology Letters, IEEE*, vol. 16, no. 2, pp. 518–520, 2004.

[58] C. F. R. Mateus, M. C. Y. Huang, L. Chen, C. Chang-Hasnain, and Y. Suzuki, "Broad-band mirror (1.12-1.62 μm) using a subwavelength grating," *Photonics Technology Letters, IEEE*, vol. 16, no. 7, pp. 1676–1678, 2004.

[59] V. Karagodsky, F. G. Sedgwick, and C. J. Chang-Hasnain, "Theoretical analysis of subwavelength high contrast grating reflectors," *Optics Express*, vol. 18, pp. 16973–16988, Aug 2010.

[60] V. Karagodsky and C. J. Chang-Hasnain, "Physics of near-wavelength high contrast gratings," *Optics Express*, vol. 20, pp. 10888–10895, May 2012.

[61] M. C. Huang, Y. Zhou, and C. J. Chang-Hasnain, "A surface-emitting laser incorporating a high-index-contrast subwavelength grating," *Nature Photonics*, vol. 1, no. 2, pp. 119–122, 2007.

[62] W. Hofmann, C. Chase, M. Müller, Y. Rao, C. Grasse, G. Böhm, M.-C. Amann, and C. Chang-Hasnain, "Long-wavelength high-contrast grating vertical-cavity surface-emitting laser," *Photonics Journal, IEEE*, vol. 2, no. 3, pp. 415–422, 2010.

[63] C. Chase, Y. Rao, W. Hofmann, and C. J. Chang-Hasnain, "1550 nm high contrast grating VCSEL," *Optics Express*, vol. 18, pp. 15461–15466, Jul 2010.

[64] M. Ortsiefer, M. Gorblich, Y. Xu, E. Ronneberg, J. Rosskopf, R. Shau, and M.-C. Amann, "Polarization Control in Buried Tunnel Junction VCSELs Using a Birefringent Semiconductor/Dielectric Subwavelength Grating," *Photonics Technology Letters, IEEE*, vol. 22, no. 1, pp. 15–17, 2010.

[65] C. Chang-Hasnain, "Tunable VCSEL," *Selected Topics in Quantum Electronics, IEEE Journal of*, vol. 6, no. 6, pp. 978–987, 2000.

[66] M. Wu, E. Vail, G. Li, W. Yuen, and C. Chang-Hasnain, "Tunable micromachined vertical cavity surface emitting laser," *Electronics Letters*, vol. 31, no. 19, pp. 1671–1672, 1995.

[67] M. C. Y. Huang, K. B. Cheng, Y. Zhou, B. Pesala, C. Chang-Hasnain, and A. Pisano, "Demonstration of piezoelectric actuated GaAs-based

MEMS tunable VCSEL," *Photonics Technology Letters, IEEE*, vol. 18, no. 10, pp. 1197–1199, 2006.

[68] F. Riemenschneider, I. Sagnes, G. BÃűhm, H. Halbritter, M. Maute, C. Symonds, M.-C. Amann, and P. Meissner, "A new concept for tunable long wavelength VCSEL," *Optics Communications*, vol. 222, no. 16, pp. 341 – 350, 2003.

[69] S.-S. Yang, J.-K. Son, Y.-K. Hong, Y.-H. Song, H.-J. Jang, J.-W. Yang, and G.-M. Yang, "Polarization-Stable Single-Mode Tunable VCSELs Using an Internal Mesa Heater," *Photonics Technology Letters, IEEE*, vol. 21, no. 11, pp. 748–750, 2009.

[70] K. Zogal, T. Gruendl, C. Gierl, C. Grasse, H. Davani, G. Boehm, P. Meissner, F. Kueppers, and M. C. Amann, "Singlemode 50 nm tunable surface micro-machined MEMS-VCSEL operating at 1.95 μm," in *Lasers and Electro-Optics (CLEO), 2012 Conference on*, pp. 1–2, 2012.

[71] B. Kogel, K. Zogal, S. Jatta, M. Maute, C. Grasse, M.-C. Amann, and P. Meissner, "Small signal dynamics of an electrically-pumped long-wavelength tunable VCSEL," in *Semiconductor Laser Conference, 2008. ISLC 2008. IEEE 21st International*, pp. 85–86, 2008.

[72] S. Jatta, B. Kogel, M. Maute, K. Zogal, F. Riemenschneider, G. Bohm, M.-C. Amann, and P. Meisner, "Bulk-Micromachined VCSEL At 1.55 μm With 76 nm Single-Mode Continuous Tuning Range," *Photonics Technology Letters, IEEE*, vol. 21, no. 24, pp. 1822–1824, 2009.

[73] C. Gierl, T. Gruendl, P. Debernardi, K. Zogal, C. Grasse, H. A. Davani, G. Böhm, S. Jatta, F. Küppers, P. Meißner, and M.-C. Amann, "Surface micromachined tunable 1.55 μm-VCSEL with 102 nm continuous single-mode tuning," *Optics Express*, vol. 19, pp. 17336–17343, Aug 2011.

[74] M. C. Huang, Y. Zhou, and C. J. Chang-Hasnain, "A nanoelectromechanical tunable laser," *Nature Photonics*, vol. 2, no. 3, pp. 180–184, 2008.

[75] T. Gründl, K. Zogal, P. Debernardi, M. Muller, C. Grasse, K. Geiger, R. Meyer, G. Bohm, M.-C. Amann, F. Kuppers, and P. Meissner, "Continuously Tunable, Polarization Stable SWG MEMS VCSELs at 1.55 μm," *Photonics Technology Letters, IEEE*, vol. 25, no. 9, pp. 841–843, 2013.

[76] R. Adler, "A study of locking phenomena in oscillators," *Proceedings of the IRE*, vol. 34, no. 6, pp. 351–357, 1946.

[77] A. L. Schawlow and C. H. Townes, "Infrared and optical masers," *Physical Review*, vol. 112, pp. 1940–1949, Dec 1958.

[78] J. P. Gordon, H. J. Zeiger, and C. H. Townes, "Molecular Microwave Oscillator and New Hyperfine Structure in the Microwave Spectrum of NH_3," *Physical Review*, vol. 95, pp. 282–284, Jul 1954.

[79] T. H. Maiman, "Stimulated optical radiation in ruby," *Nature*, vol. 187, pp. 493–494, 1960.

[80] R. N. Hall, G. E. Fenner, J. D. Kingsley, T. J. Soltys, and R. O. Carlson, "Coherent Light Emission From GaAs Junctions," *Physical Review Letters*, vol. 9, pp. 366–368, Nov 1962.

[81] H. L. Stover and W. H. Steier, "Locking of laser oscillators by light injection," *Applied Physics Letters*, vol. 8, no. 4, pp. 91–93, 1966.

[82] J. Nishizawa and K. Ishida, "Injection-induced modulation of laser light by the interaction of laser diodes," *Quantum Electronics, IEEE Journal of*, vol. 11, no. 7, pp. 515–519, 1975.

[83] C. Henry, "Theory of the linewidth of semiconductor lasers," *Quantum Electronics, IEEE Journal of*, vol. 18, no. 2, pp. 259–264, 1982.

[84] R. Lang, "Injection locking properties of a semiconductor laser," *Quantum Electronics, IEEE Journal of*, vol. 18, no. 6, pp. 976–983, 1982.

[85] C. Henry, "Theory of the phase noise and power spectrum of a single mode injection laser," *Quantum Electronics, IEEE Journal of*, vol. 19, no. 9, pp. 1391–1397, 1983.

[86] C. Lin and F. Mengel, "Reduction of frequency chirping and dynamic linewidth in high-speed directly modulated semiconductor lasers by injection locking," *Electronics Letters*, vol. 20, no. 25, pp. 1073–1075, 1984.

[87] I. Petitbon, P. Gallion, G. Debarge, and C. Chabran, "Locking bandwidth and relaxation oscillations of an injection-locked semiconductor laser," *Quantum Electronics, IEEE Journal of*, vol. 24, no. 2, pp. 148–154, 1988.

[88] R. Hui, A. Mecozzi, A. D'Ottavi, and P. Spano, "Novel measurement technique of alpha factor in DFB semiconductor lasers by injection locking," *Electronics Letters*, vol. 26, no. 14, pp. 997–998, 1990.

[89] H. Li, T. Lucas, J. G. McInerney, M. Wright, and R. Morgan, "Injection locking dynamics of vertical cavity semiconductor lasers under conventional and phase conjugate injection," *Quantum Electronics, IEEE Journal of*, vol. 32, no. 2, pp. 227–235, 1996.

[90] Z. G. Pan, S. Jiang, M. Dagenais, R. Morgan, K. Kojima, M. Asom, R. Leibenguth, G. Guth, and M. Focht, "Optical injection induced polarization bistability in vertical cavity surface emitting lasers," *Applied Physics Letters*, vol. 63, no. 22, pp. 2999–3001, 1993.

[91] S. Wieczorek, B. Krauskopf, T. Simpson, and D. Lenstra, "The dynamical complexity of optically injected semiconductor lasers," *Physics Reports*, vol. 416, no. 12, pp. 1 – 128, 2005.

[92] S. Wieczorek, T. B. Simpson, B. Krauskopf, and D. Lenstra, "Bifurcation transitions in an optically injected diode laser: theory and experiment," *Optics Communications*, vol. 215, no. 13, pp. 125 – 134, 2003.

[93] T. B. Simpson, J. M. Liu, A. Gavrielides, V. Kovanis, and P. M. Alsing, "Period-doubling cascades and chaos in a semiconductor laser with optical injection," *Physical Review A*, vol. 51, pp. 4181–4185, May 1995.

[94] S. Osborne, P. Heinricht, N. Brandonisio, A. Amann, and S. O'Brien, "Wavelength switching dynamics of two-colour semiconductor lasers with optical injection and feedback," *Semiconductor Science and Technology*, vol. 27, no. 9, p. 094001, 2012.

[95] M. C. Soriano, J. Garcia-Ojalvo, C. R. Mirasso, and I. Fischer, "Complex photonics: Dynamics and applications of delay-coupled semiconductors lasers," *Review of Modern Physics*, vol. 85, pp. 421–470, Mar 2013.

[96] H. Kasuya, M. Mori, R. Goto, T. Goto, and K. Yamane, "All optical mode locking of Fabry-Perot laser diode via mutual injection locking between two longitudinal modes," *Applied Physics Letters*, vol. 75, no. 1, pp. 13–15, 1999.

[97] K. Shi, F. Smyth, D. Reid, B. Roycroft, B. Corbett, F. H. Peters, and L. P. Barry, "Characterization of a tunable three-section slotted Fabry-Perot laser for advanced modulation format optical transmission," *Optics Communications*, vol. 284, pp. 1616–1621, Mar. 2011.

[98] X. Zhao, M. Moewe, L. Chrostowski, C.-H. Chang, R. Shau, M. Ortsiefer, M.-C. Amann, and C. Chang-Hasnain, "28 GHz optical injection-locked 1.55 μm VCSELs," *Electronics Letters*, vol. 40, no. 8, pp. 476–478, 2004.

[99] L. Chrostowski, X. Zhao, C. Chang-Hasnain, R. Shau, M. Ortsiefer, and M.-C. Amann, "50 GHz directly-modulated injection-locked 1.55 μm VCSELs," in *Optical Fiber Communication Conference, 2005. Technical Digest. OFC/NFOEC*, vol. 4, pp. 3 pp. Vol. 4–, 2005.

[100] J.-M. Liu and T. B. Simpson, "Four-wave mixing and optical modulation in a semiconductor laser," *Quantum Electronics, IEEE Journal of*, vol. 30, no. 4, pp. 957–965, 1994.

[101] S.-K. Hwang, S.-C. Chan, S.-C. Hsieh, and C.-Y. Li, "Photonic microwave generation and transmission using direct modulation of stably injection-locked semiconductor lasers," *Optics Communications*, vol. 284, no. 14, pp. 3581 – 3589, 2011.

[102] L. Chrostowski, C.-H. Chang, and C. Chang-Hasnain, "Reduction of relative intensity noise and improvement of spur-free dynamic range of an injection locked VCSEL," in *Lasers and Electro-Optics Society, 2003. LEOS 2003. The 16th Annual Meeting of the IEEE*, vol. 2, pp. 706–707 vol.2, 2003.

[103] S. Hwang and J. M. Tian, "Chirp reduction in directly-modulated semiconductor lasers subject to external optical injection," in *Lasers and Electro-Optics Society, 2005. LEOS 2005. The 18th Annual Meeting of the IEEE*, pp. 798–799, 2005.

[104] A. Hayat, A. Bacou, A. Rissons, and J.-C. Mollier, "Optical Injection-Locking of VCSELs," *Book Chapter: Advances in Optical and Photonic Devices, In—Tech*, 2010.

[105] M. San Miguel, Q. Feng, and J. V. Moloney, "Light-polarization dynamics in surface-emitting semiconductor lasers," *Physical Review A*, vol. 52, pp. 1728–1739, Aug 1995.

[106] J. Martin-Regalado, F. Prati, M. San Miguel, and N. B. Abraham, "Polarization properties of vertical-cavity surface-emitting lasers," *Quantum Electronics, IEEE Journal of*, vol. 33, no. 5, pp. 765–783, 1997.

[107] M. Sciamanna and K. Panajotov, "Two-mode injection locking in vertical-cavity surface-emitting lasers," *Optics Letters*, vol. 30, pp. 2903–2905, Nov 2005.

[108] J. Altes, I. Gatare, K. Panajotov, H. Thienpont, and M. Sciamanna, "Mapping of the dynamics induced by orthogonal optical injection in vertical-cavity surface-emitting lasers," *Quantum Electronics, IEEE Journal of*, vol. 42, no. 2, pp. 198–207, 2006.

[109] I. Gatare, M. Sciamanna, J. Buesa, H. Thienpont, and K. Panajotov, "Nonlinear dynamics accompanying polarization switching in vertical-cavity surface-emitting lasers with orthogonal optical injection," *Applied Physics Letters*, vol. 88, no. 101106, 2006.

[110] M. Sciamanna and K. Panajotov, "Route to polarization switching induced by optical injection in vertical-cavity surface-emitting lasers," *Physical Review A*, vol. 73, p. 023811, Feb 2006.

[111] A. Hurtado, I. Henning, and M. Adams, "Two-Wavelength Switching With a 1550 nm VCSEL Under Single Orthogonal Optical Injection," *Selected Topics in Quantum Electronics, IEEE Journal of*, vol. 14, no. 3, pp. 911–917, 2008.

[112] A. Hurtado, D. Labukhin, I. Henning, and M. Adams, "Injection Locking Bandwidth in 1550 nm VCSELs Subject to Parallel and Orthogonal Optical Injection," *Selected Topics in Quantum Electronics, IEEE Journal of*, vol. 15, no. 3, pp. 585–593, 2009.

[113] A. Hurtado, I. Henning, and M. Adams, "Wavelength Polarization Switching and Bistability in a 1550 nm VCSEL Subject to Polarized Optical Injection," *Photonics Technology Letters, IEEE*, vol. 21, no. 15, pp. 1084–1086, 2009.

[114] R. Al-Seyab, K. Schires, A. Hurtado, I. Henning, and M. Adams, "Dynamics of VCSELs Subject to Optical Injection of Arbitrary Polarization," *Selected Topics in Quantum Electronics, IEEE Journal of*, vol. 19, no. 4, pp. 1700512–1700512, 2013.

[115] M. van Exter and J. Woerdman, "Determination of alpha factor of Fabry-Perot-type semiconductor laser by injection locking," *Electronics Letters*, vol. 28, no. 17, pp. 1607–1608, 1992.

[116] M. van Exter, C. Biever, and J. P. Woerdman, "Effect of optical injection on bias voltage and spectrum of a semiconductor laser," *Quantum Electronics, IEEE Journal of*, vol. 29, no. 11, pp. 2771–2779, 1993.

[117] G. van Tartwijk, G. Muijres, D. Lenstra, M. van Exter, and J. Woerdman, "The semiconductor laser beyond the locking range of optical injection," *Electronics Letters*, vol. 29, no. 2, pp. 137–138, 1993.

[118] R. Hui, S. Benedetto, and I. Montrosset, "Near threshold operation of semiconductor lasers and resonant-type laser amplifiers," *Quantum Electronics, IEEE Journal of*, vol. 29, no. 6, pp. 1488–1497, 1993.

[119] A. Gavrielides, V. Kovanis, and T. Erneux, "Analytical stability boundaries for a semiconductor laser subject to optical injection," *Optics Communications*, vol. 136, no. 34, pp. 253 – 256, 1997.

[120] G. Liu, X. Jin, and S. L. Chuang, "Measurement of linewidth enhancement factor of semiconductor lasers using an injection-locking technique," *Photonics Technology Letters, IEEE*, vol. 13, no. 5, pp. 430–432, 2001.

[121] W. Hofmann, L. Gruner-Nielsen, E. Ronneberg, G. Bohm, M. Ortsiefer, and M.-C. Amann, "1.55 μm VCSEL Modulation Performance With Dispersion-Compensating Fibers," *Photonics Technology Letters, IEEE*, vol. 21, no. 15, pp. 1072–1074, 2009.

[122] W. Hofmann and M.-C. Amann, "Long-wavelength vertical-cavity surface-emitting lasers for high-speed applications and gas sensing," *IET Optoelectronics*, vol. 2, no. 3, pp. 134–142, 2008.

[123] L. Xu, W. Hofmann, H. Tsang, R. Penty, I. White, and M.-C. Amann, "1.55 μm VCSEL transmission performance up to 20 Gb/s for access networks," in *OptoElectronics and Communications Conference, 2009. OECC 2009. 14th*, pp. 1–2, 2009.

[124] A. Gatto, A. Boletti, P. Boffi, C. Neumeyr, M. Ortsiefer, E. Ronneberg, and M. Martinelli, "1.3 μm VCSEL Transmission Performance up to 12.5 Gb/s for Metro Access Networks," *Photonics Technology Letters, IEEE*, vol. 21, no. 12, pp. 778–780, 2009.

[125] K. Prince, M. Ma, T. Gibbon, C. Neumeyr, E. Ronneberg, M. Ortsiefer, and I. Monroy, "Free-Running 1550 nm VCSEL for 10.7 Gb/s Transmission in 99.7 km PON," *Optical Communications and Networking, IEEE/OSA Journal of*, vol. 3, no. 5, pp. 399–403, 2011.

[126] T. Gibbon, K. Prince, T. Pham, A. Tatarczak, C. Neumeyr, E. Rönneberg, M. Ortsiefer, and I. T. Monroy, "VCSEL transmission at 10 Gb/s for 20 km single mode fiber WDM-PON without dispersion compensation or injection locking," *Optical Fiber Technology*, vol. 17, no. 1, pp. 41 – 45, 2011.

[127] N. Nishiyama, C. Caneau, J. Downie, M. Sauer, and C.-E. Zah, "10 Gbps 1.3 and 1.55 μm InP-based VCSELs: 85C 10-km Error-free Transmission and Room Temperature 40 km Transmission at 1.55 μm with EDC," in *Optical Fiber Communication Conference, 2006 and the 2006 National Fiber Optic Engineers Conference. OFC 2006*, pp. 1–3, 2006.

[128] J. J. Kim, K.-H. Kim, M.-H. Lee, H. S. Lee, E.-H. Lee, O.-K. Kwon, J. Roh, and B.-S. Yoo, "2.5 Gb/s Hybrid Single-Mode and Multimode Fiber Transmission of 1.5 μm Wavelength VCSEL," *Photonics Technology Letters, IEEE*, vol. 19, no. 5, pp. 297–299, 2007.

[129] C.-H. Chang, L. Chrostowski, C. Chang-Hasnain, and W. Chow, "Study of long-wavelength VCSEL-VCSEL injection locking for 2.5 Gb/s transmission," *Photonics Technology Letters, IEEE*, vol. 14, no. 11, pp. 1635–1637, 2002.

[130] E. Wong, X. Zhao, C. Chang-Hasnain, W. Hofmann, and M.-C. Amann, "Optically Injection-Locked 1.55 μm VCSELs as Upstream Transmitters in WDM-PONs," *Photonics Technology Letters, IEEE*, vol. 18, no. 22, pp. 2371–2373, 2006.

[131] Q. Gu, W. Hofmann, M.-C. Amann, and L. Chrostowski, "Optically injection-locked VCSEL for bi-directional optical communication," in *Lasers and Electro-Optics, 2008 and 2008 Conference on Quantum*

Electronics and Laser Science. CLEO/QELS 2008. Conference on, pp. 1–2, 2008.

[132] A. Gatto, A. Boletti, P. Boffi, and M. Martinelli, "Adjustable-chirp VCSEL-to-VCSEL injection locking for 10 Gb/s transmission at 1.55 μm," *Optics Express*, vol. 17, pp. 21748–21753, Nov 2009.

[133] A. Ng'Oma, D. Fortusini, D. Parekh, W. Yang, M. Sauer, S. Benjamin, W. Hofmann, M.-C. Amann, and C. Chang-Hasnain, "Performance of a Multi Gb/s 60 GHz Radio Over Fiber System Employing a Directly Modulated Optically Injection-Locked VCSEL," *Lightwave Technology, Journal of*, vol. 28, no. 16, pp. 2436–2444, 2010.

[134] C. Xie, P. Dong, P. Winzer, C. Gréus, M. Ortsiefer, C. Neumeyr, S. Spiga, M. Müller, and M.-C. Amann, "960 km SSMF transmission of 105.7 Gb/s PDM 3-PAM using directly modulated VCSELs and coherent detection," *Optics Express*, vol. 21, pp. 11585–11589, May 2013.

[135] W. Cotter, P. Morrissey, D. Goulding, B. Roycroft, Y. Hua, J. O'Callaghan, B. Corbett, and F. Peters, "Coherent comb generation using integrated slotted Fabry-Perot semiconductor lasers," in *Photonics Conference (IPC), 2012 IEEE*, pp. 848–849, 2012.

[136] A. Daly, B. Roycroft, and B. Corbett, "Stable locking phase limits of optically injected semiconductor lasers," *Optics Express*, vol. 21, pp. 30126–30139, Dec 2013.

[137] X. Zhao and C. J. Chang-Hasnain, "A new amplifier model for resonance enhancement of optically injection-locked lasers," *Photonics Technology Letters, IEEE*, vol. 20, pp. 395–397, Mar. 2008.

[138] L. A. Coldren and S. W. Corzine, *Diode Lasers and Photonic Integrated Circuits*. John Wiley & Sons, Inc., Mar. 1995.

[139] T. B. Simpson, J. Liu, and A. Gavrielides, "Small-signal analysis of modulation characteristics in a semiconductor laser subject to strong

optical injection," *Quantum Electronics, IEEE Journal of*, vol. 32, no. 8, pp. 1456–1468, 1996.

[140] E. J. Doedel, A. R. Champneys, T. Fairgrieve, Y. Kuznetsov, B. Oldeman, R. Paffenroth, B. Sandstede, X. Wang, and C. Zhang, "Auto-07p: Continuation and bifurcation software for ordinary differential equations," tech. rep., Concordia University, Montreal, 2007.

[141] S. Wieczorek, W. Chow, L. Chrostowski, and C. Chang-Hasnain, "Improved semiconductor-laser dynamics from induced population pulsation," *Quantum Electronics, IEEE Journal of*, vol. 42, pp. 552–562, June 2006.

[142] Z. Jiao, Z. Lu, J. Liu, P. Poole, P. Barrios, D. Poitras, G. Pakulski, J. Caballero, and X. Zhang, "Linewidth enhancement factor of InAs/InP quantum dot lasers around 1.5 μm," *Optics Communications*, vol. 285, no. 21-22, pp. 4372–4375, 2012.

[143] K. Iiyama, K. ichi Hayashi, and Y. Ida, "Simple method for measuring the linewidth enhancement factor of semiconductor lasers by optical injection locking," *Optics Letters*, vol. 17, pp. 1128–1130, Aug 1992.

[144] P. Guo, W. Yang, D. Parekh, A. Xu, Z. Chen, and C. J. Chang-Hasnain, "An ellipse model for cavity mode behavior of optically injection-locked VCSELs," *Optics Express*, vol. 20, pp. 6980–6988, Mar. 2012.

[145] S. Bhooplapur and P. Delfyett, "Characterization of the Phase and Amplitude Modulation of Injection-Locked VCSELs at 1550 nm Using Coherent Optical Demodulation," *Selected Topics in Quantum Electronics, IEEE Journal of*, vol. 19, no. 6, pp. 6–13, 2013.

[146] S. K. Hwang, J. Liu, and J. K. White, "35 GHz intrinsic bandwidth for direct modulation in 1.3 μm semiconductor lasers subject to strong injection locking," *Photonics Technology Letters, IEEE*, vol. 16, no. 4, pp. 972–974, 2004.

[147] I. Gatare, M. Sciamanna, M. Nizette, H. Thienpont, and K. Panajotov, "Excitation of a two-mode limit cycle dynamics on the route to polarization switching in a VCSEL subject orthogonal to optical injection," in *Proc. SPIE*, vol. 6997, pp. 699713–699713–10, 2008.

[148] F. Effenberger, D. Clearly, O. Haran, G. Kramer, R. D. Li, M. Oron, and T. Pfeiffer, "An introduction to PON technologies," *Communications Magazine, IEEE*, vol. 45, no. 3, pp. S17–S25, 2007.

[149] "Vitesse Semiconductor Electronic Dispersion Compensator." https://www.vitesse.com/products/product.php?number=VSC7223.

[150] H. Bulow, F. Buchali, and A. Klekamp, "Electronic dispersion compensation," *Lightwave Technology, Journal of*, vol. 26, no. 1, pp. 158–167, 2008.

[151] "CIP - The Centre for Integrated Photonics." http://www.ciphotonics.com/.

[152] Y. Rao, W. Yang, C. Chase, M. Huang, D. Worland, S. Khaleghi, M. Chitgarha, M. Ziyadi, A. Willner, and C. Chang-Hasnain, "Long-Wavelength VCSEL Using High-Contrast Grating," *Selected Topics in Quantum Electronics, IEEE Journal of*, vol. 19, no. 4, p. 1701311, 2013.

[153] T. Gruendl, R. Nagel, P. Debernardi, K. Geiger, C. Grasse, T. Hager, M. Ortsiefer, J. Rosskopf, G. Boehm, R. Meyer, and M.-C. Amann, "Novel concept for a Monolithically Integrated MEMS VCSEL," in *Compound Semiconductor Week (CSW/IPRM), 2011 and 23rd International Conference on Indium Phosphide and Related Materials*, pp. 1–4, 2011.

[154] A. Filios, R. Gutierrez-Castrejon, I. Tomkos, B. Hallock, R. Vodhanel, A. Coombe, W. Yuen, R. Moreland, B. Garrett, C. Duvall, and C. Chang-Hasnain, "Transmission performance of a 1.5 μm 2.5 Gb/s directly modulated tunable VCSEL," *Photonics Technology Letters, IEEE*, vol. 15, no. 4, pp. 599–601, 2003.

[155] D. Sun, W. Fan, P. Kner, J. Boucart, T. Kageyama, D. Zhang, R. Pathak, R. Nabiev, and W. Yuen, "Long wavelength-tunable VCSELs with optimized MEMS bridge tuning structure," *Photonics Technology Letters, IEEE*, vol. 16, no. 3, pp. 714–716, 2004.

[156] A. Daly, C. Gierl, T. Gründl, C. Grasse, K. Zogal, D. Carey, P. Townsend, M.-C. Amann, P. Meissner, and B. Corbett, "10 Gbit/s transmission over 50 km of SMF using MEMS tunable VCSEL," *Electronics Letters*, vol. 48, no. 7, pp. 394–396, 2012.

[157] L. Colace, G. Masini, and G. Assanto, "Wavelength stabilizer for telecommunication lasers: design and optimization," *Lightwave Technology, Journal of*, vol. 21, no. 8, pp. 1749–1757, 2003.

[158] R. DeSalvo, A. Wilson, J. Rollman, D. Schneider, L. Lunardi, S. Lumish, N. Agrawal, A. Steinbach, W. Baun, T. Wall, R. Ben-Michael, M. Itzler, A. Fejzuli, R. Chipman, G. Kiehne, and K. Kissa, "Advanced components and sub-system solutions for 40 Gb/s transmission," *Lightwave Technology, Journal of*, vol. 20, no. 12, pp. 2154–2181, 2002.

[159] K. Shi, R. Watts, D. Reid, T. Huynh, C. Browning, P. Anandarajah, F. Smyth, and L. Barry, "Dynamic linewidth measurement method via an optical quadrature front end," *Photonics Technology Letters, IEEE*, vol. 23, pp. 1591–1593, Nov 2011.